



RAHUL KRISHNA

**Grafeno dopado com metais de transição para
aplicações elétricas e de energia**

**Transition metal doped graphene for energy and
electrical applications**



**RAHUL KRISHNA Grafeno dopado com metais de transição para
aplicações elétricas e de energia**

**Transition metal doped graphene for energy and
electrical applications**

Tese apresentada à Universidade de Aveiro para cumprimento dos requisitos necessários à obtenção do grau de Doutor em Nanociências e Nanotecnologia, realizada sob a orientação científica da Doutora Elby Titus, Investigadora do Departamento de Engenharia Mecânica da Universidade de Aveiro e do Doutor João Manuel de Sá Campos Gil, Professor Associado com Agregação da Universidade de Coimbra.

" Dedicado a meus pais, irmão e irmãs mais velhas "

o júri

presidente

Prof. Doutor Valeri Skliarov
Professor Catedrático, Universidade de Aveiro

Prof. Doutora Ana Cristina Moreira Freire
Professora Catedrática, Faculdade de Ciências, Universidade do Porto

Prof. Doutor João Manuel de Sá Campos Gil
Professor Associado com Agregação, Faculdade de Ciências e Tecnologia,
Universidade de Coimbra (coorientador)

Prof. Doutor Tito da Silva Trindade
Professor Associado com Agregação, Universidade de Aveiro

Prof. Doutor João Pedro Esteves de Araújo
Professor Auxiliar, Faculdade de Ciências, Universidade do Porto

Doutora Elby Titus
Professora Auxiliar Convidada, Universidade de Aveiro (orientadora)

Doutor João Oliveira Ventura
Investigador Auxiliar, Faculdade de Ciências, Universidade do Porto

Doutora Carmen Mireya Rangel Archila
Investigadora Coordenadora, Laboratório Nacional de Energia e Geologia
(LNEG), Lisboa

agradecimentos

At this moment of completion of my PhD thesis first and foremost I would like to express my special appreciation and thanks to my supervisor Dr. Elby Titus for her trust, guidance, kind support, motivation and giving an opportunity for research work. She mentor me throughout the research work over the years with her dedication, sympathy and availability. She encouraged mine new ideas and advising me during all phases of my PhD research work, giving me a freedom for solving the problems.

I am also special thankful for Professor João Manuel de Sá Campos Gil for providing the great facility of hydrogen storage and establishing a full flash lab for my research work. Without his kind support it was highly impossible for me to reach the goal. I am highly delightful for his invitation to work with him and giving a special work place for me.

I would also like to special thanks to Professor João Ventura for providing continuous facility of electrical measurements and work place for my research work. It was the great pleasure for me getting vast knowledge of experimental physics from him.

I am also very grateful for Professor Cristina Freire for providing chemical lab facilities and instruments throughout my research work and allowing me to work with her great research group.

I am sincerely thankful for Doutor Diana Mónica de Mesquita Sousa Fernandes for her kind support and guidance for instrumentations and chemical characterizations, taking care of my research work, sharing the equipment and providing her valuable suggestions for improving the research.

I would like to express my sincere gratitude to Mr. Valdemar F. Domingos and Edivagner S. Ribeiro for providing kind support for hydrogen storage work and sharing great knowledge and constant help for Sievert's instrument.

My great expression for Dr. Marc G. Willinger, FHI, Berlin, Germany for providing me a great opportunity for transmission electron microscopy (TEM) technique to characterize my samples.

My special thank to friends and colleagues for companionship, friendship and caring especially to Dr. Olena Okhay, Miss Maryam Salimian, Miss Catarina Dias.

I would like to express my deepest gratitude to my family, especially my parents, my elder brothers and sisters for motivation, support and encouragement for continuous research work for good success in my career.

Finally, I would like to acknowledge the support of FCT, TEMA-DEM, UA for providing funding and an opportunity for this work.

Last but not the least my thanks to those who, directly or indirectly, contributed to realization of this research and make possible my thesis.

palavras-chave

Grafeno, nanopartículas de níquel, nanopartículas de Pd, armazenamento de hidrogénio, produção de hidrogénio, reação catalítica, memristor, biosensor de glicose

resumo

Do ponto de vista do rápido progresso na fabricação de dispositivos eletrónicos de armazenamento de energia em nanoescala, o grafeno é um assunto de grande interesse. Como um sistema verdadeiramente bidimensional (2D), o grafeno possui propriedades extraordinárias de alta condutividade, grande mobilidade de portadores de carga, grande área de superfície ($> 2600 \text{ m}^2 / \text{g}$), flexibilidade e estabilidade química, que são favoráveis para aplicações energéticas. A síntese de grafeno de alta qualidade ainda permanece como um grande desafio na investigação no grafeno. Vários métodos, incluindo esfoliação mecânica, térmica e deposição química por vapor (CVD) são métodos utilizados para a produção de grafeno de alta qualidade. No entanto, a produção em massa de grafeno só é possível por esfoliação química de grafite sob agentes oxidantes fortes. Esta tese lida com o estado da arte de produção de óxido de grafeno reduzido (RGO) em massa usando óxido de grafeno (GO) como agente intermediário. Uma das ideias empolgantes em relação ao óxido de grafeno é a de que, devido aos grupos funcionais ligados, ele poderia actuar como um laboratório para várias reacções catalíticas e conduzir à fabricação de novos dispositivos. Os metais de transição foram usados para auxiliar a reacção e para atingir as novas propriedades desejadas.

Por reacções catalíticas, as nanopartículas de alta qualidade (NPs), tais como Ni, Co, Pd, Ag, Cu, Ni_xB , Co_xB e SiO_2 foram sintetizadas e ancoradas numa folha de grafeno para aplicações de energia. Particularmente, para o armazenamento de hidrogénio um catalisador nanocompósito contendo paládio@níquel boreto-sílica e óxido de grafeno reduzido ($\text{Pd} @ \text{Ni}_x\text{B-SiO}_2 / \text{RGO}$, abreviado como $\text{Pd} @ \text{NSG}$) foi fabricado com sucesso. A experiência de adsorção de H_2 revela diretamente o efeito de transbordo (*spillover*) no nanocompósito $\text{Pd} @ \text{NSG}$ e sua maior capacidade de absorção de H_2 (0,7 wt.%) em comparação com $\text{SiO}_2 / \text{RGO}$ (0,05 wt.%), sob uma pressão de 50 bar de hidrogénio à temperatura ambiente. Com base nos resultados um mecanismo detalhado de transbordo de hidrogénio é estabelecido que exhibe a dissociação fácil de H_2 no ativador Pd (centros activos) e o transporte subsequente de átomos de hidrogénio em locais receptores. Da mesma forma, o altamente ativo e rentável nanocompósito $\text{Co}_x\text{B} @ \text{Ni} / \text{RGO}$ foi também sintetizado para produção de hidrogénio através de oxidação eletroquímica de etanol em meio alcalino sob catálise de reacção. O comportamento eletroquímico do nanocompósito foi avaliado pela técnica de voltametria cíclica (CV). A atividade catalítica do nanocompósito foi avaliada continuamente por 50 ciclos; surpreendentemente, os resultados mostram que o aumento da densidade de corrente após 50 ciclos sugere o processo de auto-limpeza e robustez do sistema de catalisador.

resumo cont.

Para a aplicação de energia, o nanocompósito baseado em grafeno também tem sido usado para a redução catalítica de 4- nitrofenol (4- NP) poluente orgânico . Para este trabalho, uma ampla gama de catalisadores de grafeno nanocompósito foi sintetizada e o esforço foi o de reduzir o tempo de reação e o custo do sistema nanocatalisador. Finalmente, o nanocompósito baseado em grafeno (Ni / RGO) é usado para aplicações elétricas e eletrônicas, e também para fabricar os dispositivos memresistivos e biossensores de glicose.

Uma vasta gama de técnicas de caracterização, principalmente difração de raios X (XRD), espectroscopia de infravermelhos (FTIR, Raman, espectroscopia de fotoelétrons de raios-X (XPS), microscopia eletrônica de varrimento (SEM), microscopia eletrônica de transmissão (TEM), medições de corrente vs. tensão (I-V), voltametria cíclica (CV) e espectroscopia de impedância eletroquímica (EIS), foram usadas para análise de nanocompósitos de grafeno dopados com metais de transição para vários tipos de aplicações de energia.

keywords

Graphene, Nickel nanoparticles, Pd nanoparticles, hydrogen storage, hydrogen production, catalysis reaction, memristor, glucose biosensor.

abstract

In the view of rapid progress in the fabrication of nanoscale energy storage and electronic devices, graphene is a subject of great interest. As a truly two dimensional (2D) system, graphene possess extraordinary properties of high conductivity, high carrier mobility, large surface area ($>2600 \text{ m}^2/\text{g}$), flexibility, and chemical stability which are favourable for energy applications. Synthesis of high quality graphene still remains as a major challenge in graphene research. Various methods including mechanical exfoliation, thermal exfoliation and thermal chemical vapour deposition (CVD) methods are used for the production of high quality graphene. However, mass production of graphene is possible only by chemical exfoliation of graphite under strong oxidizing agents. This thesis deals with the state of the art mass production of reduced graphene oxide (RGO) using graphene oxide (GO) as the intermediate agent. One of the exciting ideas about graphene oxide is that, due to the functional groups attached, it could act as a laboratory for various catalytic reactions and led to the fabrication of novel devices. Transition metals were used to aid the reaction and to achieve desired novel properties.

By catalytic reactions, high quality nanoparticles (NPs) such as Ni, Co, Pd Ag, Cu, Ni_xB , Co_xB and SiO_2 were synthesized and anchored on graphene sheet for energy applications. Particularly, for hydrogen storage a nanocomposite catalyst containing palladium@ nickel boride–silica and reduced graphene oxide ($\text{Pd}@ \text{Ni}_x\text{B}-\text{SiO}_2/\text{RGO}$, abbreviated as $\text{Pd}@ \text{NSG}$) was successfully fabricated. The H_2 adsorption experiment directly reveals the spillover effect on the $\text{Pd}@ \text{NSG}$ nanocomposite and its enhanced H_2 uptake capacity (0.7 wt.%) compared to SiO_2/RGO (0.05 wt.%) under 50 bar hydrogen pressure at RT. On the basis of results a detailed mechanism of hydrogen spillover is established that exhibited the facile H_2 dissociation on the Pd activator (active sites) and subsequent transportation of hydrogen atoms on receptor sites. Similarly, highly active and cost effective nanocomposite $\text{Co}_x\text{B}@ \text{Ni}/\text{RGO}$ was also synthesized for hydrogen production through electrochemical oxidation of ethanol in alkaline medium under catalysis reaction. The electrochemical behavior of nanocomposite was evaluated by cyclic voltammetry (CV) technique. The catalytic activity of nanocomposite was evaluated continuously for 50 cyclic run; amazingly, results shows that the increase of current density after 50 cycle run suggests the self-cleaning process and robustness of catalyst system.

Abstract cont.

For energy application, graphene based nanocomposite has also been employed for catalysis reduction of 4-nitrophenol (4-NP) organic pollutant. For this work, a wide range of graphene nanocomposite catalysts has been synthesized and the effort was to reduce reaction time and cost of nanocatalyst system. Finally, graphene based nanocomposite (Ni/RGO) is used for electrical and electronics applications also, to fabricate the memristor devices and glucose biosensor.

A wide range of characterization techniques mainly X-ray diffraction (XRD), fourier transform infra-red (FTIR), Raman, X-ray photoelectron spectroscopy (XPS), scanning electron microscopy (SEM), transmission electron microscopy (TEM), current vs. voltage (I-V) measurements, cyclic voltammetry (CV) and electrochemical impedance spectroscopy (EIS) were employed for analysis of transition metals doped graphene nanocomposites for various kind of energy applications.

GENERAL INDEX

GENERAL INDEX	I
PUBLICATIONS LIST	VII
ABBREVIATIONS LIST	XI
SYMBOLS LIST	XIV
FIGURE INDEX	XVI
TABLE INDEX	XXIII

Chapter	1
----------------	----------

Introduction: Hydrogen storage- Issue, solutions and approaches	1
1.1 Hydrogen storage	3
1.1.1 Various options for hydrogen storage	5
1.1.1.1 High Pressure hydrogen storage	6
1.1.1.2 Liquefaction	7
1.1.1.3 Material based hydrogen storage	8
1.2 Chemical storage of hydrogen	9
1.2.1 Hydrogen storage in metal hydrides	10
1.2.2 Hydrogen storage in complex hydrides	12
1.2.3 Hydrogen storage in amides and ammonia borane compounds	14
1.3 Chemical hydrogen storage in liquid form	16
1.3.1 Chemical hydrogen storage in ammonia and hydrazine	16
1.3.2 Hydrogen storage in N-Heterocyclic compound	18
1.3.3 Hydrogen storage in ethanol	19
1.3.4 Hydrogen storage in formic acid	20
1.4 Hydrogen storage in nanoporous materials	21
1.4.1 Hydrogen storage in Zeolites	21
1.4.2 Hydrogen storage in carbonaceous materials	22
1.4.3 Hydrogen storage in MOFs	23
1.5 Theory of physisorption	25

1.6	Hydrogen storage in CNTs	27
1.7	Hydrogen storage in graphene	30
1.8	Scope of the thesis	39
1.9	References	41

Chapter 2

Hydrogenation of graphene oxide: Synthesis, characterization and results 50

2.1	Introduction	52
2.2	Synthesis of hydrogenated reduced graphene oxide (HRGO)	52
2.2.1	Experimental	53
2.2.1.1	Chemicals	53
2.2.1.2	Synthesis of GO	53
2.2.1.3	Synthesis of HRGO	54
2.2.2	Characterization techniques	54
2.2.3	Results and discussion	55
2.3	Rapid Electrochemical Synthesis of Hydrogenated Graphene Oxide Using Ni NPs	58
2.3.1	Synthesis of HGO	58
2.3.2	Results and discussion	58
2.3.3	Mechanism of HGO formation	64
2.4	Coconclusions	65
2.5	References	65

Chapter 3

Graphene nanocomposites for hydrogen storage: Synthesis, characterization and results 67

3.1	Introduction	69
3.2	Experimental	70
3.2.1	Chemicals	70
3.2.2	Synthesis of GO	71

3.2.3	Synthesis of HRGO	71
3.2.4	Synthesis of Ni _x B-SiO ₂ /RGO and Pd@NSG nanocomposite	71
3.2.5	Characterizations	72
3.3	Results and discussion	72
3.4	Conclusions	80
3.5	References	80

Chapter **4**

Theoretical aspect of hydrogen storage in nanomaterials: Grand canonical Monte Carlo simulations for hydrogen adsorption in NaA zeolites **82**

4.1	Introduction	84
4.2	Model and methods	85
4.2.1	NaA Zeolite structure	85
4.2.2	Potential Model	87
4.2.3	Henry Coefficient	88
4.3	Simulation details	89
4.4	Results	91
4.5	Conclusions	94
4.6	References	94

Chapter **5**

Transition metals doped graphene nanocomposite for electrochemically hydrogen generation: synthesis, characterization and results **96**

5.1	Introduction	98
5.2	Experimental	100

5.2.1	Syntheis	100
5.2.2	Characterization techniques	101
5.3	Results and discussion	102
5.4	Coclusions	114
5.5	References	115

Chapter **6**

Direct hydrogen generation through NaBH₄ hydrolysis reaction –potential role of graphene nanocomposite: synthesis, characterization, results and mechanism **121**

6.1	Introduction	123
6.2	Experimental	124
6.2.1	Syntheis	124
6.2.2	Characterization techniques	125
6.2.3	Hydrogen generation test	126
6.3	Results and discussion	126
6.4	Conclusion	140
6.5	References	140

Chapter **7**

Graphene nanocomposite for catalysis reaction: Synthesis, characterization and results **143**

7.1	Introduction	145
7.2	Cu@Ni/RGO nanocomposite	146
7.2.1	Experimental	146
7.2.2	Characterization	147
7.2.3	Catalytic reduction of 4-NP	147
7.2.4	Results and discussion	147
7.3	Ag@Co/RGO nanocomposite and its high catalytic activity towards hydrogenation of 4-nitrophenol to 4-aminophenol	156

7.3.1	Synthesis of Ag@Co/RGO catalyst	156
7.3.2	Catalytic reduction of 4-NP	156
7.3.3	Results and discussion	157
7.4	Hydrogenation of 4-nitrophenol to 4-aminophenol using Pd@NSG	163
7.5	Conclusions	166
7.6	References	166

Chapter **8**

<u>Electrical and electronics applications of graphene nanocomposite: structure, measurements and results</u>		169
8.1	Introduction	171
8.2	Resistive switching device based on Ni-doped graphene oxide thin films	172
8.2.1	Fabrication of MIM structure	173
8.2.2	Measurements	173
8.2.3	Results	173
8.3	Switching characteristic of hydrogenated graphene oxide thin films	177
8.4	Resistive switching in Co/RGO nanocomposite	178
8.4.1	Resistive switching in Co/RGO nanocomposite	178
8.4.2	Synthesis of Co/RGO nanocomposite	179
8.4.3	Results and discussion	179
8.5	New hybrid material Ni(OH)₂@Ni/RGO nanocomposite for resistive switching applications: Observation of large hysteresis	180
8.5.1	Synthesis of Ni(OH) ₂ @Ni/RGO nanocomposite	180
8.5.2	Results and discussion	181
8.6	Ag@SiO₂/RGO nanocomposite for memristor application	184
8.6.1	Synthesis of Ag@SiO ₂ /RGO nanocomposite	185
8.6.2	Device fabrication of Ag@SiO ₂ /RGO nanocomposite	185
8.6.3	Results and discussion	185
8.7	Conclusions	188
8.8	References	188

Ni/RGO nanocomposite for glucose biosensing: Structure, measurements and results	190
9.1 Introduction	192
9.2 Experimental	193
9.2.1 Chemicals	193
9.2.2 Synthesis of Ni/RGO nanocomposite	193
9.2.3 Preparation of Ni/RGO/Chit95/GOx Films	194
9.2.4 Characterization techniques	194
9.3 Results and discussion	195
9.4 Conclusions	199
9.5 References	200

Conclusions	201
--------------------	------------

Appendix:	205
------------------	------------

A1: Graphene conversion	206
Transformation of 2D graphene to different nanostructures: Tubes, wires, nanoribbons, triangle, parallelogram, H ₂ filled nanoballoon	207
A2 Anchoring of graphene nanosheet with various type of NPs	212
A3 Multicatalytic applications of Pd@Ni/RGO nanocomposite	213

PUBLICATIONS LIST

International Journals/ Proceedings, Conferences, Book Chapters

A. List of publications in International Journal:

1. **Rahul Krishna**, Diana M. Fernandes, João Ventura, Cristina Freire, Elby Titus. “Novel synthesis of highly catalytic active Cu@Ni/RGO nanocomposite for efficient hydrogenation of 4-nitrophenol organic pollutant”. International Journal of hydrogen energy, (2015) (*in press*) [doi:10.1016/j.ijhydene.2015.12.027](https://doi.org/10.1016/j.ijhydene.2015.12.027)
2. **Rahul Krishna**, Diana M. Fernandesb, Catarina Dias, João Ventura, Cristina Freire, Elby Titus. “Facile synthesis of novel Co-B@Ni/RGO nanocomposite: A cost effective catalyst for improved hydrogen generation with enhanced electrochemical activity”. International Journal of hydrogen energy, (2015) (*in press*) [doi:10.1016/j.ijhydene.2015.12.052](https://doi.org/10.1016/j.ijhydene.2015.12.052)
3. **Rahul Krishna**, Diana M. Fernandes, João Ventura, Cristina Freire, Elby Titus. “Facile synthesis of reduced graphene oxide supported Pd@Ni_xB/RGO nanocomposite: Novel electrocatalyst for ethanol oxidation in alkaline media”. International Journal of hydrogen energy, (2015) (*in press*) [doi:10.1016/j.ijhydene.2015.12.034](https://doi.org/10.1016/j.ijhydene.2015.12.034)
4. Priyanka Tavhare, Vijayanand Kalamse, **Rahul Krishna**, Elby Titus, Ajay Chaudhari. “Hydrogen adsorption on Ce-ethylene complex using quantum chemical methods”. International Journal of hydrogen energy, (2015) (*in press*) [doi:10.1016/j.ijhydene.2015.11.172](https://doi.org/10.1016/j.ijhydene.2015.11.172)
5. V. Kalamse, **Rahul Krishna**, Elby Titus, Ajay Chaudhari. “Boron substituted and un-substituted aromatic complexes as hydrogen storage media”. International Journal of hydrogen energy, (2015) (*in press*) [doi:10.1016/j.ijhydene.2015.11.171](https://doi.org/10.1016/j.ijhydene.2015.11.171)
6. **Rahul Krishna**, Diana M Fernandes, Valdemar F Domingos, Edvagner S Ribeiro, João Campos Gil, Catarina Dias, João Ventura, Cristina Freire, Elby Titus. “Reduction of 4-nitrophenol to 4-aminophenol using a novel Pd@ Ni_xB-SiO₂/RGO nanocomposite: enhanced hydrogen spillover and high catalytic performance”. RSC Advances, 5 (2015) pp. 60658-60666.
7. **Rahul Krishna**, Diana M Fernandes, Catarina Dias, Joao Ventura, E Venkata Ramana, Cristina Freire, Elby Titus. “Novel synthesis of Ag@ Co/RGO nanocomposite and its high catalytic activity towards hydrogenation of 4-nitrophenol to 4-aminophenol”. International Journal of Hydrogen Energy, 40 (2015) pp. 4996-5005.
8. Olena Okhay, **Rahul Krishna**, Alexander Tkach, Mathias Kläui, Luis M Guerra, João Ventura, Elby Titus, Jose Gracio. “Drastic modification of graphene oxide properties by incorporation of nickel: a simple inorganic chemistry approach”. Journal of Materials Science, 50 (2015) pp. 3425.

9. R. S. Khairnar, M. D. Wakde, M. P. Mahabole, **Rahul Krishna**, Elby Titus. "Development of Ethanol Sensor using Sodium Nano Zeolite". *International Journal of Engineering and Innovative Technology (IJEIT)*, 3 (2014) pp. 306-310.
10. **R. Krishna**, E. Titus, O. Okhay, J. C. Gil, J. Ventura, E. V. Ramana, J. Gracio. "Rapid electrochemical synthesis of hydrogenated graphene oxide using Ni nanoparticles". *International Journal of Electrochemical Society*, 9 (2014) pp. 4054-4069.
11. O. Okhay, **R. Krishna**, M. Salimian, E. Titus, J. Gracio, L. M. Guerra, J. Ventura. "Electrical properties of polycarbonate and panipol by addition of graphene oxide and reduced graphene oxide as nanofillers". *Journal of Applied Physics* 113 (2013) pp. 064307.
12. M. Salimian, O. Okhay, **R. Krishna**, E. Titus, J. Gracio, L. Guerra, J. Ventura, C. Freire, C. Pereira, P. R. Babu, R. S. Khairnar. "Electrical conductivity of LTA-zeolite in the presence of poly vinyl alcohol and poly vinylpyrrolidone polymers". *Polymer International*, 62 (2013) 1583-1588.
13. **Rahul Krishna**, Elby Titus, Luís C. Costa, José C. J. M. D. S. Menezes, Maria R. P. Correia, Sara Pinto, João Ventura, J. P. Araújo, José A. S. Cavaleiro, José J. A. Gracio. "Facile synthesis of hydrogenated reduced graphene oxide via hydrogen spillover mechanism". *Journal of Materials Chemistry A*, 22 (2012) pp. 10457-10459.
14. Sara Pinto, **Rahul Krishna**, C. Dias, G. Pimentel, G. N. P. Oliveira, J. M. Teixeira, P. Aguiar, E. Titus, J. Gracio, J. Ventura, J. P. Araujo. "Resistive switching and activity-dependent modifications in Ni-doped graphene oxide thin films". *Applied Physics Letter*, 101 (2012) pp. 063104.
15. **Rahul Krishna**, S. Chandra, N. Bardhan, M. Salimian, Y. Y. Yang, E. Titus, J. Gracio, D. Bahadur. "Design of an amperometric glucose biosensor based on Glucose oxidase (GOx)/Arginated Fe₃O₄/Glassy Carbon Electrode (GCE)". *Science of Advanced Material*, 5 (2013) pp. 333-340.
16. **Rahul Krishna**, Elby Titus, Sudeshna Chandra, Neelkanth Bardhan, Rohit Krishna, Dharendra Bahadur, Jose Gracio. "Wet-Chemical Green Synthesis of L-Lysine Amino Acid Stabilized Biocompatible Iron-Oxide Magnetic Nanoparticles", *J Nanosci Nanotechno*, 12 (2012) pp. 6645.
17. **Rahul Krishna**, Elby Titus, Neelkanth Bardhan, Sudeshna Chandra, Rohit Krishna, Dharendra Bahadur, Jose Gracio, "Fabrication of a glucose biosensor based on citric acid assisted cobalt ferrite magnetic nanoparticles". *Journal of Nanoscience and Nanotechnology*, 12 (2012) pp. 6631-6638.
18. M. K. Singh, Elby Titus, **Rahul Krishna**, R. R. Hawaldar, G. Goncalves, P. A. Marques, Jose Gracio, "Direct nucleation of silver nanoparticles on graphene sheet", *Journal of Nanoscience and Nanotechnology*, 12 (2012) pp. 6731-6736.
19. J. M. Sousa, A. L. Ferreira, D. P. Fagg, Elby Titus, **Rahul Krishna**, Jose Gracio, "Temperature dependence of the Henry's law constant for hydrogen storage in NaA zeolites: a Monte Carlo simulation study". *Journal of Nanoscience and Nanotechnology*, 12 (2012) pp. 6785-6791.

B. List of Conference proceeding papers:

1. **R. Krishna**, E. Titus. “Facile synthesis of Cu₂O/Cu/RGO nanocomposite”. Material Today Proceeding, 2 (2015) pp. 399-406.
2. **R. Krishna**, D. M. Fernandes, E. Venkataramana, C. Dias, J. Ventura, C. Freire, E. Titus. “Improved Reduction of Graphene Oxide”. Materials Today Proceedings, 2 (2015) pp. 423-430
3. **R. Krishna**, C. Dias, J. Ventura, E. Titus. “Synthesis of Ni (OH)₂@ Ni/RGO Nanocomposite: Formulation of One Dimensional Array”. Material Today Proceeding, 2 (2015) pp. 407-415.
4. Olena Okhay, Luis M Guerra, João Ventura, Alexander Tkach, Mathias Kläui, **Rahul Krishna**, Elby Titus. “Electrical and Magnetic Properties of Graphene Films with Ni Nanoparticles”. Material Today Proceeding 2 (2015) pp. 383-388.
5. Olena Okhay, **Rahul Krishna**, Elby Titus, Kateryna Andreeva, Rada Savkina, Oleksii Smirnov. “Photovoltage Study of Graphene Oxide with Ni Nanoparticles”. Material Today Proceeding (2015).
6. J. P. Araujo, S. Pinto, **R. Krishna**, C. Dias, G. Pimentel. “Switching and learning in Ni-doped graphene oxide thin films”. In proceeding of: Frontiers in Electronic Materials, DOI: ISBN 978-3 527-41191-7, 6/2012.
7. **Rahul Krishna**, Diana M. Fernandes, Catarina Dias, Cristina Freire, João Ventura, Elby Titus. “Facile synthesis of Co/RGO nanocomposite for methylene blue dye removal”. Material Today Proceeding (2016).
8. **Rahul Krishna**, Catarina Dias, João Ventura, Elby Titus. “Green and facile decoration of Fe₃O₄ nanoparticles on reduced graphene oxide”. Material Today Proceeding (2016).

C. List of Conference poster presentations:

1. **Rahul Krishna**, Diana M. Fernandes, Catarina Dias, Cristina Freire, João Ventura, Elby Titus, “Enhanced H₂ storage in graphene nanocomposite through spillover mechanism”. ANM 2015: 6th International Conference on Advanced materials.
2. **Rahul Krishna**, Catarina Dias, Diana M. Fernandes, Célia Sousa, Luís Guerra, Cristina Freire, João P. Araujo, João Ventura, Elby Titus. “Facile and rapid synthesis of hydrogenated graphene oxide and their current-rectifier property for negative bias”. ANM 2015: 6th International Conference on Advanced materials.
3. **Rahul Krishna**, Diana M. Fernandes, Catarina Dias, Cristina Freire, João Ventura, Elby Titus,

- “Synthesis of monodisperse Cu nanoparticles on graphene sheet”. **ANM 2015**: 6th International Conference on Advanced materials.
4. Vijayanand Kalamse, **Rahul Krishna**, Elby Titus, Ajay Chaudhari. “Boron substituted and un-substituted aromatic complexes as hydrogen storage media”. **ANM 2015**: 6th International Conference on Advanced materials.
 5. Priyanka Tavhare, **Rahul Krishna**, Vijayanand Kalamse, Elby Titus, Ajay Chaudhari. “Hydrogen adsorption on Ce-ethylene complex using quantum chemical methods”. **ANM 2015**: 6th International Conference on Advanced materials.
 6. **Rahul Krishna**, Elby Titus, Olena Okhay, Catarina Dias, E. V. Ramana, Joao Ventura, Jose Gracio. “Enhanced resistive switching capability of RGO-MnO₂ nanocomposite via incorporation of extra hydroxyl groups”. **ANM 2014**: 5th International Conference on Advanced materials.
 7. **Rahul Krishna**, Elby Titus, Olena Okhay, Catarina Dias, E. V. Ramana, Joao Ventura, Jose Gracio. “A new hybrid material Ni/Ni(OH)₂/RGO nanocomposite for memristive applications”. **ANM 2014**: 5th International Conference on Advanced materials.
 8. Olena Okhay, Luis M. Guerra, João Ventura, Alexander Tkach, Mathias Kläui, **Rahul Krishna**, Elby Titus, Jose Gracio. “Electrical and magnetic properties of graphene films with Ni nanoparticles”. **ANM 2014**: 5th International Conference on Advanced materials.
 9. Olena Okhay, **Rahul Krishna**, Luis M. Guerra, João Ventura, Elby Titus, Jose Gracio. “Influence of oxidation and deposition process on electrical properties of graphene films”. **ANM – 2014**: 5th International Conference on Advanced materials.

D. Published book chapters:

1. **Rahul Krishna**, Elby Titus, Maryam Salimian, Olena Okhay, Sivakumar Rajendran, Ananth Rajkumar, J. M. G. Sousa, A. L. C. Ferreira, João Campos Gil and Jose Gracio, Publisher: Intech open, **Hydrogen Storage**, Chapter: Hydrogen Storage for Energy Application, **2012**, ISBN: 978-953-51-0731-6.
2. Elby Titus, Manoj Kumar Singh, **Rahul Krishna**, Ricardo G Dias, Antonio Ferreira, Jose Gracio. Publisher: Intech open, **Electronic Properties of Carbon Nanotubes**, Chapter: Carbon Nanotube Based Magnetic Tunnel Junctions (MTJs) for Spintronics Application, **2011**, ISBN 978-953-307-499-3, 696.

Abbreviations List

AB	Ammonia borane
BDC	1,4-benzenedicarboxylic acid
BEP	Brønsted–Evans–Polanyi
BET	Brunauer–Emmett–Teller
BUs	Building units
CA	Chrono-amperometry
CCD	Charge Coupled Device
CNBs	Carbon nanobuds
CNSs	Carbon nanoscrolls
CNTs	Carbon nanotubes
CTAB	Hexadecyl-trimethyl-ammonium bromide
CV	Cyclic voltammetry
CVD	Chemical vapor deposition
DD	Double distilled
DADB	Diammoniate of diborane
DEFC	Direct ethanol fuel cells
D.O.E.	United States' Department of Energy
DOS	Density of states
EDX	Energy dispersive X-ray
EIS	Electro impedance spectroscopy
emu	Electro-magnetic unit
EOR	Ethanol oxidation reaction
equiv.	Equivalent
ETS	<i>Ger.</i> Energie-Tragende Stoffe; <i>Eng.</i> Energy carrying compounds
fcc	Face-centred cubic
FCTO	Fuel cell technologies office
Fe-Ti	Iron-titanium alloy
FTIR	Fourier transform infrared
GCE	Glassy carbon electrode
GCMC	Grand canonical Monte Carlo
gge	Gallon gasoline equivalent
GO	Graphene oxide
GOx	Glucose oxidase
JCPDS	Joint Committee on Powder Diffraction Standards
H/M	Hydrogen vs metal ratio
HGO	Hydrogenated graphene oxide
HRGO	Hydrogenated reduced graphene oxide
HRS	High resistance state
HRTEM	High resolution transmission electron microscopy
ITO	Indium-tin oxide
kWh	Kilo-watt hour
L-AA	L-ascorbic acid
LaNi ₅	Lanthanum-nickel 5

LH ₂	Liquid hydrogen
L-J	Lennard-Jones
LOHC	Liquid organic hydrogen carriers
LRS	Low resistance state
LTA	Linde-type A
LTM	long-term-memory
MHs	Metal hydrides
MgH ₂	Magnesium hydride
MgNi	Magnesium-nickel alloy
MPa	Mega Pascal
MIM	Metal-insulator-metal
MNPs	Magnetic nanoparticles
MOF	Metal organic framework
NaBH ₄	Sodium borohydride
NEC	N-ethylcarbazole
NH ₂ NH ₂	Anhydrous hydrazine
NH ₄ Cl	Ammonium chloride
NPs	Nanoparticles
PAA	Poly-acrylic acid
PBS	Phosphate buffer saline
PCT	Pressure-composition-temperature isotherm
PC	pressure-composition-isotherm
PECVD	Plasma-enhanced chemical vapor deposition
PEM	Proton exchange membrane
PEDOT	Poly(ethylenedioxythiophene)
psi	Pounds per square inch
PNP	Para-nitro phenol
PVA	Poly-vinyl alcohol
PVP	Poly-vinyl pyrrolidone
QHE	Quantum hall effect
RRAM	Resistive random access memory
RB	Round bottom
RLC	Reset-like condition
RGO	Reduced graphene oxide
rms	Root mean square
rpm	Rotation per minute
RS	Resistive switching
RT	Room temperature
SAED	Selected area electron diffraction
SBU _s	Secondary building units
SEM	Scanning electron microscopy
SHE	Standard hydrogen electrode
SLC	Set-like condition
S _{spec}	Specific surface area
SWNT	Single-walled nanotubes
TEM	Transmission electron microscopy
TGA	Thermogravimetric analysis
THF	Tetrahydrofuran
VSM	Vibrating sample magnetometer

XRD,
XPS
UV-vis
4-NP
4-AP

X-ray diffraction
X-ray photoelectron spectroscopy
Ultra-violet visible
4-nitrophenol
4-aminophenol

Symbols List

Ag	Silver
B	Boron
C	Carbon
C ⁻	Carbide
CH ₄	Methane
CH ₃ OH	Methanol
C ₂ H ₅ OH	Ethanol
CO	Carbon monoxide
Co	Cobalt
CO ₂	Carbon dioxide
Cu	Copper
E	Electric field
E _a	Activation energy
E _{1/2}	Half wave potential
E _{pa}	Anodic peak potential
E _{pc}	Cathodic peak potential
eV	Electron volt
E _{pf}	Forward peak
E _{pb}	Backward peak
ΔG	Gibbs free energy change
H ⁺	Proton
H [•]	Hydrogen radical
ΔH	Enthalpy change
H ₂	Hydrogen molecule
H ⁻	Hydride
HCOOH	Formic acid
H _z	Frequency
I _{pa}	Anodic peak current
I _{pc}	Cathodic peak current
I _D /I _G	Raman intensity ratio D and G bands
j _{pf}	Forward current density
j _{pb}	Backward current density
k	Rate constant
K	Kelvin
KZ	Potassium zeolite
K _H	Henry coefficient
Li	Lithium
NaZ	Sodium Zeolite
Ni	Nickel
P _a	Pascal
Pd	palladium
q	Electric charge
SiO ₂	Silicon dioxide

R	Rydberg's constant (Gas constant)
R_{ct}	Charge transfer resistance $R\Omega$ Cell resistance
T	Temperature
T_c	Critical temperature point
T_{dec}	Decomposition temperature
wt.%	Weight percentage
W_{th}	Theoretical work
$^{\circ}C$	Degree centigrade
\$	Dollar
Λ	de Broglie wavelength
λ	Wavelength
ν	Frequency
Ω	Ohm
ρ	Density
μ	Chemical potential

FIGURE INDEX

Chapter 1

Figure 1.1 Various options of hydrogen energy storage	4
Figure 1.2 Hydrogen storage in tanks (a) outer jacket (b) recently, reported inner tube lining of compressed tanks made by carbon nanofibers (CNFs)	6
Figure 1.3 Liquid hydrogen storage tank, horizontal mounted with double gasket and dual seal...	7
Figure 1.4 Chemically hydrogen storage in ammonia borane	8
Figure 1.5 A survey plot of hydrogen storage in various metal hydrides.....	10
Figure 1.6 Pressure composition (<i>p-c</i>) isotherm for the hydrogen absorption in a typical inter-metallic compound: (a) the solid solution (α -phase), the hydride phase (β -phase) formation and the region of the coexistence of the two phases flat plateau ($\alpha + \beta$) phase and their end at critical point (T_c), (b) the construction of the van't Hoff plot to calculate the enthalpy and entropy of the system, (c) demonstration of hysteresis in the isotherms between desorption/ absorption process, and (d) schematic example of metal hydride formation by loading and release of hydrogen inside of metal alloy.....	11
Figure 1.7 Schematic diagram of the crystal structure of NH_3BH_3 (a) and a view along z axis (b) at room temperature (298 K).....	15
Figure 1.8 Schematic representation of ammonia borane (AB) decomposition for hydrogen generation. Three different methods, (i) most common thermal decomposition method, however, it shows major drawback formation of thermodynamically stable by products borazine and their analogues, (ii) catalytic decomposition and (iii) hydrolysis in presence of catalyst.....	15
Figure 1.9 Decomposition of hydrous hydrazine in the presence of metal NPs (metal/ N_2H_4) 1:10) at 298 K. The inset shows respective TEM image of Rh(0) NPs and the corresponding SAED pattern.....	17
Figure 1.10 Hydrogenation/dehydrogenation of NEC.....	18
Figure 1.11 Schematic representation of PEM fuel cell.....	19
Figure 1.12 Schematic representation of reversible and recyclable hydrogen storage of formic acid on the surface of organic ligands encapsulated with Ir catalyst.....	20
Figure 1.13 A unit cell of sodium zeolite with cage and cavity.....	21
Figure 1.14 A complete survey plot of hydrogen storage in metal hydrides and carbon materials...	23
Figure 1.15 Structure and H_2 adsorption of MOF with and without doping.....	24
Figure 1.16 Unit cell of MOF with octahedral cluster structure	24
Figure 1.17 Representation of the structure of MIL-53 showing the expansion effect due to the removal of a water molecule from the cavities, (a) hydrated (left), (b) dehydrated (right); octahedra: $\text{MO}_4(\text{OH})_2$, $\text{M} = \text{Al}^{3+}$, Cr^{3+} . The dehydrated form of MIL-53 was tested for the hydrogen adsorption experiment.....	25
Figure 1.18 Polarization effect on adsorbate and adsorbent.....	25
Figure 1.19 Hydrogen storage on Ni (111) catalyst support and (b) energy diagram for adsorption of hydrogen on to the catalyst surface.....	26
Figure 1.20 Hydrogen storage in carbonaceous materials.....	27
Figure 1.21 Hydrogen storage in CNTs.....	28
Figure 1.22 Hydrogenation and unzipping of CNTs	29

Figure 1.23 Band structure of mono layer graphene.....	30
Figure 1.24 Structure of graphane in the chair conformation. The carbon atoms are shown in gray and the hydrogen atoms in red. The figure shows the hexagonal network with carbon in the sp^3 hybridization.....	31
Figure 1.25 Schematic representation of the crystal structure of graphene and theoretically predicted graphane. Carbon atoms are shown as blue spheres, and hydrogen atoms are shown as red spheres.....	31
Figure 1.26 Raman spectra of graphene (green), graphane (blue) and dehydrogenated product.....	32
Figure 1.27 Pillared graphane. A novel 3-D network proposed for hydrogen storage	33
Figure 1.28 Theoretical results of hydrogen storage in pillared graphane.....	33
Figure 1.29 Linking of boronic ester with graphene oxide (GO) and construction of graphene oxide framework (GOF) material by the incorporation of layers graphene oxide sheets with benzenediboronic acid pillars (B14DBA).....	34
Figure 1.30 Catalytic hydrogenation of graphene film in presence of Ni catalyst at 820 °C.....	35
Figure 1.31 Interconvertible patterning of graphane to graphene.....	36
Figure 1.32 A systematic theoretical approach for making the hydrogenation assisted graphene origami (HAGO) for programmable molecular hydrogen storage	37
Figure 1.33 AFM image of graphene cutting which clearly shows that the formation of triangles with each edge related of 60° movement, a schematic representation also (inset image).....	37
Figure 1.34 Anisotropic cutting of graphene. (a) Schematic drawing of graphene cutting by metal nanoparticles. (b), (c) AFM of graphene and graphite after cutting, respectively.....	38
Figure 1.35 Hydrogen spillover mechanism on metal catalyst site and storage of hydrogen in receptor layers through bridge building mechanism.....	39

Chapter 2

Figure 2.1 Schematic illustration for synthesis of HRGO using nickel via <i>in-situ</i> generated atomic hydrogen.....	53
Figure 2.2 displays (a) XRD of GO and HRGO and (b) FTIR spectra of GO HRGO and RGO (after the annealing). (c) XPS spectra of HRGO after deconvolution and peak fitting. (d) Raman spectra of GO, HRGO and RGO (after the annealing).....	56
Figure 2.3 (a) TEM image and (b) SAED of HRGO.....	57
Figure 2.4 Instrumental setup and representation of HGO synthesis.....	59
Figure 2.5 (a) XRD pattern of the GO, Ni-GO and HGO, (b) UV-vis. spectra of the GO, HGO and RGO, (c) FTIR spectra of the GO and HGO, and (d) Raman spectra of the GO and HGO.....	60
Figure 2.6 Fitted Raman spectra of HGO after deconvolution of D and G band.....	61
Figure 2.7 (a) and (b) SEM images of initial material GO and Ni nanoparticles, (c) and (d) SEM images of intermediate Ni-GO composite material in lower and higher magnification, and (e) and (f) SEM images of final product HGO in lower and higher magnification.....	62
Figure 2.8 (a) and (b) TEM images of intermediate Ni-GO in lower and higher magnification, and (c) and (d) TEM images of final product HGO in lower and higher magnification. Corresponding inset image of (c) is SAED and (d) 4X magnified area.....	63
Figure 2.9 Schematic representation of GO to HGO formation via intermediate species Ni-GO through continuous hydrogen spillover process during the reaction.....	64

Chapter 3

Figure 3.1 Schematic illustration of H ₂ spillover on Pd and Ni _x B@ SiO ₂ (left) and adsorption of H ₂ in Pd@NSG nanocomposite (right).....	70
Figure 3.2 Spectroscopic analysis of GO, Ni _x B-SiO ₂ /RGO and Pd@NSG nano-composite: (a) XRD pattern, (b) FTIR and (c) Raman spectroscopy; and (d) Interpretation of Raman spectroscopy with accordance of I _D /I _G ratio of GO, Ni _x B-SiO ₂ /RGO and Pd@NSG nanocomposite.....	73
Figure 3.3 (a) and (b) show the C 1s deconvoluted XPS spectra of GO and Pd@NSG nanocomposites, respectively.....	74
Figure 3.4 SEM images of: GO (a) and (b), SiO ₂ /RGO (c) and (d) and Ni _x B-SiO ₂ / RGO nanocomposites (e) and (f) in higher and lower magnifications, respectively.....	75
Figure 3.5 SEM images of Pd@NSG nanocomposite at different magnifications: 6000x (a) 15000x (b) and 40000x (c); (d) EDX spectra of Pd@NSG.....	76
Figure 3.6 TEM images (a) and (b) of Pd@NSG nanocomposite at lower and higher magnifications, respectively.....	77
Figure 3.7 HRTEM image of highly crystalline spherical Pd NPs synthesized in mild reducing condition (scale bar 2 nm).....	77
Figure 3.8 H ₂ adsorption isotherm of SiO ₂ and Pd@NSG nanocomposite up to 50 bar pressure at RT.....	79

Chapter 4

Figure 4.1 Unit cell of the zeolite NaA with site position of Na atoms as respective in α and β cages, oxygen atoms in red, T-atoms in gray and representative positions of the three types of Na ⁺ in purple.....	86
Figure 4.2 Simulated hydrogen adsorption isotherms at various temperatures. (a) The points correspond to individual simulations for temperatures of, respectively from top to bottom, 77, 100, 150, 200, 250, 273, 293, 303K. For the first three temperatures, the dashed lines simply connect the points, whereas, for the remaining higher temperatures, the curves are fits of the Langmuir isotherm function (7). (b) Adsorption data surface in P-T space.....	91
Figure 4.3 Variation of the Henry coefficient as a function of temperature.....	92
Figure 4.4 Low pressure isotherms. The points are GCMC simulations for temperatures of, from top bottom, 150, 200, 250, 273, 293, 303K. The solid lines are the corresponding Henry isotherms with KH computed directly from the particle insertion method. Visual comparison shows that the solid lines follow the slope of the simulated curves adequately.....	92
Figure 4.5 Contour maps of the total potential energy βU_i of one H ₂ molecule in an empty zeolite, averaged over all possible orientations, along two (001) planes: plane (a) goes through the center of the α cage, and is parallel to the large windows of the cage; plane (b) goes through the center of the sodalites and contains the α cage windows (8-oxygen rings). Only negative values of βU_i are plotted. Calculated for a temperature of $T=293K$. Also represented are the positions of the zeolite atoms in the vicinity of the plane: oxygens (\blacksquare), T-atoms (*), Na-I (\diamond), Na-II (\circ), Na-III (\square).....	93

Chapter 5

Figure 5.1 XRD pattern of graphite powder, GO and Pd@Ni _x B /RGO nanocomposite.....	103
Figure 5.2 FTIR of GO and Pd@Ni _x B /RGO nanocomposite.....	104
Figure 5.3 SEM images of: Pd@Ni _x B/RGO nanocomposite at lower (a) and higher (b) magnifications; Pd@Ni _x B NPs at lower (c) and higher (d) magnifications.....	105
Figure 5.4 (a) SEM image of Pd@Ni _x B/RGO nanocomposite, and (b-d) corresponding elemental mapping of C, Ni and Pd elements in respective images.....	106
Figure 5.5 TEM image of (a) GO and (b) Pd@Ni _x B/RGO nanocomposite.....	107
Figure 5.6 Deconvoluted XPS spectra for Pd@Ni _x B/RGO nanocomposite: (a) C 1s, (b) O 1s, (c) Ni 2p, (d) Pd 3d and (e) B 1s.....	108
Figure 5.7 CV of Pd@Ni _x B/RGO/GCE in 1 M KOH (black solid line, reference); the first (blue solid line) and the 50 th (red solid line) cycle run in 1 M KOH + 1 M EtOH at a scan rate of 0.050 V s ⁻¹	109
Figure 5.8 CV of Pd@Ni _x B/GCE in 1 M KOH (black solid line, reference), the 1 st (blue solid line) and the 50 th (red solid line) cycle run in 1 M KOH + 1 M EtOH at a scan rate of 0.050 V s ⁻¹	111
Figure 5.9 CV of Pd@Ni _x B/RGO/GCE in 1 M KOH + 1 M EtOH (blue solid line), and in 1M KOH + 1 M CH ₃ COOK (orange solid line) at a scan rate of 0.050 V s ⁻¹	113
Figure 5.10 Chronoamperometric (CA) measurements for the EOR in 1 M KOH and 1 M ethanol at -0.30 V vs. Ag/AgCl on a GCE modified electrodes with Pd@Ni _x B/RGO nanocomposite (red curve) and Pd@Ni _x B NPs (blue curve).....	114

Chapter 6

Figure 6.1 (a) XRD pattern and (b) FTIR spectra of GO, Co-B/RGO, Ni/RGO and Co-B@Ni/RGO nanocomposite.....	127
Figure 6.2 TGA of GO and Co-B@Ni/RGO nanocomposite	128
Figure 6.3 SEM images of: GO (a) and (b), Co-B/RGO (c) and (d), Ni/ RGO nanocomposites (e) and (f), in lower and higher magnifications, respectively.....	129
Figure 6.4 SEM images of Co-B@Ni/RGO nanocomposites (a) and (b) lower and higher magnifications, respectively. (c) Elemental mapping and (d) EDX analysis of Co-B@Ni/RGO nanocomposite.....	130
Figure 6.5 TEM images of (a) GO, (b) Co-B/RGO, (c) Ni/ RGO and (d) Co-B@Ni/RGO nanocomposites.....	131
Figure 6.6 Schematic illustration of reduction of Co ²⁺ ion under alkaline NaBH ₄ reducing condition and also H ₂ spillover mechanism on Ni/RGO and defect creation inside in graphene sheet due to H radicals.....	132
Figure 6.7 Catalytic hydrogen generation from the hydrolysis of mix solution of 1 wt. % of NaBH ₄ + NaOH at 30 °C (a) comparative study of three catalysts (i) Ni/RGO, (ii) Co-B/RGO and (iii) Co-B@Ni/RGO, (b) effect of NaOH extent (1 wt. %, 5 wt. %, 10 wt %, 15 wt. %) for hydrolysis of NaBH ₄ at 30 °C (c) temperature dependent comparative catalytic activity of Co-B@Ni/RGO nanocomposite at 25 °C, 30 °C, 35 °C and 40 °C. (d) Arrhenius plot ln k vs. the reciprocal temperature 1/T.....	133
Figure 6.8 Catalytic hydrogen generation from the hydrolysis of mix solution of 1 wt. % of NaBH ₄ + NaOH at 30 °C using Co-B@Ni/RGO (a) comparative study at three different weight (b) recyclability test of catalyst in three successive cycles.....	135

Figure 6.9 Cyclic voltammograms of Co/RGO immobilized at a GC electrode in 1 mol dm ⁻³ KOH solution at different scan rates from 0.010 to 0.500 V s ⁻¹ (a); Plots of log <i>i</i> _{pc2} and <i>i</i> _{pa2} vs. log v (b).	136
Figure 6.10 Cyclic voltammograms of CoB@Ni/RGO immobilized at a GC electrode in 1 mol dm ⁻³ KOH solution at different scan rates from 0.010 to 0.500 V s ⁻¹ (a); Plots of log <i>i</i> _{pc1} and <i>i</i> _{pa1} vs. log v (b).	137
Figure 6.11 Cyclic voltammograms of CoB@Ni/RGO, CoB/RGO and Ni/RGO modified GC electrodes in 1 mol dm ⁻³ KOH solution at 0.10 Vs ⁻¹	138
Figure 6.12 Complex plane impedance spectra of CoB@Ni/RGO modified GC electrodes in 1 mol dm ⁻³ KOH solution at different applied potentials.	138
Figure 6.13 Complex plane impedance spectra of CoB@Ni/RGO, CoB/RGO and Ni/RGO modified GC electrodes in 1 mol dm ⁻³ KOH solution at 0.5 V (a) and 0.4 V (b).	139

Chapter 7

Figure 7.1 (a) XRD spectra and (b) Raman spectra of GO, Ni/RGO and Cu@Ni/RGO nanocomposite.	149
Figure 7.2 (a) and (b) SEM images of Ni/RGO in lower and higher magnifications, respectively; and (c) elemental mapping of Ni. (d) and (e) SEM images of Cu@Ni/RGO in lower and higher magnifications, respectively; and (f) elemental mapping of Cu.	151
Figure 7.3 EDX spectra of Cu@Ni/RGO nanocomposite.	151
Figure 7.4 (a) and (b) TEM images of Ni/RGO in lower and higher magnifications, respectively, and corresponding HRTEM image showing the lattice spacing of Ni (111) (inset image of Fig.4b)	152
Figure 7.5 (a) and (b) TEM images of Cu@Ni/RGO nanocomposite in lower and higher magnifications, respectively, and (c) corresponding HRTEM image showing the lattice spacing of C (002) (point A, inset image of Fig. 7.5 (c)), lattice spacing of Cu NPs (111) (point B, inset image of Fig. 7.5 (c)) and lattice spacing of Cu-Ni alloy (111)) (point C, inset image of Fig. 7.5 (c))	153
Figure 7.6 UV-vis spectra of (a) time dependent reduction process of 4-NP after the addition of Cu@Ni/RGO nanocatalyst in reaction medium. (b) Pseudo-first order plots of 4-NP reduction reaction catalysed by Cu@Ni/RGO nanocatalyst (red line) and decrement of relative absorbance (blue line). (c) Comparison of pseudo-first order plots of 4-NP reduction reaction catalysed by different catalysts Ni/RGO, Cu/RGO and Cu@Ni/RGO nanocatalyst, in the presence of NaBH ₄ . (d) Stability measurement of Cu@Ni/RGO nanocatalyst during 5 successive cycles.	154
Figure 7.7 XRD spectra of GO and Ag@Co/RGO nanocomposite.	158
Figure 7.8 RT magnetization plot (M-H) of Ag@Co/RGO nanocomposite.	159
Figure 7.9 FTIR spectra of GO and Ag@Co/RGO nanocomposite.	159
Figure 7.10 Raman spectra of Ag@Co/RGO nanocomposite.	160
Figure 7.11 SEM images of (a) GO and (b) RGO. Images (c) and (d) Ag@Co/RGO nanocomposite in higher and lower magnifications, respectively.	160
Figure 7.12 EDX spectra of Ag@Co/RGO nanocomposite.	161
Figure 7.13 UV-Vis spectra of (a) 4-NP reduction using Ag@Co/RGO nanocomposite; (b) stability measurement of catalyst during 5 successive cycles.	162
Figure 7.14 UV-vis spectra of (a) 4-NP molecule initially and after the addition of NaBH ₄ in aqueous medium at 25 °C and (b) time dependent reduction process after the addition of Pd@NSG nanocatalyst in reaction medium. (c) Pseudo-first order plots of 4-NP reduction	163

<p>catalysed by Pd@NSG in the presence of NaBH₄ (red) and Ni_xB-SiO₂/RGO (blue). (d) Stability measurement of Pd@NSG nanocatalyst during 5 successive cycles.....</p> <p>Figure 7.15 Schematic representation of 4-NP molecule reduction on Pd@NSG nanocomposite in presence of NaBH₄ in aqueous medium.....</p>	165
--	-----

Chapter 8

<p>Figure 8.1 I-V characteristics of samples of series (a) 1 and (b) 2, with W (open circles) and Cu (squares) contacts. The arrows indicate the switching polarity. Inset: I-V curves in a log-log scale; lines are linear fits to the experimental data.</p>	174
<p>Figure 8.2 I-V characteristics of (left) series 1 and (right) series 2, with Cu contacts, produced at different times (A,B). Arrows indicate the switching polarity. Inset: endurance measurements up to 100 cycles.....</p>	175
<p>Figure 8.3 Maximum conductance of a sample of series 1 after consecutive positive (circles) and negative (squares) voltage sweeping cycles.....</p>	176
<p>Figure 8.4 Characteristic I vs V curve of GO and HGO in bias range of (-10 to +10V). The voltage is swept in the direction as follows: 0 V → 10 V → 0 V → -10 V → 0 V.....</p>	177
<p>Figure 8.5 I vs V curve of HGO in bias range of (a) sweeping voltage (-15 to +15V) and (b) (-20 to +20V). The voltage is swept in the direction as follows: 0 V → 10 V → 0 V → -10 V → 0 V.....</p>	178
<p>Figure 8.6 Characteristic I vs V curve of GO (Left panel) and Co/RGO nanocomposite (Right panel) in bias range of [-10, +10] V. The voltage is swept in the direction as follows: 0 V → 10 V → 0 V → -10 V → 0 V. The middle circle represents the Set and Reset like conditions of current under bias voltage, in respective quadrants.....</p>	179
<p>Figure 8.7 XRD pattern of GO, Ni/RGO and Ni(OH)₂@Ni/RGO nanocomposite.....</p>	181
<p>Figure 8.8 RT magnetic measurement of Ni(OH)₂@Ni/RGO nanocomposite.....</p>	182
<p>Figure 8.9 SEM images of (a and b) GO, (c and d) Ni/RGO and (e and f) Ni(OH)₂@Ni/RGO nanocomposite at lower and higher magnifications, respectively.....</p>	183
<p>Figure 8.10 I vs V curve of Ni/RGO (Left panel) and Ni(OH)₂@Ni/RGO nanocomposite (Right panel) under bias voltages. The voltage is swept in the direction as follows: 0 V → + V → 0 V → - V → 0 V.....</p>	184
<p>Figure 8.11 Schematic representation of device fabrication based on Ag@SiO₂/RGO nanocomposite.....</p>	185
<p>Figure 8.12 SEM images of SiO₂ nanotubes (a) and (b) in lower and higher magnifications, respectively and (c) and (d) Ag@SiO₂/RGO nanocomposite at lower and higher magnifications, respectively.....</p>	186
<p>Figure 8.13 I vs V curve of Ag@SiO₂/RGO nanocomposite (Right panel) under bias voltages. The voltage is swept in the direction as follows: 0 V → + V → 0 V → -V → 0 V.....</p>	186
<p>Figure 8.14 I vs V curve of Ag@KZ/RGO nanocomposite (Right panel) under bias voltages. The voltage is swept in the direction as follows: 0 V → + V → 0 V → -V → 0 V.....</p>	187

Chapter 9

<p>Figure 9.1 XRD of GO and Ni/RGO.....</p>	195
<p>Figure 9.2 FTIR of GO and Ni/RGO.....</p>	196

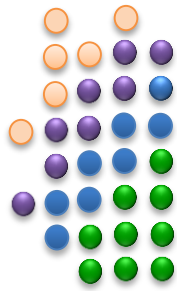
Figure 9.3 Morphological characterization of Ni/RGO nanocomposite: SEM, (a) and (b), and TEM images, (c) and (d), in lower (a and c) and higher (b and d) magnifications, respectively.....	196
Figure 9.4 CV response of different modified electrodes: GCE (red), GCE/GOx (black), GCE/Chit95/GOx (green, dash), GCE/Chit95 (green, solid) and GCE/Ni/RGO (blue), respectively in 50 mM PBS solution with scan rate of 50 mVs ⁻¹	197
Figure 9.5 (a) CV response of different modified electrodes: bare GCE (black, dash), GCE/GOx (black, solid), GCE/Chit95/GOx (green), and GCE/Ni/RGO/Chit95/GOx (blue solid and dash after the cycles) in 0.05 M PBS (pH 7.3) + 2 mM [Fe(CN) ₆] ^{3-/4-} + 1 mM glucose (dashed lines). (b) Nyquist plot of GCE/Ni/RGO/Chit95/GOx electrode obtained at 0.15 V using a 10 mV amplitude. The plots were fitted to a Randles equivalent circuit, double layer capacitance (C _{DL}) and charge transfer resistance (R _{CT}), respectively.....	198

Appendix

Figure A. 1 Schematic illustration of graphene nanobelts formation by the simultaneous reduction of GO and Ni ²⁺ in presence of Zn metal. Where, <i>in-situ</i> generated Ni NPs and radical hydrogen (H [•]) works as scissors and cut the graphene in small belts.....	207
Figure A.2 (a,b) TEM images of GO. (c,d,e and f) TEM images of graphene nanobelts. Inset of (c) shows the corresponding SAED of graphene and Ni NP.....	208
Figure A.3 Conversion of graphene to one dimensional array: (a) TEM images of GO. (b) and (c) TEM images of graphene tubes. (d) TEM image of graphene nanowire.....	209
Figure A.4 Conversion of graphene to geometry (a) TEM images of graphene triangle. (b) TEM images of graphene parallelogram. (c) TEM image of graphene square and rectangle shapes.....	210
Figure A.5 Graphene fabrication: SEM image of graphene sheets stitching to graphene nanoballoons filled with H ₂ gas can use for further energy transportation medium and for catalysis reduction reactions.....	211
Figure A.6 Graphene sheet decoration with different kind of NPs: SEM image (a) Cu NPs chain on graphene sheet. (b) Cu nanopyramid. (c) Ni NPs nanoflower on graphene. (d) Conversion of graphene sheets to nanorose with assistance of Cu ²⁺ ions. (e) MnO ₂ nanowire on graphene sheet and (f) One dimensional array of Ni/Ni (OH) ₂ on graphene.	212
Figure A.7 (a) TEM image of Pd@Ni/RGO nanocomposite. Applications of Pd@Ni/RGO nanocomposite for various catalysis reactions (b) Electro-oxidation of formic acid, (c) Potassium dichromate reduction, and (d) MB dye reduction.....	213

TABLE INDEX

Table 1.1	Technical system targets for onboard hydrogen storage for light-duty fuel cell operated vehicles.....	5
Table 1.2	Metallic and intermetallic compounds and their hydrogen storage properties.....	12
Table 1.3	Physical properties of some selected complex hydrides.....	13
Table 5.1	Comparison of the electrochemical performance of Pd@Ni _x B/RGO nanocomposite and Pd@Ni _x B NPs towards the EOR.....	112

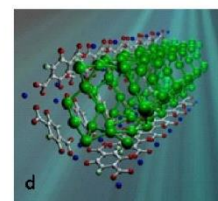
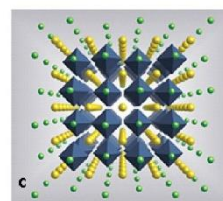
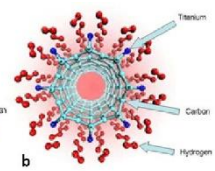
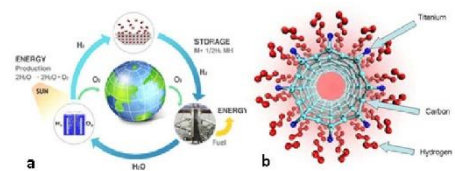


CHAPTER 1

INTRODUCTION:

Hydrogen storage-

Issue, solutions and approaches



Chapter 1

Introduction: Hydrogen storage- Issue, solutions and approaches	1
1.1 Hydrogen storage	3
1.1.1 Various options for hydrogen storage	5
1.1.1.1 High Pressure hydrogen storage	6
1.1.1.2 Liquefaction	7
1.1.1.3 Material based hydrogen storage	8
1.2 Chemical storage of hydrogen	9
1.2.1 Hydrogen storage in metal hydrides	10
1.2.2 Hydrogen storage in complex hydrides	12
1.2.3 Hydrogen storage in amides and ammonia borane compounds	14
1.3 Chemical hydrogen storage in liquid form	16
1.3.1 Chemical hydrogen storage in ammonia and hydrazine	16
1.3.2 Hydrogen storage in N-Heterocyclic compound	18
1.3.3 Hydrogen storage in ethanol	19
1.3.4 Hydrogen storage in formic acid	20
1.4 Hydrogen storage in nanoporous materials	21
1.4.1 Hydrogen storage in Zeolites	21
1.4.2 Hydrogen storage in carbonaceous materials	22
1.4.3 Hydrogen storage in MOFs	23
1.5 Theory of physisorption	25
1.6 Hydrogen storage in CNTs	27
1.7 Hydrogen storage in graphene	30
1.8 Scope of the thesis	39
1.9 References	41

INTRODUCTION:**Hydrogen storage-Issue, solutions and approaches**

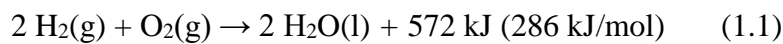
The aim of this chapter is to introduce various options of hydrogen storage, such as high pressure storage method, liquefaction technique and solid phase storage (based on metal hydrides and porous structures such as metal organic frameworks, zeolites, carbon nanotubes and graphene). It comprises main features of all these methods, techniques and their mechanism for hydrogen storage, current status and related critical issues. The last section of this chapter devoted for general introduction of graphene and their hydrogenated derivative ‘graphane’. Recently, graphene has been growing interest in many areas such as catalysis, energy storage, electronic device fabrications, medicine and materials science due to its specific structural and chemical properties and characteristic such as 2-D structure, large surface area, high electrical and thermal conductivity, robustness, chemical and thermal stability etc.

1.1 Hydrogen storage

Nowadays, worldwide increasing demand of energy is a central issue which continuously urges the scientific community to explore more sustainable energy resources to maintain the harmony of this planet [1]. To conquer this major problem, the reduction of fossil fuel dependency and energy saving criteria are two major holistic way to control such an apprehensions, which might be able to subside emission of greenhouse threats [2]. Nevertheless, efforts are going on to circumvent such kind of problems [3]. In this contest, continuous work is going on to develop new class of composite materials to play massive role for future energy economy based on environmentally clean resources and carriers [4].

In subtle engineering, nanotechnology is an important tool which already involved to solve several intricate issues, making a hope to resolve the energy challenges also [5]. Due this reason, vast range of progressive research are going on to unveil and discover numerous type of smart nanomaterials due to their specific bulk to nanomaterials properties and structure [6]. Moreover, to stimulate the research environment also, it has been already proved that nanotechnology is a very fertile ground for great scientific and technological discoveries especially, for the hydrogen storage also [7,8].

Hydrogen, is a fuel of choice and it is light weight (molar mass, 2.01588 g), contains high energy density (compressed at 700 bar, 5.6 MJ/L or 142MJ/kg) and its combustion emits no harmful chemical by-products and exothermally it combust in air and produces (-286 kJ/mol) energy as following equation 1.1 [9-12]:



Vehicles and other systems powered by hydrogen has the advantage due to it emits only water as a waste product. Moreover, hydrogen is considered as a green energy, because it can be generated from renewable sources without non-polluting manner [1,13]. Nevertheless, there is a still significant challenge are remaining that hinders the widespread application of hydrogen as the fuel of choice in mobile transportation, namely, the lack of a safe and easy method of storage [11,14].

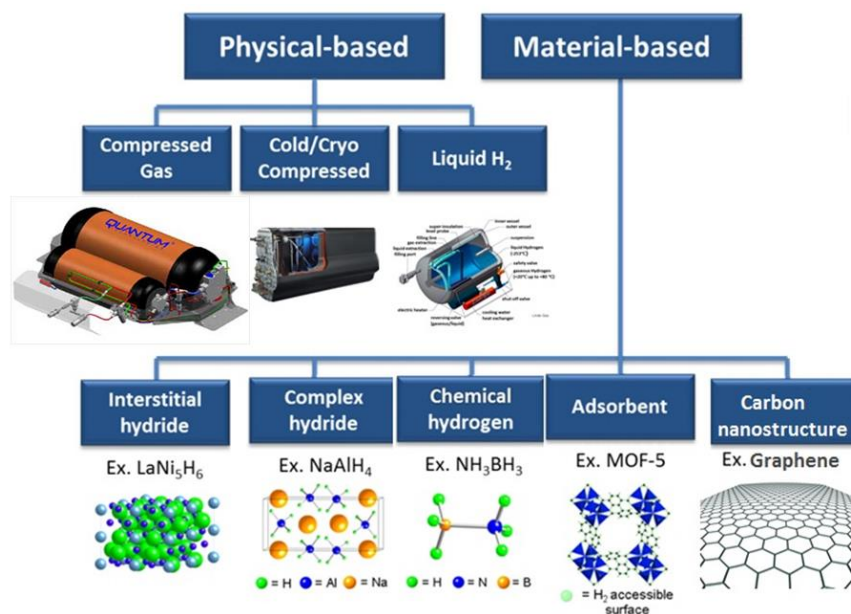



Figure 1.1 Various options of hydrogen energy storage [14].

The efficient and safe storage of hydrogen is crucial for promoting the “hydrogen economy” and developed systems are shown in Fig.1.1 [14]. The fuel cell technologies office (FCTO) under United States’ Department of Energy (D.O.E.) has established requirements that have to be met by 2017; regarding the reversible storage of hydrogen according to which the required gravimetric density should be 5.5 wt. % and the volumetric capacity should be 40 g/L of H₂ as described in Table 1.1 [15]:

Storage parameters	Units	2017	Ultimate
System gravimetric capacity: Usable, specific-energy from H ₂ (net useful energy/max system mass)	kWh/kg (kg H ₂ /kg system)	1.8 (0.055)	2.5 (0.077)
System volumetric capacity: Usable energy density from H ₂ (net useful energy/max system volume)	kWh/L (kg H ₂ /L system)	1.3 (0.04)	2.3 (0.07)
Storage system cost:			
➤ Fuel cost	\$/kWh net (\$/kgH ₂) \$/gge* at pump	12 400 2-4	8 266 2-4
Durability/operability:			
➤ Operating ambient temperature	°C	-40/60 (sun)	-40/60 (sun)
➤ Min/Max delivery temperature	°C	-40/85	-40/85
➤ Operational cycle life (1/4 tank to full)	Cycles	1500	1500
➤ Min delivery pressure from storage system	bar (abs)	5	3
➤ Max delivery pressure from storage system	bar (abs)	5	12
Charging/discharging rates:			
➤ System fill time (5 kg)	min (kg H ₂ /min)	3.3 (1.5)	2.5 (2.0)
➤ Minimum full flow rate	(g/s)/kW	0.02	0.02
➤ Start time to full flow (20°C)	s	5	5
➤ Start time to full flow (20°C)	s	15	15
* 1 gal. gasoline equivalent (gge) ≈ 1kg H ₂  lower heating value for H ₂ is 33.3 kWh/kg H ₂			

1.1.1 Various options for hydrogen storage

At the moment, there are three possible hydrogen storage options are available. Each is briefly described, along with main concern problems with special examples and references of current status of technology [1].

1.1.1.1 High Pressure hydrogen storage

The most common method of hydrogen storage is compression of the gas phase at high pressure (> 200 bars or 2850 psi) [1, 11, 15]. Compressed hydrogen in hydrogen tanks at 350 bar (5,000 psi) and 700 bar (10,000 psi) is used in hydrogen vehicles [16-18]. There are two approaches to increase the gravimetric and volumetric storage capacities of compressed gas tanks. The first approach involves cryo-compressed tanks as shown in Fig. 1.2 [17]. This is based on the fact that at fixed pressure and volume, the gas tank volumetric capacity increases as the tank temperature decreases. Thus, by cooling a tank from RT to liquid nitrogen temperature (77 K), its volumetric capacity increases by a factor of four [1,11,16,17]. However, total system volumetric capacity is less than one because of the increased volume required for the cooling system. The limitation of this system is the energy needed to compression of the gas. Approximately, 15 to 20 percent of the energy content of hydrogen is lost due to the storage method [16]. Moreover, the main problem consisting with conventional materials for high pressure hydrogen tank related to embrittlement of hydrogen storage cylinder material, during the numerous charging/discharging cycles [16-18]. These issues can be resolve only by the development of new class of lightweight composite cylinders which can allow pressure to be increased by a factor of 4 and long term durability for operation.

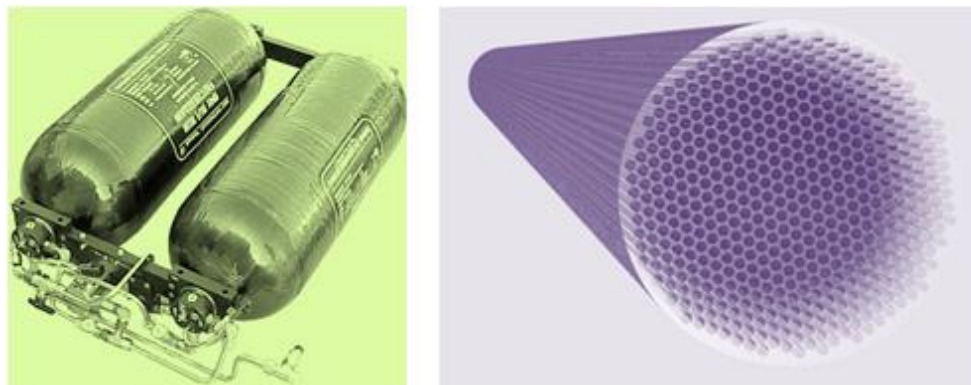


Figure 1.2 Hydrogen storage in tanks (a) outer jacket (b) recently, reported inner tube lining of compressed tanks made by carbon nanofibers (CNFs) [16,19].

1.1.1.2 Liquefaction

The energy density of hydrogen can be improved by storing hydrogen in a liquid state which also known as slush hydrogen [20]. This is useful for cryogenic engine and often used as concentrated form of it. Due to this reason this technology developed during the early space age, as it was brought along on the space vessels but nowadays, on-board fuel cells also operated with them. In terms of volumetric capacity, it may store 0.070 kg L^{-1} of hydrogen compared to 0.030 kg L^{-1} of compressed gas tanks [18]. In this storage method, first gas phase is compressed at high pressure then liquefy at cryogenic temperature (liquid nitrogen, 77 K) in liquid hydrogen tank (LH_2), due to its low critical temperature (33.2 K) and low inversion temperature (202 K) of Joule-Thompson expansion [16,21]. Further, liquid helium is used to maintain the sub-zero temperature due to its low boiling point (20.28 K) [22]. In this case the storage tanks should well insulated and the condition of low temperature is maintained by using cylinder (as jacket) as shown in Fig. 1.3 [23]. Although, this technology appears to be very promising; however, it shows many short comings. For instance, to liquefy the hydrogen some extra energy or technical work always require which is correspond to the $\sim 15.2 \text{ kWh/kg}$ and this value is almost 4.8 times of theoretical energy ($W_{th} = 3.23 \text{ kWh/kg}$) [16]. Due to this reason approximately, 30 to 40 percent of the energy content of hydrogen consumes which lowering their heating value for safe combustion [1,16,18,22]. In this quest, many other issues are also considerable they all must to be resolve before their wide utilization as choice of fuel [1].

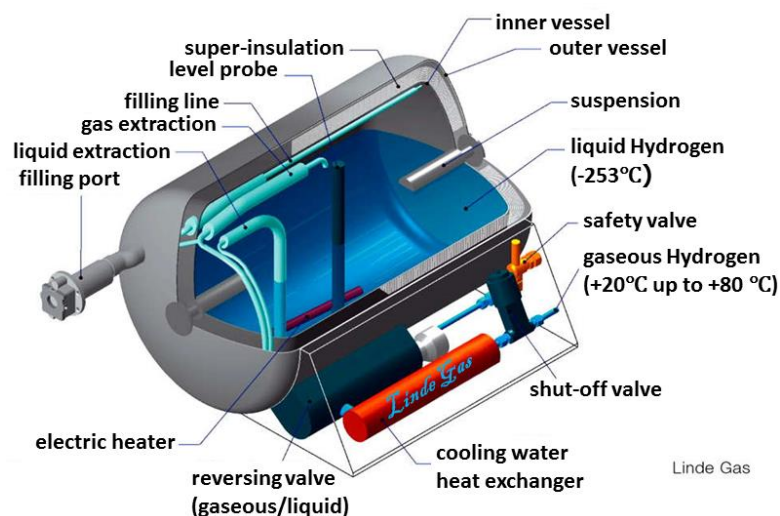


Figure 1.3 Liquid hydrogen storage tank, horizontal mounted with double gasket and dual seal [23].

For instance, weight, volume and high cost of storage tank and boiling-off of hydrogen are some central issues especially, the boiling-off issue of liquid hydrogen is due to its low critical temperature (33.2 K) [16]. In this regard, relatively large amount of energy necessary for liquefaction and the continuous boil-off of liquid limit this storage system for utilizations. The process of liquefaction involves tight binding of hydrogen atoms or molecules with other elements. Nowadays, a vast research is centered around the development of composite tank materials (combination of liquid hydrogen with a metal hydride, like Fe-Ti, to minimize the boil-off issue) [24]. Although, safety is also another issue with the handling of liquid hydrogen as does the car's tank integrity, when it storing, pressurizing and cooling the element to such extreme temperatures.

1.1.1.3 Material based hydrogen storage

As mentioned above, certainly some practical problems, which cannot be easily circumvented, such as safety concerns (for high pressure containment) and boil-off issues (for liquid storage) both are challenging for hydrogen storage [1, 16, 25]. There is a third possibility presents itself, in the form of material based hydrogen storage [1, 11, 16, 26-29]. In these systems, hydrogen molecules are stored in the materials either by chemical storage or physisorption [16,30,31]. In recent decades, many types of hydrogen storage materials have been developed and investigated, that includes vast range of hydrogen storage alloys, metal-hydrides, carbonaceous materials, metal nitrides and imides [1,11,16,28,32-37]. Mesoporous materials along with nanocomposite of them such as silica (SBA-15) incorporated with ammonia borane (NH_3BH_3) is also an example as shown in Fig. 1.4 [38].

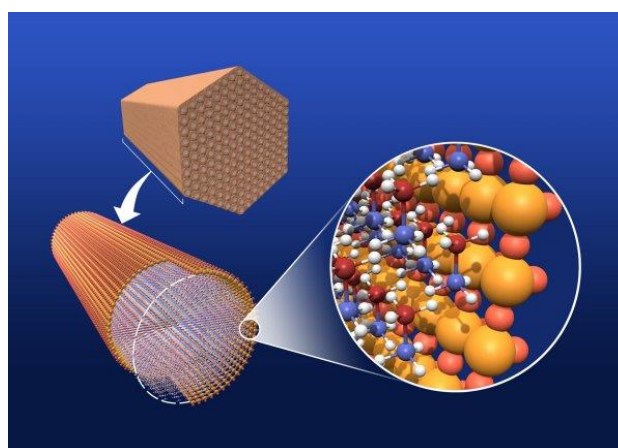


Figure 1.4 Chemically hydrogen storage in ammonia-borane [38].

Recently, hydrogen storage by adsorption (physisorption) gained lot of interests potentially due to the lowering of overall system pressure for an equivalent amount of gas, yielding safer operating conditions of their storage [1,39]. Currently, several kind of porous materials are under investigation among of them zeolites, metal organic framework (MOF), carbon nanotubes (CNTs), and graphene gained much more interest due to their light weight and high gravimetric uptake of hydrogen [1,4, 40-45]. In following section material based hydrogen storage is briefly discuss:

1.2 Chemical storage of hydrogen

Nowadays, chemical storage of hydrogen is vastly investigated and a great deal of effort has been made due to their safety perspective such that an extra amount of energy (thermal heat or electrochemical energy) or deriving force (acid, base, water or catalyst) inputs must be included to release the hydrogen for use. In this storage method, hydrogen atoms are chemically bonded or complexed with chemical storage media or incorporated into small organic molecules. There are two categories of bound hydrogen with storage media (i) solid phase and (ii) liquid form [46]. Both can releases molecular hydrogen under appropriate conditions of temperature and catalysts. When material is subjected to thermal decomposition usually an exothermic process accomplishes and self-sustainable reaction progresses, as in the case of sodium borohydride (NaBH_4) hydrolysis in presence of water and acid [47]. Although, in some cases an external energy or heat is require to release the hydrogen due to their endothermic enthalpy of decomposition for example MgH_2 [48]. Particular challenges involve in this field are storage capacity of system, operating temperature and pressure, number of cycles for reversible charging and discharging, required amount of catalyst and itself stability of the base material and/or catalytic systems [4,11,16,29,46]. Among of various storage methodologies, solid phase based chemical hydrogen storage systems can be categorized in four major classes: (i) metal hydrides with metal hydride alloys (ii) complex hydrides (borohydrides, alanates and complex metal hydrides) (iii) amides, imides and ammonia-borane compounds and (iv) nonporous materials such as zeolite, MOF, activated carbon and graphene etc. [1,16,46].

1.2.1 Hydrogen storage in metal hydrides

Initially, metal alloys, such as LaNi_5 , TiFe and MgNi alloys were proposed as materials for hydrogen storage tanks due their easily metal hydrides formation characteristic as shown in Fig. 1.5 [16]. Regarding vehicle applications, metal hydrides (MHs) can be distinguished into high or low temperature materials [31,49]. This depends on the temperature at which hydrogen absorption or desorption is taking place. Normally, in MHs hydrogen uptake and release kinetics is considered as above or below of $150\text{ }^\circ\text{C}$, respectively. La-based and Ti-based alloys are some examples of low temperature materials with their main drawback of very low gravimetric capacity ($<2\text{ wt. \%}$) of hydrogen storage.

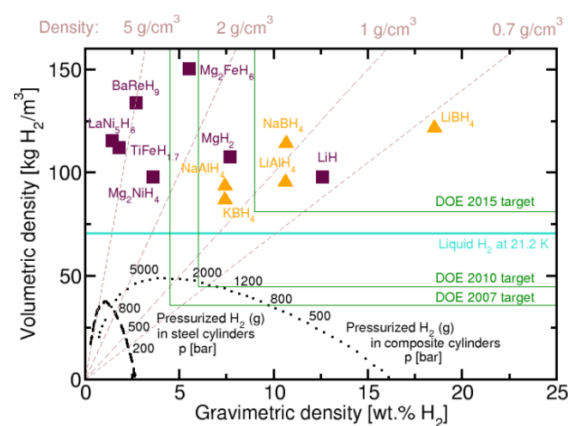


Figure 1.5 A survey plot of hydrogen storage in various metal hydrides [16].

The formation of metal hydride is well described on the basis of thermodynamic aspect of gaseous hydrogen pressure-composition-temperature (PCT) isotherms, which is also called as pressure-composition-isotherm ($p-c$) as shown in Fig. 1.6 (a). Isotherm shows that pressure is the function of concentration of hydrogen in a hydride phase (measured at a constant temperature), yielding a ratio of absorbed hydrogen with respect to metal (H/M) and wt.% of H [11]. In the graph x- and y-axes represent the H/M ratio and pressure, respectively. Plot reveals that formation of hydride compound in such a way of alloy saturation. When alloy starts to absorb hydrogen a solid solution region is observed in the graph that indicates an initial formation of an α -phase (due to the dissolution of some extent of hydrogen inside of the host metal), which was continuously transform to the β phase with increase pressure of hydrogen. At the saturation or finish point graph shows the region completely belongs to β phase [16]. In between the α and β phases, a flat plateau is also observed in $p-c$ isotherms that refers the coexistence of two phases ($\alpha + \beta$) due to the interaction of hydrogen atoms, nucleation and growth of the hydride phase.

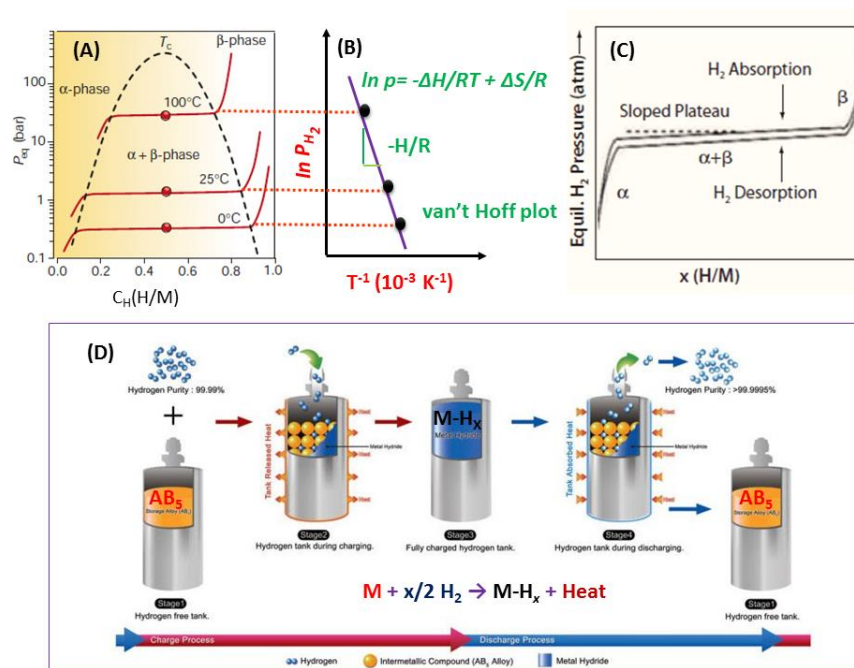


Figure 1.6 Pressure composition (p - c) isotherm for the hydrogen absorption in a typical intermetallic compound: (a) the solid solution (α -phase), the hydride phase (β -phase) formation and the region of the coexistence of the two phases flat plateau ($\alpha + \beta$) phase and their end at critical point (T_c), (b) the construction of the van't Hoff plot to calculate the enthalpy and entropy of the system, (c) demonstration of hysteresis in the isotherms between desorption/absorption process, and (d) schematic example of metal hydride formation by loading and release of hydrogen inside of metal alloy [11,16, 50,51].

The length of the flat plateau demonstrates the amount of reversibly stored hydrogen with small pressure variations. Similarly, with varying temperatures many isotherms are obtained that are called as “mid-plateau” and they all finish at the critical point (T_c) which indicates the finalization of the process. Above T_c , regions indicate the direct transition of the hydride alloy from $\alpha \rightarrow \beta$ phase. The data points from the mid-plateau provide the enthalpy of formation, which is given by $(-\Delta H/R)$ by plotting $\ln P$ versus $1/T(K)$, yielding a van't Hoff plot, and the slope of the van't Hoff line gives $\Delta H/R$ as shown in Fig. 1.6 (b) [16]. More importantly, p - c describes the hysteresis in the isotherms between desorption/absorption processes as shown in Fig. 1.6 (c) [50]. In which, as pressure decreases, a desorption process occurs. Fig. 1.6 (d) displays the schematic hydrogenation/dehydrogenation process where the metal entity (M , for example AB_5 alloy) first forms the metal hydride ($M-H_x$), which restores its structure after the dehydrogenation process [51]. Typical metal hydrides and their properties and hydrogen storage capacities are summarized in Table 1.2 [50].

Table 1.2 Metallic and intermetallic compounds and their hydrogen storage properties

Type	Metal	Hydride	Space group/ structure	Mass%	p_{eq}, T
Elemental	Pd	PdH _{0.6}	<i>Fm3m</i>	0.56	0.02 bar, 298 K
Elemental	Mg	MgH ₂	<i>hexagonal</i>	7.6	1 bar, 573 K
AB ₅	LaNi ₅	LaNi ₅ H ₆	<i>P6/mmm</i>	1.37	2 bar, 298 K
AB ₃	CaNi ₃	CaNi ₃ H _{4.4}	<i>Hexagonal</i>	1.8	0.5 bar, 298 K
AB ₂	ZrV ₂	ZrV ₂ H _{5.5}	<i>Fd3m</i>	3.01	10 ⁻⁸ bar, 323 K
AB	FeTi	FeTiH ₂	<i>Pm3m</i>	1.89	5 bar, 303 K
A ₂ B	Mg ₂ Ni	Mg ₂ NiH ₄	<i>P6222</i>	3.59	1 bar, 555 K
Solid solution	TiV ₂	TiV ₂ H ₄	<i>b.c.c</i>	2.6	10 bar, 313 K

Table 1.2 displays that the high temperature materials like Mg-based alloys can reach a theoretical maximum capacity of hydrogen storage of 7.6 wt. %; however, they suffering from poor hydrogenation/ dehydrogenation kinetics and thermodynamics [4,11,16,46].

1.2.2 Hydrogen storage in complex hydrides

Hydrogen storage in complex metal hydride of light weight elements such as Li, Mg, B, Al is very interesting due to their excess number of hydrogen atoms per metal atom (sometimes it is two) [11, 52-54]. Presently, hydride complexes of borane such as the tetrahydroborates M(BH₄) and alane tetrahydroaluminate M(AlH₄) receives special interest due to their high gravimetric density of hydrogen storage; however, they were known to be stable and decompose only at elevated temperatures and often above the melting point of the complex [46,54]. Schlesinger *et al.* (1939) first time introduced the covalent bonded inorganic complex metal hydride Al(BH₄)₃ compound, which consists of two light weight metal elements such belongs to the I and III groups of periodic table [55]. However, its low boiling point (44.5), high reactivity with water, volatile nature, pyrophoric behavior and high decomposition temperature not allows it as a choice of fuel. Soon after, same group reported the lithium borohydride (LiBH₄) material which consist of hydrogen upto 18.3 wt.%.

Such a high gravimetric extent of hydrogen in complex metal hydride compared to above described metallic hydrides is only due to the main difference between chemical bonding. In these compounds hydrogen atoms situated at the corner of the tetrahedra (as methane: CH₄) and covalently bonded with tri-valent metal such as boron or aluminum which adopts the center position, makes a tetrahedral structure. The negative charge of the anion, such as in [BH₄]⁻ and [AlH₄]⁻ compensated by a cation, e.g. Li or Na [55]. Anyway, Al(BH₄)₃ compound not suggested as promising candidate of hydrogen storage material due to their poor dehydrogenation process [53]. Zuttel *et al.* demonstrated its detailed reaction kinetics

and they investigated above 600 °C temperature is require for their decomposition and only 10 wt.% of hydrogen liberated at this condition. Some, recent research shows that addition of silica powder lowered its decomposition temperatures to 400 °C. Due to these all reasons, the low extent of hydrogen generation, high thermodynamic stability and very complex recycling process abandoned it for practical application.

Another material LiAlH_4 (LAH) also suffer from similar kind of problems. It also contains high gravimetric weight ratio of hydrogen, seems a good candidate of hydrogen storage however, only at high temperature (~ 400 °C) it decomposes to $\text{LiH} + \text{Al}$ species, shows lower hydrogen conversion capacity (7.96 wt.%) of them. For the recycling also, its spent material requires an extremely high pressure (excess of 10000 bar). Due to these reasons, many substantial research are going on for increasing their stability during recycling process and lowering decomposition temperature.

Apart of them, NaBH_4 is a good candidate for hydrogen storage material, was intensively studied for hydrogen generation and was first described in 1953 by the same group. It demonstrates high hydrogen content as well as stability in ambient conditions [31]. Instead of thermal decomposition, this is well known for its hydrolysis reaction. In hydrolysis process it provided own content of hydrogen along with 2 moles of hydrogen from water. Due to this reason now many categories of complex hydrides are in central point of research as indicated in Table [54,57] 1.3:

Formula	Mw (g mol ⁻¹)	ρ (g cm ⁻³)	T _m (°C)	T _{dec} (°C)	x (mass%)
LiBH_4	21.784	0.66	268	380	18.4
NaBH_4	37.83	1.074	505	400	10.6
LiAlH_4	37.95	0.917	>125	125	9.5
KBH_4	53.94	1.178	585	500	7.4
NaAlH_4	54	1.27	178	210	7.4
Mg_2NiH_4	111.3	2.72		280	3.6
Mg_2FeH_6	110.5	2.72		320	5.4
Mg_3MnH_7	134.9	2.3		280	5.2
BaReH_9	332.5	4.86		<100	2.7

Mw: molecular weight, ρ : density, T_m: melting point, T_{dec}: decomposition temperature, and
x: gravimetric hydrogen density

1.2.3 Hydrogen storage in amides and ammonia borane compounds

Around one century ago, Dafert (1910) reported that formation of Li_3NH_4 compound by a reaction between lithium nitride (Li_3N) and H_2 [58]. Although, it was discovered in first decade of last century but it was boosted only on this century by the pioneering work of Chen *et al.* (2002) [59]. This compound is in reality a mixture of lithium amide (LiNH_2) and lithium hydride (LiH). In this material maximum 10.4 wt.% of hydrogen storage is predicted; however, only 5.2 wt.% of stored hydrogen is achievable under reasonable temperature and pressure conditions [46]. Recently, to improve their thermal decomposition at low temperature various promoters are investigated; mainly, are based on Ti based inorganic salts and oxides [60-61]. Due to this reason, presently one more metal-N-H system gained much interest which known as Mg-N-H. It composed of magnesium hydride (MgH_2) and $\text{Mg}(\text{NH}_2)_2$ and shows the 7.4 wt.% of hydrogen content on it, commences hydrogen release at a lower temperature compare to Li-N-H system [62]. However, Mg-N-H system also shows their some drawback, the major problem concern with it reversibility of end product Mg_3N_2 to precursors MgH_2 and $\text{Mg}(\text{NH}_2)_2$ due to endothermic nature of reverse reaction [63].

Apart of them, recently ammonia borane (AB) emerges as a promising solid hydrogen carrier, due to its very high hydrogen gravimetric capacity (19.6 wt.%) and stability in air and water [46,64-67]. It is a low molecular weight (30.7 g mol^{-1}) monomeric adduct compound of NH_3BH_3 as schematically shown in Fig. 17 [64]. Its structure shows that dative bonding between the electron rich NH_3 and electron deficient BH_3 groups through *sp* hybridization and their covalent bonding with surrounding H atoms.

AB shows the system-level H_2 energy storage density around 2.74 kWh/L, and can able to releases hydrogen relatively low temperatures as compares to other metal hydride [64-66]. For their decomposition presently three methods are well established; they are namely, thermal decomposition of the solid material, catalytic dehydrocoupling in solvents and catalyzed solvolysis in water as schematically shown in Fig. 1.8 [46]. Thermal decomposition or thermolysis of AB generates 2 moles of hydrogen along with borazine, monomeric aminoborane, and diborane species as the side products. However, hydrolysis process shows the formation mainly ammonia borate as side product [67].

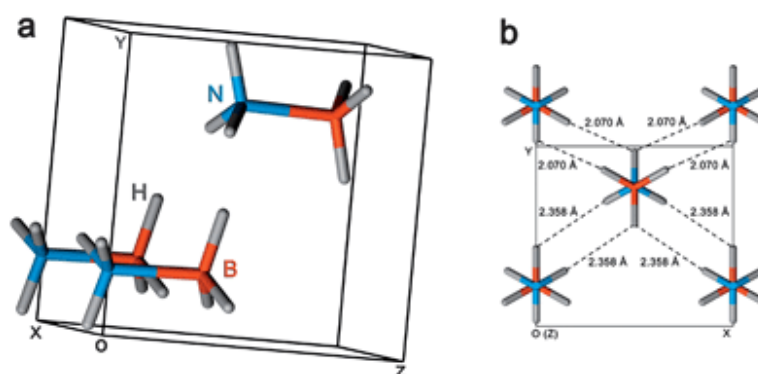


Figure 1.7 Schematic diagram of the crystal structure of NH_3BH_3 (a) and a view along z axis (b) at (298 K) [64].

The main problem concerned with the AB is long time dehydrogenation process that would be due to the involvement of induction period. Bluhm *et al.* reported the thermal decomposition of solid state AB at 85 °C, at this temperature negligible H_2 was detected in the first 3 h, but after 17 h, 0.9 equiv. H_2 was produced. After that, no further H_2 was released even after prolonged heating to 67 h, indicates the requirement of induction energy for their decomposition [68].

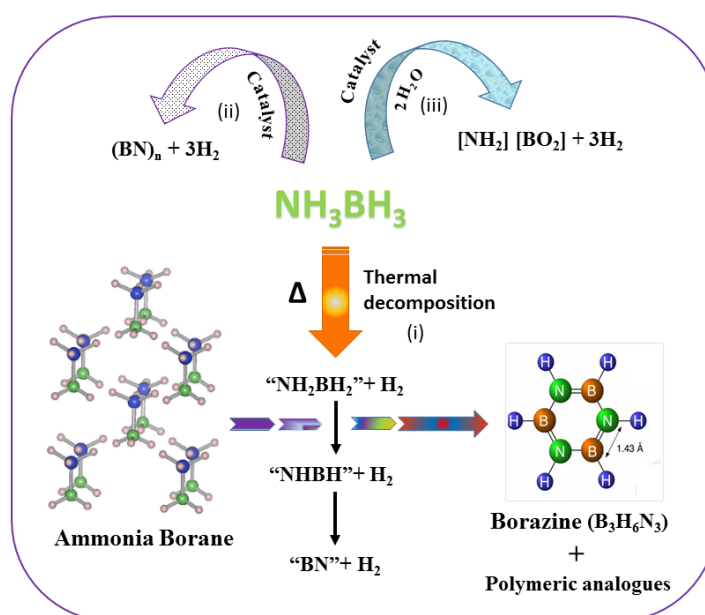


Figure 1.8 Schematic representation of ammonia borane (AB) decomposition for hydrogen generation. Three different methods, (i) most common thermal decomposition method, however, it shows major drawback formation of thermodynamically stable by products borazine and their analogues, (ii) catalytic decomposition and (iii) hydrolysis in presence of catalyst.

To enhance the hydrogen release from AB various efforts has been made. Heldebrant *et al.* demonstrated that the addition of diammoniate of diborane (DADB) or ammonium chloride (NH_4Cl) dopants led the improvement in AB dehydrogenation [69]. Similarly, Goldberg *et al.* reported very motivating results, releasing of 1 equiv. of H_2 at RT within 14 min after addition of 0.5 mol % of catalyst. They, used the transition metal complex catalysts based on iridium pincer complex such as (POCOP) $\text{Ir}(\text{H})_2$ where (POCOP = $[\eta^3\text{-}1,3\text{-}(\text{OP-tert-Bu}_2)_2\text{C}_6\text{H}_3])$ [70]. However, due to high cost of Iridium complexes this strategy seems to be not feasible for commercial application such as AB dehydrogenation.

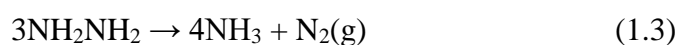
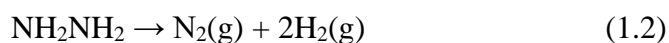
1.3 Chemical hydrogen storage in liquid form

Recently, hydrogen economy based on liquid hydrogen media is rapidly growing field of research due to their high gravimetric and volumetric content of hydrogen, easy handling of solution under ambient temperature and pressure conditions with existing transportation and refueling infrastructure. The energy sources of hydrogen carriers in liquid form are ammonia, hydrazine, N-ethyl carbazole, alcohols and formic acid [46,71-73].

1.3.1 Chemical hydrogen storage in ammonia and hydrazine

Gaseous ammonia was first isolated by Joseph Priestley in year 1774 [74]. However, process of ammonia synthesis was developed by Fritz Haber and Carl Bosch in 1909 [75]. Moreover, presently ammonia is a second demanding chemical in worldwide due to its wide applications for synthesizing of many industrial products such as urea fertilizer and organo-nitrogen compounds. It shows very high hydrogen gravimetric densities ~17 wt.% or 0.107 kg/L volumetric (~3.60 kWh/L at 25° C) [76-80]. The volumetric hydrogen density of it approx. ~ 1.7 times higher than liquid hydrogen at 0.1 MPa at -253°C. However, it shows some drawback as hydrogen energy carrier; mainly concerns due to its physical and chemical properties such as high vapor pressure at ambient conditions, high coefficient of thermal expansion, and extremely high reactivity with water, high toxicity and pungent smell. Along with, PEM fuel cells which cannot tolerate ammonia, and require very effective filtration system and cracking reactor to avoid presence of this. These major hurdles still staggered it as a choice for fuel in automobile vehicles [79-82].

Instead of that, some recent studies shows that the anhydrous hydrazine (NH_2NH_2) also an viable option of hydrogen storage due to its high gravimetric density of hydrogen (12.5 wt.%) [46,73]. Hydrazine can be decompose by two ways: complete decomposition and incomplete decomposition as following equations 1.2 and 1.3, respectively.



However, due to explosive nature of anhydrous hydrazine (>98%), its monohydrate adduct ($\text{NH}_2\text{NH}_2 \cdot \text{H}_2\text{O}$) is frequently used, which contains 7.9 wt.% of hydrogen [83]. For its complete decomposition indeed catalyst must be needed. A recent work of Singh *et al.* shows the decomposition of hydrous hydrazine in presence of Rh (0) catalyst [84]. They formulated its decomposition pathway on the basis of ^{15}N NMR spectra signals and Mass spectra profile as shown in equation 1.4:



Experimental results show that for their decomposition under investigation with Rh (0) catalyst more than 3 h were consumed, and when other catalyst such as Ni or Co were applied the selectivity and % decomposition both were very poor and almost reaction was uncompleted as shown in Fig. 1.9.

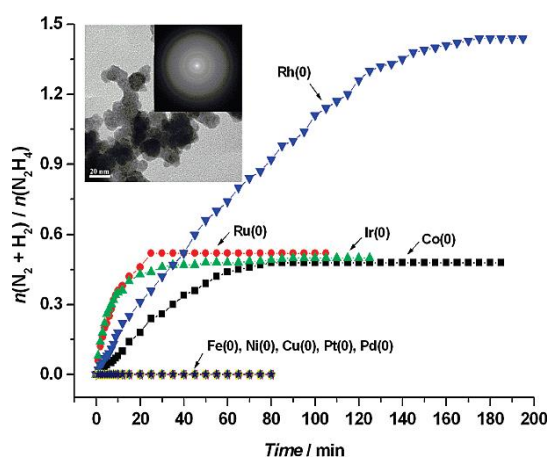


Figure 1.9 Decomposition of hydrous hydrazine in the presence of metal NPs (metal/ N_2H_4) 1:10 at 298 K. The inset shows respective TEM image of Rh(0) NPs and the corresponding SAED pattern.

These results infer that the dependency of noble metal catalyst (Rh) for their decomposition along with a long reaction time for its complete decomposition mitigate its general appearance for choice of fuel. Moreover, safety concerns due to its explosive and toxic nature and economical point of view such as synthesis from ammonia oxidation are not allow it's as a promising candidate for hydrogen storage media [46,73].

1.3.2 Hydrogen storage in N-Heterocyclic compound

Due to the above mentioned practical barriers with ammonia and hydrazine recently, scientific efforts have been made for liquid organic hydrogen carriers (LOHC) as hydrogen reservoir, to get the privilege of existing infrastructures [46,73,85]. These compounds can chemically hydrogenated/dehydrogenated as per the requirements, can easily transported to the desired place where it can decouple the stored hydrogen through catalytic reaction, the energy-lean compound transport back for recycling process. In this manner, these compounds known as Energy carrying compounds or ETS due to (German name “Energie-Tragende Stoffe”) [86]. In the beginning, in this category scientists has been investigated only alkane-arene pairs such a decalin-naphthalene, but due to their endothermicity of the release step they moved to another option which is known as N based heterocyclic compounds such as pyrrolidine and piperidine [87,88]. The presence of N in the ring favors the dehydrogenation process of organic molecule due to less bond energy of N–H bond compare to the C–H bond [88]. Nowadays, a hetrocyclic N compound which is in focus for LOHC research is N-ethylcarbazole (NEC) [85,87]. It can reversibly hydrogenated/dehydrogenated in presence of catalyst. For instance, it can be completely hydrogenated in presence of Ru catalyst at 130-150 °C under 7 MPa of hydrogen gas pressure and dehydrogenated on Pd based catalyst at 150-170 °C as suggested in Fig. 1.10 [46].

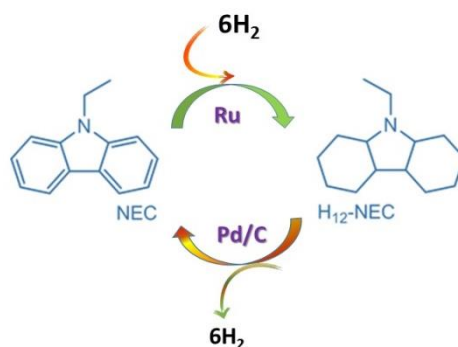


Figure 1.10 Hydrogenation/dehydrogenation of NEC.

However, NEC shows some limitations to become a potential vector for ETS such as low gravimetric amount of hydrogen storage (6-8 wt.%) compare to ammonia borane, and requirement of noble metal based catalysts for both hydrogenation/dehydrogenation process. Moreover, toxicity and smell of heterocyclic compounds are also some key issues with it for practical application [46,73,85].

1.3.3 Hydrogen storage in ethanol

Nowadays, vast research is going on for developing proton exchange membrane (PEM) fuel cells due to their several advantages such as high energy density, carbon free emission, low temperature operability and safety concerns [46,73,89]. In PEM fuel cell, hydrogen gas is pass through the membrane and provide the electrons in external electrical circuit as schematically shown in Fig. 1.11 [90]. Ethanol is widely usable fuel for PEM as energy source due to it offers almost closed CO₂ loop with high energy conversion efficiency. Ethanol can readily obtain from fermentation of several biomasses such as energy plants and waste materials from agro-industries including forestry residues also [91].

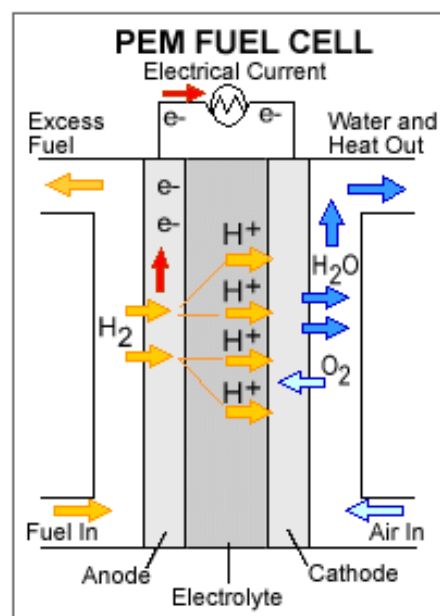
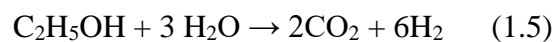


Figure 1.11 Schematic representation of PEM fuel cell [90].

The reactions involve for producing hydrogen from ethanol is steam reforming as follows equation 1.5 [92]:



However, steam reforming reaction of ethanol is not straight forward. It involves high temperature process and suffers with presence of significant amounts of toxic CO and CH₄ gases. For the application of hydrogen in PEM fuel cells, the CO content should be reduced to less than 10 ppm. The major challenge with ethanol to develop highly active and selective catalysts for steam reforming reaction which may reduce CO and CH₄ gaseous content from outlet [89-94].

1.3.4 Hydrogen storage in formic acid

Formic acid (HCOOH) is also an attractive option for hydrogen storage in liquid form. It is dense, viscous and high boiling point liquid. However, its diluted form (85%) is more often as energy carrier due to easy to handle, relatively nontoxic, noncorrosive, and nonflammable behavior. It contains 4.4 wt.% of gravimetric H₂ content lesser than other liquid H₂ storage options such as hydrazine hydrate, N-ethylcarbazole and ethanol but exceptionally, it pertains high volumetric hydrogen storage capacity 53 g/L [46,73,95,96]. This value is higher than that of most other liquid hydrogen storage materials used today and this is due to its high density (d = 1.22 g/L). Hydrogen stored in formic acid can be released on demand by decomposing it on a catalytic surface such as Au/ZrO₂ nanocatalyst [95]. The co-product of HCOOH oxidation the CO₂ still was the significant challenge but according to a recent research by Hull *et al.* that might be also used as a hydrogen vector as shown in Fig. 1.12 [97]. They developed a hydrogenation process by which CO₂ can be convert back to formic acid on the catalytic surface.

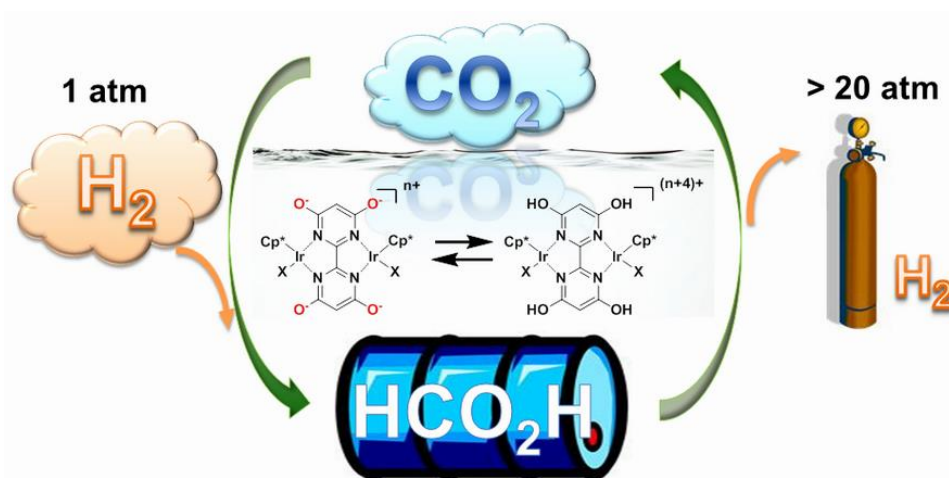


Figure 1.12 Schematic representation of reversible and recyclable hydrogen storage of formic acid on the surface of organic ligands encapsulated with Ir catalyst [97].

In this work, they demonstrated the reversible and recyclable hydrogen storage system under mild temperatures and pressure conditions based on proton-switchable iridium catalyst in aqueous media. They used CO₂, formate and formic acid as the feed that was able to produce CO free hydrogen. They used functionalized ligands for activation and binding sites of Ir catalyst. If it will be industrially possible this technique will become an ultimate carbon-neutral cycle on earth.

1.4 Hydrogen storage in nanoporous materials

Among various options of hydrogen storage, physical adsorption (physisorption) of hydrogen into porous materials has great advantages and presents itself as an attractive option for them [1]. Mostly, physisorption process shows that the fast and reversible kinetics of hydrogen uptake and release [98]. Due to this reasons, vast efforts are carrying on for development of high-surface area porous materials for boosting the hydrogen economy [41,46,73]. Presently, porous structures of zeolites, carbonaceous materials and MOFs gained more attention due their finite geometries, tunable pore sizes, comparable high thermal, mechanical and chemical stabilities, and wide industrial applications [1,30,46,98]. All options are briefly discussed in next paragraph.

1.4.1 Hydrogen storage in Zeolites

Zeolites are prominent candidates for hydrogen storage due to their structural stability and a large internal surface area [1]. Zeolites contains well defined open-pore structure, with often tunable pore size, and shows the notable guest-host chemistry, with important applications in catalysis, gas adsorption, purification and separation [1,42,99-105]. Additionally, this material is cheap and has been widely used in industrial processes for many decades. The extensive experimental survey depicts the hydrogen storage capacity of zeolites to be < 2 wt% at cryogenic temperatures and < 0.3 wt% at RT and above [42,100-103]. Fig.1.13 shows that the structure of these minerals is most commonly based on a framework of alternating AlO_4^- and SiO_4^- species, with charge balancing (hydroxyl or cationic) entities, forming networks of cavities, channels with openings in varying dimensions [105].

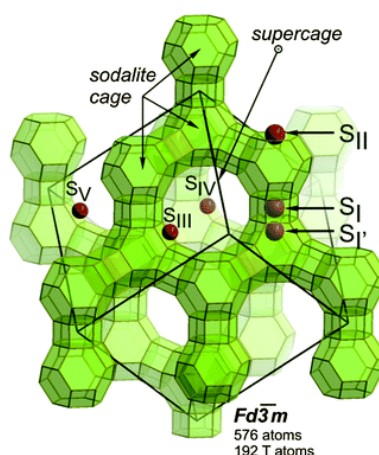


Figure 1.13 A unit cell of sodium zeolite with cage and cavity [105].

The specific structural configuration of the zeolite provides great influence for their properties with respect to adsorption, selectivity and mobility of the guest molecules. An important property of zeolites is their high ion-exchange capacity, which allows for the direct manipulation of the available void space inside the material, as well as the chemical properties of the binding sites, greatly influencing their storage capacity [1,99]. Theoretical modeling also provides a close insight of the hydrogen storage capacity of zeolite materials. More recently, Smith and Maeson described the molecular simulation of adsorption in zeolite systems [104]. In the previous decade, Darkrim *et al.* demonstrated the potential model of hydrogen storage in zeolite systems [106]. For this aspect they have deal interactions between zeolite and hydrogen adsorbates. They developed a theoretical model for adsorption of molecular hydrogen in zeolite substrate on the basis of three interaction forces (i) van-der Waals interactions, (ii) coulomb electrostatic potential, and (c) charge polarization [100].

1.4.2 Hydrogen storage in carbonaceous materials

Among the vast range of porous materials, carbonaceous materials received enormous research interest due to their light weight, high surface area and chemical stability [1,46]. Therefore, hydrogenation of carbonaceous materials e.g., activated carbon, graphite, carbon nanotubes and carbon foams, have been gained large technological and scientific interest for hydrogen storage and were included in the group of hydrogen storage materials as shown in Fig.1.14 [73, 107-109].

Early experimental data for hydrogen storage particularly, in single walled carbon nanotubes (SWCNTs) was initially promising, indicating high hydrogen storage capacity in that material exceeding of DOE targets [107]. However, later experimental results unveil that such a high storage of hydrogen is beyond of proximities [110]. Although, above prediction stimulated the scientific community for further research for hydrogen storage particularly, for nanoporous carbon material [1].

After the discovery of “graphene” the research moved in this direction due to their highest specific surface area-per-unit masses in nature, far superior to even CNTs and fullerenes [1,111]. It can store individual hydrogen atoms in a metallic lattice, through chemical bonding to a metallic host [112]. Besides the physisorption the chemisorption of hydrogen, graphene is even more interesting for catalysis and electronic purposes also [113-115]. Moreover, it is the material that may make easily composite with different kind of NPs

and other carbon structures such as CNTs, carbon nanoscrolls (CNSs) and fullerene [116-118].

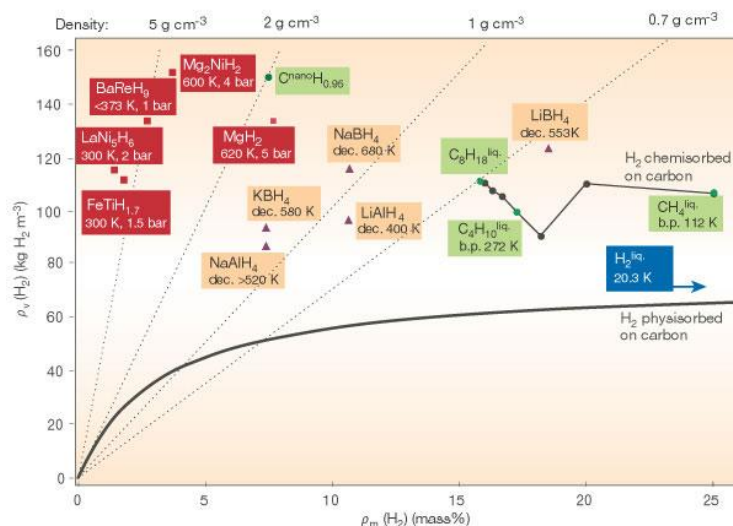


Figure 1.14 A complete survey plot of hydrogen storage in metal hydrides and carbon materials [11].

1.4.3 Hydrogen storage in MOFs

Lately, novel nanoporous materials like metal organic frameworks (MOFs) have been targeted to the hydrogen storage problem [120]. The research interests on hydrogen storage in MOFs have been growing since 2003 when the first MOF-based hydrogen storage material was introduced [121]. MOFs are highly crystalline inorganic-organic hybrid structures that contain metal clusters or ions or secondary building units (SBUs) as nodes and organic ligands as linkers as shown in Fig. 1.14 [122]. When guest molecules (solvent) occupying the pores are removed during solvent exchange and heating under vacuum, porous structure of MOFs can be achieved without destabilizing of the framework, and hydrogen molecules will be adsorbed onto the surface of the pores by physisorption [123]. Compared to traditional zeolites and porous carbon materials, MOFs contains very high number of pores and surface area which allow higher hydrogen uptake in a given volume [46,73,121]. However, due to infinite geometrical and chemical variations of MOFs scientists are trying to explore most approachable solution for maximum hydrogen uptake. Recently, Klontzas *et al.* theoretically investigated that insertion of light metal cation such as Li^+ inside of MOFs porous network can improve their hydrogen storage capacity up to 10 wt.% at 77 K under 100 bar pressure as shown in Fig. 1.15 [125]. However, experimental results shows that less extent of hydrogen

storage in MOFs. For instance, Férey *et al.* reported the hydrogen adsorption in the nanoporous metal-benzenedicarboxylate $M(OH)(O_2C-C_6H_4-CO_2)$ ($M = Al^{3+}, Cr^{3+}$), MIL-53 systems [126].

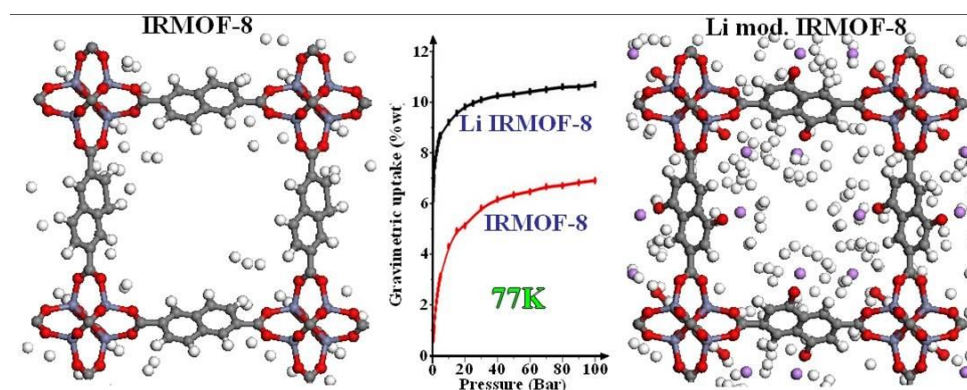


Figure 1.15 Structure and H₂ adsorption of MOF with and without doping.

They have analyzed nanoporous metal-benzenedicarboxylate $M(OH)(O_2C-C_6H_4-CO_2)$ ($M = Al^{3+}, Cr^{3+}$) and 3.8 and 3.1 wt.% hydrogen storage was obtained at 77 K under 1.6 MPa hydrogen pressure, respectively. This solid nanoporous structure was synthesized by simple chemical mixing method of precursors such as (aluminium nitrate or chromium nitrate/HF) and 1,4-benzenedicarboxylic acid (BDC). They have built a three-dimensional metal–organic framework based on encapsulation of non-reacted BDC within the pores as shown in Fig. 1.16.

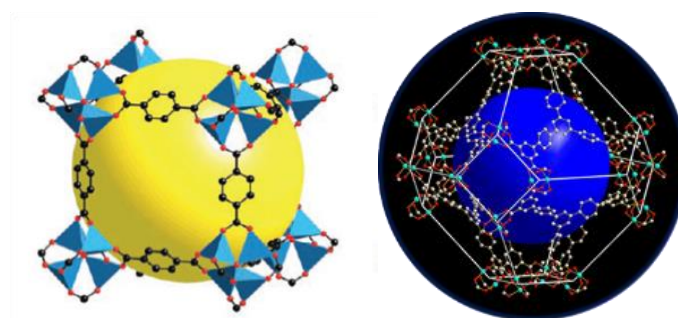


Figure 1.16 Unit cell of MOF with octahedral cluster structure [121].

The structure was built up by *trans* corner sharing of octahedral $MO_4(OH)_2$ chains with linkage of BDC molecules. That makes 1D lozenge-shape tunnels as shown in Fig.1.17 [126]. These tunnels were occluded by the BDC species which provided porous solid network after further heating at (300–320 °C) due to the decomposition and evaporation of organic species and water. The annealing process make sure the formation of porous structure with pores size of 8.5 Å with average BET surface area of 1100 m²/ g.

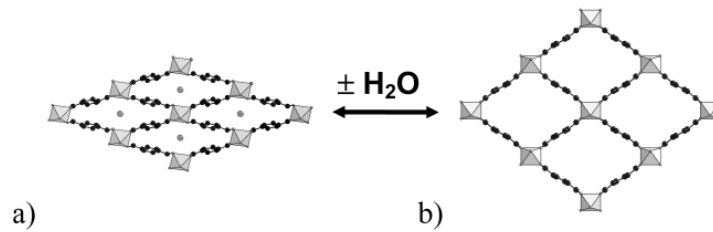


Figure 1.17 Representation of the structure of MIL-53 showing the expansion effect due to the removal of a water molecule from the cavities, (a) hydrated (left), (b) dehydrated (right); octahedra: $\text{MO}_4(\text{OH})_2$, $M = \text{Al}^{3+}$, Cr^{3+} . The dehydrated form of MIL-53 was tested for the hydrogen adsorption experiment [126].

1.5 Theory of physisorption

In porous materials hydrogen storage is highly dependent on physisorption phenomenon. This phenomenon is led by the van der Waals interaction between gases and solids under appropriate conditions and typically, 10–100 meV binding energy is involve [1, 127-133]. Due to the amount of this energy is very less, the interaction between of substrate (S) and the hydrogen molecule (H_2) describes on the basis of London- Dispersion forces ($E_{\text{S-H}_2}$), as shown in following equation 1.6 :

$$E_{\text{S-H}_2} \sim \frac{\alpha_{\text{H}_2}}{R^6} \quad (1.6)$$

where, α refer the polarizability and R denote the interdistance between hydrogen and substrates molecules as shown in Fig.1.18 [132]. However, due to the non-polar behavior of H_2 molecule, the adsorption capacity can only enhance by the increase of polarizability factor of substrate molecule as α_{H_2} is fixed. Due to this reason the only way to increase the value of $E_{\text{S-H}_2}$ using of highly polarizable substrates, e.g. substrates which contains π electron systems.

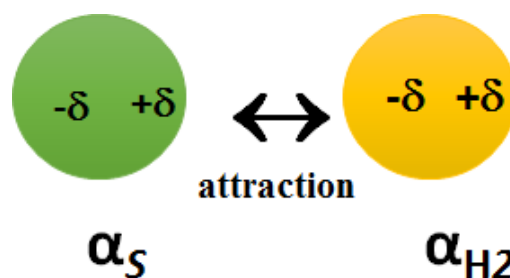


Figure 1.18 Polarization effect on adsorbate and adsorbent [132].

Normally, in adsorption phenomenon a monolayer of gaseous molecules is adsorbed above the boiling point of the adsorbent and their value depends on the adsorption stereometry [127]. In this case, equilibrium between gas attraction and gas repulsion on the surface creates an energy minimum between 1 and 10 kJ mol⁻¹. For hydrogen, the average value of energy minimum is 4-5 kJ mol⁻¹ and this represents a very weak interaction between adsorbate and adsorbents as shown in Fig.1.19 (a) and (b) [129]. However, the exact value for the hydrogen adsorption on a flat carbon surface can be estimated by Langmuir isotherm equation 1.7 [130]:

$$K = \frac{k}{k_{-1}} = \frac{\theta}{(1 - \theta)P} \quad \text{or} \quad \theta = \frac{KP}{1 + KP} \quad (1.7)$$

where, P is the partial pressure of the adsorbent gas (hydrogen in our case), K is rate constant, and θ is the surface coverage area at very low pressures $\theta \approx KP$ and for high pressure $\theta \approx 1$. Therefore, maximum value of hydrogen adsorption on any particular material can be estimated on the basis of monolayer formation on that one [131, 133].

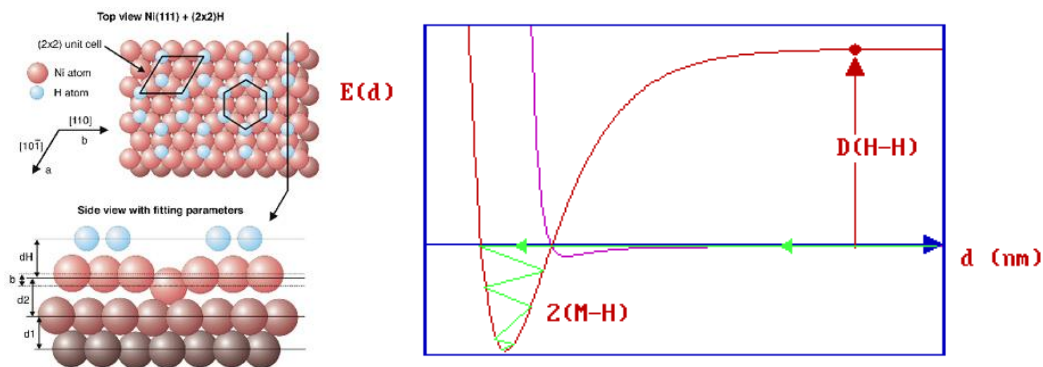


Figure 1.19 Hydrogen storage on Ni (111) catalyst support and (b) energy diagram for adsorption of hydrogen on to the catalyst surface [48].

Yao (2010) recently mentioned a calculation about the hydrogen storage in carbon based materials [132]. He describes that the “assumptionally, if we consider the structure of the adsorbed hydrogen is closed-packed face centered, the minimum estimated surface area required for the adsorption of 1 mol of hydrogen gas to be $S_{mL}(\text{H}_2) = 85.917 \text{ m}^2 \text{ mol}^{-1}$, where S_{mL} : minimum surface area required for one mole adsorption of gaseous species .

Based on this approximation the theoretical hydrogen storage capacity (m_{ads}) can be calculated from the specific surface of the carbon (S_{spec}):

$$m_{\text{ads}} \approx S_{\text{spec}} \times 2.27 \times 10^{-3} \text{ wt.}\% \quad (1.8)$$

The amount of adsorbed hydrogen correlates with the specific surface of carbon as shown in Fig.1.20 [132]. Taking equation (1.8) into account a theoretical carbon surface area of $2650 \text{ m}^2/\text{g}$ would be necessary to meet the 2010 DOE target. Fortunately, the surface area of a single graphene sheet ($2600 \text{ m}^2 \text{ g}^{-1}$) match the maximum value for the storage capacity of hydrogen adsorbed on the carbon system and which is calculated to be about 6.0 wt.%. This value, however, can be reached only at very low temperatures [132]. Therefore, hydrogen is adsorbed at very low temperature and desorbed with increasing temperature, and very little hydrogen adsorption is observed on carbon at elevated temperatures.

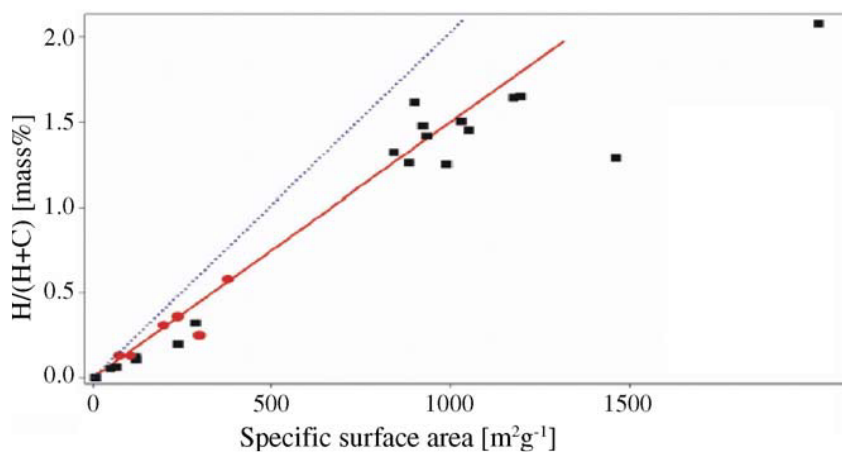


Figure 1.20 Hydrogen storage in carbonaceous materials [132].

1.6 Hydrogen storage in CNTs

There are some specific methods for hydrogenation of carbon systems and storing the hydrogen for particular interest [1]. Although, the experimental results for hydrogen storage in CNTs scatter over several orders of magnitudes. The hydrogen-storage capacity CNTs is reported between 0.2 and 10 wt.% [107,132,134-136]. Initial studies showed that CNTs were as a good material for reversible hydrogen storage, but it was later revealed that under ambient conditions, pristine CNTs are not such as promising [1,46,73]. Numerous studies has been carried out for the direct reaction of CNTs with hydrogen [134-136].

In most studies, it has been assumed that atomic hydrogen is produced by the decomposition of molecular hydrogen in the presence of catalyst, as shown in Fig.1.21 [1,46,137,138]. However, the liquid phase hydrogenation is more generous as compare to gaseous phase because in this method there is no need of external high temperature source or specific instrumental deal to dissociate the hydrogen molecule [139]. In this regards, the doped CNTs with lithium atoms can considerably increase their hydrogen storage capacity [140]. However, later studies says that D.O.E.'s target remains unapproachable, and innovative materials indeed needful to reach them [73].

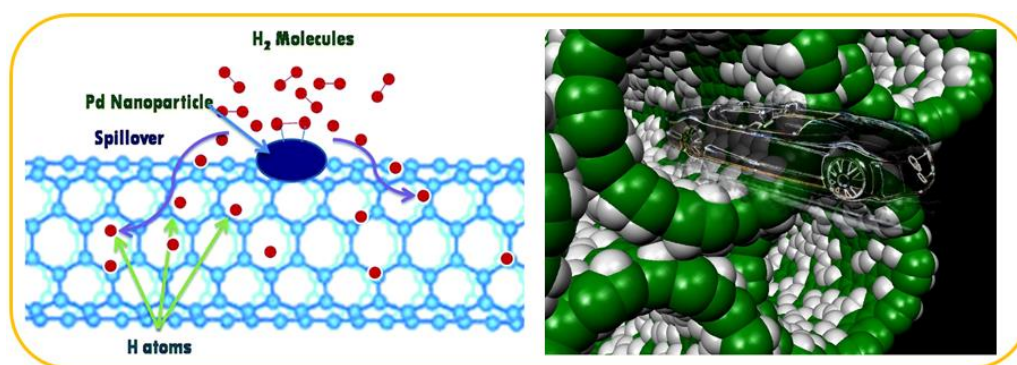
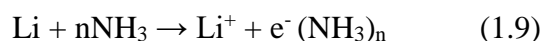
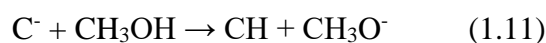


Figure 1.21 Hydrogen storage in CNTs [137,138].

In the previous decade, Pekker *et al.* (2001) reported the hydrogenation of CNTs and graphite in liquid ammonia solution [141]. They synthesized the CNTs by arc discharge method and hydrogenation reaction was carried out via a dissolved metal reduction method (in Li/liquid ammonia). For this, they have mixed 200 mg of CNTs and 100 mg of metallic Li in a glove box in presence of methanol as solvent and liq. ammonia was used as hydrogen carrier at low temperature (-33 °C). This reduction method is well known as Birch reduction where liq. ammonia directly react with metallic species Na/Li which produces the solvated cations and electrons [142]. This Birch reduction can be applied for the partial reduction of conjugated systems also and a similar reaction was used previously, for the hydrogenation of fullerenes [143]. The typical hydrogenation of CNTs was carried out by this reaction as follows: In the first steps of the hydrogenation reaction, metallic lithium reacts with ammonia (as equation 1.9) and afterward solvated anion reacted with C (due their strong basicity) and produces carbanion complex as shown in equation 1.10:



Further, carbanion reacted with methanol and decomposes it into methoxide species (CH_3O^-) as shown in equation 1.11. During course of this reaction, a covalent species also formed as hydrogenated carbon derivative (CH) which led the change in hybridization of C as sp^2 to sp^3 .



Although, direct production of hydrogen was also proposed through carbanion reaction instead of methoxide formation as shown in equation (1.12):



Later, it was recognized that direct hydrogenation of CNTs is also feasible without exceptionally care of glove box and liquid ammonia (due to their toxic and explosive behavior). In the previous decade Elby *et al.* successfully demonstrated that the hydrogenation of as-grown CNTs in presence of microwave plasma [144]. Recently, Talyzin *et al.* reported the hydrogenation, purification, and unzipping of CNTs by reaction with molecular hydrogen as shown in Fig. 1.22 [145]. They synthesized the SWCNTs and carbon nanobuds (CNBs) by aerosol CVD method through pyrolysis of ferrocene molecules. By this method they have synthesized 1.5 nm thick (diameter) and 300 nm long CNTs. They have performed hydrogenation reaction in presence of hydrogen gas at high temperature and high pressure with long time of gaseous exposure around ~ 78 h.

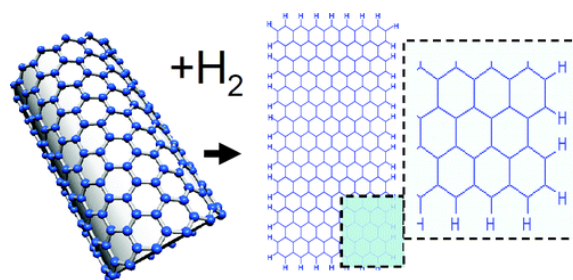


Figure 1.22 Hydrogenation and unzipping of CNTs [145].

Bhowmick *et al.* also reported the hydrogen storage in CNTs in presence of Pt catalyst. They analyzed the hydrogen storage capacity of Pt-SWNT composites and demonstrated the formation of stable C-H bond through spillover mechanism on Pt active sites [146]. Interestingly, this method can be applied to hydrogenate various forms of carbon including graphene.

1.7 Hydrogen storage in graphene

The recent discovery of graphene, atomically thin layers of 2-D graphitic carbon system brought historic revolution in the beginning of 21st century [147]. For the first time, it was possible to isolate two dimensional mono layers of atoms. A suspended single layer of graphene is one of the stiffest known materials characterized by a remarkably high Young's modulus of ~ 1 TPa. The high thermal conductivity ($\sim 3000 \text{ Wm}^{-1} \text{ K}^{-1}$), high electron mobility ($15000 \text{ cm}^2 \text{ V}^{-1} \text{ s}^{-1}$), and high specific surface area of graphene nanosheet are also few amazing characteristics of this material [1,46,73,111]. As an electronic material, graphene represents a new playground for electrons in 2, 1, and 0 dimensions where the rules are changed due to its linear band structure. Very low scattering in this material allowing its for observation of the Quantum Hall Effect (QHE), and the unique band structure of graphene provides old effect in a new twist as shown in Fig.1.23 [148].

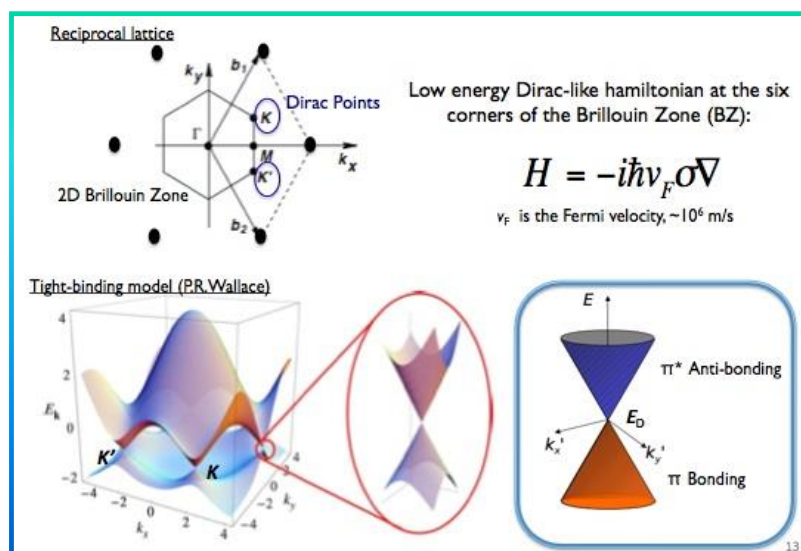


Figure 1.23 Band structure of mono layer graphene [147].

Recently, graphene has triggered enormous interest in the area of composite materials and solid state electronics. When incorporated into a polymer, its peculiar properties manifest as remarkable improvements in the host material. The mechanical and thermal properties of these materials rank among the best in comparison with other carbon-based composites. For energy applications graphene is a very suitable candidate to fabricate ultra-high charge capacitor or super capacitors. Here, storage capacity must be realized by rapid charging and discharging of composite materials [149-152]. Regarding of hydrogen storage in previous decade Sofo *et al.* coined the idea for hydrogenation of graphene through first-principle total

energy calculations to form a stable two dimensional hydrocarbon based on sp^3 hybridized (-C-H) bonded carbon structure by the saturation of sp^2 (-C=C) bonding [153]. The compound termed as graphane, it was a fully saturated hydrocarbon derived from a single graphene sheet with formula CH. All of the carbon atoms are in sp^3 hybridization forming a hexagonal network and the hydrogen atoms are bonded to carbon on both sides of the plane in an alternating manner as shown in Fig.1.24 [154].

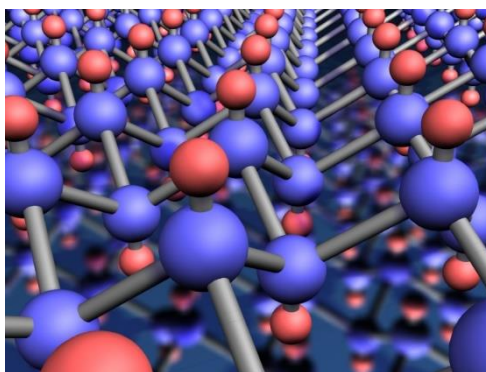


Figure 1.24 Structure of graphane in the chair conformation. The carbon atoms are shown in gray and the hydrogen atoms in red. The figure shows the hexagonal network with carbon in the sp^3 hybridization [154].

Later, Elias *et al.* practically demonstrated that graphene could be hydrogenated using cold plasma [112]. They suggested the storage of individual hydrogen atoms (H) in its hexagonal lattices through chemical bonding and formation of graphane structure where graphene acts as a metallic host and adopted the buckle structure as depicted in Fig. 1.25. It appears in the form of pulled up and down arrangement of alternating carbon atoms.

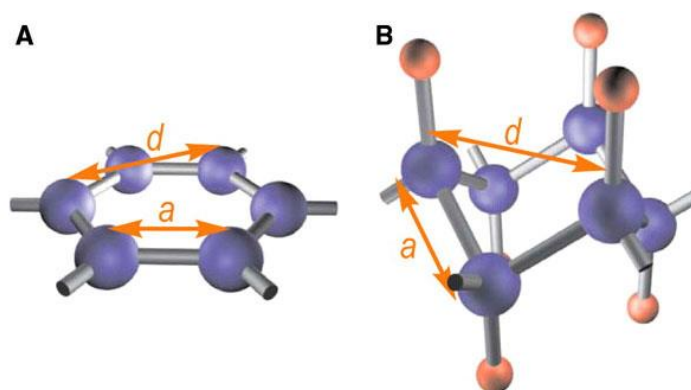


Figure 1.25 Schematic representation of the crystal structure of graphene and theoretically predicted graphane. Carbon atoms are shown as blue spheres, and hydrogen atoms are shown as red spheres [112].

Further, they confirmed the hydrogenation of graphene system (single sheet of graphene) using Raman spectroscopy. Particularly, Raman technique is very sensitive and useful for investigating the structural change in carbon materials such as diamond, CNTs and graphene, which directly provide the close information inside of carbon system [155-157]. In their work, they revealed that after the hydrogenation a new band D' was arise at 1620 cm^{-1} in their Raman spectra as shown in Fig. 1.26 [112].

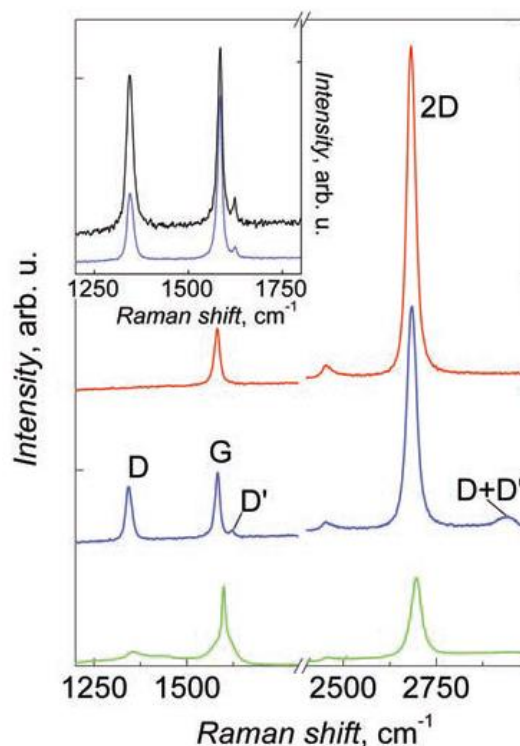


Figure 1.26 Raman spectra of graphene (green), graphane (blue) and dehydrogenated product (red) [112].

Interestingly, after the annealing (dehydrogenation process) both defect bands (D and D') were diminished and Raman spectra of graphene was recovered, suggested the reversible hydrogenation of graphene. Due to this reason they revealed the idea for chemisorption of H_2 in graphene instead of physisorption. However, later Dimitrakakis *et al.* suggested the physisorption also accessible in graphene [158]. They conceptually constructed the pillared graphene *via* linking of CNTs with pristine graphene sheets as shown in Fig. 1.27; and theoretically predicted 7.6 wt.% storage of H_2 storage at 77 K. Moreover, they have estimated a volumetric up-take of H_2 (70 g/L) at 77 K under 100 bar pressure in pillared material to meet the DOE target.

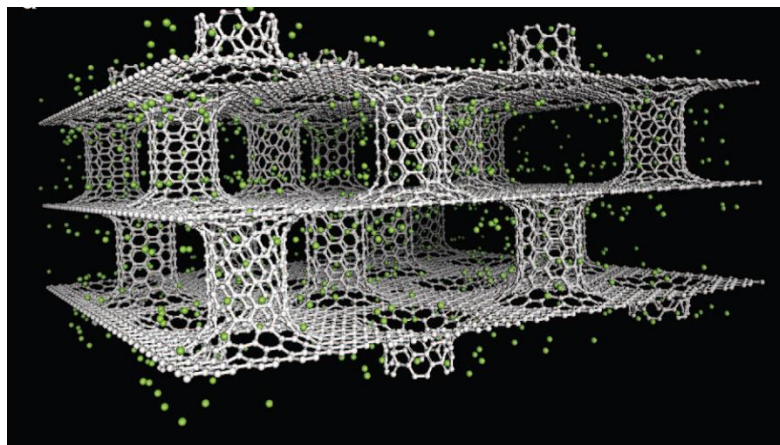


Figure 1.27 Pillared graphene. A novel 3-D network proposed for hydrogen storage [158].

However, results shows that poor hydrogen uptake in pure carbonaceous material (graphene, CNTs and pillared) and that was only enhanced after doping of Li in pillared 3-D framework as shown in Fig. 1.28.

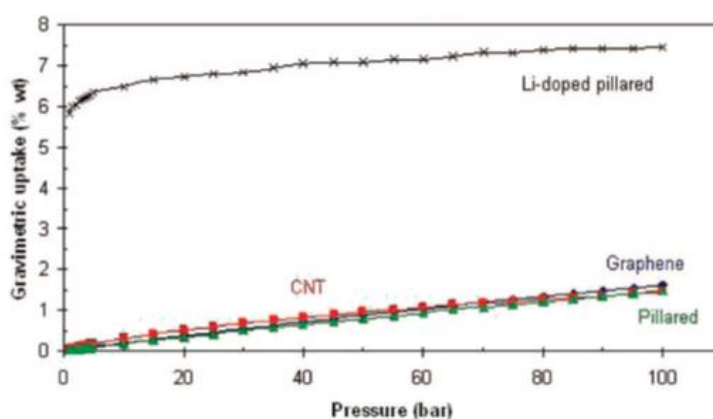


Figure 1.28 Theoretical results of hydrogen storage in pillared graphene [158].

Similarly, Bieri *et al.* also demonstrated the role of Li cations for hydrogen storage in graphene system [159]. They describes the change in electronic structure of graphene by using different dopant level of Li atoms and demonstrated the enhanced adsorption of H₂ molecules at defect sites. Recently, Fair *et al.* also theoretically demonstrated the hydrogen storage in graphene by insertion of alkaline metals Mg and Sr (instead of Li) and expected the storage of six molecule of H₂ per adatoms [160]. However, all these predictions are still far from real achievement and experimental results reveals that only 0.4 wt.% and 0.2 wt. % of H₂ storage in graphene at 77 K and RT, respectively under 6 MPa pressure condition [161]. Srinivas *et al.* experimentally demonstrated the only 0.092 wt.% storage of hydrogen in graphene system at 298 K under 10 bar H₂ pressure [162].

Anyway, synthesis of graphene in bulk amount for such kind of application is also a key issue. Graphene synthesis either by mechanical exfoliation and CVD are not satisfactory for the manufacture of high quality mass production [1]. On the other hand, the wet chemical exfoliation of graphite in presence of strong oxidizing agents is a well-known synthesis method of graphene. This chemically modified form of graphite is considered as graphene oxide (GO) [149]. GO exhibits strong covalent attachment with some oxygen functionalities such as hydroxyls, carbonyl, carboxylic and epoxides. Burress *et al.* reported the H₂ storage in GO [163]. They demonstrated the pillaring of material for better hydrogen uptake by the linkage of boronic acid and hydroxyl groups of GO as shown in Fig.1.29 [163]. However, results were not dramatically enhanced and only 1 wt.% of H₂ uptake was observed at 77 K.

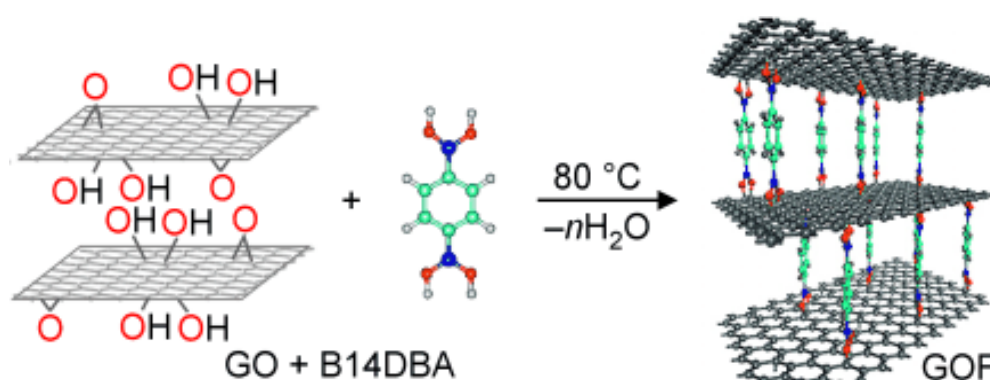


Figure 1.29 Linking of boronic ester with graphene oxide (GO) and construction of graphene oxide framework (GOF) material by the incorporation of layers graphene oxide sheets with benzenediboronic acid pillars (B14DBA) [163].

The efficient hydrogenation of graphene can also be possible by catalytic conversion where catalyst provides a new reduction pathway of graphene through dissociation of hydrogen molecule formation of radical (H) [164]. Zheng *et al.* demonstrated the graphene hydrogenation at high temperature in presence of Ni catalyst as schematically shown in Fig.1.30 [165]. They intercalated Ni NPs inside of the alumina matrix and kept it in the flow of H₂ at 820 °C to dissociate the molecular hydrogen, and successfully demonstrated the catalytic hydrogenation of graphene films and proved it by Raman technique. Although, this method is interesting for chemical storage of hydrogen; however, this approach suffers from requirement of such a high temperature for hydrogenation of graphene. Instead of that, hydrogen storage at ambient temperature is more encouraging.

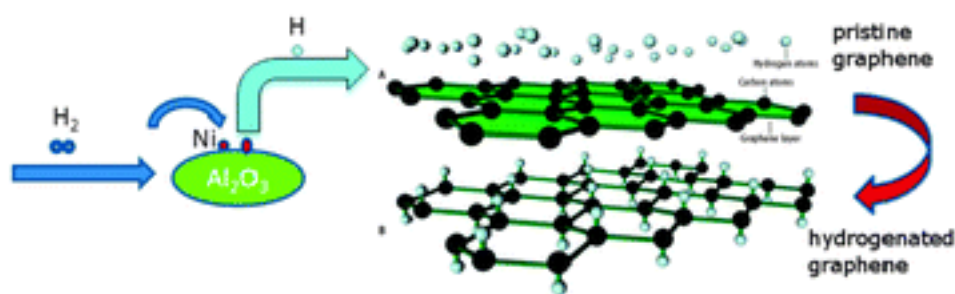


Figure 1.30 Catalytic hydrogenation of graphene film in presence of Ni catalyst at 820 °C [165].

Huang *et al.* reported the 0.15 wt.% of H₂ storage in graphene system at 303 K after integration of precise metal Pt NPs with them [166]. Later, it was realized that incorporation of other kind of porous material, for example, MOF can also be able to induce more viable way of hydrogen storage at RT. For instance, Zhou *et al.* demonstrated the 0.77 wt.% hydrogen storage in Pt-loaded graphene oxide/HKUST-1 composite under 80 bar pressure [167]. However, high price and limited number of resources of Pt metal limit its wide usability to make the scalable amount of nanocomposite for commercial application [168]. Instead of that, Pd is widely investigated and encouraged for H₂ storage due to its less price and low density compared to Pt [169-171]. Moreover, it can easily form PdH_x hydride alloy which has constitution of ($\alpha+\beta$) phase of hydride species on the basis of concentration of H₂ atmosphere [171]. Very recently, Li *et al.* has been reported the H₂ storage capacity in Pd crystal and Pd loaded HKUST at 303 K [172]. They compared the storage capacity and demonstrated enhanced H₂ storage in Pd loaded porous network of HKUST. However, specific synthesis protocol of porous material HKUST and over-all dependency on precise metals either Pt or Pd remains challengeable issue to approach real field of applications.

Concisely, chemisorption of carbon based system such as graphene can provide more viable options for hydrogen storage due to the large abundance of carbon sources such as graphite and hydrocarbons. The conversion of graphene to graphane and their reverse reaction (the dehydrogenation of graphene) is really very interesting field of research. In this process the chemisorption/desorption of hydrogen led the changes in hybridization state of hexagonal graphene system. Recently, Wang *et al.* has been reported the highly efficient conversion of graphane-to-graphene via plasma-enhanced chemical vapor deposition (PECVD) method as shown in Fig. 1.31 [173].

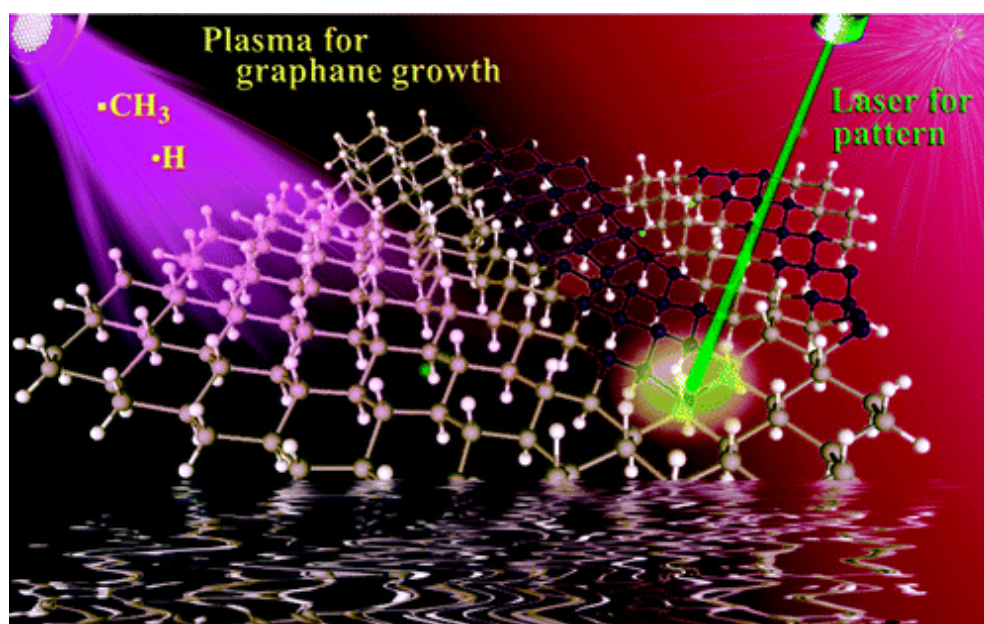


Figure 1.31 Interconvertible patterning of graphane to graphene [173].

They mentioned that the inter-convertibility between graphane and graphene film which was deposited on Cu/Ti-coated SiO₂-Si substrate. In their experiment, exfoliated graphene sample was used which was hydrogenated by the radio frequency plasma (RF plasma). After the hydrogenation they identify the change in electrical conductivity of graphene system due to the change of electronic states and recognized their advantageous position for various electronic applications. However, synthesis of high quality of graphene in bulk extent with reduced cost is still challengeable particularly, purpose of hydrogen storage. Although, scientific efforts are continuously going on to resolve all the issues.

Recently, Zhu *et al.* demonstrated that the conversion of graphene sheets in box type of structure (graphene nanocage) can able to provide an ultimate solution of hydrogen storage as shown in Fig. 1.32 [174]. In their work they theoretically demonstrated that the hydrogenation process led the formation of graphene origami (as box) through the specific patterning of graphene sheet via cutting, molding and stitching of graphene sheet. Moreover, in their work they proposed a programmable system for molecular hydrogen gas uptake, their storage, and finally release through an external electrical field. Regarding of hydrogen uptake and release they used the molecular dynamic simulation approach and exhibited that reaching to the ultimate goal of US DOE target.

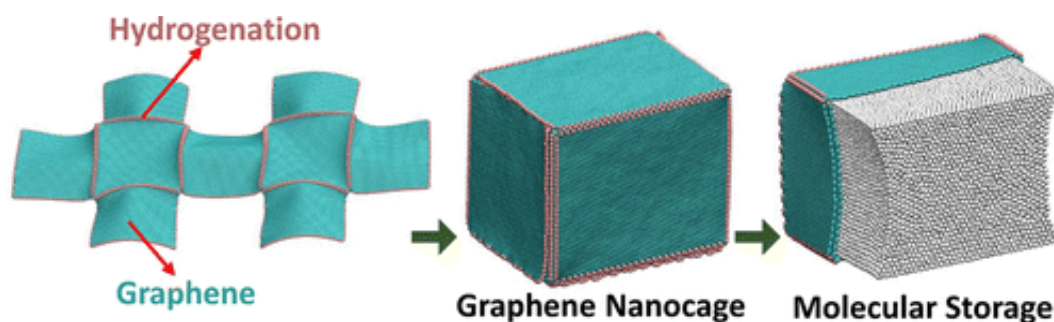


Figure 1.32 A systematic theoretical approach for making the hydrogenation assisted graphene origami (HAGO) for programmable molecular hydrogen storage [174].

Although the above idea, making the graphene origami seems very interesting but the cutting of graphene sheet (only on diagonal sides along with middle flappy region with 90 degree angle as shown in above Figure 1.32: left image) is highly cumbersome especially, removing of square pieces from specific regions. Then after, molding of small graphene pieces to make the box or graphene nanocage (center image) really, needed a highly tentative idea. Though, the initial work of graphene sheet cutting by the Ci *et al.* shows that the graphene sheet can cut in the pattern of triangular shape as shown in Fig 1.33 [175].

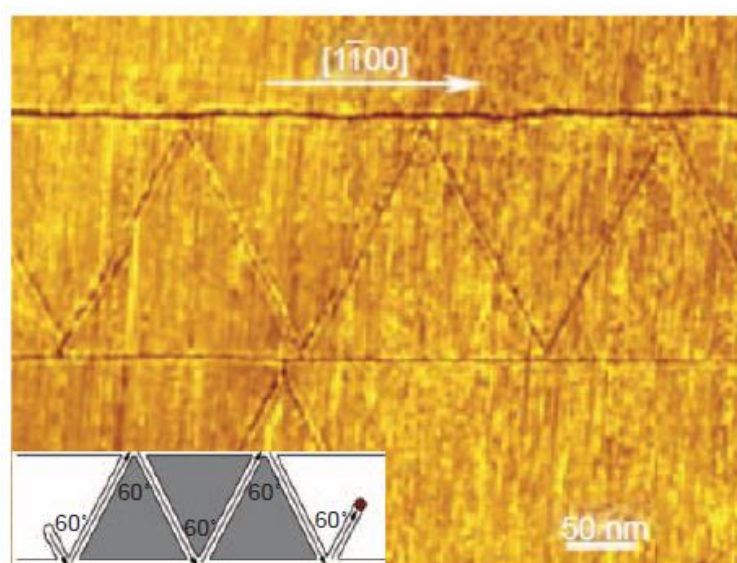


Figure 1.33 AFM image of graphene cutting which clearly shows that the formation of triangles with each edge related of 60° movement, a schematic representation also (inset image) [175].

They, investigated that graphene sheet can cut only in 60 and 120 degree angles, not in the angles of 45 and 90 degrees. This was probably, due to hexagonal networking of graphene sheets itself. In the hexagonal network each carbon atoms situated with 60 degree angle. Therefore, the line defects or cutting only feasible in regular fashion (related to

minimum energy requirement for fragmentation of carbon skeleton) that yielded the triangles. Similar kind of results also demonstrated by Campos *et al.* for the synthesis of graphene nanoribbons [176]. They found that when graphene sheet was etched with Ni NPs under hydrogen environment at high temperature (at 1000 °C) some trench were formed (due to the movement of Ni NPs) as shown in Fig. 1.34. But all the trenches turns only on angles of 60° or 120° it might be due to the symmetric bouncing of NPs in particular direction.

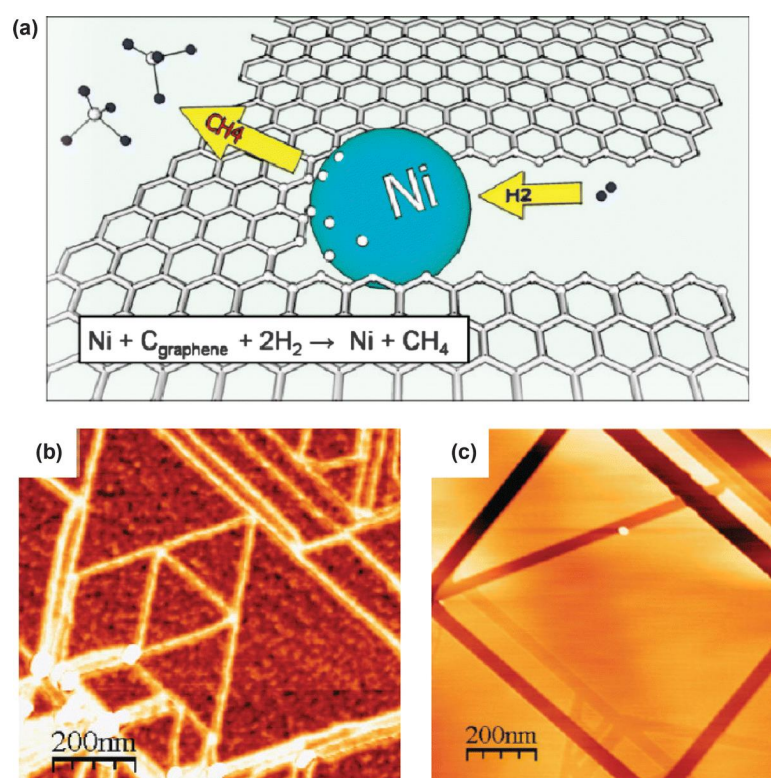


Figure 1.34 Anisotropic cutting of graphene. (a) Schematic drawing of graphene cutting by metal nanoparticles. (b), (c) AFM of graphene and graphite after cutting, respectively [176].

Anyway, high temperature reaction condition and cutting of few layers of graphene on substrate in triangular fashion or making the graphene origami are not enough approaches to reach the goal of hydrogen storage. In this regards, there are two approaches with graphene system they itself existing together such as chemisorption (saturation of $-\text{C}=\text{C}$ bonding to make $-\text{CH}$) and physisorption in porous materials. Particularly, chemisorption *via* hydrogen spillover is very interesting in which metal NPs dissociate the molecular hydrogen and host graphene layers accommodate the hydrogen atoms as shown in Fig. 1.35 [1].

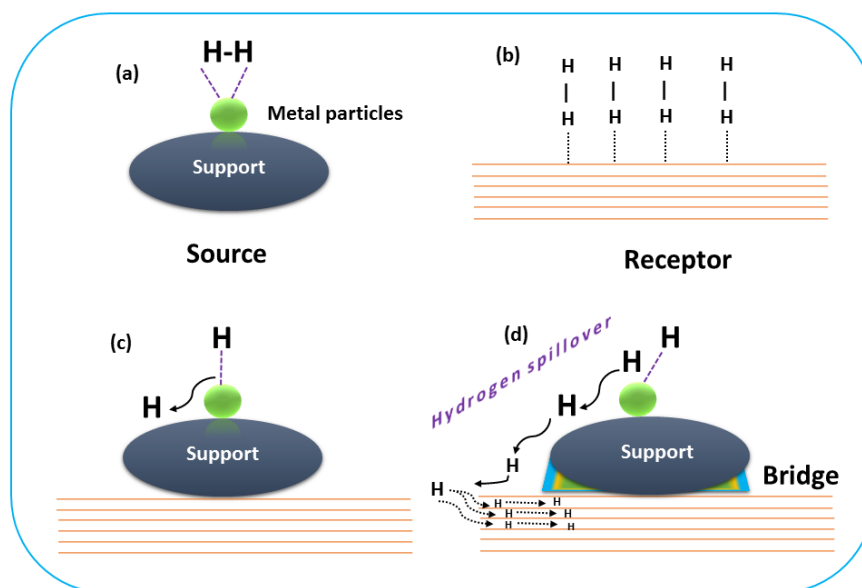


Figure 1.35 Hydrogen spillover mechanism on metal catalyst site and storage of hydrogen in receptor layers through bridge building mechanism [1].

Therefore, it is crucial and important to introduce an innovative way for storing the high gravimetric amount of H_2 with reduced cost using graphene as host material or receptor site and metal NPs as catalyst.

1.8 Scope of the thesis

The main aim of this thesis is the development of transition metals doped graphene based novel materials to solve the world wide challengeable issue of energy economy. Efforts has been made on hydrogen energy storage, their production and energy saving also (during the catalysis reactions). Moreover, graphene nanocomposites were applied for electrical and electronics applications also. This work is mainly focused on five distinct applications (i) hydrogen storage (ii) hydrogen generation (iii) catalysis process based on hydrogenation reaction (iv) electronics application (memristor property), and (v) biosensor applications.

Chapter 2 demonstrate a novel method for hydrogenation of GO on the basis of hydrogen spillover mechanism. This chapter comprises two parts: the first part shows the synthesis of hydrogenated reduced graphene oxide (HRGO) on bulk Ni metal and, second part represents the synthesis of hydrogenated graphene oxide (HGO) based on nano Ni powder. The product HRGO was fully characterized by XRD, FTIR, Raman, XPS and TEM/HRTEM techniques. Here, a detailed mechanism of hydrogen spillover on Ni also established.

Chapter 3 presents the hydrogen storage in Pd@Ni_xB-SiO₂/RGO nanocomposite. The synthesized nanocomposite was fully characterized by XRD, FTIR, Raman and XPS techniques. The morphological features were accessed by SEM and TEM techniques. The study of hydrogen storage was performed using Sievert's instrument. The H₂ up take measurements were performed at RT till 50 bar pressure. For the comparison, Pd@SiO₂/RGO, Ni_xB-SiO₂/RGO and SiO₂/RGO nanocomposite were also tested. On the basis of hydrogen storage results, a detailed mechanism has been established to clarify the primary and secondary spillover sites inside of nanocomposite.

Chapter 4 is about the theoretical modelling of hydrogen storage in nanozeolite material. Here, grand canonical Monte Carlo (GCMC) simulation technique was applied for assessment of hydrogen storage in nanomaterial.

Chapter 5 presents the hydrogen generation through electrochemical oxidation of ethanol in alkaline medium. In this work Pd@Ni_xB/RGO nanocomposite was used for catalysis reaction and the electrochemical behavior of nanocomposite evaluated by cyclic voltammetry (CV) technique. The structural and morphological features were also characterized by XRD, FTIR, XPS, SEM and TEM techniques. The catalytic activity of Pd@Ni_xB/RGO nanocomposite was evaluated continuously for 50 cyclic run; Interestingly, results shows the increase of current density after 50 cycle run, suggests the self-cleaning process on catalyst and robustness of catalyst infers the futuristic hope for hydrogen economy.

Chapter 6 describes the direct hydrogen production through hydrolysis of NaBH₄ in aqueous basic medium. In this work, a novel nanocomposite CoB@Ni/RGO was synthesized by a facile route. Nanocatalyst was fully characterized by XRD, FTIR, Raman, SEM and TEM techniques. Moreover, stability and performance of CoB@Ni/RGO nanocatalyst were also investigated by CV and impedance spectroscopy (EIS) techniques. A detailed mechanism of NaBH₄ decomposition on CoB@Ni/RGO nanocomposite was also elaborated.

Chapter 7 describes the catalysis reactions on the surface of graphene nanocomposites to save the energy and environment. 4-nitrophenol is an industrial pollutant and for their degradation catalyst involvement is highly required. A wide range of catalysts has been synthesized and efforts are especially, has been made for decrease of reaction time and reaction temperature, along with price of nanocatalyst system.

Chapter 8 is about the study of resistive switching and memristor behavior of graphene nanocomposite system for nanoelectronics applications. Here, MIM structure is fabricated to understand the mechanism in detail.

Chapters 9 describes the biosensors work based on Ni/RGO nanocomposite system.

Chapter 10 of this thesis is dedicated to the final conclusions.

1.9 References

- [1] R. Krishna, E. Titus, M. Salimian, O. Okhay, S. Rajendran, A. Rajkumar, J. M. G. Sousa, A. L. C. Ferreira, J. C. Gil, J. Gracio. Hydrogen Storage for energy application, Intech Open, Europe (2012). ISBN: 978-953-51-0731-6, InTech, DOI: 10.5772/51238
- [2] P. Jena. J Phys Chem Lett, 2(2011), pp. 206-211.
- [3] E. David. J Mater Process Technol, 162-163 (2005), pp. 169-177.
- [4] J. Yang, A. Sudik, C. Wolverton, D. J. Siegel. Chem Soc Rev, 39(2010), pp. 656-675.
- [5] Q. Zhang, E. Uchaker, S. L. Candelaria, G. Cao. Chem Soc Rev, 42 (2013), pp. 3127-3171.
- [6] M. Yoshida, J. Lahann. ACS Nano, 2 (2008) pp. 1101-1107.
- [7] M. U. Niemann, S. S. Srinivasan, A. R. Phani, A. Kumar, D. Y. Goswami, E. K. Stefanakos. J Nanomater, 2008 (2008), pp. 950967-9509775.
- [8] L. M. Kustov, A. L. Tarasov, J. Sung, D.Y. Gudovsky. Mendeleev Commun, 24 (2014), pp. 1-8.
- [9] D. R. Gaskell. Introduction to the Thermodynamics of Materials, Taylor & Francis (5e), 2008.
- [10] S. A. Sherif, D. Y. Goswami, E.K. (Lee) Stefanakos, A. Steinfeld. Handbook of Hydrogen Energy, CRC Press, Taylor & Francis group, (2015). ISBN: 9781420054477
- [11] L. Schlapbach, A. Züttel. Nature, 414 (2001), pp. 353-358.
- [12] S. McAllister, J. Y. Chen, A. C. F. Pello. Fundamentals of Combustion Processes, Springer Link (2011). ISBN: 978-1-4419-7942-1
- [13] D. P. Broom, Hydrogen Storage Materials, Springer-Verlag London Limited, 2011.
- [14] <http://energy.gov/eere/fuelcells/hydrogen-storage>
- [15] <http://www1.eere.energy.gov/hydrogenandfuelcells/mypp/pdfs/storage.pdf>
- [16] A. Zuttel. Mater Today, 6 (2003), pp. 24-33.
- [17] <https://hydrogen.wsu.edu/hydrogen-storage/>

- [18] R. K. Ahluwalia, T. Q. Hua, J. K. Peng, S. Lasher, K. McKenney, J. Sinha. Technical assessment of cryo-compressed hydrogen storage tank systems for automotive applications (2009).
- [19] <http://www.autoblog.com/2009/12/14/hydrogen-storage-breakthrough-could-come-from-russian-space-prog/>
- [20] S. Gürsu, S. A. Sheriff, T. N. Veziroçlu, J.W. Sheffield. *Int J Hydrogen Energy*, 19 (1994), pp. 491-496.
- [21] E. A. Zavala, B. A. E. Elizarraraz, F. A. Brown. *The Open Thermodynamics Journal*, 3 (2009), pp. 17-22.
- [22] S. A. Sherif, N. Zeytinoçlu, N. Veziroçlu. *Int J Hydrogen Energy*, 22 (1997), pp. 683-688
- [23] <http://www.eoearth.org/view/article/153626/>
- [24] S. H. Fan. *Chemical looping systems for fossil energy conversions*. John Wiley & Sons, Inc, Hoboken, New Jersey (2010).
- [25] L. Zhou. *Renew Sustain Energy Rev*, 9 (2005), pp. 395-408.
- [26] U. Eberle, G. Arnold, R.V. Helmholt. *J Power Sour*, 154 (2006), pp. 456-460.
- [27] L. Zaluski, A. Zaluska, J.O. Ström-Olsen. *J Alloys Compds*, 253 (1997), pp. 70-79.
- [28] I. Jain, P. Jain, A. Jain. *J Alloys Comp*, 503 (2010), pp. 303-339.
- [29] Y. Song. *Phys Chem Chem Phys*, 15 (2013), pp. 14524-14547.
- [30] Neto et al. *Energy Environ Sci*, 5 (2012), pp. 8294-8303.
- [31] M.V. Lototsky, V.A. Yartys, B.G. Pollet, R.C. Bowman Jr. *Int J Hydrogen Energy*, 39 (2014), pp. 5818-5851.
- [32] N. Jasminská, T. Brestovič, M. Puškár, R. Grega, J. Rajzinger. *Measurement*, 56 (2014), pp. 219-230.
- [33] Ley et al. *Mater Today*, 17 (2014), pp. 122-128.
- [34] Lai et al. *Chemsuschem*, 8 (2015), pp.2789-2825.
- [35] K. Lu. *Materials in Energy Conversion, Harvesting, and Storage*, John Wiley & Sons, Inc. (2014) ISBN: 978-1-118-88910-7
- [36] H. J. Cao, Y. Zhang, J.H. Wang, Z.T. Xiong, G.T. Wu, P. Chen. *Prog Natl Sci-Mater Int*, 22 (2012), pp. 550-560.
- [37] Y. Nakamori, G. Kitahara, K. Miwa, N. Ohba, T. Noritake, S. Towata, S. Orimo. *J Alloys Comp*, 404 (2005), pp. 396-398
- [38] H. Kim, A. Karkamkar, T. Autrey, P. Chupas, T. Proffen. *J Am Chem Soc*, 131 (2009), pp. 13749-13755.

- [39] L. Klebanoff. Hydrogen storage technology: materials and applications, CRC press, Taylor & Francis (2012) ISBN 9781439841075 - CAT# K11909.
- [40] L. Wang, R. T. Yang. Energy Environ Sci, 1(2008), pp. 268-279.
- [41] K. M. Thomas. Catal Today, 120 (2007), pp. 389-398.
- [42] J. X. Dong, X. Y. Wang, H. Xu, Q. Zhao, J. P. Li. Int J Hydrogen Energy, 32 (2007), pp. 4998-5004.
- [43] J. Sculley, D. Q. Yuan, H. C. Zhou. Energy Environ Sci, 4 (2011), pp. 2721-2735.
- [44] C. H. Chen, C. C. Huang. Int J Hydrogen Energy, 32 (2007), pp. 237-246.
- [45] V. Tozzini, V. Pellegrini. Phys Chem Chem Phys, 15 (2013), pp. 80-89.
- [46] A. F. Dalebrook, W. Gan, M. Grasemann, S. Moret, G. Laurency. Chem Commun, 49 (2013), pp. 8735-8751.
- [47] L. Damjanović, M. Majchrzak, S. Bennici, A. Auroux. Int J Hydrogen Energy, 36 (2011), pp. 1991-1997.
- [48] M. Polanski, J. Bystrzycki. Int J Hydrogen Energy, 34 (2009), pp. 7692-7699.
- [49] K. H. Young, J. Nei. Materials, 6 (2013), pp. 4574-4608.
- [50] <http://www.sigmaaldrich.com/technical-documents/articles/material-matters/metal-hydrides-nimh-batteries.html>
- [51] <http://www.mabelite.com/mh-storage-technology>
- [52] J. Graetz. Chem Soc Rev, 38 (2009), pp. 73-82.
- [53] S. I. Orimo, Y. Nakamori, J.R. Eliseo, A. Züttel, C.M. Jensen Chem Rev, 107 (2007), pp. 4111-4132.
- [54] M. B. Ley. Mater Today, 17 (2014), pp. 122-128.
- [55] M. Hirscher. Handbook of hydrogen storage new materials for future energy storage, Weinheim Wiley-VCH-Verl (2010) ISBN: 978-3-527-32273-2
- [56] <http://www.sigmaaldrich.com/technical-documents/articles/material-matters/metal-borohydrides.html>
- [57] P. Vajeeston, P. Ravindran, A. Kjekshus, H. Fjellvag. J Alloys Compound, 387 (2005), pp. 97-104.
- [58] F.W. Dafert, R. Miklauz. Monatsh Chem, 31(1910), pp. 981.
- [59] P. Chen, Z. Xiong, J. Luo, J. Lin, K.L. Tan. Nature, 420 (2002), pp. 302-304.
- [60] H. Y. Leng, T. Ichikawa, S. Hino, N. Hanada, S. Isobe, H. Fujii. J Phys Chem B, 108 (2004), pp. 8763-8765.
- [61] S. Isobe, T. Ichikawa, N. Hanada, H. Y. Leng, M. Fichtner, O. Fuhr, H. Fujii. J Alloys Compd, 404 (2005), pp. 439-442.

- [62] Y. Nakamori, G. Kitahara, K. Miwa, S. Towata, S. Orimo, *Appl Phys A: Mater Sci Process*, 80 (2005), pp. 1-3.
- [63] J. Hu, G. Wu, Y. Liu, Z. Xiong, P. Chen, K. Murata, K. Sakata, G. Wolf. *J Phys Chem B*, 110 (2006), pp. 14688-14692.
- [64] B. Peng, J. Chen. *Energy Environ Sci*, 1 (2008), 479-483.
- [65] F. H. Stephens, V. Pons, R. T. Baker. *Dalton Trans*, 25 (2007), pp. 2613-2626.
- [66] T. B. Marder, *Angew Chem Int Ed*, 46 (2007), pp. 8116-8118.
- [67] G. Moussa, R. Moury, U. B. Demirci, P. Miele. *Int J Hydrogen Energy*, 38 (2013), pp. 7885-7895.
- [68] M. E. Bluhm, M. G. Bradley, R. Butterick, III, U. Kusari, L. G. Sneddon. *J Am Chem Soc*, 128 (2006), pp. 7748-7749.
- [69] D. J. Heldebrant, A. Karkamkar, N. J. Hess, M. Bowden, S. Rassat, F. Zheng, K. Rappe, T. Autrey. *Chem Mater*, 20 (2008), pp. 5332-5336.
- [70] M. C. Denney, V. Pons, T. J. Hebden, D. M. Heinekey, K. I. Goldberg. *J Am Chem Soc*, 128 (2006), pp. 12048-12049.
- [71] Q. L. Zhu, Q. Xu. *Energy Environ Sci*, 8 (2015), pp. 478-522.
- [72] X. Zhou, Y. Huang, W. Xing, C. Liu, J. Liao, T. Lua. *Chem Comm*, (2008), pp. 3540-3542.
- [73] M. Yadav, Q. Xu. *Energy Environ Sci*, 5 (2012), pp. 9698-9725.
- [74] L. Abraham. *Marvell and alchemy*, Aldershot Scholar, (1990) ISBN 0-85967-774-5.
- [75] J. W. Erisman, M. A. Sutton, J. Galloway, Z. Klimont, W. Winiwarter. *Nature Geoscience*, 1(2008), pp. 636 – 639.
- [76] <http://www.essentialchemicalindustry.org/chemicals/ammonia.html>
- [77] C. E. Housecraft, A. G. Sharpe. *Inorganic chemistry (2e)*, Pearson Prentice Hall, England (2005), 0130-39913-2.
- [78] <http://www.easychem.com.au/monitoring-and-management/maximising-production/industrial-uses-of-ammonia>
- [79] A. Klerke, C. H. Christensen, J. K. Nørskov, T. Vegge. *J Mater Chem*, 18 (2008), 2304-2310.
- [80] David et al. *J Am Chem Soc*, 136 (2014), pp. 13082-13085.
- [81] The facts about ammonia, Technical information, department of health (USA)
https://www.health.ny.gov/environmental/emergency/chemical_terrorism/docs/ammonia_tech.pdf

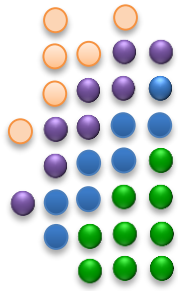
- [82] Ammonia handling manual.
<http://www.hydroinstruments.com/files/ammonia%20handling%20manual.pdf>
- [83] S. K. Singh, Q. Xu. *Catal Sci Technol*, 3(2013), pp. 1889-1900.
- [84] S. K. Singh, X. B. Zhang, Q. Xu. *J Am Chem Soc*, 131 (2009), pp. 9894-9895.
- [85] D. Teichmann, W. Arlt, P. Wasserscheid, R. Freymann. *Energy Environ Sci*, 4 (2011), pp. 2767-2773.
- [86] B. Müller, K. Müller, D. Teichmann, W. Arlt. *Chem Ing Tech*, 83 (2011), pp. 2002.
- [87] M. Markiewicz, Y. Q. Zhang, A. Bösmann, N. Brückner, J. Thöming, P. Wasserscheid S. Stolte. *Energy Environ Sci*, 8 (2015), pp. 1035-1045.
- [88] C. M. Araujo, D. L. Simone, S. J. Konezny, A. Shim, R. H. Crabtree, G. L. Soloveichik, V. S. Batista. *Energy Environ Sci*, 5 (2012), pp. 9534-9542.
- [89] Y. Wang, K.S. Chen, J. Mishler, S.C. Cho, X.C. Adroher. *Applied Energy*, 88 (2011), pp. 981-1007
- [90] <http://energy.gov/eere/fuelcells/types-fuel-cells>
- [91] S. P. S. Badwal, S. Giddey, A. Kulkarni, J. Goel, S. Basu. *Applied Energy*, 145(2015), pp. 80-103.
- [92] M. Z. F. Kamarudin, S. K. Kamarudin, M. S. Masdar, W. R.W. Daud. *Int J Hydrogen Energy*, 38 (2013), pp. 9438-9453.
- [93] S. Giddey, S. P. S. Badwal, A. Kulkarni, C. Munnings. *Prog Energy Combust Sci*, 38 (2012), pp.360-399.
- [94] P. D. Vaidya, A. E. Rodrigues. *Chem Engg J*, 117 (2006), pp.39-49.
- [95] I. Schmidt, K. Müller, W. Arlt. *Energy Fuels*, 28 (2014), pp. 6540-6544.
- [96] Q. Y. Bi, X. L. Du, Y. M. Liu, Y. Cao, H. Y. He, K. N. Fan. *J Am Chem Soc*, 134 (2012), pp. 8926-8933.
- [97] Hull et al. *Nature Chemistry*, 4 (2012), pp. 383-388.
- [98] D. Stolten. *Hydrogen and Fuel Cells: Fundamentals, Technologies and Applications*, Wiley-VCH (2010) ISBN: 978-3-527-32711.
- [99] M. Salimian, O. Okhay, R. Krishna, E. Titus, J. Gracio, L. Guerra, J. Ventura, C. Freire, C. Pereira, P. R. Babu, R. S. Khairnare. *Polym Int*, 62 (2013), pp. 1583-1588.
- [100] J. M. G. Sousa, A. L. C. Ferreira, E. Titus, R. Krishna, D. P. Fagg, J. Gracio. *J Nanosci Nanotechnol*, 12 (2012), pp. 6785-6791.
- [101] C. Anderson, D. F. Coker, J. Eckert, A. L. R. Bug. *J Chem Phys* 111 (1999), pp. 7599-7613.
- [102] S. Liu, X. Yang. *J Chem Phys*, 124 (2006), pp. 244705.

- [103] J. Weitkamp, M. Fritz, S. Ernst. *Int J of Hydrogen Energy*, 20 (1995), pp. 967-970.
- [104] B. Smit, T. L. M. Maesen, *Chem Review*, 108 (2008), pp. 4125-4184.
- [105] R. A. Schoonheydt, P. Geerlings, E. A. Pidko, R. A. van Santen. *J Mater Chem*, 22 (2012), pp. 18705-18717.
- [106] F. Darkrim, A. Aoufi, P. Malbrunot, D. Levesque. *J Chem Phys*, 112 (2000), pp. 5991-5999.
- [107] A. C. Dillon, K. M. Jones, T. A. Bekkedahl, C. H. Kiang, D. S. Bethune, M. J. Heben. *Nature* 386 (1997), pp. 377-379.
- [108] R. Ströbel, J. Garche, P.T. Moseley, L. Jörissen, G. Wolf. *J Power Sources*, 159 (2006), pp. 781-801.
- [109] A. Zuttel, P. Sudan, P. Mauron, T. Kiyobayashi, C. Emmenegger, L. Schlapbach. *Int J Hydrogen Energy*, 27 (2002), pp. 203-212.
- [110] W. C. Xu et al. *Int J Hydrogen Energy*, 32 (2007), pp. 2504-2512.
- [111] A. K. Geim, K. S. Novoselov. *Nature Mater* 6 (2007), pp. 183-191.
- [112] D. C. Elias et al. *Science* 30 (2009), pp. 610-613.
- [113] J. Y. Son, Y.H. Shin, H. Kim and H. M. Jang. *ACS Nano*, 4 (2010), 2655-2658.
- [114] B. F. Machado, P. Serp. *Catal Sci Technol*, 2 (2012), pp. 54-75.
- [115] X. Zhang, H. Zhang, C. Li, K. Wang, X. Sun, Y. Ma. *RSC Advances*, 4 (2014), pp. 45862-45884.
- [116] Q. Li, N. Mahmood, J.h. Zhu, Y.L. Hou, S.H. Sun. *Nanotoday*, 9 (2014), pp. 668-683.
- [117] S. Nardecchia, D. Carriazo, M. L. Ferrer, M.C. Gutierrez, F. del Monte. *Chem Soc Rev*, 42 (2013), pp. 794-830.
- [118] D. Xia, Q.Z. Xue, J. Xie, H.J. Chen, C. Lv, F. Besenbacher, M.D. Dong. *Small*, 6 (2010), pp. 2010-2019.
- [119] M.Q. Yang, N. Zhang, Y.J. Xu. *ACS Applied Mater Interfaces*, 5 (2013), pp. 1156-1164.
- [120] M. O’Keeffe, M. Eddaoudi, H. Li, T. Reineke, O. M. Yagh. *J Sol State Chem*, 152 (2000), pp. 3-20.
- [121] N. L. Rosi, J. Eckert, M. Eddaoudi, D. T. Vodak, J. Kim, M. O’Keeffe, O. M. Yaghi. *Science*, 300 (2003), pp. 1127-1129.
- [122] N.L. Rosi, M. Eddaoudi, J. Kim, M. O’Keeffe, O.M. Yaghi. *Angew Chem Int Ed*, 41 (2002), pp. 284-287.
- [123] B.J. Burnett, P.M. Barron, C. Hu, W. Choe. *J Am Chem Soc*, 133 (2011), pp. 9984-9987.

- [124] O. M. Yaghi, M. O’Keeffe, N.W. Ockwig, H.K. Chae, M. Eddaoudi, J. Kim. *Nature*, 423 (2003), pp. 705-714.
- [125] E. Klontzas, A. Mavrandonakis, E. Tylianakis, G. E. Froudakis. *Nano Lett*, (2008), pp. 1572-1576.
- [126] G. Férey, M. Latroche, C. Serre, F. Millange, *Chem Comm*, (2003), pp. 2976-2977.
- [127] K. Oura, V. G. Lifshits, A. Saranin, A.V. Zotov, M. Katayama. *Surface Science, An Introduction*, (2003) Berlin: Springer, ISBN 978-3-540-00545-2.
- [128] R. Ströbel, J. Garche, P.T. Moseley, L. Jörissen. G. Wolf. *J. Power Sources* 159 (2006), pp. 781.
- [129] L. Hammer, H. Landskron, W. N. Pecher, A. Fricke, K. Hein, K. Müller. *Phys Rev B*, 47 (1993), pp.15969.
- [130] H. C. Van Ness. *Ind Eng Chem Fundamen*, 8 (1969), pp. 464-473.
- [131] M. M. Dubinin. *Chem Rev*, 60 (1960), pp. 235-241.
- [132] Y. Yao. *Hydrogen Storage Using Carbon Nanotubes*, Intech Open (2010).
- [133] S. Brunauer, P. H. Emmett, E. Teller. *J Am Chem Soc* 60 (1938), pp. 309.
- [134] R. Oriňáková, A. Oriňák. *Fuel*, 90 (2011), pp. 3123-3140.
- [135] G. E. Ioannatos, X. E. Verykios. *Int J Hydrogen Energy*, 35 (2010), pp. 622-628.
- [136] P. Chen, X. Wu, J. Lin, K.L. Tan. *Science*, 285 (1999), pp. 91-93.
- [137] T. Das, S. Banerjee, K. Dasgupta, J. B. Joshi, V. Sudarsan. *RSC Advances*, 5 (2015), pp. 41468-41474.
- [138] <http://ssrl.slac.stanford.edu/nilssongroup/research.html>
- [139] G. P. Miller, J. Kintigh, E. Kim, P. F. Weck, S. Berber, D. Tomanek. *J Am Chem Soc*, 130 (2008), pp. 2296-2303.
- [140] J. H. Cho, C. R. Park. *Catal Today*, 120 (2007), pp.407-412.
- [141] S. Pekker, J. P. Salvetat, E. Jakab, J.-M. Bonard, L. Forro. *J Phys Chem B*, 105 (2001), pp. 7938-7943.
- [142] A. A. Akhrem. *Birch reduction of aromatic compounds*, Springer (2012).
- [143] A. Hirsch, M. Brettreich. *Fullerenes: Chemistry and Reactions*. Wiley-VCH Verlag GmbH & Co. KGaA (2005). DOI: 10.1002/3527603492
- [144] M. C. Coelho, E. Titus, G. Cabral, V. Neto, J. C. Madaleno, Q.H. Fan, A. C. M. Sousa , J. Grácio. *J Nanosci Nanotechnol*, 8 (2008), pp. 4023.
- [145] A. V. Talyzin et al. *ACS Nano* 5 (2011), pp. 5132-5140.
- [146] R. Bhowmick et al. *J Am Chem Soc*, 133 (2011), pp. 5580-5586.

- [147] K. S. Novoselov, A. K. Geim, S. V. Morozov, D. Jiang, Y. Zhang, S. V. Dubonos, I. V. Grigorieva, A. A. Firsov. *Science*, 306 (2004), pp. 666-669.
- [148] A. H. C. Neto, F. Guinea, N. M. R. Peres, K. S. Novoselov, A. K. Geim. *Rev Mod Phys*, 81 (2009), pp. 109-162.
- [149] D. R. Dreyer, S. Park, C. W. Bielawski and R. S. Ruoff. *Chem Soc Rev*, 39 (2010), pp. 228-240.
- [150] N. Zhang, H.X. Qiu, Y. Liu, W. Wang, Y. Li, X. D. Wang, J. P. Gao. *J Mater Chem*, 21 (2011), pp. 11080-11083.
- [151] H. Wang, J. T. Robinson, G. Diankov, H. Dai. *J Am Chem Soc*, 132 (2010), pp. 3270-3271.
- [152] X. Zhang, H. Zhang, C. Li, K. Wang, X. Sun, Y. Ma. *RSC Advances*, 4 (2014), pp. 45862-45884.
- [153] J.O. Sofo, A.S. Chaudhari, G.D. Barber. *Phys Rev B*, 75 (2007), pp.153401.
- [154] <http://thefutureofthings.com/3979-graphene-based-insulator-developed/>
- [155] Y. Wang, D.C. Alsmeyer, R.L. McCreery. *Chem Mater*, 2 (1990), pp. 557-563.
- [156] A. Sadezky, H. Muckenhuber, H. Grothe, R. Niessner, U. Pöschl. *Carbon*, 43 (2005), pp. 1731-1742.
- [157] S. D. M. Brown, A. Jorio, M. S. Dresselhaus, G. Dresselhaus. *Phys Rev B*, 64 (2001), pp. 073403.
- [158] G. K. Dimitrakakis, E. Tylianakis, G. E. Froudakis. *Nano Lett*, 8 (2008), 3166-3170.
- [159] M. Bieri et al. *Chem Commun*, 45 (2009), pp. 6919-6921.
- [160] K. M. Fair, X. Y. Cui, L. Li, C. C. Shieh, R. K. Zheng, Z. W. Liu, B. Delley, M. J. Ford, S. P. Ringer, C. Stampf. *Phys Rev B*, 87 (2013), pp. 014102.
- [161] L. P. Ma, Z. S. Wu, J. Li, E. D. Wu, W. C. Ren, H. M. Chen. *Int J Hydrogen Energy*, 34 (2009), pp. 2329-2332.
- [162] G. Srinivas, Y. Zhu, R. Piner, N. Skipper, M. Ellerby, R. S. Ruoff. *Carbon*, 48 (2010), pp. 630-635.
- [163] J. W. Burrell, S. Gadipelli, J. Ford, J. M. Simmons, W. Zhou, T. Yildirim. *Angew Chem Int Ed*, 49 (2010), pp. 8902-8904.
- [164] S. Gadipelli, Z. X. Guo. *Progress in Materials Science*, 69 (2015), pp. 1-60.
- [165] L. Zheng, Z. Li, S. Bourdo, F. Watanabe, C. C. Ryerson, A. S. Biris. *Chem Commun*, 47 (2011), pp. 1213-1215.
- [166] C.C. Huang, N.W. Pu, C.A. Wang, J.C. Huang, Y. Sung, M.D. Ger. *Separ Purif Tech*, 82 (2011), pp. 210-215.

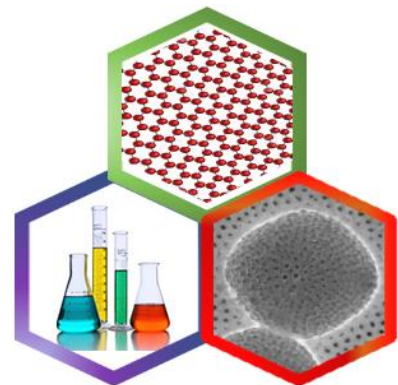
- [167] H. Zhou, X. Liu, J. Zhang, X. Yan, Y. Liu, A. Yu. *Int J Hydrogen Energy*, 39 (2014), pp. 2160-2167.
- [168] F.A. Lewis. *The Palladium–Hydrogen System*. Academic Press, London (1967).
- [169] A. Pundt, C. Sachs, M. Winter, M.T. Reetz, D. Fritsch, R. Kirchheim. *J Alloys Compd*, 293 (1999), pp. 480-483.
- [170] W. Grochala, P. P. Edwards. *Chem Rev*, 104 (2004), pp. 1283-1315.
- [171] S. Kishore, J. Nelson, J. Adair, P. Eklund. *J Alloy Compd*, 389 (2005), pp. 234–242.
- [172] G. Li et al. *Nature Materials*, 13 (2014), pp. 802–806.
- [173] Y. Wang et al. *ACS Nano*, 4 (2010), pp. 6146-6152.
- [174] S. Zhu, T. Li. *ACS Nano*, 8 (2014), pp. 2864-2872.
- [175] L. Ci et al. *Nano Res*, 1 (2008), pp.116-122.
- [176] L. C. Campos et al. *Nano Lett*, 9 (2009), pp. 2600-2604.



CHAPTER 2

HYDROGENATION OF GRAPHENE OXIDE:

Synthesis, characterization and results



Chapter 2

<u>Hydrogenation of graphene oxide: Synthesis, characterization and results</u>	50
2.1 Introduction	52
2.2 Synthesis of hydrogenated reduced graphene oxide (HRGO)	52
2.2.1 Experimental	53
2.2.1.1 Chemicals	53
2.2.1.2 Synthesis of GO	53
2.2.1.3 Synthesis of HRGO	54
2.2.2 Characterization techniques	54
2.2.3 Results and discussion	55
2.3 Rapid Electrochemical Synthesis of Hydrogenated Graphene Oxide Using Ni NPs	58
2.3.1 Synthesis of HGO	58
2.3.2 Results and discussion	58
2.3.3 Mechanism of HGO formation	64
2.4 Coclusions	65
2.5 References	65

HYDROGENATION OF GRAPHENE OXIDE:**Synthesis, characterization and results****2.1 Introduction**

Ever since the discovery of two dimensional graphene, extensive research is going on to explore this material for energy application [1-2]. Recently, hydrogenation of graphene to make graphane has attracted tremendous attention to exploit the possibilities for hydrogen storage [3]. Graphane is suggested to be useful for hydrogen storage since the sp^3 C–H bond generated by hydrogenation of graphene and reduced graphene gets easily dehydrogenated on photothermal heating [4]. Nevertheless, these unique properties are obtained only by efficient hydrogenation of graphene. Hydrogenation of graphene was first reported by Sofo *et al.* through their first principles calculation and the idea was instantly transformed into reality by the experimental production of hydrogenated graphene (graphane) [5].

2.2 Synthesis of hydrogenated reduced graphene oxide (HRGO)

Nickel is known to be a very active hydrogenation catalyst and a hydrogen spillover initiator [6]. Zheng *et al.* demonstrated the catalytic hydrogenation of graphene films by using Ni/Al₂O₃ with the flow of H₂ at 820 °C [7]. Subrahmanyam *et al.* also showed that Birch reduction of few-layer graphene samples at -33 °C gives rise to hydrogenated samples containing up to 5 wt.% of hydrogen [8]. However, these attempts have been limited to *ex-situ* hydrogenation of graphene under extreme conditions. The reduction of GO by metal catalysts (Al, Fe and Zn) is reported in other's work also [9-13]. In the light of above reports, this is highly important to develop a facile and energy saving method for the reduction of GO to HRGO under ambient conditions. In this work, bulk nickel powder used as an active hydrogenation catalyst due to their hydrogen production capability (in acidic media) and

spillover effect. The possible mechanism of hydrogen spillover and its role in formation of HRGO are analyzed. Fig. 2.1 illustrates the reduction of GO by bulk Ni powder and formation of HRGO at RT via *in-situ* generated atomic hydrogen.

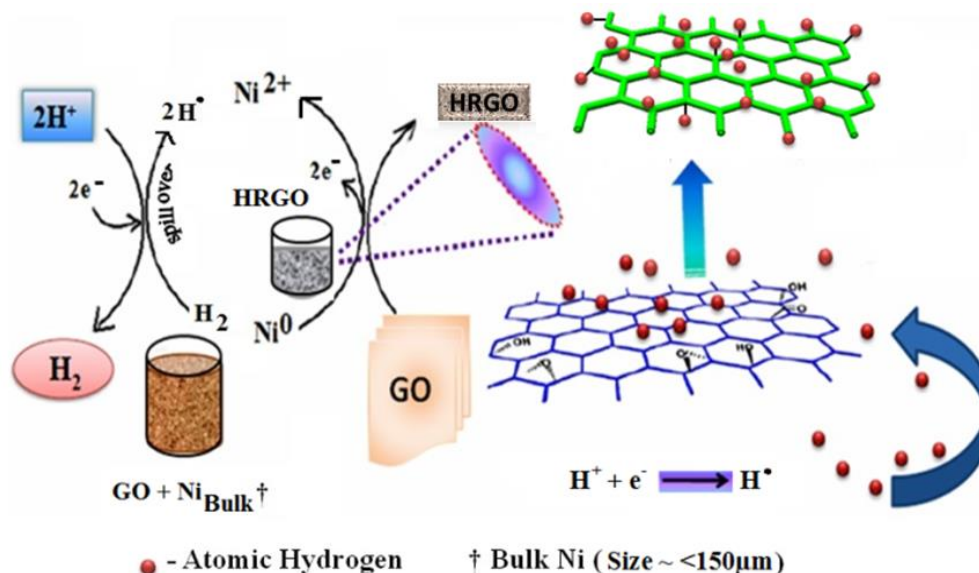


Figure 2.1 Schematic illustration for synthesis of HRGO using nickel via *in-situ* generated atomic hydrogen.

2.2.1 Experimental

2.2.1.1 Chemicals

Commercially available natural flake graphite, sulfuric acid (95-98%), potassium permanganate, hydrogen peroxide, nickel powder (<150 μ m, 99.99% trace metals basis) and hydrochloric acid (36.5-38%) were purchased from Sigma-Aldrich and used as received. Other reagents were of analytical grade and were used as received without further purification. All aqueous solutions were prepared with deionised distilled (DD) water (>18.2M Ω .cm) from a Milli-Q Plus system (Millipore).

2.2.1.2 Synthesis of GO

Graphene oxide (GO) was synthesized by chemical exfoliation method of graphite powder [14]. The resultant suspension was extensively washed with DD water and dilute HCl until the pH of the filtrate was neutral and subsequently centrifuged (3000 rpm) in order to remove residual unexfoliated graphite and oxidizing agents. GO slurry was then freeze-dried and stored in a vacuum oven at RT.

2.2.1.3 Synthesis of HRGO

Dry GO powder (0.075 g) was initially dispersed in DD water (100 ml) under sonication (15 min). Subsequently, Ni powder (1.25 g) was added to the GO suspension in a round bottom (RB) flask and re-sonicated (10 min) followed by stirring (200 rpm for 15 min) under ambient conditions. Finally, 70.0 ml of conc. HCl was slowly poured to the above solution and continuously stirred for next 24 hrs. After the completion of reaction final product was centrifuged (6000 rpm, 15 min) to remove any remaining impurities and repeatedly washed with DD water and dried at 70 °C in oven.

2.2.2 Characterization techniques

Phase purity and presence of crystalline phases of GO and HRGO samples were analysed by X-ray diffraction (XRD) analysis (Rigaku Geigerflex D/Max, C Series, Tokyo, Japan; CuK α radiation; 2 θ angle range 5–75°; step 0.02°/s). The FTIR spectra were recorded using a Bruker Tensor 27 FT-IR spectrometer by mixing the sample in KBr (Aldrich, 99%, FT-IR grade). X-ray photoelectron spectroscopy (XPS) measurements were performed using an ESCALAB 200A, VG Scientific (UK). For analysis, an achromatic Al (K α) X-ray source operating at 15 kV (300 W) was used, and the spectrometer was operated in CAE mode with 20 eV pass energy. Data acquisition was performed with a pressure lower than 10⁻⁶ Pa. Spectral analysis was performed using the XPS Peak software with Gaussian–Lorentzian peak shape. The binding energies of XPS spectra were determined by curve deconvolution using non-linear least squares fitting routine after a Shirley-type background subtraction. The Raman spectra were obtained at RT in back scattering configuration with a Jobin-Yvon Lab Ram HR equipped with a Multichannel air cooled (-70 °C) CCD detector. The samples for TEM were prepared by dipping an aliquot of suspension (HRGO in acetone, 0.1 mg/ ml) on to a carbon-coated copper grid. A conventional high-resolution (HR) TEM (JEOL 2200F TEM) was performed to analyze the crystallinity and quality of HRGO sample. Results were collected at 200 kV with a point resolution of 0.16 nm.

2.2.3 Results and discussion

In this work, XRD was used to probe the reduction of GO. Fig. 2.2 (a) shows the XRD patterns of GO and HRGO, respectively. In GO, a strong peak observed at around 10.91° corresponds to the (001) basal plane [9-12]. However, in HRGO the peak at 10.91° was diminished and a new peak appeared at around 25.2° corresponding to the (002) lattice plane, which infers the reduction of GO by the removal of oxygen functionalities.

Fig. 2.2 (b) shows the FTIR spectra of GO, HRGO and RGO which clearly depicts the change in carbon structure and provide the evidence for successful hydrogenation of GO. The spectrum of GO showed no peaks in fingerprint region related to C-H stretching mode of vibration between 2700 and 3100 cm^{-1} . However, the spectrum of HRGO displayed three well defined fingerprint C-H peaks at around 2853 , 2923 and 2970 cm^{-1} . The first two peaks were attributed to symmetric and asymmetric stretching modes of vibration of the $\text{sp}^3\text{-CH}_2$ bond. The additional mode of vibration at around 2970 cm^{-1} is due to asymmetric $\text{sp}^3\text{-CH}_3$ stretching vibration which clearly shows the formation of graphane. Similar peak positions have been noticed in earlier work of catalytic assisted hydrogenation of graphene by a catalytic chemical vapour deposition (rf-cCVD) method at 820°C [7]. The typical triple features in C-H vibration have also been seen in hydrogenated graphene by Birch reduction [8], and in carbon nanotubes by dissociation of the H_2 molecule at $400\text{-}550^\circ\text{C}$ [15]. The reduction of GO to HRGO was further analysed by XPS. Fig. 2.2 (c) shows the C1s XPS spectra of the HRGO sample fitted with four different peaks centered at 281.8 , 284.6 , 284.8 and 286.5 eV which are attributed to C-C, $\text{sp}^2\text{-C}$, $\text{sp}^3\text{-C}$ and C-O respectively [9]. The intensity of the C1s $\text{sp}^3\text{-C}$ peak (284.8) was higher compared to the C1s $\text{sp}^2\text{-C}$ (284.6) peak. It shows more C-H coupling and less conjugated π systems due to the reduction by atomic hydrogen. Interestingly, here an additional peak was also observed at around 281.8 eV which can be attributed to a Ni-C_x carbide bond [16].

Further, the successful hydrogenation of the new product, HRGO, is also reflected in the Raman spectrum as shown in Fig. 2.2 (d). The Raman spectrum of GO displayed two characteristic D and G bands at 1352 and 1592 cm^{-1} with an I_D/I_G ratio of 0.91 . The G band is an intrinsic feature of graphene oxide that is closely related to vibrations in all sp^2 carbon materials [9]. The activation of the D band becomes prominent in GO due to the reduction in size of the in-plane sp^2 domains, probably by extensive chemical oxidation [9-12]. Along with the intensity increase of the D peak (I_D/I_G ratio of 1.12), we observed shifts in D and G bands to 1345 and 1576 cm^{-1} in the final product which is clear evidence of transformation of GO to

HRGO. Our results are in agreement with the report of Wang *et al.* who showed a shift in D (1345 cm^{-1}) and G (1580 cm^{-1}) band positions due to the reversion of graphane to graphene by dehydrogenation [17]. In addition, a shoulder peak also appeared in our sample at around 1608 cm^{-1} which has been assigned as D' activated by defects *via* a double resonance Raman process [3].

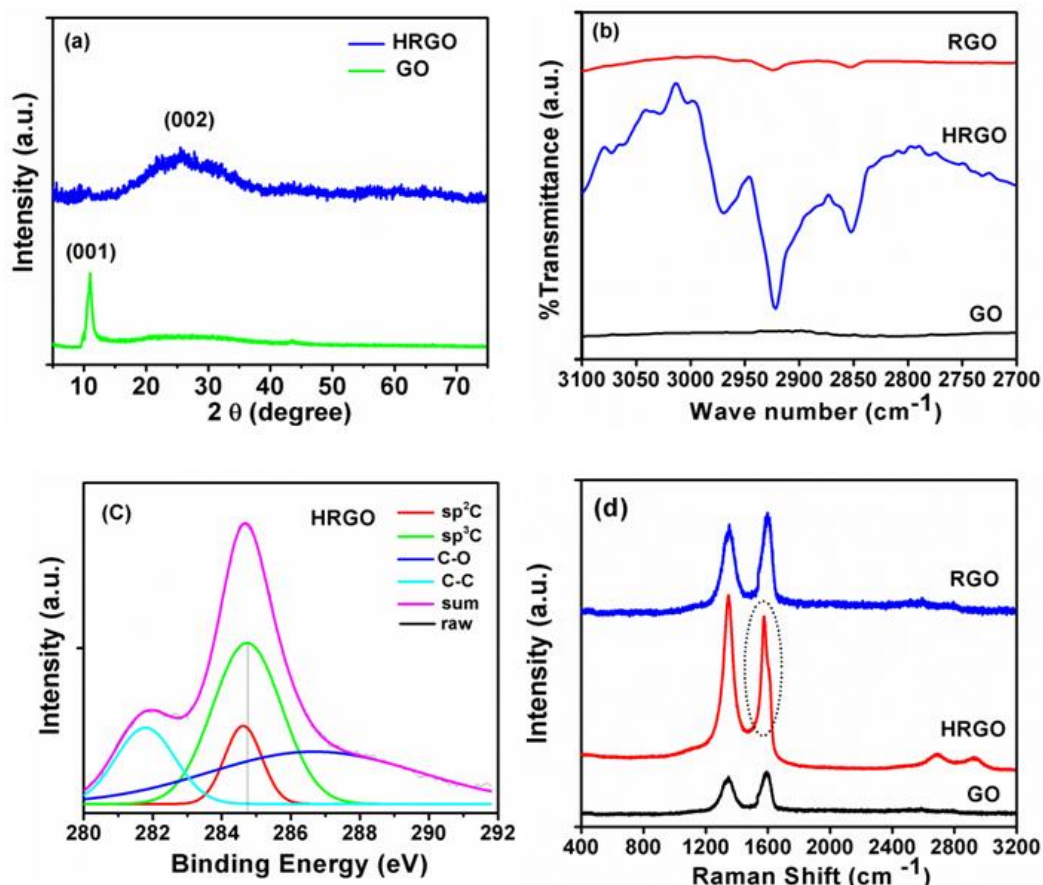


Figure 2.2 displays (a) XRD of GO and HRGO and (b) FTIR spectra of GO HRGO and RGO (after the annealing). (c) XPS spectra of HRGO after deconvolution and peak fitting. (d) Raman spectra of GO, HRGO and RGO (after the annealing).

Luo *et al.* also noticed the appearance of three defect induced peaks at 1340 , 1620 and 2920 cm^{-1} after hydrogenation of graphene under hydrogen plasma [18]. In their work, the appearance of the D' band and the higher intensities of 2D (2690 cm^{-1}) and D + G (2921 cm^{-1}) bands in HRGO confirm the hydrogenation during the reduction process and formation of $\text{sp}^3\text{ C-H}$ bonds or saturation of the -C=C- bond by the H atom. The G band shift in graphene and carbon nanotubes is directly related to change in their electronic properties. Talyzin *et al.*

observed the shift in the G band from 1550 cm^{-1} to 1570 cm^{-1} and is attributed to the typical sign of conversion from metallic to semiconducting single walled carbon nanotubes by hydrogenation [15].

Transmission electron microscopy (TEM) analysis was performed to investigate the structure and morphology of HRGO in detail. Fig. 2.3 (a) shows the TEM of HRGO sheets with single to few layers of graphene. In order to probe the geometry of the resulted material, selective area electron diffraction (SAED) was performed focusing the electron beam on HRGO sheet as shown in Fig. 2.3 (b). The SAED pattern reflected distorted hexagonal lattice with diffused spots. These diffused spots are due to the hydrogenation and buckling in saturated (sp^3 hybridized) hexagonal ring system. In this work, the SAED shown in earlier reports are different probably, due to the difference in method of graphene hydrogenation.

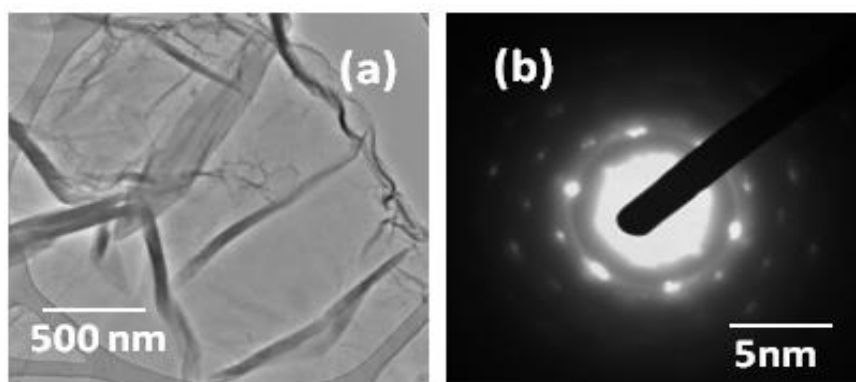


Figure 2.3 (a) TEM image and (b) SAED of HRGO.

For example, the SAED exhibited in Elias *et al.*'s work is from single sided hydrogenated graphene on substrate and retains periodic hexagonal diffraction spots even after hydrogenation [3]. This might be due to the hydrogenation of pristine graphene, and maintaining of their perfect hexagonal structure after hydrogenation process.

2.3 Rapid Electrochemical Synthesis of Hydrogenated Graphene Oxide Using Ni Nanoparticles

Due to the large demand of hydrogenated graphene and low reactivity of bulk Ni (slow dissolution in acidic medium and agglomeration of bulk counterpart); it is highly important to modify the method to fulfill the energy need [19]. To solve such kind of problem for the first time, Ni nanoparticles (Ni NPs size ~10-25 nm) were used to make the hydrogenated graphene oxide (HGO) [20]. Due to the nano-size effect, particles are well dispersed on the graphene sheet and the whole synthesis was accomplished within 3 h as compared to bulk Ni (24 h) and provided the hydrogenated graphene oxide.

2.3.1 Synthesis of HGO

Hydrogenated graphene oxide (HGO) was synthesized by the electrochemical hydrogenation of GO [19] and Ni NPs in acidic conditions. In this reaction, H₂ gas was *in-situ* generated by the electrochemical reaction of Ni NPs and HCl (Ni/H⁺).

2.3.2 Results and discussion

Fig. 2.4 illustrates the instrumental representation for the synthesis of HGO. In this work, 30 mL of well-dispersed GO suspension (2 mg/mL) was poured into a 250 mL round-bottom (RB) flask. Followed by, a pre-calculated amount of Ni NPs (300 mg) were dispersed in the GO suspension for 15 min of ultrasonication at room temperature (RT) and the homogenized suspension is referred to as Ni-GO intermediate species. Further, 39 mL of concentrated HCl was added to the above suspension in three equal parts (13 mL each, with a time interval of 45 min) and the suspension was continuously stirred by a teflon-coated mechanical stirrer for 3 h. To ensure the maximum hydrogenation of GO by *in-situ* generated H₂, the reaction was carried out at RT (25 °C) and the acid was slowly poured during the reaction. The whole reaction was accomplished in a well-ventilated fume hood with a temperature controller. After the completion of the reaction, the top part of the product (HGO) was precisely collected and the bottom part of the solution was discarded to remove the maximum extent of impurities. Finally, the product was 2-3 times centrifuged (4000 rpm, 10 min) to remove the cationic and anionic impurities and repeatedly washed with distilled (DD) water and dried at 100 °C.

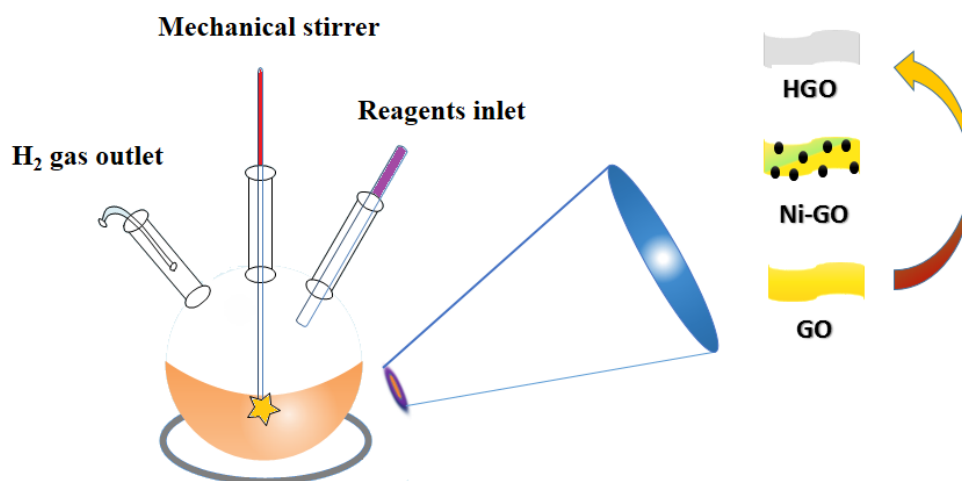


Figure 2.4 Instrumental setup and representation of HGO synthesis.

Fig. 2.5 (a) shows the XRD patterns of GO, intermediate species Ni-GO and HGO samples. GO exhibits a sharp peak at around 9.09° corresponding to the (001) basal plane with d spacing of ($d_{001} = 0.961\text{nm}$). This value was higher than the interlayer spacing of graphite flakes ($d\text{-spacing} = 0.334\text{nm}$, $2\theta = 26.4^\circ$), due to the presence of oxygenated functional groups and intercalated water molecules [9-13]. After the intercalation of Ni NPs with GO three additional peaks (1 1 1), (2 0 0) and (2 2 0) were observed in intermediate species Ni-GO that were related to the various crystallographic planes of face-centred cubic (fcc) Ni-NPs [JCPDS card No. 04-0850] and the highest intense diffraction peak at around 44.4° suggest the crystallinity of Ni-NPs [21]. In HGO all these three additional peaks were eliminated and only one peak was observed with small shift at 10.9° indicates hydrogenation of GO (in presence of Ni NPs) was more significant compared to the restoration of graphitic domains. However, normal reduction profile suggests the formation of RGO by XRD peak shifting towards characteristic graphitic peak position, either using of hydrazine hydrate or other kind of reducing metal species like (Mg, Al, Fe and Zn) in acidic medium [9-13]. Further, UV-vis absorption spectra was analyzed to under the reduction process in more detail. Fig. 2.5 (b) shows that the UV-vis spectra of GO, HGO and RGO. In this work RGO was synthesized by the reduction of GO reduced in presence of Zn/HCl (in same reaction condition, for comparison to investigate the recovery of conjugative C=C bonding). Spectra displays that GO possess two characteristic absorption bands at 230 nm and 300 nm (assigned as in shoulder form). These bands were related to the $\pi \rightarrow \pi^*$ aromatic (C=C) and $n \rightarrow \pi^*$ (C=O) transitions, respectively [9-12]. While in HGO a broad band was observed in the range of 250-280 nm suggests the some reduction of carbonyl functionalities and enrichment of (-C-H) saturated bonds. Whereas, spectra of RGO shows clear distinction from GO and HGO, depicts a strong sharp peak at

around 267 nm suggests almost removal of oxygen functionality and establishment of C=C conjugated graphene structure.

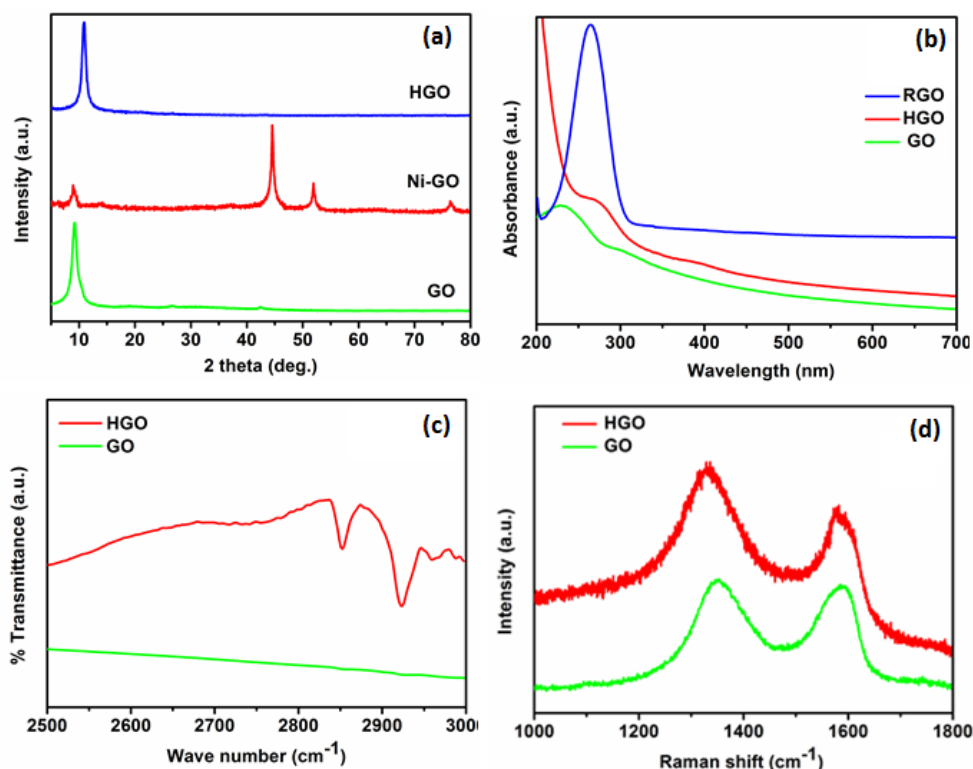


Figure 2.5 (a) XRD pattern of the GO, Ni-GO and HGO, (b) UV-vis. spectra of the GO, HGO and RGO, (c) FTIR spectra of the GO and HGO, and (d) Raman spectra of the GO and HGO.

Fig. 2.5 (c) shows the FTIR spectra of GO and HGO samples (in the range of 2500-3000 cm^{-1}). In HGO, two sharp peaks were observed at around 2853 and 2923 cm^{-1} and both were attributed as corresponding symmetric and asymmetric C-H stretching mode of $\text{sp}^3\text{-C}$ ($\nu_{\text{C-H}}$) vibrations. The evolution of these two peaks in HGO (with distinction of GO) directly infers the hydrogenation of GO. Further, to ascertain the successful hydrogenation of GO and HGO, Raman spectroscopy was used. This technique is very useful for assigning the corresponding changes of graphene material on the basis of peak position and intensity. Fig. 2.5 (d) shows the Raman spectrum of GO and HGO in the range of 1000-1800 cm^{-1} . In GO spectra two prominent bands D and G were located at 1349 cm^{-1} at 1588 cm^{-1} with respective $I_{\text{D}}/I_{\text{G}}$ ratio of 0.98. This is well known fact that G band is an intrinsic feature of graphitic system and it corresponds to the first-order scattering of the $\text{E}_{2\text{g}}$ mode of sp^2 domain of carbon (related to the all sp^2 carbon vibrations in long-wavelength optical phonons TO and LO). D band is arising after the defect introduction and related to the characteristic breathing mode of $\text{A}_{1\text{g}}$ symmetry. Whereas in HGO, both D and G bands were shifted to lower wave number (red-shifted) and appeared at

1333 and 1584 cm^{-1} , respectively with increased I_D/I_G ratio of ~ 1.36 . This increment of I_D/I_G ratio in HGO provides a clear evidence for corresponding changes inside of carbon system after the reduction. Moreover, asymmetric shape and broadening of G band in HGO also suggests the possible hydrogenation of carbon system. Fig. 2.6 shows that the Laurentian peak fitted data of HGO and after the deconvolution of G band, two peaks were clearly observed and higher wave number peak around at $\sim 1608 \text{ cm}^{-1}$ represents the D' defect band. This was already reported that D' band is related to nonzero phonon density of states above the G band and become active after the defect introduction or double resonance process [22]. This was due to the Raman scattering near to the “intra-valley” by the promotion of ‘out-of-plane’ ripple induced sp^3 hybridization (-C-H bonding) mediated by phonons nearby Γ and K (or K') points. A recent Monte Carlo simulation study also supports the sp^3 (-C-H) bonding is favourable in rippled graphene than that of flat graphene [23]. To confirm this, we have also performed the microscopic analysis to investigate the morphology and microstructure of our product.

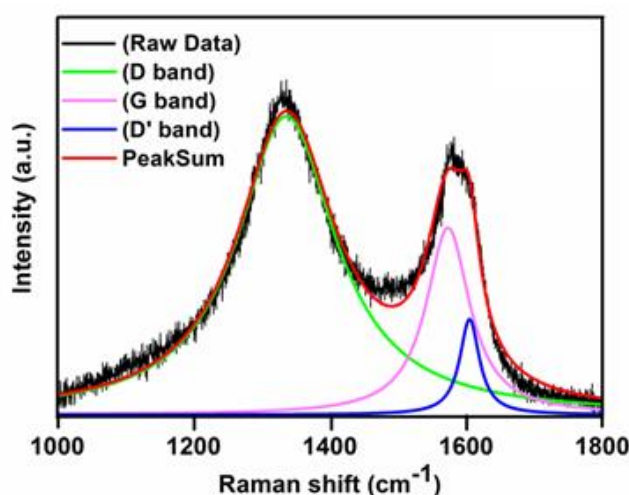


Figure 2.6 Fitted Raman spectra of HGO after deconvolution of D and G band.

Further, systematic microscopic investigation was carried out of initial materials (GO and Ni NPs) with intermediate composite material Ni-GO (after the loading of Ni NPs within the GO matrix) and final product HGO as shown in Fig. 2.7. In which Fig. 2.7 (a) and (b) shows the SEM images of GO and Ni nanoparticles, respectively. Image of GO clearly exhibits the few layer of graphitic carbon with typical wrinkle behavior. Image (b) displays the initial morphology and size of the Ni NPs and shows that all particles were in nano regime with spherical shape.

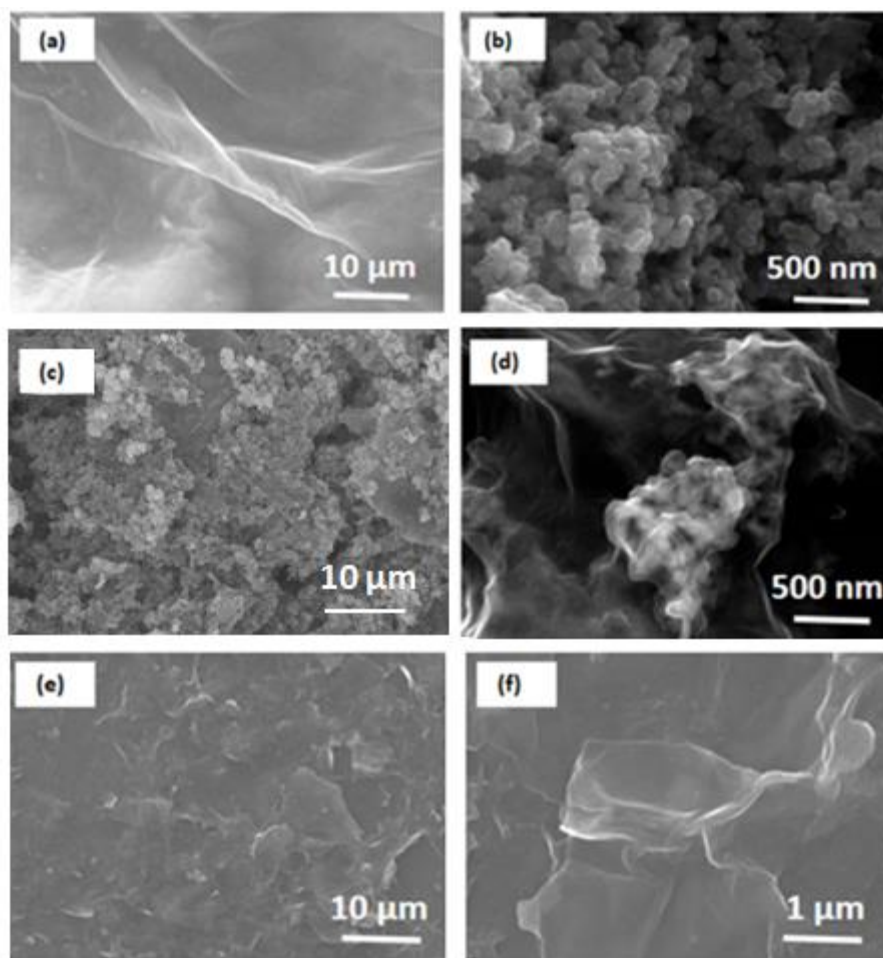


Figure 2.7 (a) and (b) SEM images of initial material GO and Ni nanoparticles, (c) and (d) SEM images of intermediate Ni-GO composite material in lower and higher magnification, and (e) and (f) SEM images of final product HGO in lower and higher magnification.

Fig. 2.7 (c) and (d) shows the SEM images of intermediate species Ni-GO after the loading of Ni NPs with GO. Both the images depicts well intercalation of Ni NPs with graphitic flakes and image contrast in higher magnification image (white spots on black background) clearly reveals the covering of Ni NPs by single or few layers graphene sheets. Fig. 2.7 (e) and (f) displays the lower and higher magnifications SEM images of HGO after the reduction and apparently there was no particles were observed. The absence of Ni NPs was obvious because during the reduction process Ni NPs were oxidized by conc. HCl and produces the cations that were removed after washing. Interestingly, in HGO carbon sheet was less agglomerated as compared to Ni-GO and GO. This can be explained as: during the reduction process internal hydrogen bonding of carbon system related to carboxylic and carbonyl ($-C=O$) group of GO disrupted and these polar functionalities sp^2 might be transformed in to the sp^3 ($-C-H$) moiety and later species is less polar which pursuit's weak interaction between graphene sheets.

Finally, TEM analysis was performed for detailed investigation of morphology and internal structure. Fig. 2.8 (a) and (b) shows the lower and higher magnification TEM images of Ni-GO. Here, we clearly visualized the Ni NPs homogeneously distributed on graphene sheet and higher magnification image shows that the all particles were lesser than 20 nm size and in spherical shape. Fig. 2.8 (c) and (d) shows the TEM images of final product HGO and in lower and higher magnifications, respectively. This can be explained as, after the hydrogenation, oxygen functionalities and graphitic domains get saturated and led to the formulation of sp^3 (-C-H) structure. However, initial experimental work related to hydrogenation of graphene (graphane synthesis) reflects the equidistance position of diffraction spots. This was probably due to the hydrogenation of consistent hexagonally arranged initial material (graphene) which pertains the sp^2 hybridized regular hexagonal ring structure [3].

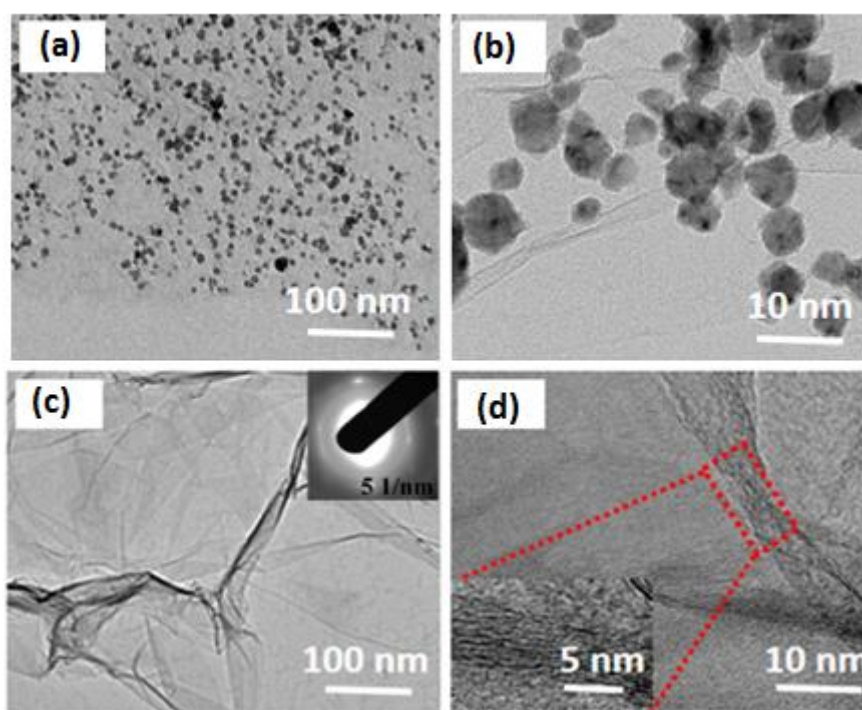


Figure 2.8 (a) and (b) TEM images of intermediate Ni-GO in lower and higher magnification, and (c) and (d) TEM images of final product HGO in lower and higher magnification. The corresponding inset image of (c) is SAED and (d) 4X magnified area.

2.3.3 Mechanism of HGO formation

On the basis of experimental results finally, a detailed mechanism of HGO formation was elaborated as schematically shown in Fig. 2.9. Initially, during the course of reaction an intermediate Ni-GO was formed. Which further reacts with HCl (aq.) and produces the Ni^{2+} and 2e^- through electrochemical reaction between Ni and hydrochloric acid ($\text{Ni} + 2\text{HCl} = \text{Ni}^{2+} + 2\text{Cl}^- + 2\text{H}^+ + 2\text{e}^-$). Meanwhile, proton and electrons combines together ($2\text{H}^+ + 2\text{e}^- = \text{H}_2$) and produces the hydrogen gas. In this process Ni NPs were continuously reacted with acid and reduces own size.

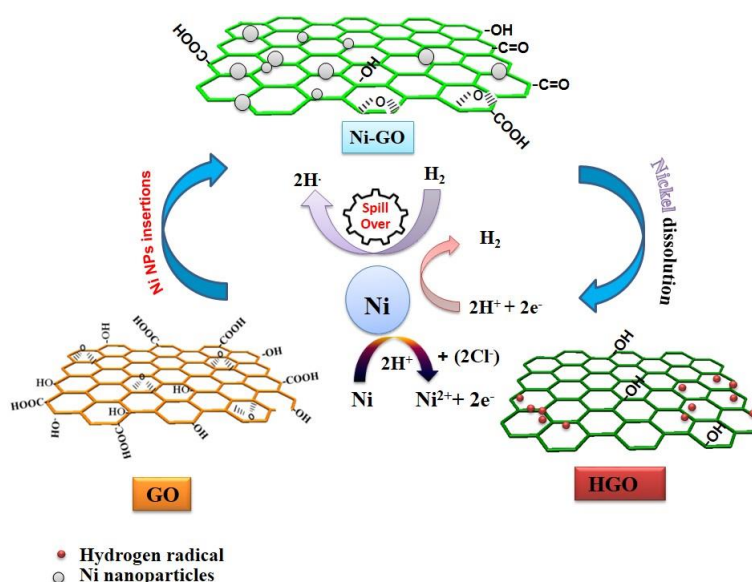


Figure 2.9 Schematic representation of GO to HGO formation via intermediate species Ni-GO through continuous hydrogen spillover process during the reaction.

These NPs pursue very high catalytic activity (more smaller size tends to larger surface area and higher surface energy) and enhances the spillover of hydrogen ($\text{H}_2 = 2\text{H}^\cdot$) on its surfaces and makes the radical hydrogen (H^\cdot) which is easily adsorbed onto the GO and forms the HGO ($\text{GO} + 2\text{H}^\cdot = \text{HGO}_{\text{Red}} + \text{H}_2\text{O}$). GO can also be reduced by direct attachment of H^+ and e^- ($\text{GO} + \text{mH}^+ + \text{ne}^- = \text{RGO} + \text{pH}_2\text{O}$), but due to its low redox potential ($\text{Ni} = -0.28\text{V}$) it loses electrons very slowly and instead the forming of RGO makes the HGO. It has been already reported that the Ni is very prominent catalyst for hydrogenation of olefinic and benzene double bond and for unsaturated benzene derived carbonyl functionalities also. Thermodynamic stability data of hydrogenation of double bond also favors the dissociative chemisorption of hydrogen. This was already explained as: initially an adduct species is formed on the surface of

catalyst by the breaking of π - π bonding and simultaneously hydrogen molecule also dissociates in to radical hydrogen ($H-H = 2H^{\cdot}$) making the metal hydride species (Ni-H). The generated radical H migrates from Ni catalyst surface to the C-C bond through a “bridge” built and completes the process. However, in our case hydrogen molecule is generated inside the system through electrochemical reaction without any external source, further *in-situ* produced hydrogen easily spillover on own generator (nano Ni surface) and readily transforms to the unsaturated carbon sites. To describe this migration of H, here we are assuming that one Ni particles works as a (source, *S*) and simultaneously another nanoparticle works as an (activator, *Act*) to dissociate the hydrogen molecule and finally the unsaturated carbon skeleton ($-C=O$ or $-C=C$) behaves as a (receptor, *Rec*). In this heterogeneous catalysis, the source and activator is metal (Ni) and the receptor is also semimetal (graphene) and this feature can be explained as diffusion of hydrogen inside the carbon system (C) like $S \rightarrow H_2 \text{---} Act \rightarrow 2H$, $H + C \rightarrow H @ C$. Moreover, here we assume that big graphene sheet own it's on also enhances the hydrogenation process via charge polarization of H_2 molecule as ($H^{+\delta} - H^{-\delta}$) due to its delocalized (six membered, p - π) electron cloud structure [24].

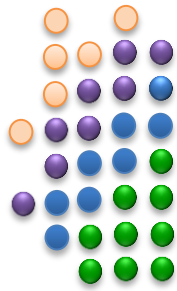
2.4 Coclusions

In summary, HRGO and HGO were successfully synthesized at room temperature by a new approach. We used the bulk and nano nickel catalysts for hydrogenation of GO and a full descriptive mechanism is also established for hydrogen spillover on Ni catalysts. A vast range of characterization techniques such as FTIR, Raman, XPS and TEM/SAED were employed to confirm the formation of hydrogenated product.

2.5 References

- [1] K. S. Novoselov, A. K. Geim, S. V. Morozov, D. Jiang, Y. Zhang, S. V. Dubonos, I. V. Grigorieva, A. A. Firsov. *Science*, 306 (2004) pp. 666- .
- [2] A. K. Geim, K. S. Novoselov. *Nat Mater*, 6 (2007) pp. 183-
- [3] D. C. Elias, R. R. Nair, T. M. G. Mohiuddin, S. V. Morozov, P. Blake, M. P. Halsall, A. C. Ferrari, D. W. Boukhvalov, M. I. Katsnelson, A. K. Geim, K. S. Novoselov. *Science*, 323 (2009) pp. 610-
- [4] S. Ryu, M. Y. Han, J. Maultzsch, T. F. Heinz, P. Kim, M. L. Steigerwald, L. E. Brus. *Nano Lett* 8 (2008) pp. 4597-
- [5] J. O. Sofo, A. S. Chaudhari, G. D. Barber. *Phy Rev B: Condens Matter Mater Phys*, 75 (2007) pp. 153401-

- [6] Y. Okamoto, Y. Nitta, T. Imanaka, S. Teranishi. *J Catal*, 64 (1980) pp. 397-
- [7] L. Zheng, Z. Li, S. Bourdo, F. Watanabe, C. C. Ryersonb, A. S. Biris. *Chem Commun*, 47 (2011) pp. 1213-
- [8] K. S. Subrahmanyam, P. Kumar, U. Maitra, A. Govindaraj, K. P. S. S. Hembram, U. V. Waghmare, C. N. R. Rao. *Proc Natl Acad Sci U. S. A.*, 108 (2011) pp. 2674-
- [9] Z. Fan, K. Wang, T. Wei, J. Yan, L. Song, B. Shao, *Carbon*, 48 (2010) pp. 1686-
- [10] Z. J. Fan, W. Kai, J. Yan, T. Wei, L. J. Zhi, J. Feng, Y. M. Ren, L. P. Song, F. Wei. *ACS Nano*, 5 (2011) pp. 191-
- [11] Y. Liu, Y. Li, M. Zhong, Y. Yang, Y. Wen, M. Wang. *J Mater Chem*, 21 (2011) pp. 15449-
- [12] X. Mei, J. Ouyang. *Carbon*, 49 (2011) pp. 5389-
- [13] B. K. Barman, K. K. Nanda. *Chem Commun*, 49 (2013) pp. 8949-8951.
- [14] A. Lerf, H. He, M. Forster, J. Klinowski. *J Phys Chem B* 102 (1998) pp. 4477-4482.
- [15] A. V. Talyzin, S. Luzan, I. V. Anoshkin, A. G. Nasibulin, H. Jiang, E. I. Kauppinen, V. M. Mikoushkin, V. V. Shnitov, D. E. Marchenko, D. Noreusz, *ACS Nano*, 5 (2011) pp. 5132-
- [16] T. Ujvari, A. Toth, G. J. Kovacs, G. Safran, O. Geszti, G. Radnoczi, I. Bertoti. *Surf Interface Anal*, 36 (2004) pp. 760-
- [17] Y. Wang, X. Xu, J. Lu, M. Lin, Q. Bao, B. Ozyilmaz, K. P. Loh. *ACS Nano*, 4 (2010) pp. 6146-
- [18] Z. Luo, T. Yu, Z. Ni, S. Lim, H. Hu, J. Shang, L. Liu, Z. Shen, J. Lin. *J. Phys Chem C*, 115 (2011) pp. 142-
- [19] R. Krishna, E. Titus, L. C. Costa, J. C. J. M. D. S. Menezes, M. R. P. Correia, S. Pinto, J. Ventura, J. P. Araújo, J. A. S. Cavaleiro, J. J. A. Gracio. *J Mater Chem*, 22 (2012) pp. 10457-.
- [20] R. Krishna, E. Titus, O. Okhay, J. C. Gil, J. Ventura, E. V. Ramana, J. J. A. Gracio. *Int J Electrochem Sci*, 9 (2014) pp. 4054-4069.
- [21] Z. Wang, Y. Hu, W. Yang, M. Zhou, X. Hu. *Sensor*, 12 (2012) pp. 4860.
- [22] Z. Luo, T. Yu, K.J. Kim, Z. Ni, Y. You, S. Lim, Z. Shen, S. Wang, J. Lin, *ACS Nano*, 3 (2009) pp. 1781.
- [23] C. N. R. Rao, A. K. Sood, K. S. Subrahmanyam, A. Govindaraj, *Angew Chem Int Ed*, 48 (2009) pp. 7752.
- [24] R. Krishna, E. Titus, M. Salimian, O. Okhay, S. Rajendran, A. Rajkumar, J. M. G. Sousa, A. L. C. Ferreira, J. C. Gil and J. Gracio, *Hydrogen Storage for energy application*, Intech Open, Europe (2012).



CHAPTER 3

GRAPHENE NANOCOMPOSITES FOR HYDROGEN STORAGE:

Synthesis, characterization and results



Chapter 3

<u>Graphene nanocomposites for hydrogen storage: Synthesis, characterization and results</u>	67
3.1 Introduction	69
3.2 Experimental part	70
3.2.1 Chemicals	70
3.2.2 Synthesis of GO	71
3.2.3 Synthesis of HRGO	71
3.2.4 Synthesis of Ni _x B-SiO ₂ /RGO and Pd@NSG nanocomposite	71
3.2.5 Characterizations	72
3.3 Results and discussion	72
3.4 Conclusions	80
3.5 References	80

GRAPHENE NANOCOMPOSITES FOR HYDROGEN STORAGE:

Synthesis, characterization and results

This chapter deals the synthesis of novel graphene based nanomaterial for hydrogen storage application. A nanocomposite catalyst containing palladium–nickel boride–silica and reduced graphene oxide (Pd@Ni_xB–SiO₂/RGO, abbreviated as Pd@NSG) was successfully synthesized, well characterized with XRD, FTIR, Raman and XPS techniques. Surface morphology were investigated by SEM and TEM techniques. The H₂ adsorption experiment directly reveals the spillover effect on the Pd@NSG nanocomposite due to its enhanced H₂ uptake capacity (0.7 wt.%) compared to SiO₂/RGO (0.05 wt.%) under 50 bar pressure at RT. Experimental results shows that the facile H₂ dissociation on the Pd activator (active sites) and subsequent transportation of hydrogen atoms on receptor sites. On the basis of results a detailed hydrogen spillover mechanism has been established.

3.1 Introduction

H₂ is the most promising energy fuel for automobiles and small portable devices (eg. mobile phones and laptops) due to its light weight, high energy density and clean combustion [1-4]. Yet, significant challenges hinder its widespread application as a choice of fuel due to the lack of a safe and easy method of its storage [5]. Very recently, Li *et al.* reported the H₂ storage capacity of Pd crystal and Pd loaded HKUST at 303 K [6]. However, specific synthesis protocol of porous material HKUST and overall dependency on precious metal (Pd) were major drawback for their use for real field of application.

Recently, graphene has triggered for hydrogen storage application [7-9]; however, it is not yet to be choice for hydrogen storage due to mass production of high quality of graphene is not economically viable option, and itself graphene cannot store an appreciable amount of hydrogen [5]. For instance, Srinivas *et al.* reported the synthesis of graphene-like nanosheets and investigated their H₂ adsorption capacity [10]. They have measured H₂ adsorption-desorption at 298 K at pressures up to 10 bar, and yielded 0.092 wt.% of hydrogen.

Therefore, it is crucial and important to introduce an innovative way of storing the high gravimetric amount of H₂ with reduced cost. Concisely, here we have developed an idea for efficient storage of H₂ at RT in an economic way using low cost materials Ni_xB, SiO₂ and RGO as major constituents and a small percentage of Pd as an activator, and the fact that Pd and Ni_xB are well-known materials for hydrogen spillover as shown in Fig. 3.1. Moreover, it has been reported that Ni_xB is a well-known material for NaBH₄ decomposition and Ni is a prominent catalyst for different kind of hydrogenation reaction due to its spillover capability [11]. Here, we demonstrate a stepwise synthesis of Pd@Ni_xB@SiO₂/RGO nanocomposite for H₂ storage at RT in scalable amount (<1 g) by convenient chemical method and referred as Pd@NSG.

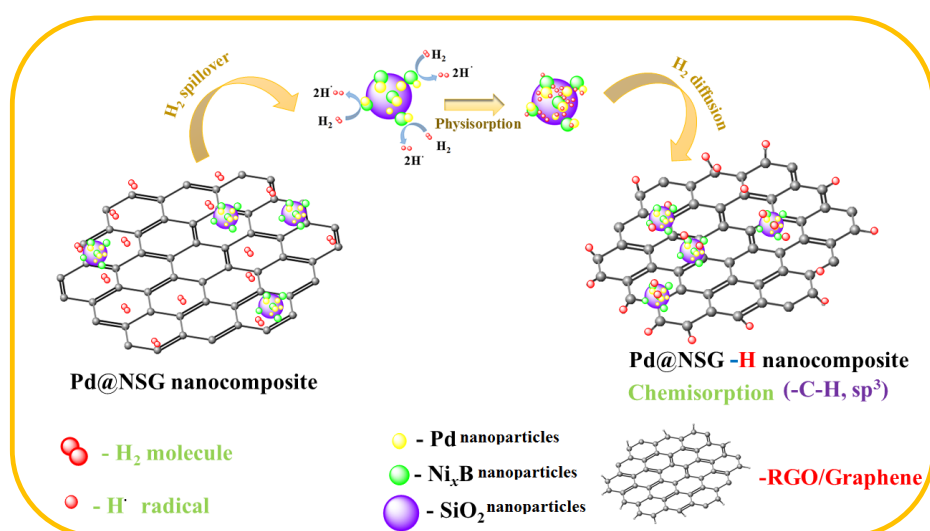


Figure 3.1 Schematic illustration of H₂ spillover on Pd and Ni_xB@ SiO₂ (left) and adsorption of H₂ in Pd@NSG nanocomposite (right).

3.2 Experimental

3.2.1 Chemicals

Flake graphite powder (particle size 100 mesh), palladium acetate, nickel (II) acetate, KMnO₄, NaNO₃, H₂O₂ (30% v/v), NH₄OH, TEOS (98%, A.R.), conc. H₂SO₄ (95-98%), conc. HCl (36.5-38%), methanol, ethanol and isopropanol (A.R. grades) and NaBH₄ were purchased from Sigma-Aldrich Co. All other chemicals were of analytical grade and all aqueous solutions were prepared in Milli-Q water (>18.2MΩ.cm).

3.2.2 Synthesis of GO

GO was synthesized by modified Hummer's method as described in previous work [11]. Briefly, flakes graphite powder (2.5 g) were dispersed in conc. H_2SO_4 (90 mL) by magnetic stirring (45 min) at low temperature (0-5 °C). Later a calculated amount of NaNO_3 (1.25 g) and KMnO_4 (12.5 g) were added slowly and continuously stirred for 2 h. Next, temperature was raised to 35 °C for 1 h and 800 mL Milli-Q water was slowly poured in to the acidic mixture. Furthermore, temperature was increased to 98 °C for 2 h. Finally, 35 mL of 30% v/v H_2O_2 was slowly poured to the reaction mixture to subside the further process. After completion of reaction, resultant suspension was centrifuged (3000 rpm) and washed (with Milli-Q water and dil. HCl) and finally, freeze-dried and stored in a vacuum oven at RT.

3.2.3 Synthesis of SiO_2 /RGO nanocomposite

SiO_2 nanoparticles were synthesized by modified Stöber method using TEOS as precursor [12]. Subsequently, 100 mL dispersion of GO was prepared in methanol (1 mg/mL) by bath sonication (2 h). Later, for the preparation of RGO- SiO_2 nanocomposite, SiO_2 nanoparticles were mixed in GO dispersion by repeated sonication and for GO reduction 50 mg NaBH_4 was added and mixed by magnetic stirring for 2 h at RT.

3.2.4 Synthesis of $\text{Ni}_x\text{B-SiO}_2$ /RGO and Pd@NSG nanocomposite

To synthesize the $\text{Ni}_x\text{B-SiO}_2$ /RGO nanocomposite, first nickel (II) acetate (240 mg) was dissolved in 5 mL DD water at RT and mixed in above suspension. Subsequently, 20 mL alkaline aqueous solution of NaBH_4 (27 mg/mL, pH ~12.5) was slowly poured and mixed by mechanical stirring for 45 min at RT. After completion of reaction, resultant product was centrifuged (3000 rpm) and washed with Milli-Q water and ethanol. To synthesize the Pd@NSG nanocomposite first, $\text{Ni}_x\text{B-SiO}_2$ /RGO nanocomposite was dispersed in 100 ml anhydrous methanol by repeated sonication (30 min) at RT. Later, in above dispersion 10 mL palladium acetate solution (conc. 6 mg/mL in anhydrous methanol) was added and mixed by mechanically stirring for 2 h at 45 °C. Finally, synthesized product was centrifuged at 3000 rpm and multiply washed with Milli-Q water and methanol to remove the impurities and dried at 250 °C for 8 h.

3.2.5 Characterization

Phase purity and crystallinity were accessed by X-ray diffraction (XRD) technique (Rigaku, Japan, $\text{CuK}\alpha$ radiation; 2θ angle range $10\text{--}80^\circ$; step $0.02^\circ/\text{s}$). FTIR spectra of samples were recorded in ATR powder mode. Raman spectra were obtained at RT in back scattering configuration with a Jobin-Yvon Lab Raman HR equipment. The XPS analysis was performed using a Kratos AXIS Ultra HSA, with VISION software for data acquisition and CASAXPS software for data analysis. The analysis was carried out with a monochromatic Al $\text{K}\alpha$ X-ray source (1486.7 eV), operating at 15 kV (90 W), in FAT mode (Fixed Analyser Transmission), with a pass energy of 40 eV for regions ROI and 80 eV for survey. Data acquisition was performed with a pressure lower than 10^{-6} Pa, and a charge neutralisation system was used. The effect of the electric charge was corrected by the reference of the carbon peak (285 eV). The deconvolution of spectra was carried out using the XPSPEAK41, in which a peak fitting is performed using Gaussian-Lorentzian peak shape and Shirley type background subtraction. Surface morphology of GO and products were investigated by scanning electron microscope (SEM) SU-70 Hitachi in EDX mode. For TEM analysis conventional high-resolution (HR) TEM technique was used. The sample for TEM was prepared by dipping an aliquot of suspension (in methanol, 0.1 mg/mL) on to a carbon-coated copper grid and dried at RT. Volumetric H_2 storage measurements were carried out at 298 K using Sievert's instrument. Approximate, 1 g samples were used for adsorption isotherm and prior to measurements, samples were out gassed at 250°C for 12 h. Each time, the calibration and void volume calculation were carried out at RT under high purity helium atmosphere.

3.3 Results and discussion

Fig. 3.2 (a) shows the XRD of GO, $\text{Ni}_x\text{B-SiO}_2/\text{RGO}$ and Pd@NSG nanocomposite. GO exhibits a sharp peak at around 11.2° which corresponds to the (001) basal plane suggesting the good exfoliation of graphite flakes due to the larger value of d-spacing (0.79 nm) of GO compared to 0.334 nm of graphite ($2\theta = 26.4^\circ$) [13]. It is well-known that after a vigorous oxidation of graphitic flakes in strong oxidizing environment, different kinds of oxygenated functional groups are attached to the graphitic plane and increase the interlayer spacing of graphitic sheets [14]. In XRD spectra of $\text{Ni}_x\text{B-SiO}_2/\text{RGO}$ nanocomposite, the peak related to GO was completely suppressed and a new peak observed at 22.8° , which suggests the successful reduction process and formation of reduced graphene oxide (RGO) [15]. The XRD spectra of Pd@NSG shows some additional peaks also due to the diffraction from various crystallographic

planes of Pd/PdO phase. The major diffraction peaks at 39.9° and 46.4° can be assigned as diffraction from (111) and (200), respectively, planes of face-centered cubic (fcc) crystal lattice structure of Pd [16]. The other two peaks at 34.29° and 59.9° indicates the reflection from PdO (due to surface oxidation of Pd) [17]. In addition, in order to elucidate the structure of Pd@NSG nanocomposite and reaction mechanism in more detail, we have also carried out the FTIR spectroscopy. Fig. 3.2 (b) shows the FTIR spectra of GO, $\text{Ni}_x\text{B-SiO}_2/\text{RGO}$ and Pd@NSG nanocomposite (in the range of $4000\text{-}800\text{ cm}^{-1}$).

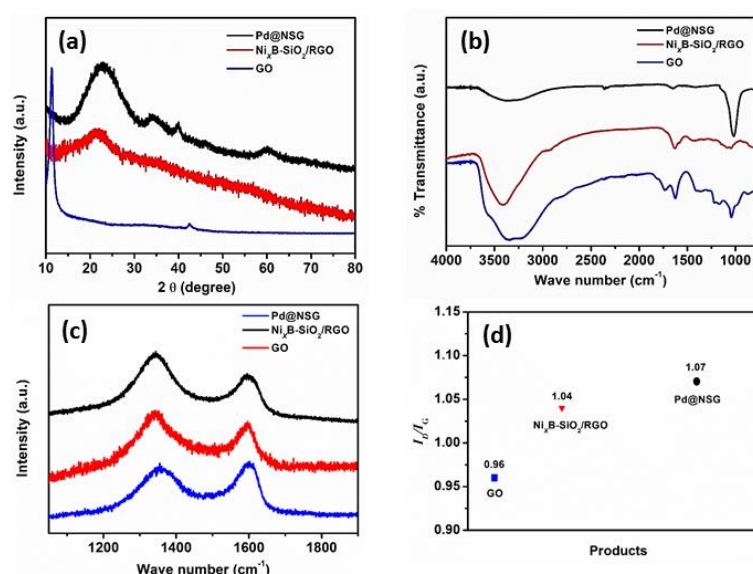


Figure 3.2 Spectroscopic analysis of GO, $\text{Ni}_x\text{B-SiO}_2/\text{RGO}$ and Pd@NSG nano-composite: (a) XRD pattern, (b) FTIR and (c) Raman spectroscopy; and (d) Interpretation of Raman spectroscopy with accordance of I_D/I_G ratio of GO, $\text{Ni}_x\text{B-SiO}_2/\text{RGO}$ and Pd@NSG nanocomposite.

In FTIR spectra of GO, a strong broad band was observed in the high frequency area ($3400\text{-}3200\text{ cm}^{-1}$) which is assigned to the vibration stretching mode of -OH groups due to the surface adsorbed water molecules [18]. After the reduction, the intensity of this band was continuously decreased from $\text{Ni}_x\text{B-SiO}_2/\text{RGO}$ to Pd@NSG nanocomposites which suggests the subsequent removal of surface adsorbed water molecules during the reduction process. Moreover, the peak related to the vibration stretching mode of carbonyl functionality also became deprived in $\text{Ni}_x\text{B-SiO}_2/\text{RGO}$ to Pd@NSG nanocomposites indicating the elimination of edge related -C=O groups and formation of GO to RGO. Finally, the absorption peaks at 1385 cm^{-1} (stretching vibration of C-O of carboxylic acid) and 1110 cm^{-1} (C-OH of alcohol) were also efficiently reduced in both samples compared to the GO. However, in $\text{Ni}_x\text{B-SiO}_2/\text{RGO}$ and Pd@NSG nanocomposites a new peak was observed at 1008 cm^{-1} which indicates the incorporation of

SiO₂ nanoparticles [19]. Next, to ascertain the change in carbon system Raman spectroscopy was also performed. This technique is very useful for assigning the corresponding changes of graphene material on the basis of peak position and intensity [20]. Fig. 3.2 (c) shows the Raman spectra of GO, Ni_xB-SiO₂/RGO and Pd@NSG nanocomposite in the range of 1050-1900 cm⁻¹. The Raman spectrum of GO displays the two characteristic D and G bands at 1353 and 1598 cm⁻¹, respectively, with an I_D/I_G ratio of 0.96. It has already been reported that the G band is an intrinsic feature of graphene and closely related to the vibrations in all sp² carbon materials [1]. The D band become prominent when defects are introduced in graphene system and in GO it is activated due to the reduction in size of the in-plane sp² domains due to the attachment of various functionalities in edge and basal plane sites [15]. In Ni_xB-SiO₂/RGO and Pd@NSG nanocomposite spectra, these two prominent bands (D and G) were shifted to lower wave numbers and are located at 1346 and 1596 and 1343 and 1594 cm⁻¹, respectively. In both spectra I_D/I_G ratio was increased compared to GO. The continuous increment of I_D/I_G ratio from GO to Ni_xB-SiO₂/RGO and Pd@NSG nanocomposite can be clearly observed in Fig. 3.2 (d) suggested the clear change in carbon system due to the incorporation of some extra defects in graphene. Further, we performed the XPS analysis to identify the degree of reduction from GO to RGO. Fig. 3.3 (a) and (b) show the C 1s deconvoluted XPS spectra of GO and Pd@NSG nanocomposites, respectively. The C 1s XPS spectrum of GO as displayed in Fig. 2(a) shows the two large broad peaks that are deconvoluted into four peaks at approximately 284.3, 285.2, 287.2 and 288.9 eV. The peaks at 284.3 and 285.2 eV attributed to the sp² C=C and sp³ C-C bonding, respectively. The peak at around 287.2 eV is assigned to the binding energies of carbon in C-O and C=O and that at 288.9 eV to carbon in COOH groups [21-22].

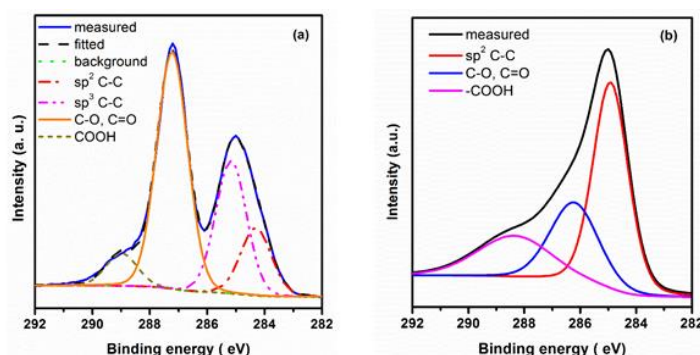


Figure 3.3 (a) and (b) show the C 1s deconvoluted XPS spectra of GO and Pd@NSG nanocomposites, respectively.

However, the C 1s spectrum of Pd@NSG (Fig. 3.2(b)) shows only one intense broad peak that is deconvoluted into three peaks at approximately 284.6, 286.7 and 288.8 eV. These peaks are assigned to sp^2 C=C, C=O and COOH, respectively. It is obviously seen that the peak intensity of C=O and C=O is very high in GO, but in Pd@NSG they were tremendously reduced; whereas, intensity of C=C peak was dramatically increased, indicated the partial reduction of GO to RGO during the metal nanoparticles (Ni and Pd) deposition on graphene sheet [1].

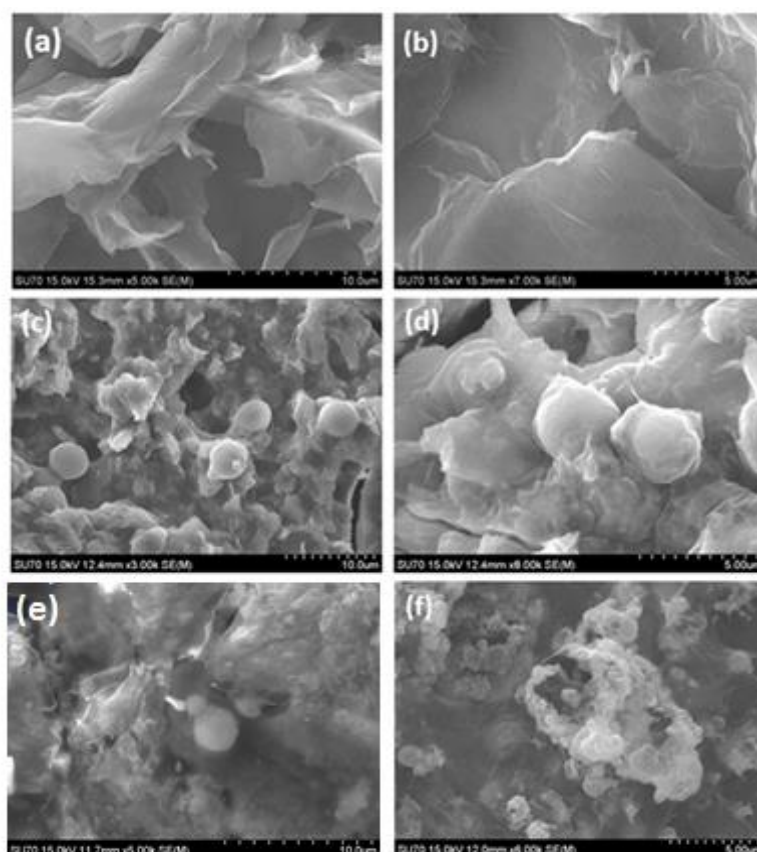


Figure 3.4 SEM images of: GO (a) and (b), SiO₂/RGO (c) and (d) and Ni_xB-SiO₂/RGO nanocomposites (e) and (f) in higher and lower magnifications, respectively.

Further, systematic microscopic investigations were carried out to understand the surface morphology of initial material GO, intermediate composite material RGO-SiO₂, Ni_xB-SiO₂/RGO nanocomposite and final product Pd@NSG nanocomposite. Fig. 3.4 (a) and (b) show the SEM images of GO (after the 2 h exfoliation in methanol at RT) at higher and lower magnifications, respectively. Images of GO clearly exhibit the presence of few layers of graphitic carbon with typical wrinkle behaviour. Fig. 3.4 (c) and (d) display the initial

morphology and size of the SiO₂ nanoparticles with graphene sheet and show that all particles were small sized and with spherical shape. Moreover, images shows that SiO₂ NPs are covered with carbon sheets and well separated without any specific agglomerations. Similar behaviour was observed after the intercalation of Ni_xB nanoparticles on SiO₂/RGO as observed in Figs. 3.4 (e) and (f). Additionally, these two images show higher density of nanoparticles compared to previous images of SiO₂/RGO indicating the successful formation of Ni_xB-SiO₂/RGO nanocomposite. Fig. 3.5 (a-c) shows the SEM images of the final product Pd@NSG at different magnifications. Fig. 3.5 (a) and (b), at lower magnification, show the intercalation of tiny Pd nanoparticles on Ni_xB-SiO₂/RGO nanocomposite at a superficial position and Fig. 3.5 (c) depicts the arrangement of the nanoparticles in a cone-type structure. This arrangement may be due to the grafting of small Pd nanoparticles on high defect sites of Ni_xB-SiO₂/RGO nanocomposite and the filling of cavities by them. Moreover, to confirm the presence of Ni and Pd elements, we also have carried out the EDX analysis.

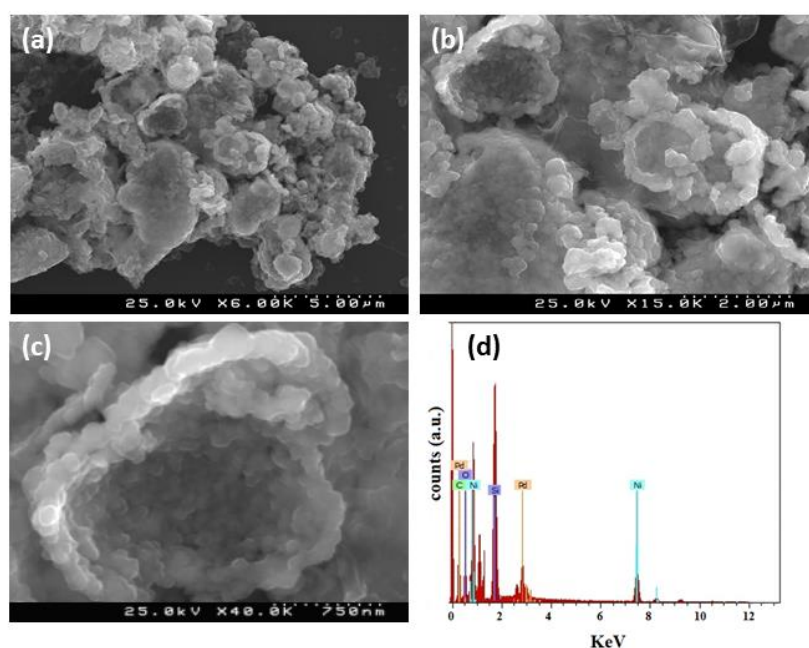


Figure 3.5 SEM images of Pd@NSG nanocomposite at different magnifications: 6000x (a) 15000x (b) and 40000x (c); (d) EDX spectra of Pd@NSG.

Fig. 3.5 (d) displays the EDX spectrum of Pd@NSG nanocomposite and results show the presence of all elements: Pd, Ni, Si, C and O with the exception of the light weight elements B and H. TEM analysis was also performed to confirm the shape, morphology and internal structure of Pd@NSG nanocomposite for detailed investigation of final product. Fig. 3.6 (a) and (b) show the TEM images at lower and higher magnification, respectively. The images

clearly displays the homogeneous distribution of NPs on the graphene sheets; the higher magnification image shows that all particles have spherical shape without any specific kind of agglomeration of them.

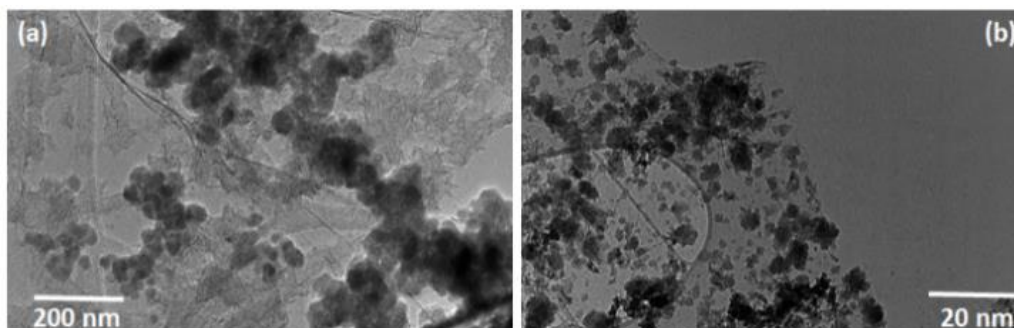


Figure 3.6 TEM images (a) and (b) of Pd@NSG nanocomposite at lower and higher magnifications, respectively.

Furthermore, to establish the detailed mechanism of reduction of Pd²⁺ ions to Pd (0) in presence of anhydrous methanol (CH₃OH), we have also carried out the HRTEM analysis of bare Pd NPs which clearly shows the formation of monodisperse small Pd NPs in the range of (2.5-4 nm) without any agglomeration as shown in Fig. 3.7.

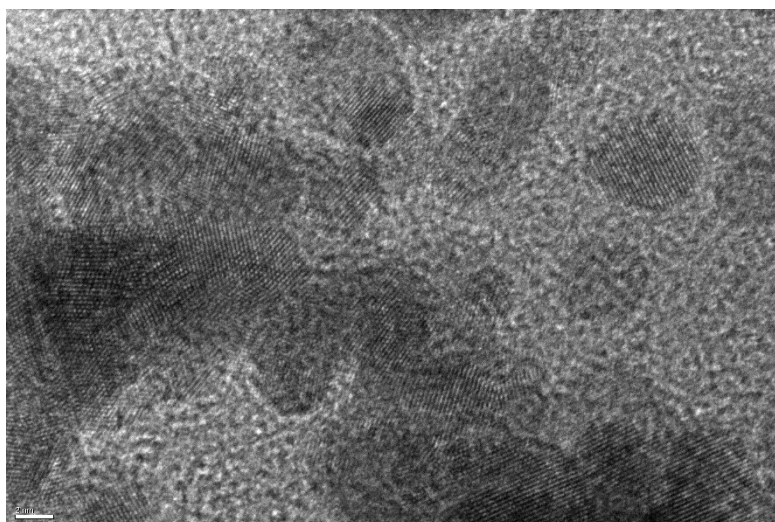
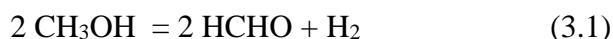
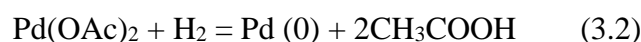


Figure 3.7 HRTEM image of highly crystalline spherical Pd NPs synthesized in mild reducing condition (scale bar 2 nm).

This was due to the choice of precursor and reaction conditions, Pd(OAc)₂ precursor and methanol as solvent provided the reducing conditions. At moderate temperature at 45 °C under sonication condition methanol easily decomposed and generated the reducing species H₂ in the reaction medium as per the following equation (3.1):



Next, produced H₂ reduces the Pd (OAc)₂ to Pd(0) as shown in equation (3.2)



Finally, to investigate the spillover effect we have performed the physical H₂ storage measurement using Sievert's instrument and isotherms were recorded under pressure from 1-50 bar. Fig. 3.8 shows the H₂ uptake characteristic of SiO₂/RGO, Ni_xB-SiO₂/RGO, Pd-SiO₂/RGO and Pd@ NSG nanocomposite at RT. As displayed in the graph, the H₂ storage increases in the materials with increasing pressure. At 50 bar, the maximum H₂ storage of SiO₂/RGO is 0.25 mmol while, after insertion of NPs in SiO₂/RGO matrix the H₂ uptake capacity was dramatically increased. For Ni_xB-SiO₂/RGO and Pd-SiO₂/RGO nanocomposites, and the maximum H₂ uptake was estimated to be 0.76 and 1.55 mmol, respectively. At similar adsorption isotherm conditions the major changes were obtained for Pd@NSG nanocomposite which shows a 3.5 mmol H₂ uptake. This value was approximately 14 times higher than SiO₂/RGO nanocomposite. The corresponding wt.% values were 0.05 and 0.7, respectively. This shows the enhancement of H₂ uptake in Pd@NSG sample which was higher than SiO₂/RGO in the whole range of pressures tested.

Above Fig. 3.1 illustrates the H₂ spillover mechanism and subsequent diffusion in Pd@NSG nanocomposite. Here, the metal NPs (Pd and Ni_xB@SiO₂) act as spillover centre for H₂ molecules and dissociates the molecular H₂ in to H[•] radicals. The generated H[•] radicals then migrates from the catalyst centre to the storage material and easily diffuses into the graphene layers. Especially, they migrate to the defect sites of graphene sheets such as the edges locations and saturated the hexagonal sp² hybridized (-C=C) network. This phenomenon can be explained through the formation of "bridge" built structure on catalyst centre where H₂ molecules easily form the dangling bonds with catalyst centre and dissociate into H[•] radicals. In detail, the Pd NPs work as a source, the Ni_xB NPs act as an activator to dissociate the H₂ molecules and finally, RGO and SiO₂ play the role of receptor [1].

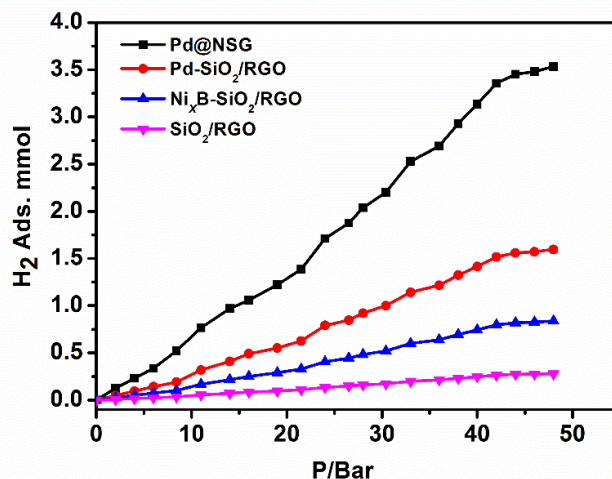


Figure 3.8 H₂ adsorption isotherm of SiO₂ and Pd@NSG nanocomposite up to 50 bar pressure at RT.

Due to this process an adduct species on catalyst surface is formed by the dissociation of H₂ molecule and subsequently, π - π bonding ($-C=C$) of graphene gets saturated and form sp^3 (C-H) bonding. Finally, RGO works as a primary receptor site for preferential storage of H[•] radicals via chemisorption and SiO₂ NPs act as a secondary receptor to adsorb the H₂ molecule by physisorption. Due to these facts, the obtained result of H₂ uptake for Pd@NSG nanocomposite at RT was remarkably higher than previously reported works. Huang *et al.* reported 0.15 wt. % of H₂ storage in Pd-Gr nanocomposite at similar conditions (298 K and 60 bar) [23]. Although, they have noticed that after loading of Pd metal on the graphene sheet, the H₂ uptake was doubled. It is obviously due to the spillover capability of Pd to dissociate the H₂ molecules and subsequent migration of H atoms on graphene sheet. The results reported here are also better than those obtained by Anson *et al.* [24]. They reported a 0.16 wt. % H₂ storage at RT in Pd nanoparticles intercalated single walled carbon nanotube (SWNT) after applying 90 bar. However, in our work we applied only a maximum pressure of 50 bar and a 4 times higher H₂ storage was observed. This may be attributed due to the porous structure of SiO₂, edge defects and large surface area of graphene along with the presence of two spillover centres. Our results of storage capacity of Pd@NSG are higher compared to Latroche *et al.* in the giant-pore MOF MIL-101 (~0.43 wt. % at 80 bar), and Campesi *et al.* in Pd nanoparticles loaded porous carbon template composites at 298 K (0.08 wt. % H₂ storage) [25-26].

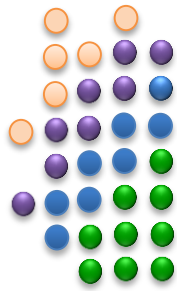
3.4 Conclusions

In this work, Pd@NSG nanocomposite was successfully synthesized and characterised by various techniques. The successful reduction of GO was analysed by XRD, FTIR Raman and XPS techniques and they exhibited the change in carbon structure. Moreover, the formation of Pd nanoparticles was also studied using the XRD technique. To investigate the presence of Ni element in nanocomposite (due to formation of amorphous phase Ni_xB) EDX analysis was also carried out. H₂ uptake measurements of up to 50 bar pressure clearly exhibited 14 times more storage at RT in Pd@NSG nanocomposite compared to SiO₂/RGO. Such a high storage of H₂ is attributed to the spillover mechanism on Pd and Ni_xB on graphene sheet which can make the avenue for new developments in future H₂ economy.

3.5 References

- [1] R. Krishna, D. M. Fernandes, V. F. Domingos, E. S. Ribeiro, J. C. Gil, C. Dias, J. Ventura, C. Freire, E. Titus. RSC Adv, 5 (2015) pp. 60658-60666.
- [2] Y. Qin, J. Wang, F. Meng, L. Wang, X. Zhang. Chem Commun, 49 (2013) pp. 10028-30.
- [3] S. J. Peighambaroust, S. Rowshanzamir, M. Amjadi. Int J Hydrogen Energy, 35 (2010) pp. 9349-9384.
- [4] G.K. Dimitrakakis, E. Tylianakis, G. E. Froudakis. Nano Lett, 8 (2008) pp. 3166-3170.
- [5] R. Krishna, E. Titus, M. Salimian, O. Okhay, S. Rajendran, A. Rajkumar, J. M. G. Sousa, A. L. C. Ferreira, J. C. Gil and J. Gracio, Hydrogen Storage for energy application, Intech Open, Europe (2012).
- [6] G. Li et al. Nat Mater, 13 (2014) pp. 802-806.
- [7] D. C. Elias, R. R. Nair, T. M. G. Mohiuddin, S. V. Morozov, P. Blake, M. P. Halsall, A. C. Ferrari, D. W. Boukhvalov, M. I. Katsnelson, A. K. Geim, K. S. Novoselov. Science, 323 (2009) pp. 610-
- [8] V. Tozzini, V. Pellegrini. J Phys Chem C, 115 (2011) pp. 25523.
- [9] S. Casolo, O. M. Løvvik, R. Martinazzo, G. F. Tantardini. J Chem Phys 130 (2009) pp. 074504
- [10] G. Srinivas, Y. Zhu, R. Piner, N. Skipper, M. Ellerby, R. S. Ruoff. Carbon, 48 (2010) pp. 630-635.
- [11] R. Krishna, E. Titus, O. Okhay, J. C. Gil, J. Ventura, E. V. Ramana, J. J. A. Gracio. Int J Electrochem Sci, 9 (2014) pp. 4054-4069.

- [12] C. C. Huang, N. W. Pu, C. A. Wang, J. C. Huang, Y. Sung, M. D. Ger. *Separ Purif Tech*, 82 (2011) pp. 210-215.
- [13] Z. Fan, K. Wang, T. Wei, J. Yan, L. Song, B. Shao, *Carbon*, 48 (2010) pp. 1686-
- [14] R. Krishna, D. M. Fernandes, C. Dias, J. Ventura, E. Venkata Ramana, C. Freire, E. Titus. *Int J Hydrogen Energy*, 40 (2015) pp. 4996-5005.
- [15] Z. J. Fan, W. Kai, J. Yan, T. Wei, L. J. Zhi, J. Feng, Y. M. Ren, L. P. Song, F. Wei. *ACS Nano*, 5 (2011) pp. 191-
- [16] B. K. Barman, K. K. Nanda. *Appl Catal A Gen*, 491 (2015) pp. 45-51.
- [17] C. J. Huang, F. M. Pan, T. C. Tzeng, L. Chang, J. T. Sheu. *J Electrochem Soc*, 156 (2009) pp. J28-31.
- [18] X. Mei, J. Ouyang. *Carbon*, 49 (2011) pp. 5389-
- [19] H. R. Nikabadi, N. Shahtahmasebi, M. R. R. Abadi, M. M. B. Mohagheghi, E. K. Goharshadi. *Phys Scr*, 87 (2013) pp. 025802.
- [20] Y. Wang, X. Xu, J. Lu, M. Lin, Q. Bao, B. Ozyilmaz, K.P. Loh. *ACS Nano*, 4 (2010) 6146-6152.
- [21] D.R. Dreyer, S. Park, C.W. Bielawski, R.S. Ruoff. *Chem Soc Rev*, 39 (2010), pp. 228-240.
- [22] S. Park, J. An, J.R. Potts, A. Velamakanni, S. Murali, R.S. Ruoff. *Carbon*, 49 (2011), pp. 3019-3023.
- [23] C. C. Huang, N. W. Pu, C. A. Wang, J. C. Huang, Y. Sung, M. D. Ger. *Separ Purif Tech*, 82 (2011) pp. 210-215.
- [24] A. Ansón, M. a. Callejas, a. M. Benito, W. K. Maser, M. T. Izquierdo, B. Rubio, J. Jagiello, M. Thommes, J. B. Parra and M. T. Martínez. *Carbon*, 42 (2004) pp. 1243-1248.
- [25] M. Latroche, S. Surblé, C. Serre, C. Mellot-Draznieks, P. L. Llewellyn, J. H. Lee, J. S. Chang, H. J. Sung and G. Férey, *Angew. Chemie - Int. Ed.* 45 (2006) pp. 8227-8231.
- [26] R. Campesi, F. Cuevas, R. Gadiou, E. Leroy, M. Hirscher, C. Vix-Guterl, M. Latroche. *Carbon*, 46 (2008) pp. 206-214.

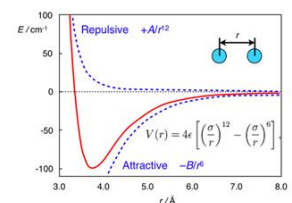
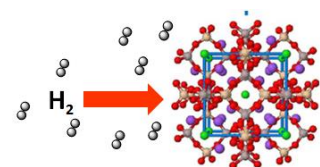


CHAPTER 4

THEORETICAL ASPECT OF HYDROGEN STORAGE IN NANOMATERIALS:

STORAGE IN NANOMATERIALS:

Grand Monte Carlo simulations for hydrogen adsorption in NaA zeolites



Chapter 4

<u>Theoretical aspect of hydrogen storage in nanomaterials: Grand canonical Monte Carlo simulations for hydrogen adsorption in NaA zeolites</u>	82
4.1 Introduction	84
4.2 Model and methods	85
4.2.1 NaA Zeolite structure	85
4.2.2 Potential Model	87
4.2.3 Henry Coefficient	88
4.3 Simulation details	89
4.4 Results	91
4.5 Conclusions	94
4.6 References	94

**THEORETICAL ASPECT OF HYDROGEN STORAGE
IN NANOMATERIALS:
Monte Carlo simulations of hydrogen adsorption in
NaA zeolites**

The aim of this chapter is to provide the information of theoretical aspect of hydrogen storage in porous materials. The idea is to get an insight into storage properties while using graphene-porous material nanocomposites. The chapter comprises in three parts, first part related to vast investigation of NaA zeolite unit cell structure and its potential cell model with innovative idea of Henry constant. The second part consists of systematic description of GCMC procedure and finally, third part related to the comprehensive evaluation of result and discussion.

4.1 Introduction

Hydrogen storage in mesoporous material is well established area of research [1]. Among the various mesoporous materials (like silica gel, activated carbon, lime minerals) zeolites are most prominent candidate for storage and separation of selective gaseous species [2-7]. Due to its specific geometry, stereographic rigid and regular systems and intrinsic polarity and charge separation phenomenon makes it a suitable candidate for such an application [8-11]. The use of molecular simulation techniques for gaseous adsorption in zeolites has been recently reviewed. Anderson *et al.* reported the kinetic selectivity and molecular sieving of small gaseous molecules in zeolite framework due to their specific geometry which shows the cavities and channels with size ranging of 3 Å -10 Å [6]. The zeolite framework consists of alternating arrangement of AlO_4^- and SiO_4^- tetrahedral species with cation positioning inside of them [5]. Here, AlO_4^- tetrahedral species produces the negative charge on to the aluminosilicate zeolite

framework [4]. This negative charge on frame-work negotiated by counter charge balancing (hydroxyl and cationic) species and provide the polarizability for guest species [2].

In this work, we point out the grand canonical ensemble Monte Carlo (GCMC) simulations of single-component of small molecule hydrogen and NaA framework based zeolite system. The simple structure of NaA zeolite offers great hope for adsorption of small molecule along with its illustrate generalized guest-host interaction for other adsorbent/adsorbate systems and site selection of guest entities [10].

To construct the theoretical model, we have selected one unit cell of NaA zeolite framework built with alternating Al and Si T-sites, and randomized the positions of the Na (II) and Na(III) atoms with adsorption of hydrogen gas into the NaA zeolite structure at different temperatures and gas pressures. For GCMC simulations the number of H₂ molecules, and their positions, is allowed to fluctuate, at a constant chemical potential, temperature and volume. Subsequently, simulation was performed for a wide range of step wise growth of temperatures and pressure from $T = 77$ to 300 K and pressures $P = 1$ to 180 MPa. Innovatively, here we have included Henry's constant to evaluate the partial pressure of gas in the zeolite motif at the very low pressure at $P \rightarrow 0$ and theoretically computed adsorption kinetics as accordance the adsorption behavior of guest molecule in the host active sites [10].

4.2 Model and methods

4.2.1 NaA Zeolite structure

Fig. 4.1 shows the dehydrated NaA zeolite crystal structure, which represent the Linde Type A (LTA) framework. This structure exhibits the cubic arrangement of unit cells with composition of $\{\text{Na}_{12}[(\text{AlO}_2)_{12}(\text{SiO}_2)_{12}]\}_8$. The unit cell constant is ($a = 24.55 \text{ \AA}$), space group $Fm\bar{3}c$, and the coordinate positions of the atoms are taken from x-ray diffraction studies. The LTA framework constructed by the four and six edge faces of the truncated octahedron. This is worthwhile that building blocks are alternating AlO_4 and SiO_4 species where Si or Al atoms (known as a T atom), those are linked with each other by corner sharing in tetrahedral arrangement. Further, it is considerable that each T (aluminum or silicon) atom situated at the center position and surrounded by 4 corner sharing oxygen atom by single covalent bonding [2,10]. Each oxygen atom is therefore connected to two different T atoms. These species are arranged in space to form a porous network of small (β) and large (α) cavities. The β cages also known as sodalite cage with an approximate dimension of $a = \sim 8.82 \text{ \AA}$, which are connected by their square faces in a cubic arrangement. This skeleton provide large opening on the center

of eight sodalites Per BU (per building unit) and formed α cavity with minimum free diameter of 11.4 Å. The porous nature of Zeolite-A is due to formation of 8-oxygen rings, which have a net opening of 4.1 Å through which the adsorbates can easily enter to the hollow space inside of the cavity where most of the adsorption is expected to be occur [5].

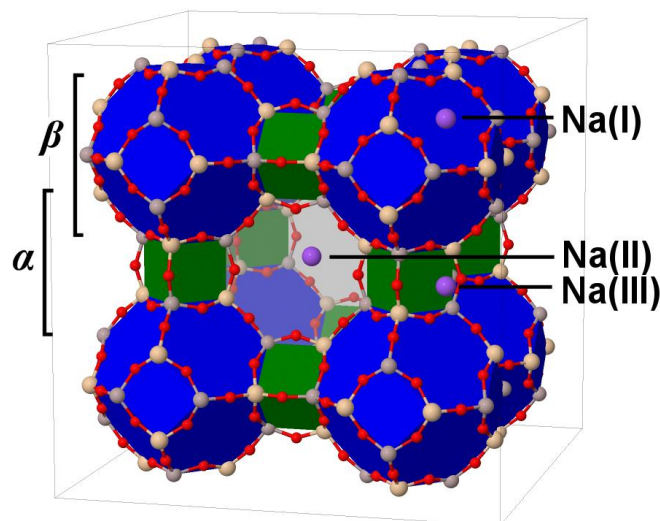


Figure 4.1 Unit cell of the zeolite NaA with site position of Na atoms as respective in α and β cages, oxygen atoms in red, T-atoms in gray and representative positions of the three types of Na^+ in purple.

The net negative charge of the Al-O-Si framework, caused by the aluminum atom in the O- corner sharing tetrahedral position, which is compensated by the introduction of positively, charged ions in extra positions of the framework. For the particular LTA case the counter ions such as Na^+ can be easily replaced by other cations. Here, it is important to know the position of cations in the zeolite LTA framework for studying the hydrogen adsorption in the particular zeolite structure. In this regards, there are three different types of sodium cation and they are situated as accordance to their sites location. If we consider single unit cell of Linde type zeolite structure, there are 64 Na atoms of type I, 24 of type II, and 8 of type III means are total 96 Na atoms. The Na(I) atoms have well defined positions on the center of each 6-oxygen ring that make up the windows of the sodalite (β) cages. The Na(II) have an occupancy of 1/4, and each one will occupy one of four possible positions on the center of the α cage windows (8-Oxygen rings), all have approximate equal probability to get specific site location. Particularly, about of Na(III) atoms they have least occupancy instead of previous two around 1/12, are placed off-plane at the center of the 4-oxygen rings that connect the two sodalite cages as shown in above Fig.1.

For simulation purpose we consider single unit cell, which built with alternating Al and Si T-sites, and as accordance randomized the positions of the Na(II) and Na(III) atoms. In general, we found that this randomization has no influence on the simulation results of the adsorption properties, within statistical accuracy. We also assume the rigid structure with some mobility of Na(III) atoms inside the framework [12-14].

4.2.2 Potential Model

We have employed the potential model of Darkrim *et al.* to describe the interactions between the zeolite and the hydrogen adsorbates and between the hydrogen molecules themselves [10]. This potential model built by three major contributions viz. van der Waals interactions (subscript w), modeled by a Lennard-Jones 12-6 potential; Coulomb electrostatic potential (c); and a polarization term due to interactions of the electric field with the induced H₂ dipole (p) and all can describes as equation 4.1-4.2:

$$U^{H_2} = U_w + U_c + U_p \quad (4.1)$$

$$U_w = \sum_{i,j} 4\epsilon \left[\left(\frac{\sigma}{r_{ij}} \right)^{12} - \left(\frac{\sigma}{r_{ij}} \right)^6 \right] \quad (4.2)$$

$$U_c = \frac{1}{4\pi\epsilon_0} \sum_{i,j} \frac{q_i q_j}{r_{ij}} \quad (4.3)$$

$$U_p = \frac{1}{2} \sum_i \alpha^{H_2} \bar{\mathbf{E}}_i^2(r_i) \quad (4.4)$$

Where, the indexes i and j run over three Cartesian coordinates and represent the summations of each molecule, those are carried over all the zeolite atoms and all the hydrogen molecules, as explained below. For the energy U_w , each zeolite atom and H₂ molecule are represented by an interaction site with a specific value of Lennard-Jones parameters σ (sigma) and ϵ (epsilon).

To use equation 4.1 for a set of atoms i and j the cross L-J parameters was computed by Berthelot's rules $\sigma = (\sigma_i \sigma_j)/2$ and $\epsilon = \sqrt{\epsilon_i \epsilon_j}$. Here H₂-zeolite and H₂-H₂ interactions also taken into account for calculating the value of U_w . Regarding of Coulomb interactions U_c , each zeolite atom is described by a fixed partial point charge, and in this case for each H₂ molecule a quadrupole model was constructed by the distribution of 3 charges, in the way of 2 charges were at the position of the protons (separated by $d=0.741\text{\AA}$) with charge $q = 0.4829 |e|$ and one at the center of mass with charge $-2q$. Finally, U_c was evaluated for the interaction between each of above 3 charges along with all the zeolite atoms, as well as the other sets of charges on the remaining H₂ in the gas. The polarization energy, U_p , of an H₂ molecule of index I was calculated by evaluating the square of the electric field $\mathbf{E}(\mathbf{r}_i)$ produced by all the charges of the zeolite at the center of mass of the molecule, \mathbf{r}_i . Importantly, here it was assumed that the H₂-H₂ mutual interactions are negligible and the polarization is independent of the orientation of the molecule.

The polarization energy of a molecule was calculated by evaluating the electrical field produced by all the charges of the zeolite at the center of the mass of molecule. The assumptions used in above that the H₂-H₂ mutual interactions are negligible and the polarization is independent of the orientation of the molecule (α cage hydrogen set for the mean polarization value for rest hydrogen molecules). Although, this is a fair assumption at room temperature, but its validity can be suspected at lower temperatures. Next, to investigate the limit of low pressure of hydrogen gas we have evaluated the effect of Henry gas constant.

4.2.3 Henry Coefficient

In the limit of low pressures, the density of adsorbed molecules in the zeolite (ρ_a) is directly proportional to the pressure of the gas in the reservoir, and the proportionality constant is the Henry coefficient, K_H :

$$\rho_a = K_H P \quad (4.5)$$

The Henry coefficient can then be calculated by the slope of the isotherm curve as $P \rightarrow 0$. This requires many simulations to be carried out in this regime. An alternative method follows from the fact that K_H is related to the excess chemical potential of the adsorbed molecules as shown in equation 4.6 :

$$K_H = \beta \exp(-\beta \mu_{ex}) \quad (4.6)$$

Further, to compute this quantity directly the integral was taken in account as shown in equation 4.7:

$$K_H = \beta \langle \exp(-\beta \Delta U) \rangle \quad (4.7)$$

where, ΔU is the energy of an H₂ molecule only due to interactions with the zeolite framework. This integral can be resolved by a Monte Carlo method where a guest particle is added at various random positions in an empty zeolite (because the condition for equation (4.7) to hold is that at low pressures the hydrogen gas behaves like an ideal gas) and its energy ΔU is computed, until the average converges. This is computationally much less expensive than performing several different GCMC simulations in the low pressure regime and it is useful in the sense that it can be used to check the consistency of the simulation results. For higher pressures, it is common to describe the adsorption isotherms with the single-site Langmuir isotherm:

$$\rho_a = \rho_{sat} \frac{bp}{1+bp} \quad (4.8)$$

where, ρ_{sat} and b are adjustable parameters, and ρ_{sat} corresponds to the maximum density of adsorbed molecules. In the limit $P \rightarrow 0$ equation (4.8) transforms back into the linear relation of equation (4.5) and $\rho_{sat}b = K_H$.

4.3 Simulation details

GCMC simulations of the adsorption of hydrogen into the zeolite structure were performed at different temperatures and gas pressures [11]. This simulations technique designed as: the sample consider as a phase space where the number of H₂ molecules, and their positions, is allowed to fluctuate, at a constant chemical potential, temperature and volume. At a given Monte Carlo step, one trial move was attempted that consists of an insertion of one H₂ at a random position in the zeolite or a removal of a random H₂ from the configuration, and is accepted or rejected with a probability that is a function of $\exp(-\beta \Delta U)$ where ΔU is the energy change in the system.

This probability injection or rejection of H₂ molecule also depends on the thermodynamic state (μVT) where the simulation is taking place. The two operations are attempted with a 50% chance each. The displacement/rotation of a random particle are also sometimes used with this technique, but were seems unnecessary for this work. The GCMC

simulation takes as one input the chemical potential μ of the hydrogen gas reservoir, which is related to its pressure P by an equation of state. At low pressures, the ideal gas relation $\beta p = \exp(\beta\mu)/\Lambda^3$ can be used, where Λ is the thermal de Broglie wavelength. At higher pressures, however, a theoretical equation of state of the model fluid, or an experimental one, can be used.

We have employed the Lennard-Jones equation using the parameters for the hydrogen molecule, to transform pressures into input chemical potential. By using the Widom insertion method with the full H₂-H₂ potential (LJ plus the electrostatic term) and we confirmed that this is a good enough approximation of chemical potential at the temperature and pressure range considered.

We used a simulation cell with a size of one unit cell of the NaA zeolite as described previously, with randomized positions of the Na II and III atoms and periodic boundary conditions to simulate an infinite volume. A cutoff distance of half the side of the unit cell (12.5) was used for the L-J potential and the usual long range corrections to the energy were applied. As the coulomb potential is long-ranged, the Ewald summation method was used. Here, the interaction of a point charge q_i with a charge q_j is calculated for all the images of q_j in the infinite crystal volume, by using a mathematical technique which transforms the series into a rapidly converging finite sum in reciprocal space. We have calculated the electric field at a point \mathbf{r}_i , with accuracy and computational efficiency, by direct derivation of Ewald formulas for the coulomb energy of a unitary charge at that position, rather than evaluating the gradient numerically.

A typical simulation run consisted of 3×10^6 MC steps (one insertion or removal attempt). A fraction (about a third) was intended to equilibrate the system and was discarded. From that point, the number of observed H₂ molecules per unit cell was registered every 10 MC steps, in order to calculate the ensemble average. The Henry coefficient was calculated by the particle insertion method for about 40 temperatures between 200 and 600 K. For each temperature, 3×10^6 different random positions were generated in the unit cell, where one H₂ molecule was placed with a random orientation, and equation (4.7) was evaluated.

4.4 Results

GCMC Simulations were performed for a wide range of temperatures, from $T = 77$ to 300 K, and pressures $P = 1$ to 180 MPa. The results for the simulated average number of H_2 molecules adsorbed in one unit cell of NaA zeolite plotted in Fig. 4.2. For temperatures starting from $T=200K$, the results were fitted to a simple Langmuir isotherm (equation (4.8)). For lower temperatures, however, the fitting of this simple isotherm was not satisfactory. It is important to stress that, while molecular simulation yields the total amount of molecules inside the cell volume (the absolute value N_{abs}) experiments are usually concerned only with that portion of the gas that is adsorbed into a thin layer adjacent to the surface of the solid.

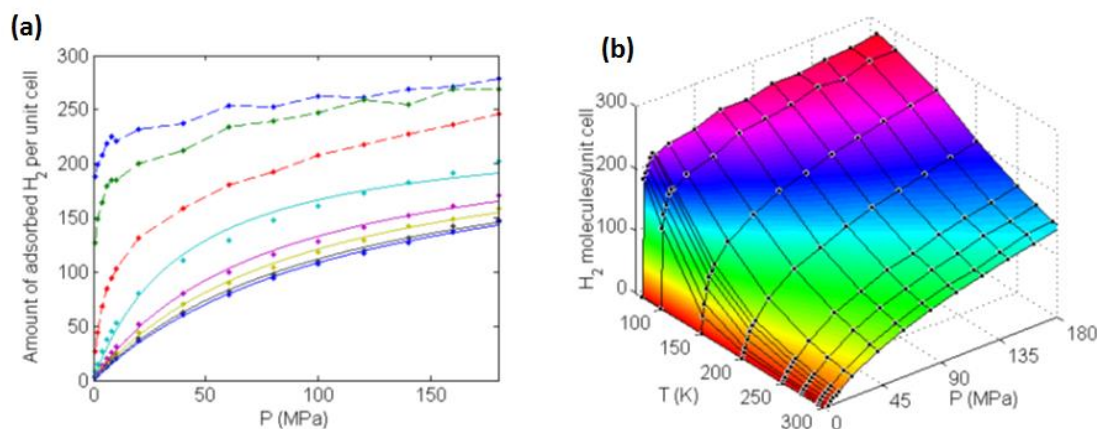


Figure 4.2 Simulated hydrogen adsorption isotherms at various temperatures. (a) The points correspond to the individual simulations for temperatures of, respectively from top to bottom 77, 100, 150, 200, 250, 273, 293, 303K. For the first three temperatures, the dashed lines simply connect the points, whereas, for the remaining higher temperatures, the curves are fits of the Langmuir isotherm function. (b) Adsorption data surface in P - T space.

For $P = 2$ MPa we report a hydrogen uptake of 5.0 H_2 molecules per unit cell, less than half of the experimental data. Previous report shows a hydrogen uptake for the NaA zeolite of 1.54 wt. % at 1.5 MPa [15]. Whereas, our results shows that almost a factor of two (2.7 wt.%) storage of hydrogen. This is might be due to the in this low temperature regime the simulation is much more sensitive to small variations in UH_2 and a very precise interactions model is required that may provide more accurate results as this one. Further, the Henry coefficient was calculated by using the equation (6) for temperatures from 200 K up to 600 K and the results are plotted in Fig. 4.3.

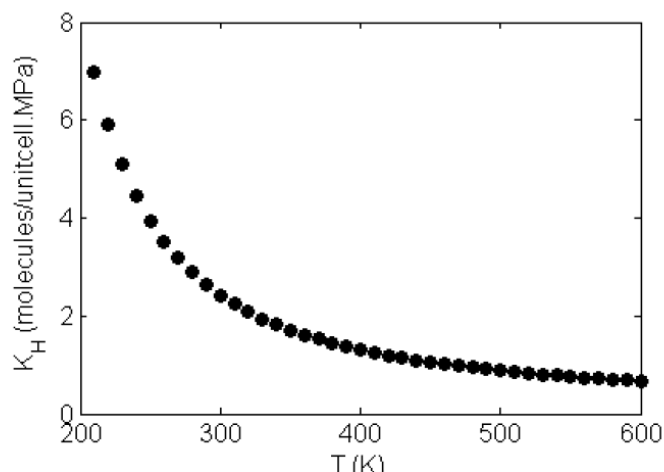


Figure 4.3 Variation of the Henry coefficient as a function of temperature.

Moreover, we have checked the consistency of these results by comparing the Henry coefficient calculated in this matter with the same value taken from GCMC simulations at low pressures. For this purpose, 10 additional GCMC simulations were carried out between 0.1 and 1 MPa as represented in Fig. 4.4. Which demonstrated that the both methods yielded the same results and they are mutually consistent.

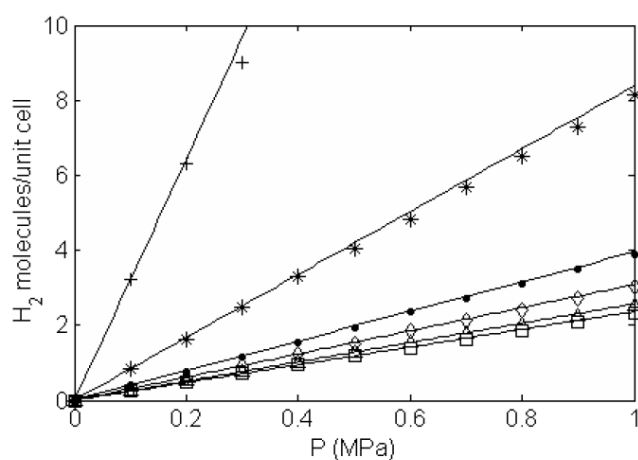


Figure 4.4 Low pressure isotherms. The points are GCMC simulations for temperatures of, from top to bottom 150, 200, 250, 273, 293, 303K. The solid lines are the corresponding Henry isotherms with KH computed directly from the particle insertion method. Visual comparison shows that the solid lines follow the slope of the simulated curves adequately.

Next, we have constructed the contour maps to visualization of adsorption affinity of the different regions of the unit cell as shown in Fig. 4.5. It represented the full guest-host potential energy (equations 4.1-4.4) of one H_2 molecule along two different planes of the zeolite. The negative part of the potential is corresponds to those regions of the plane where the

framework atoms will exert an attractive interaction on the guest particle. The white regions on the figures are areas that lay in the repulsive part of this potential, which increases very rapidly (r^{-12}) as the atoms begin to overlap. From classical statistical mechanics, the probability of finding a particle at site \mathbf{r}_i , with energy $U_i(\mathbf{r}_i)$ is proportional to $\exp(-\beta U_i)$ so that adsorption is expected to occur for the lowest values of βU_i .

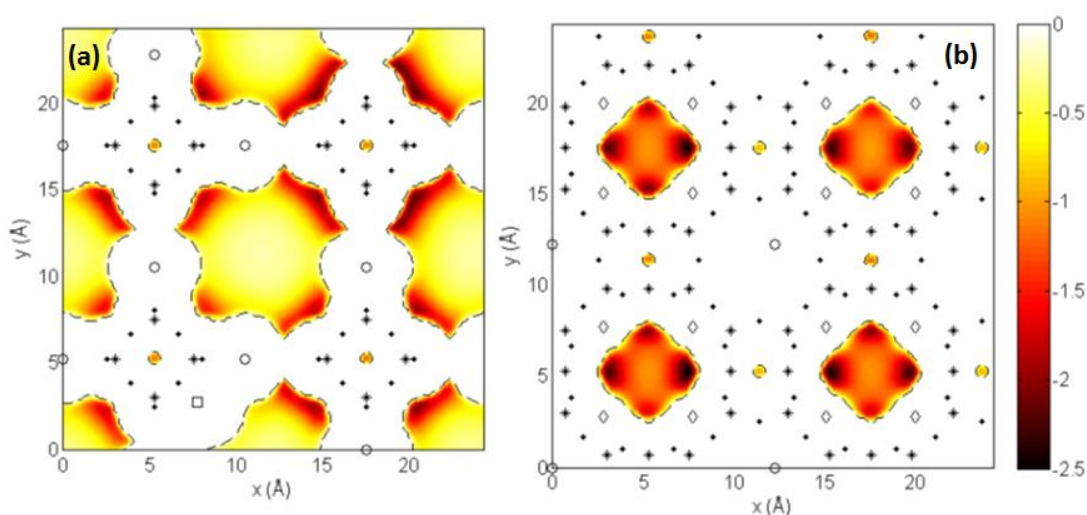


Figure 4.5 Contour maps of the total potential energy βU_i of one H_2 molecule in an empty zeolite, averaged over all possible orientations, along two (001) planes: plane (a) goes through the center of the α cage, and is parallel to the large windows of the cage; plane (b) goes through the center of the sodalites and contains the α cage windows (8-oxygen rings). Only negative values of βU_i are plotted. Calculated for a temperature of $T=293\text{K}$. Also represented are the positions of the zeolite atoms in the vicinity of the plane: oxygens (\bullet), T-atoms ($*$), Na-I (\diamond), Na-II (\circ), Na-III (\square).

In Fig. 4.5 (a) clearly shows that the large volume inside the α cages are the optimal adsorption sites. There is a strong energy minimum in a thin layer adjacent to the internal surface of the cage, interrupted only by the repulsive effect of the large sodium atoms (largest values of σ). Darkrim *et al.* [10] previously demonstrated that the parameter σ^{Na} ($=3.5 \text{ \AA}$) shows most influential weightage for the simulated number of encapsulated molecules, and they justified by the fact that these atoms, positioned on the windows and inside the α cage, largely accommodate the available void volume.

However, at the center of the α cage, the interaction felt by the particles is only slightly attractive and the hydrogen molecules would be mostly unconstrained there. Fig. 5 (b) shows that there is an energetically favorable region in a small volume inside the sodalite cages, mostly constrained by the 8 Na (I) atoms positioned on the 6-oxygen ring windows and guest molecules were accumulated there only for transient time.

4.5 Conclusions

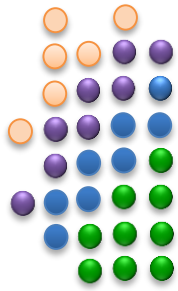
In this work, an extended simulation results are presented for adsorption of hydrogen molecules in side of NaA zeolite. A wider range of temperatures and pressures were applied for the simulation purpose. Simulated results shows that good agreement for moderate to high pressures; however, at low pressures there were some limitations. Due to this we also verify the linear relation between the hydrogen uptake and input pressure in the limit of zero loading, and calculate the corresponding proportionality constant with the Henry coefficient. Therefore, systematic validation of any model at low pressures can be done by comparing such a curve with experimental observations of $KH(T)$ that might be help to develop new, optimal, hydrogen storage materials.

4.6 References

- [1] M. G. Nijkamp, J. E. M. J. Raaymakers, A. J. van Dillen, K.P. de Jong. Appl Phys A, 72 (2001) pp. 619-623.
- [2] J. M. G. Sousa, A. L. C. Ferreira, E. Titus, R. Krishna, D. P. Fagg, J. Gracio. J Nanosci Nanotechnol, 12 (2012) pp. 6785-6791.
- [3] S.B. Kayiran, F.L. Darkrim. Surf Interf Anal, 34 (2002) pp.100-104.
- [4] R. Krishna, E.Titus, M.Salimian, O. Okhay, S. Rajendran, A. Rajkumar, J. M. G. Sousa, A. L. C. Ferreira, J. C. Gil and J. Gracio, Hydrogen Storage for energy application, Intech Open, Europe (2012).
- [5] M. Salimian, O. Okhay, R. Krishna, E. Titus, J. Gracio, L. Guerra, J. Ventura, C. Freire, C. Pereira, P. R. Babu, R. S. Khairnare. Polym Int, 62 (2013) pp. 1583-1588.
- [6] C. Anderson, D. F. Coker, J. Eckert, A. L. R. Bug. J Chem Phys 111 (1999) pp. 7599-7613.
- [7] S. Liu, X. Yang. J Chem Phys, 124 (2006) pp. 244705.
- [8] J. Weitkamp, M. Fritz, S. Ernst. Int J of Hydrogen Energy, 20 (1995) pp. 967-970.
- [9] B. Smit, T. L. M. Maesen, Chem Review, 108 (2008) pp. 4125-4184.
- [10] F. Darkrim, A. Aoufi, P. Malbrunot, D. Levesque. J Chem Phys, 112 (2000) pp. 5991-5999.
- [11] S. Liu, X. Yang. J Chem Phys, 124 (2006) pp. 244705.
- [12] J. J. Pluth, J. V. Smith. J Am Chem Society, 102 (1980) pp. 4704-4708.
- [13] D. A. Faux, W. Smith, T. R. J Phys Chem B 101 (1997) pp. 1762-1768.

[14] O. Talu, A. L. Myers. Coll Surf A: Physicochem Eng Aspects 83 (2001) pp.187-188.

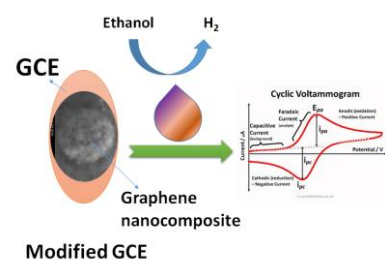
[15] H. Langmi et al. J Alloy Comp 404 (2005) pp. 637-642.



CHAPTER 5

TRANSITION METALS DOPED GRAPHENE NANOCOMPOSITE FOR ELECTRO-CHEMICAL HYDROGEN GENERATION:

Synthesis, characterization and results



Chapter 5

<u>Transition metals doped graphene nanocomposite for electrochemically hydrogen generation: synthesis, characterization and results</u>	96
5.1 Introduction	98
5.2 Experimental	100
5.2.1 Synthesis	100
5.2.2 Characterization techniques	101
5.3 Results and discussion	102
5.4 Conclusions	114
5.5 References	115

TRANSITION METALS DOPED GRAPHENE NANOCOMPOSITE FOR ELECTROCHEMICAL HYDROGEN GENERATION:

Synthesis, characterization and results

5.1 Introduction

Nowadays, the development of novel catalysts with high electrocatalytic activity for fuel cells application is a central issue to accelerate the clean energy technology in an affordable manner [1- 4]. Pt and Pt-based alloys are superlative have been extensively investigated for most of the fuel cells reactions to solve the future energy challenges [5-7]. For example, Niu and coworkers have prepared carbon microspheres supported Pt NPs and demonstrated their good electrocatalytic activity for fuel cell application [8]. However, the high price of Pt, its limited supply, low tolerance to CO poisoning, aggregation and dissolution in harsh electrochemical environments are some of the major practical challengeable issues that need to be resolve prior to Pt-based materials commercialization [9-11]. Alternatively, Pd-based electrocatalysts gained lot of interest owing to their high efficiency, high selectivity, and greater resistance to CO poisoning and comparable low price due their high abundance [12-14].

Among the several liquid fuels, ethanol is the most studied and encouraged for energy applications such as for direct ethanol fuel cells (DEFC) applications. This is due to its low toxicity, high energy conversion efficiency, high power density, low pollution, easy storage and handling [12,15], along with its large production from agricultural products and biomass resources [16]. Moreover, in DEFC it can directly provide the electrical energy in a continuous manner. Therefore, many efforts have been devoted to the preparation of Pd-based nanocatalysts for the electrooxidation of ethanol in alkaline solution [17-20].

To improve the electrocatalytic activity, bimetallic nanocatalysts were widely investigated due to the possibility of extra catalytic centers and improvement of CO tolerance capability of Pd. For instance, Smiljanić *et al.* demonstrated the ethanol oxidation on Pd/Au(111) bimetallic surfaces in alkaline solution [21]. Similarly, Abbasi *et al.* showed the electrocatalytic oxidation of ethanol on Pd/Ag nanodendrites [22]. However, using noble metals (such as Au or Ag) in binary-alloys is not cost effective, limits their wide acceptability [23]. Instead of these, the low price material Ni provides the cost affordability along with co-catalytic activity [24]. It has been previously reported that Ni addition to Pd refreshes the Pd active sites and increases the electrocatalytic activity of the nanocatalyst [25]. For instance, Zhang *et al.* demonstrated the role of Ni for activation of Pd catalytic sites and discussed their synergetic effect [26]. The oxidation state of Ni plays an important role in the electrooxidation of ethanol and it has been also reported that the addition of metal oxides such as NiO improves the catalytic activity of Pd nanocatalysts [27].

The role and use of catalyst support have also been investigated in order to develop electrocatalyst with higher efficiencies [28]. Recently, graphene has triggered a wide interest due to their high thermal and electrical conductivities, structural properties, large surface area, robustness and chemical inertness [29]. Due to these properties graphene has been considered as a promising catalyst support material in fuel cell electrodes [30]. A recent work of Ghosh *et al.* demonstrated when Pd NPs were incorporated within RGO, the electrocatalytic activity towards ethanol oxidation was surprisingly increased [31]. Similarly, Tan *et al.* reported the improved electrocatalytic activity towards ethanol oxidation using Pd-Ni/RGO nanocomposite [32].

However, synthesis of uniform Ni NPs, without surfactant, is critical due to its magnetic behaviour and to the tendency to agglomerate in its absence. The reduction of Ni²⁺ ions to Ni (0) is also a time consuming process and occasionally it needed harsh reaction conditions, such as the involvement of toxic chemicals (hydrazine hydrate) and high-temperature reaction conditions (to decompose the organometallic precursors), which disfavours the process easiness [33-35]. Instead of that, Ni_xB can be easily synthesised by the simple reduction of Ni²⁺ ions with NaBH₄ at RT. Ni_xB is a pronounced hydrogenation catalyst and a hydrogen generator and it conveniently decomposes aqueous solution of NaBH₄ [36].

Considering the increasing need for efficient electrocatalytic ethanol oxidation and the fact that Pd and Ni_xB are well-known hydrogenation catalyst, we report a stepwise synthesis of Pd@Ni_xB/RGO nanocomposite. This is an economically viable method since it uses, as major components, low cost materials such as Ni_xB, and RGO and a small percentage of Pd on superficial on them. The nanocomposite was fully characterized by several techniques which confirmed its successful preparation. Finally, the electrochemical studies revealed promising results of this type of nanocomposite towards the ethanol electrooxidation reaction.

5.2 Experimental

5.2.1 Synthesis

All chemicals were of analytical grade and all aqueous solutions were prepared in Milli-Q water (>18.2MΩ.cm). GO was synthesized by modified Hummer's method as described in previous work [37]. Briefly, graphite flakes powder (2.5 g) were dispersed in conc. H₂SO₄ (90 mL) by magnetic stirring (45 min) at low temperature (0-5 °C). Then, a calculated amount of NaNO₃ (1.25 g) and KMnO₄ (12.5 g) were added slowly and continuously stirred for 2 h. Next, the temperature was raised to 35 °C for 1 h and 800 mL Milli-Q water was slowly poured in to the acidic mixture. Furthermore, temperature was increased to 98 °C for 2 h. Finally, 35 mL of 30% v/v H₂O₂ was slowly poured to the reaction mixture to subside the further process. After completion of reaction, resultant product was centrifuged (3000 rpm), washed (with Milli-Q water and dil. HCl) and freeze-dried. Finally, prepared a suspension of GO in Milli-Q water (1 mg/mL). To synthesize the Ni_xB/RGO nanocomposite, first nickel chloride (240 mg) was dissolved in 5 mL Milli-Q water at RT and added to a GO suspension (45 mL). Then, 20 mL of alkaline aqueous solution of NaBH₄ (27 mg/mL, pH ~12.5) was slowly poured and mixed by mechanical stirring for 45 min. After completion of reaction, the resultant product was centrifuged (3000 rpm) and washed with Milli-Q water and ethanol. First, Ni_xB/RGO nanocomposite (25 mg) was dispersed in 100 mL anhydrous methanol by repeated sonication (30 min) at RT. Later, to the above dispersion, palladium acetate (50 mg) was added and mixed by mechanically stirring for 2 h at 45 °C. Finally, the synthesized product was centrifuged at 3000 rpm and washed several times with Milli-Q water and methanol to remove the impurities and dried in vacuum oven at 250 °C for 8 h.

5.2.2 Characterization techniques

Phase purity and crystallinity were accessed by X-ray diffraction (XRD) technique (Rigaku, Japan, CuK α radiation; 2θ angle range 10–80°; step 0.02°/s). FTIR spectra of samples were recorded in ATR powder mode. The XPS analysis was performed using a Kratos AXIS Ultra HSA, with VISION software for data acquisition and CASAXPS software for data analysis. The analysis was carried out with a monochromatic Al K α X-ray source (1486.7 eV), operating at 15kV (90 W), in FAT mode (Fixed Analyser Transmission), with a pass energy of 40 eV for regions ROI and 80 eV for survey. Data acquisition was performed with a pressure lower than 1.E-6 Pa, and it was used a charge neutralisation system. The effect of the electric charge was corrected by the reference of the carbon peak (285 eV). The deconvolution of spectra was carried out using the XPSPEAK41, in which a peak fitting is performed using Gaussian-Lorentzian peak shape and Shirley type background subtraction. Surface morphology of GO and products were investigated by scanning electron microscope (SEM) SU-70 Hitachi in EDX mode. For TEM analysis conventional high-resolution (HR) TEM technique was used. The sample for TEM was prepared by dipping an aliquot of suspension (in methanol, 0.1 mg/mL) on to a carbon-coated copper grid and dried at RT. Cyclic voltammetry (CV) and chronoamperometry (CA) measurements were carried out using an Autolab PGSTAT 30 potentiostat/galvanostat (EcoChimie B.V.) controlled by the GPES software. A conventional three-electrode system was used using the following electrodes: reference - Ag/AgCl (sat. KCl) (BAS, MF-2052); auxiliary - platinum wire (7.5 cm, BAS, MW-1032) and working - glassy carbon electrode, GCE, (3 mm diameter, BAS, MF-2012). The working cell was surrounded by a grounded Faraday cage and all studies were carried out at RT and under an argon flow. Ultra-pure water (Millipore, 18.2 M Ω cm, 25 °C) was used to prepare the 1M KOH electrolyte solution. Prior to modification the GCE electrode was conditioned by a polishing/cleaning procedure using diamond pastes of 6, 3 and 1 μ M (Buehler) on a nylon polishing pad (BAS Bioanalytical Systems Inc.) and finally aluminium oxide of particle size 0.3 μ m (Buehler) on a microcloth polishing pad (BAS Bioanalytical Systems Inc.). Then, the electrode was rinsed with ultra-pure water and finally sonicated for 5 min in ethanol and ultra-pure water. Dispersions used to produce the modified electrodes were prepared as follows: a 0.5% Nafion dispersion (1 mL) of the selected material - Pd@Ni $_x$ B/RGO and Pd@Ni $_x$ B, for comparison (5 mg) was sonicated for 10 min. Electrode modification consisted in depositing a 10 μ L drop of the dispersion of the selected composite material onto the surface of the glassy carbon electrode and the solvent was evaporated under a flow of air.

5.3 Results and discussion

GO was prepared *via* modified Hummer's method [37,38] and it contains a large number of oxygen-containing functional groups, which allows GO to be well-dispersed in an aqueous solution [39]. In the beginning, Ni_xB NPs were synthesized on graphene sheets by simultaneous reduction of GO and Ni²⁺ ions. This step was crucial to synthesize the Pd@Ni_xB entity due to the high redox potential and hydrogen spillover capability of Pd compared to Ni [37]. The species Ni_xB can only form in the absence of Pd whereas, in one step synthesis (mixing of Pd²⁺ and Ni²⁺ ions salt) there was a chance of formation of Pd-Ni alloy [24, 40], instead of Pd@Ni_xB entity. Mechanistically, in this work the amphiphilic nature of GO sheets serves as surfactant; Ni_xB NPs were dispersed on large surface area of graphene and attached on GO surface. During the process there was a chance of some agglomeration of RGO sheets due to the π - π interactions, van der Waals forces and hydrogen bonding interactions between graphene sheets [35, 37, 39]. However, in our case the stacking of RGO sheets were less, due to the specific reaction conditions which prevented their restacking. Here, we synthesized the Ni_xB NPs by addition of alkaline aqueous solution of NaBH₄ (pH ~12.5) at RT. Normally, Pd NPs were synthesized by the reduction of salt at high temperature or using specific reducing agents such as L-ascorbic acid, NaBH₄, redox metallic species (such as Ni or Zn), and some times toxic chemical hydrazine hydrate [41-46] however, we adopt the green approach.

Here, XRD was used to prove the crystallinity of nanomaterial. Fig. 5.1 shows the XRD of graphite powder, GO and Pd@Ni_xB /RGO nanocomposite. The XRD of graphite powder shows a peak at 26.6° which corresponds to the diffraction from (002) plane [38,47]. However, after the treatment of graphite powder in harsh acidic condition the oxygenated GO exhibits a sharp peak at around 11.2° which corresponds to the (001) basal plane, suggesting the good exfoliation of graphite flakes due to the larger value of d-spacing (0.79 nm) of GO compared to 0.334 nm of graphite ($2\theta = 26.4^\circ$) [37, 38, 47].

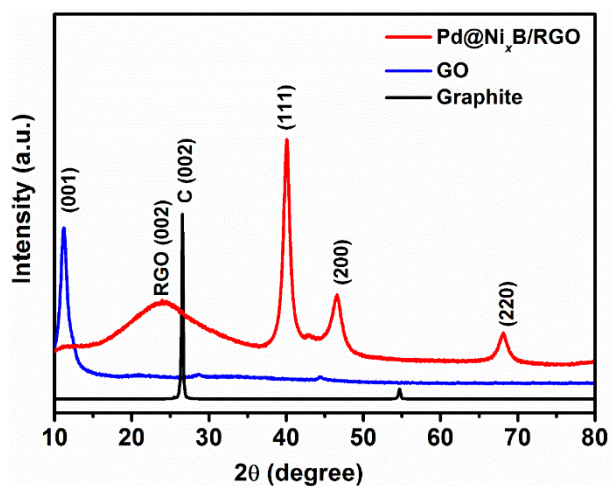


Figure 5.1 XRD pattern of graphite powder, GO and Pd@Ni_xB /RGO nanocomposite.

It is well known that after a vigorous oxidation of graphitic flakes in strong oxidizing environment, different kinds of oxygenated functional groups are attached to the graphitic plane and increase the interlayer spacing of graphitic sheets [39, 47]. In XRD spectra of Pd@Ni_xB /RGO nanocomposite, the peak related to GO was completely suppressed and a new peak is observed at 22.8°, which suggests the successful reduction process and formation of RGO [37, 41]. The XRD spectra of Pd@Ni_xB/RGO nanocomposite also shows some additional peaks that are related to the different crystallographic diffraction planes of Pd. The major diffraction peaks at 39.9°, 46.4° and 67.8°, corresponding to the (111), (200) and (220) crystalline planes of face centered cubic (FCC) Pd [41], indicated the successful reduction of Pd²⁺ ions in anhydrous methanol reducing solvent [46]. The main diffraction peak (111) of crystalline Pd at around 39.9° was found to shifted slightly towards lower angle as compared with bulk Pd ($2\theta = 40.1^\circ$, JCPDS 00–005-0681) [48]. It was due to the increment of Pd-Pd interatomic distance related to their nanosize, which is consistent with a previous report [41]. The average crystallite size of the Pd nanoparticles was estimated from the half-widths of highest intensity peak (111) by using the Debye-Scherrer formula [33], and was estimated to be about 5.7 nm.

Fig. 5.2 shows the FTIR spectra of GO and Pd@Ni_xB/RGO nanocomposite (in the range of 4000-500 cm⁻¹). In FTIR spectrum of GO, a strong broad band was observed at around 3300 cm⁻¹, assigned to the stretching mode of vibration of -OH groups due to the surface adsorbed water molecules [49]. After reduction, the intensity of this band decreased and shifted to the higher wave number (3425 cm⁻¹) in Pd@Ni_xB/RGO nanocomposite which suggests the removal of surface adsorbed water molecules from graphitic planes during the reduction process.

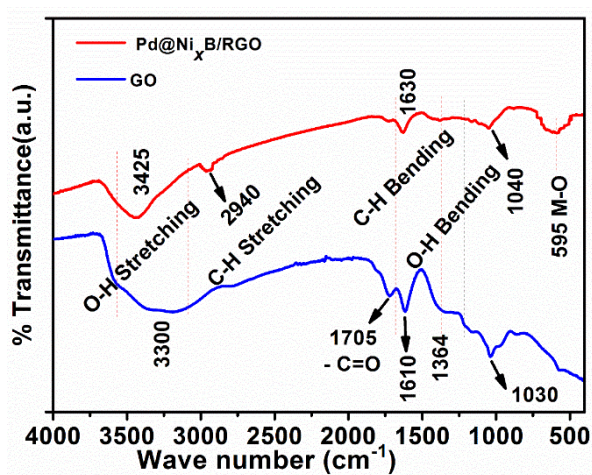


Figure 5.2 FTIR of GO and Pd@Ni_xB/RGO nanocomposite.

Moreover, the peak related to the stretching mode of vibration i.e. carbonyl functionality (-C=O) at approximately 1705 cm⁻¹ also decreased in the reduced product and a new peak was observed close to 1630 cm⁻¹, indicating the elimination of edge related -C=O groups and the restoration of conjugated alkene (-C=C-) system [47]. Moreover, in Pd@Ni_xB/RGO nanocomposite the absence of peaks at 1364 cm⁻¹, 1250 cm⁻¹, and 1030 cm⁻¹ suggested the removal of epoxide and the hydroxyl groups attached to the basal plane of GO [37, 39, 49]. Interestingly, in Pd@Ni_xB/RGO nanocomposite one new peak was observed at 2940 cm⁻¹ attributed the C-H stretching band of vibration through H₂ spillover mechanism on Ni_xB entity and subsequent, migration of radical hydrogens to receptor sites of graphene [37]. Due the presence of Ni, a peak appears at 590 cm⁻¹ in Pd@Ni_xB/RGO nanocomposite attributed to the M-O stretching band between Ni and oxygen residual of RGO which confirms the well-incorporation of Ni NPs within RGO. Fig. 5.3 (a) and (b) show the SEM images of Pd@Ni_xB/RGO nanocomposite at lower and higher magnifications, respectively. Both images clearly depicts the exfoliated graphene nanosheets structure with well intercalation and uniform distribution of Pd and Ni_xB NPs on graphene surface [37]. The exfoliation of graphene sheets can be rationalized as: at the time of synthesis of Ni_xB NPs the oxygen containing functional groups of GO (such as epoxy, hydroxyl, carbonyl and carboxylic acid) were reduced and on their position some defects were introduced in carbon structure which provided the favourable sites for Ni_xB NPs[47].

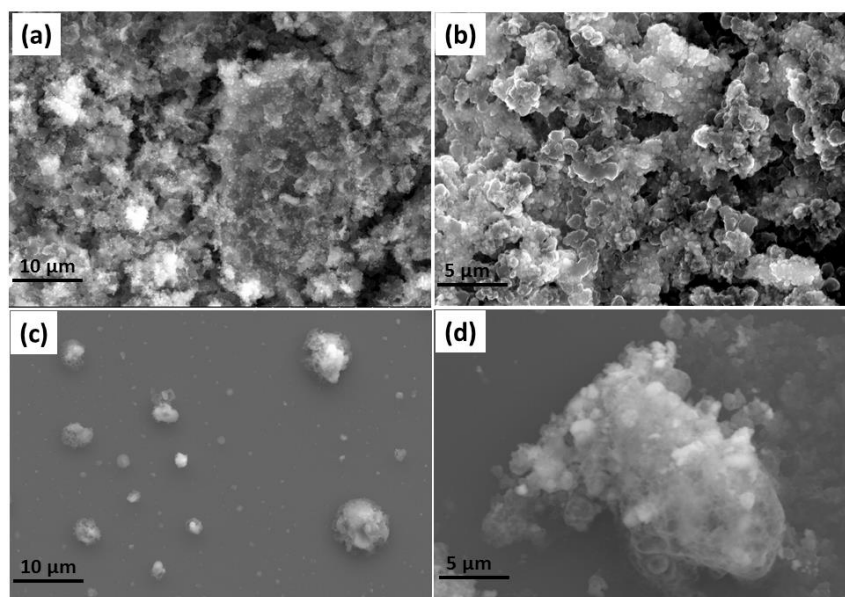


Figure 5.3 SEM images of: Pd@Ni_xB/RGO nanocomposite at lower (a) and higher (b) magnifications; Pd@Ni_xB NPs at lower (c) and higher (d) magnifications.

The remaining oxygen containing functional group such as hydroxy (-OH) holds the Ni_xB NPs and works as surface capping agents preventing their agglomeration. Moreover, hydrogen was produced through the hydrolysis of NaBH₄ (Equation 5.1) [50]. The produced hydrogen also prevents the restacking of graphene layers, maintains their exfoliated condition and decreases the van der Waals interaction between them.



In absence of support (RGO nanosheets), Pd@Ni_xB NPs were highly agglomerated as shown in Fig. 5.3 (c) and (d) at lower and higher magnifications, respectively. This is due to several factors such as high surface energy, attractive van der Waals forces and coalescence between the NPs in absence of RGO nanosheets or any external surface capping agents [51-53]. Thermodynamically, agglomeration can be expressed as: formation of bonding between adjacent particles through dangling bond led the change in enthalpy of the system to negative side which compensated the negative entropy of the system. That resulted to the Gibbs free energy change to negative ($\Delta G = -ve$) and provides a driving force for agglomeration. Whence the driving force was eliminated at equilibrium ($\Delta G = 0$) the system became thermodynamically stable and particle growth was stopped [53].

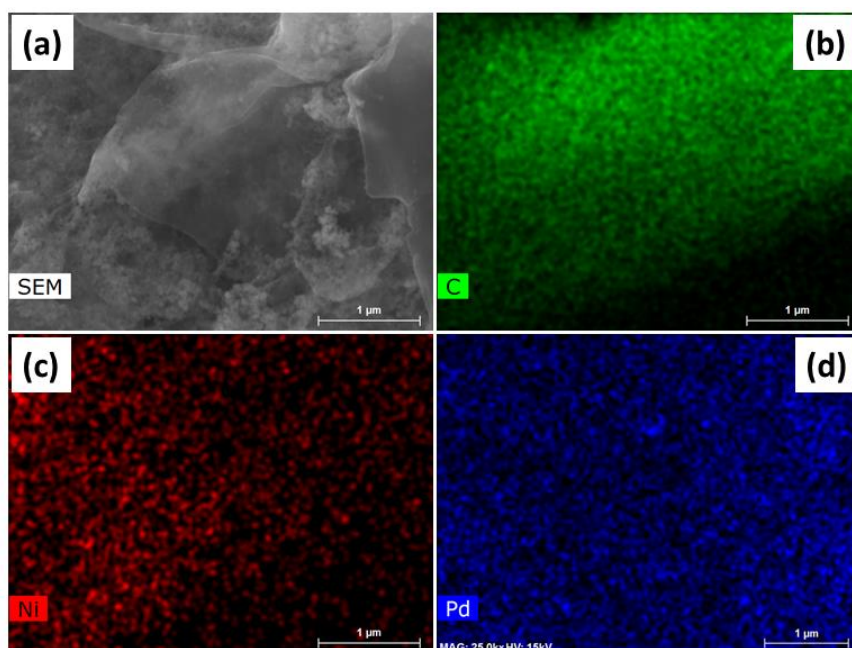


Figure 5.4 (a) SEM image of Pd@Ni_xB/RGO nanocomposite, and (b-d) corresponding elemental mapping of C, Ni and Pd elements in respective images.

Further, to corroborate the fact that RGO sheets preventing the NPs agglomeration, we have carried out the SEM with elemental mapping as shown in Fig. 5.4 (b-d). Images clearly depict the uniform distribution of elements (C, Ni and Pd with exception of light weight B and H), proving the role of RGO layers for the prevention of NPs agglomeration. Moreover, it confirms the presence of Ni and Pd elements in Pd@Ni_xB/RGO nanocomposite.

To understand the reaction mechanism in detail, we have also carried out the TEM/HRTEM analysis of Pd@Ni_xB/RGO nanocomposite along with bare Pd NPs. Fig. 5.5 (a) depicts the TEM image of GO where thin layers of graphene sheets were observed. Fig. 5.5 (b) shows the TEM image of Pd@Ni_xB/RGO nanocomposite in which Pd@Ni_xB NPs were uniformly dispersed onto the graphene sheets with a narrow size distribution. The average size of as-synthesized Pd@Ni_xB NPs on RGO were about 8–12 nm. TEM result suggested that the simplicity and efficacy of our synthesis protocol.

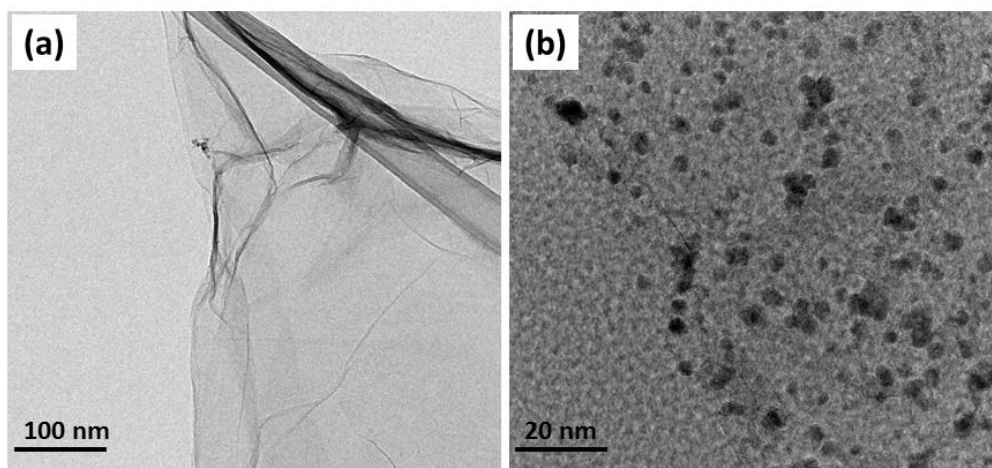


Figure 5.5 TEM image of (a) GO and (b) Pd@Ni_xB/RGO nanocomposite.

XPS experiments were performed to identify the elemental composition of the Pd@Ni_xB/RGO nanocomposite. Fig. 5.6 (a) depicts the C 1s core level XPS spectrum of RGO in which an intense peak was observed. After the deconvolution three major peaks were identified and assigned as sp² C=C at 284.6 eV (due to the graphitic carbon), sp³ C-O at 286.4 eV (due to the hydroxyl and epoxy groups with graphene framework) and sp² C=O at 288.8 eV (corresponds to the COOH groups) [47]. The reduction level of RGO was also evaluated by the analysis of O 1s core level spectrum of Pd@Ni_xB/RGO nanocomposite as shown in Fig. 5.6 (b). The major peak of C-O bonding was deconvoluted into 2 main peaks at around 531.7 eV and 533.4 eV and were assigned as O=C-OH and O-C or C-OH, respectively [47]. In which peak intensity of sp² carbonyl (-C=O) was much lesser than the sp³ hydroxyl or epoxy (-C-O) peak which clearly indicated the degree of reduction of RGO. Fig. 5.6(c) shows the XPS core level spectrum of 2p Ni which was deconvoluted into 2p_{3/2} and 2p_{1/2} doublets caused by spin-orbital coupling [37, 38]. The two main peaks at 856.9 and 874.5 eV in the Ni 2p XPS spectra are assigned to the Ni 2p_{3/2} and Ni 2p_{1/2}, respectively. Additionally, there was a small peak at approximately 853.4 eV which is attributed to metallic nickel [37] and two other peaks at 862.2 and 880.6 eV assigned to the formation of NiO and NiOOH species, respectively. Fig. 5.6 (d) shows the Pd 3d core level XPS spectrum of the Pd@Ni_xB/RGO nanocomposite. The binding energies of Pd 3d can be resolved into 3d_{5/2} and 3d_{3/2} doublets caused by spin-orbital coupling. Upon deconvolution of the spectra, the curves are fitted with two pairs of binding energies for Pd (0) and Pd (II) at 335.8 and 341.1 eV and 337.4 and 342.7 eV, respectively [37].

These values were in good agreement with previously reported work of Pd NPs synthesis onto RGO [41]. The intensities of Pd (0) peaks were quite larger than those of Pd (II) which indicates the major contribution of metallic Pd phase. Moreover, the existence of B element was also confirmed by XPS by the presence of one peak at approximately 193 eV (Fig. 5.6 (e)).

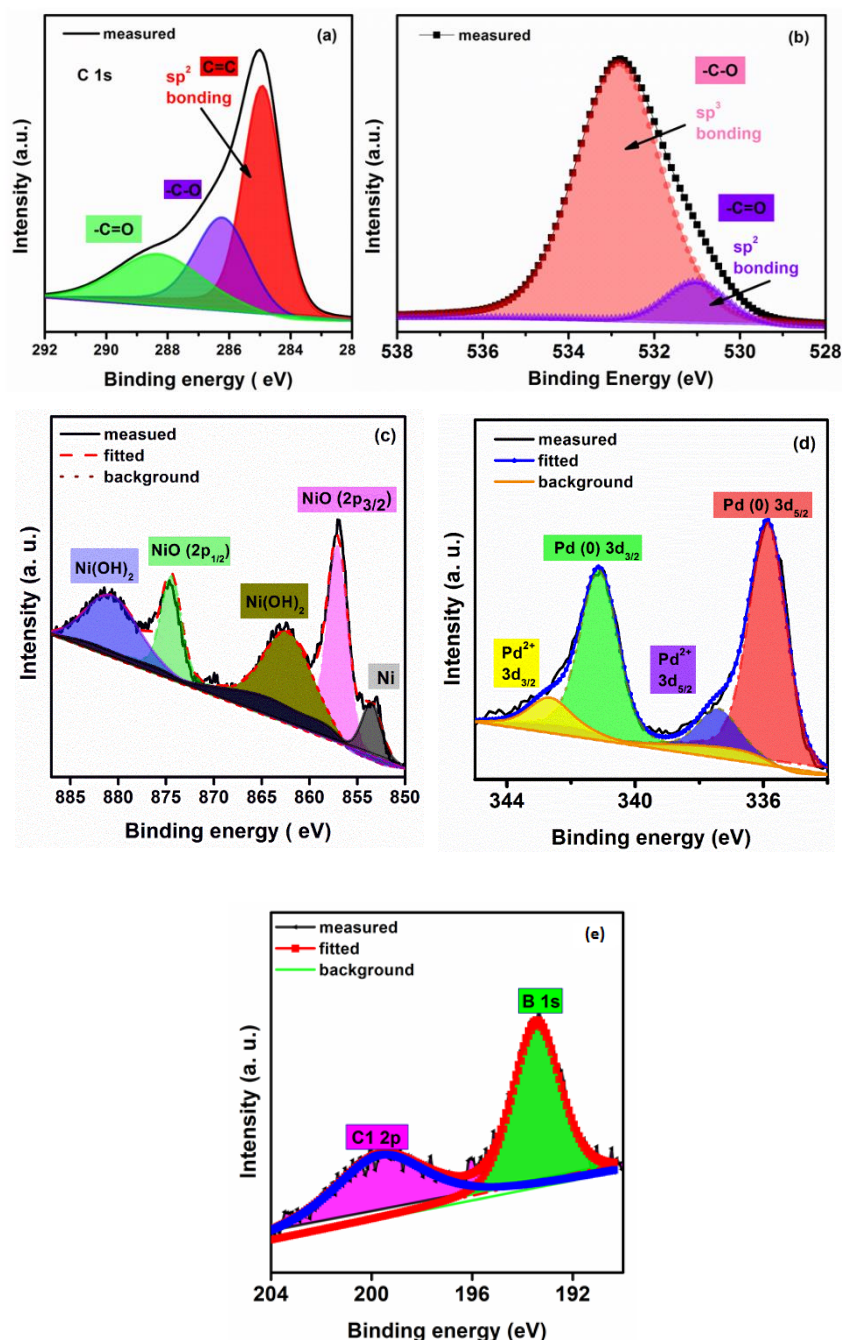


Figure 5.6 Deconvoluted XPS spectra for Pd@Ni_xB/RGO nanocomposite: (a) C 1s, (b) O 1s, (c) Ni 2p, (d) Pd 3d and (e) B 1s.

The electrochemical behavior of Pd@Ni_xB/RGO was studied in a N₂-saturated 1 M KOH solution at a scan rate of 0.050 V s⁻¹ in the potential range between 0.6 V and -0.4 V. Fig. 5.7 (black line) shows the CV of the Pd@Ni_xB/RGO modified electrode in 1 M KOH. The CV presents one cathodic peak at $E_{pc} \approx -0.301$ V which is attributed to the reduction of Pd (II) oxide according to the following equation (5.2):

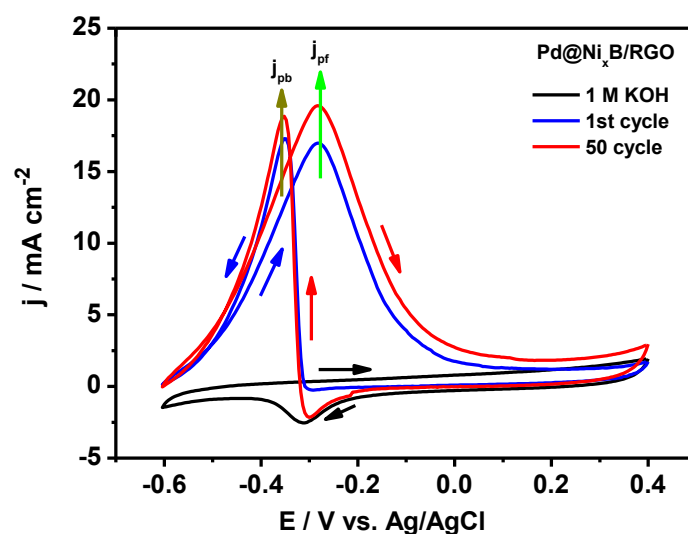
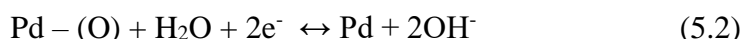
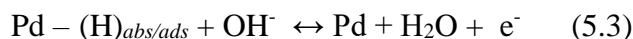
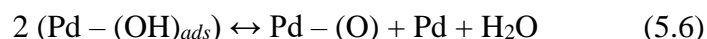
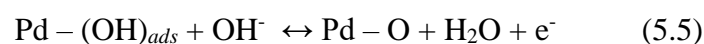
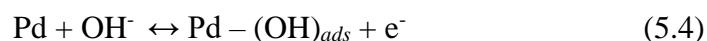


Figure 5.7 CV of Pd@Ni_xB/RGO/GCE in 1 M KOH (black solid line, reference); the first (blue solid line) and the 50th (red solid line) cycle run in 1 M KOH + 1 M EtOH at a scan rate of 0.050 V s⁻¹.

According to previously published works [31, 54], for potential ranges lower than approximately -0.450 V vs Ag/AgCl the oxidation of the absorbed and adsorbed hydrogen occurs as following equation (5.3):



For higher potential ranges (≈ -0.100 V) there is the formation of a layer of palladium (II) oxide onto the surface of the catalyst [54-56]. Although the oxidation process is still not clearly understood it is well accepted that the OH⁻ ions are first chemisorbed in the initial step of the oxide formation [54]. The mechanism of the oxidation reaction may be explained by the following reactions (5.4-5.6) [57]:



After addition of ethanol (1M in 1 M KOH) the peak corresponding to the Pd redox process disappeared and two new well defined anodic peaks were observed at -0.280 V and -0.350 V (1st cycle, blue line). These are related to the ethanol oxidation process and are defined as forward (E_{pf}) and backward (E_{pb}) peaks, respectively. The oxidation peak during the forward scan is attributed to the oxidation of freshly chemisorbed species from dissociative adsorption of ethanol (equation (5.7)) and, the oxidation peak at the backward scan represents the removal of adsorbed carbonaceous species such as ethoxi, $(\text{CH}_3\text{CO})_{\text{ads}}$ from catalyst surface [54, 55, 57, 58]. This suggests the reactivation of the Pd surface through the reduction of the Pd (II) oxide (equation (5.8)) before complete blockage of catalyst surface by Pd-O species [54]. Recently, Liang *et al.* has been proposed the mechanism of ethoxi removal from Pd electrode during the cyclic run and suggested the two-step process [57]. According to them, the first step associated the adsorption of carbonaceous species onto the Pd active sites which led the blockage of ab/adsorption of hydrogen. However, in the second step adsorbed intermediates (carbonaceous species) were stripped-off from the Pd electrode with the adsorbed oxygen-containing species ($\text{Pd}-\text{OH}_{\text{ads}}$). Very recently, Ghosh *et al.* also suggested that the generation of Pd-OH onto the surface of catalyst that imparts the positive impact for current continuity in ethanol oxidation reaction (EOR) through the development of channels of electron at the surface of the materials [31]. As a result, EOR proceeded continuously such that the current continues to increase with the potential, leads to the formation a triangular peak (as backward peak current) which is maintained during the ethanol oxidation process after several runs [54].

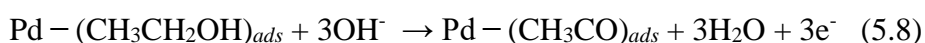


Fig. 5.7 also shows the CV of Pd@Ni_xB/RGO nanocomposite after 50 cycle run of EOR (red line). Results show that the main features determined from the CV were not significantly changed from the 1st to 50th cycle. The onset potential of faradaic currents (E_{onset}) only changes slightly ($\approx 0.005\text{V}$) and the E_{pf} and E_{pb} are the same for the 1st to 50th cycle. The forward anodic peak current density (j_{pf}) and the backward peak current density (j_{pb}) were increased after 50 cycles from 16.9 to 19.7 mA/cm² and 17.3 to 18.7 mA/cm², respectively. It results in an increase

of j_{pf}/j_{pb} ratio from 0.98 to 1.05 from the 1st to the 50th cycle which suggests that no loss of catalyst activity during the experiment and confirms their anti-poisoning characteristic towards the carbonaceous species for EOR [54]. Previously, published works have also shown that when pores and channels of Pd-based catalysts are open there were no losses of catalyst activity [31] and [59]. In present case, for Pd@Ni_xB/RGO nanocomposite, the Pd NPs were adhere onto the surface of Ni_xB/RGO entity and easily participated in the hydrogen ab/adsorption reaction. The Ni_xB entity provided the tolerance capacity of catalyst towards the CO poisoning and the grain boundaries and dislocations of Pd and Ni_xB NPs surfaces provided easy access of ethanol molecules. At the same time, RGO nanosheets provided the support for Pd and Ni_xB NPs and also facilitated the high electron mobility due to conjugated sp² network of delocalized electrons [32, 37]. Further, in order to investigate the role of RGO support towards the oxidation od ethanol we have also carried out the same experiments for Pd@Ni_xB NPs in 1 M KOH with 1 M Ethanol. Fig. 5.8 depicts the EOR for a glassy carbon electrode modified only with Pd@Ni_xB NPs.

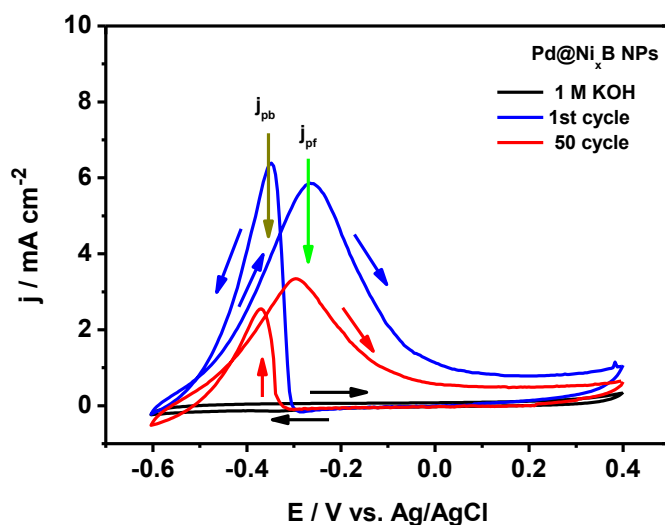


Figure 5.8 CV of Pd@Ni_xB/GCE in 1 M KOH (black solid line, reference), the 1st (blue solid line) and the 50th (red solid line) cycle run in 1 M KOH + 1 M EtOH at a scan rate of 0.050 V s⁻¹.

The cyclic voltammetric results show that in 1 M KOH (black line) there is no peak corresponding to the palladium (II) oxide reduction which suggests slower kinetics of Pd@Ni_xB in comparison with the Pd@Ni_xB/RGO. Second, the current densities ($j_{pf} = 5.9$ and $j_{pb} = 6.7$ mA/cm²) for the 1st cycle were comparably smaller and almost half of Pd@Ni_xB/RGO nanocomposite. Moreover, after 50 cycle run both current densities were decreased to 3.3 and

2.7 mA/cm², respectively, leading to a j_{pf}/j_{pb} ratio for the 50th cycle of 1.22 which was higher than the 1.04 obtained for the Pd@Ni_xB/RGO nanocomposite. Similar behavior was already observed by Ghosh *et al.* [31] where the less active system presented the higher j_{pf}/j_{pb} ratio. The comparison of the electrochemical performance of Pd@Ni_xB/RGO and Pd@Ni_xB NPs electrocatalysts toward the EOR are also summarized in Table 5.1.

Table 5.1 Comparison of the electrochemical performance of Pd@Ni_xB/RGO nanocomposite and Pd@Ni_xB NPs towards the EOR.			
Electrodes (after 1 st cycles)	j_{pf} (mA/cm ²)	j_{pb} (mA/cm ²)	j_{pf}/j_{pb}
Pd@Ni _x B/RGO nanocomposite	16.9	17.3	0.98
Pd@Ni _x B NPs	5.9	6.7	0.88
Electrodes (after 50 th cycles)	j_{pf} (mA/cm ²)	j_{pb} (mA/cm ²)	j_{pf}/j_{pb}
Pd@Ni _x B/RGO nanocomposite	19.7	18.7	1.04
Pd@Ni _x B NPs	3.3	2.7	1.22

The results that Pd@Ni_xB/RGO nanocomposite is more efficient than Pd@Ni_xB NPs which indicates that the graphene support is highly advantageous as it favors the easy electron transportation and charge transfer accessibility at the electrode/electrolyte interface [31, 32]. It provides higher accessible electrochemically surface area and avoids the NPs agglomeration. Moreover, in presence of graphene, the hydroxyl (-OH) functional groups on its surface greatly modified the nanostructure into 3D network/texture which helps to regenerate the active Pd@Ni_xB NPs via self-cleaning process [31]. Based on these results, it can be concluded that the RGO support plays a vital role for enhancement of catalytic activity of Pd@Ni_xB NPs towards the electrooxidation of ethanol.

Mechanistically, it has been mentioned that main final product of EOR is acetate instead of acetaldehyde [12]; therefore, to understand in more detail regarding of ethanol dissociative product in alkaline solution the CV measurements were carried out using the Pd@Ni_xB/RGO/GCE in a 1 M KOH solution containing 1M potassium acetate (CH₃COOK) and 1 M ethanol. (CH₃CHO) [54]. Fig. 5.9 shows that in the presence of 1 M CH₃COOK no oxidation peak related to EOR was observed which suggests the complete surface coverage by CH₃COO⁻ species and passivation of Pd catalytic active sites. Mechanistically this can be represented by the following equations (5.9 and 5.10) where, equation (5.9) represents the rate determining step [54]:

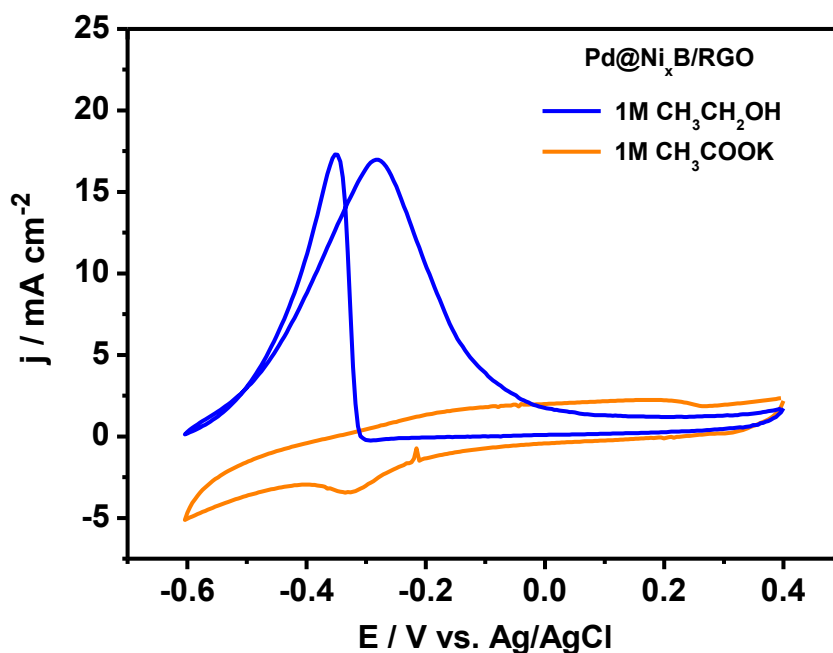
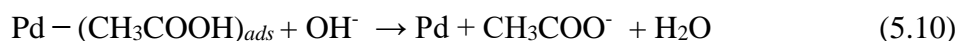
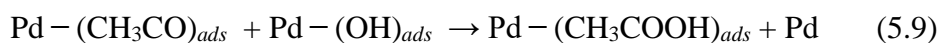


Figure 5.9 CV of Pd@Ni_xB/RGO/GCE in 1 M KOH + 1 M EtOH (blue solid line), and in 1M KOH + 1 M CH₃COOK (orange solid line) at a scan rate of 0.050 V s⁻¹.



Finally, we have carried out CA measurements in which the current density *vs.* time (*j vs. t*) curves was recorded at constant potentials as shown in Fig. 5.10. This is well known that the catalyst stability as a function of time is an important parameter for fuel cells technology for practical commercial application such as DEFC. The CA experiments for Pd@Ni_xB/RGO nanocomposite and Pd@Ni_xB NPs electrocatalysts were performed in 1M KOH with 1 M ethanol solution under a constant potential of 0.3 V for 1200 s. In the beginning, both catalysts exhibited a pronounced current decay with time but, the initial decay of current density with Pd@Ni_xB/RGO nanocomposite was higher than for Pd@Ni_xB NPs which can be attributed to the accumulation of poisonous intermediates on surface of RGO sheets of electrocatalysts [31]. However, after 450 s it became under steady state condition due to the gradual self-cleaning process of nanocomposites film on GCE surface, maintained own stable electrocatalytic performance towards EOR.

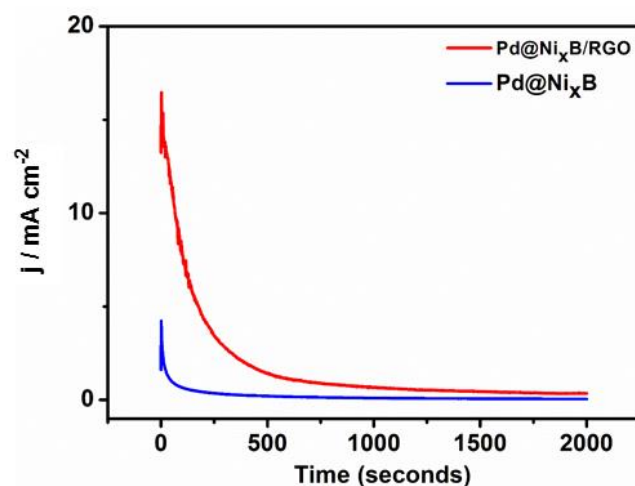


Figure 5.10 Chronoamperometric (CA) measurements for the EOR in 1 M KOH and 1 M ethanol at -0.30 V vs. Ag/AgCl on a GCE modified electrodes with Pd@Ni_xB/RGO nanocomposite (red curve) and Pd@Ni_xB NPs (blue curve).

More importantly, in the CA experiment, Pd@Ni_xB/RGO nanocomposite exhibited higher initial current density compared to the Pd@Ni_xB NPs with current limiting value. It can be rationalized that the surface properties of Pd@Ni_xB/RGO nanocomposite are more favorable for EOR and lower degradation rate during the reaction progress. The enhanced EOR activity and stability of the Pd@Ni_xB/RGO electrocatalyst also demonstrated the role of RGO. Which facilitated the easy electron transportation and provide an easy access for ethanol molecules to the catalytic sites.

5.4 Conclusions

In this work, we have successfully synthesized Pd@Ni_xB/RGO nanocomposite by a facile and green method. XRD, FTIR and XPS studies clearly displays the reduction of GO and formation of RGO. XRD and XPS studies shows the crystallinity and oxidation state of Pd NPs. SEM and TEM images confirms the formation of small NPs without any specific agglomeration. SEM elemental mapping displays the homogeneous dense distribution of Ni and Pd NPs on graphene surface and confirmed the presence of both metallic elements in Pd@Ni_xB/RGO nanocomposite. The synthesized Pd@Ni_xB/RGO nanocomposite exhibited good electrocatalytic activity towards ethanol oxidation. Moreover, it showed the enhanced catalytic performance upon cycling and increased current density after 50 cycles. CA plot clearly shows the stability of Pd@Ni_xB/RGO nanocomposite. The obtained results provided valuable information for the development of new electrocatalyst to solve the ethanol electrooxidation issue.

5.5 References

- [1] E. Antolini, Effect of the structural characteristics of binary Pt-Ru and ternary Pt-Ru-M fuel cell catalysts on the activity of ethanol electrooxidation in acid medium. *ChemSusChem*, 6 (2013), pp. 966-973.
- [2] J. M. Gregoire, M. E. Tague, S. Cahen, S. Khan, H. D. Abruna, F.J. DiSalvo, *et al.* Improved fuel cell oxidation catalysis in Pt_{1-x}Ta_x. *Chem Mater*, 22 (2010), pp. 1080-1087.
- [3] S. Ha, R. Larsen, R.I. Masel. Performance characterization of Pd/C nanocatalyst for direct formic acid fuel cells. *J Power Sources*, 144 (2005), pp. 28-34.
- [4] Z. Guo, X. Zhang, H. Sun, X. Dai, Y. Yang, X. Li, T. Meng. Novel honeycomb nanosphere Au@ Pt bimetallic nanostructure as a high performance electrocatalyst for methanol and formic acid oxidation. *Electrochimica Acta*, 134 (2014), pp. 411-417.
- [5] R. Ahmadi, M.K. Amini, J.C. Bennett. Pt-Co alloy nanoparticles synthesized on sulfur-modified carbon nanotubes as electro-catalysts for methanol electro-oxidation reaction. *J Catalysis*, 292 (2012), pp. 81-89.
- [6] E. Antolini, J.R.C. Salgado, E.R. Gonzalez. The methanol oxidation reaction on platinum alloys with the first row transition metals-the case of Pt-Co and -Ni alloy electro-catalysts for DMFCs: A short review. *Applied Catalysis B*, 63 (2006), pp. 137-149.
- [7] S. K. Meher, G.R. Rao. Morphology-controlled promoting activity of nanostructured MnO₂ for methanol and ethanol electro-oxidation on Pt/C. *J Physical Chemistry C*, 117 (2013), pp. 4888-4900.
- [8] X. Niu, H. Zhao, M. Lan, L. Zhou. Platinum Nanoparticles Encapsulated in Carbon Microspheres: Toward Electro-Catalyzing Glucose with High Activity and Stability. *Electrochimica Acta*, 151 (2015), pp. 326-331.
- [9] X. Cheng, Z. Shi, N. Glass, L. Zhang, J. Zhang, D. Song, Z. S. Liu, H. Wang, J. Shen. A review of PEM hydrogen fuel cell contamination: Impacts, mechanisms, and mitigation. *J Power Sources*, 165 (2007), pp. 739-756.
- [10] E. Christoffersen, P. Liu, A. Ruban, H. L. Skriver, J. K. Nørskov. Anode Materials for Low-Temperature Fuel Cells: A Density Functional Theory Study. *J Catalysis*, 199 (2001), pp. 123-131.

- [11] T.V. Reshetenko, J. St-Pierre. Study of acetylene poisoning of Pt cathode on proton exchange membrane fuel cell spatial performance using a segmented cell system. *J Power Sources*, 287 (2015), pp. 401-415.
- [12] T. Sheng, W. F. Lin, C. Hardacre, P. Hu. Role of water and adsorbed hydroxyls on ethanol electrochemistry on Pd: New mechanism, active centers, and energetics for direct ethanol fuel cell running in alkaline medium. *J Physical Chemistry*, 118 (2014), pp. 5762-5772.
- [13] P.S. Roy, S.K. Bhattacharya. Size-controlled synthesis and characterization of polyvinyl alcohol-coated platinum nanoparticles: role of particle size and capping polymer on the electrocatalytic activity. *Catal Sci Technol*, 3 (2013), pp. 1314-1323.
- [14] L. Ma, D. Chu, R.R. Chen. Comparison of ethanol electro-oxidation on Pt/C and Pd/C catalysts in alkaline media. *Int J Hydrogen Energ*, 37 (2012), pp. 11185-11194.
- [15] S.Y. Shen, T.S. Zhao, J.B. Xu, Y.S. Li. Synthesis of PdNi catalysts for the oxidation of ethanol in alkaline direct ethanol fuel cells. *J Power Sources*, 195 (2010), pp. 1001-1006.
- [16] U. B. Demirci. Direct liquid-feed fuel cells: thermodynamic and environmental concerns. *J Power Sources*, 169 (2007), pp. 239.
- [17] N. Li, Y. X. Zeng, S. Chen, C. W. Xu, P. K. Shen. Ethanol oxidation on Pd/C enhanced by MgO in alkaline medium. *Int J Hydrogen Energy*, 39 (2014), pp. 16015-16019.
- [18] X. Wang, G. Ma, F. Zhu, N. Lin, B. Tang, Z. Zhang. Preparation and characterization of micro-arc-induced Pd/TM (TM = Ni, Co and Ti) catalysts and comparison of their electrocatalytic activities toward ethanol oxidation. *Electrochim Acta*, 114 (2013), pp. 500-508.
- [19] Z. Qi, H. Geng, X. Wang, C. Zhao, H. Ji, C. Zhang, *et al.* Novel nanocrystalline PdNi alloy catalyst for methanol and ethanol electro-oxidation in alkaline media. *J Power Sources*, 196 (2011), pp. 5823-5828.
- [20] E. Antolini. Palladium in fuel cell catalysis. *Energy Environ Sci*, 2 (2009), pp. 915-931.
- [21] M. Smiljanić, Z. Rakočević, S. Štrbac. Ethanol oxidation on Pd/Au(111) bimetallic surfaces in alkaline solution. *Int J Electrochem Sci*, 8 (2013), pp. 4941-4954.
- [22] N. Abbasi, P. Shahbazia, A. Kiani. Electrocatalytic oxidation of ethanol at Pd/Ag nanodendrites prepared via low support electrodeposition and galvanic replacement. *J Mater Chem A*, 1 (2013), pp. 996-9972.

- [23] K.H. Ye, S.A. Zhou, X.C. Zhu, C.W. Xu, P.K. Shen. Stability analysis of oxide (CeO₂, NiO, Co₃O₄ and Mn₃O₄) effect on Pd/C for methanol oxidation in alkaline medium. *Electrochim Acta*, 90 (2013), pp. 108-111.
- [24] Q. Yi, Q. Chen. In situ preparation and high electrocatalytic activity of binary Pd-Ni nanocatalysts with low Pd-loadings. *Electrochimica Acta*, 182 (2015) pp. 96-103.
- [25] A. M. Sheikh, E. L. Silva, L. Moares, L. M. Antonini, M. Y. Abellah, C. F. Malfatti. Pd-based Catalysts for Ethanol Oxidation in Alkaline Electrolyte. *Am J Min Metal*, 2 (2014) pp. 64-69.
- [26] Z. Zhang, T.M. Nenoff, K. Leung, S.R. Ferreira, J.Y. Huang, D.T. Berry, P.P. Provencio, R. Stumpf. *J Physical Chemistry C*, 114 (2010), pp. 14309-14318.
- [27] F. P. Hu, C. L. Chen, Z. Y. Wang, G.Y. Wei, P. K. Shen. *Electrochim Acta*, 52 (2006), pp. 1087-1091.
- [28] C. Xu, P.K. Shen, Y. Liu. Ethanol electrooxidation on Pt/C and Pd/C catalysts promoted with oxide. *J Power Sources*, 164 (2007), pp. 527-531.
- [29] R. Krishna, E. Titus, M. Salimian, O. Okhay, S. Rajendran, A. Rajkumar, et al. Hydrogen storage for energy application. *Intech Open, Europe* (2012).
- [30] L. Dong, R. R. S. Gari, Z. Li, M. M. Craig, S. Hou. Graphene-supported platinum and platinum–ruthenium nanoparticles with high electrocatalytic activity for methanol and ethanol oxidation. *Carbon*, 48 (2010), pp. 781-787.
- [31] S. Ghosh, H. Remita, P. Kar, S. Choudhury, S. Sardar, P. Beaunier, P. S. Roy, S. K. Bhattacharya, S. K. Pal. Facile synthesis of Pd nanostructures in hexagonal mesophases as promising electrocatalyst for ethanol oxidation. *J Mater Chem A*, 3 (2015), pp. 9517-9527.
- [32] J. L. Tan, P. G. Villar, A. Jesus, B. J. V. Tongo. A green approach to the synthesis of Pd-Ni/graphene via electrochemical exfoliation of graphite from used battery for the electrocatalysis of ethanol. *J Chin Chem Soc*, 61 (2014), pp.774-777. DOI: 10.1002/jccs.201400065
- [33] Y. Hou, S. Gao. Monodisperse nickel nanoparticles prepared from a monosurfactant system and their magnetic properties. *J Mater Chem*, 13 (2003), pp. 1510-1512.

- [34] M. Shviro, D. Zitoun. Nickel nanocrystals: fast synthesis of cubes, pyramids and tetrapods. *RSC Adv*, 3 (2013), pp. 1380-1387.
- [35] Z. Ji, X. Shen, G. Zhu, H. Zhou, A. Yuan. Reduced graphene oxide/nickel nanocomposites: facile synthesis, magnetic and catalytic properties. *J Mater Chem*, 22 (2012), pp. 3471-3477.
- [36] Z. Wu, X. Mao, Q. Zi, R. Zhang, T. Dou, A.C.K. Yip. Mechanism and kinetics of sodium borohydride hydrolysis over crystalline nickel and nickel boride and amorphous nickel-boron nanoparticles. *J Power Sources*, 268 (2014), pp. 596-603.
- [37] R. Krishna, D. M. Fernandes, V. F. Domingos, E. S. Ribeiro, J. C. Gil, C. Dias, J. Ventura, C. Freire, E. Titus. Reduction of 4-nitrophenol to 4-aminophenol using novel Pd@Ni_xB-SiO₂/RGO nanocomposite: Enhanced hydrogen spillover and high catalytic performance. *RSC Adv*, 5 (2015), pp. 60658-60666.
- [38] B. Li, H. Cao, J. Yin, Y. A. Wu, J. H. Warner. Synthesis and separation of dyes via Ni@reduced graphene oxide nanostructures. *J Mater Chem*, 22 (2012), pp. 1876-1883.
- [39] M. J. F. Merino, L. Guardia, J. I. Paredes, S. V. Rodil, P. S. Fernández, A. M. Alonso, J. M. D. Tascón. Vitamin C is an ideal substitute for hydrazine in the reduction of graphene oxide suspensions. *J Physical Chemistry C*, 114 (2010), pp. 6426-6432.
- [40] Y.Y. She, Z. Lu, W. Fan, S. Jewell, M.K.H. Leung. Facile preparation of PdNi/rGO and its electrocatalytic performance towards formic acid oxidation. *J Mater Chem A*, 2 (2014), pp. 3894-3898.
- [41] S. Yang, J. Dong, Z. Yao, C. Shen, X. Shi, Y. Tian, S. Lin, X. Zhang. One-Pot Synthesis of Graphene-Supported Monodisperse Pd Nanoparticles as Catalyst for Formic Acid Electro-oxidation. *Scientific Reports*, 4 (2014) pp. 4501. DOI: 10.1038/srep04501
- [42] Z.L. Wang, J.M. Yan, H.L. Wang, Y. Ping, Q. Jiang. Pd/C synthesized with citric acid: an efficient catalyst for hydrogen generation from formic acid/sodium formate. *Scientific Reports*, 2 (2012), pp. 598. doi: 10.1038/srep00598
- [43] F. Kettemann, M. Wuithschick, G. Caputo, R. Kraehnert, N. Pinna, K. Rademann, J. Polte. Reliable palladium nanoparticle syntheses in aqueous solution: the importance of understanding precursor chemistry and growth mechanism. *Cryst Eng Comm*, 17 (2015) pp. 1865-1870.

- [44] Y. Zhang, Y. Dong, L. Wang, S. Wang. Scalable synthesis of a Pd nanoparticle loaded hierarchically porous graphene network through multiple synergistic interactions. *Chem Commun*, 51 (2015), pp. 8357-8360.
- [45] B. K. Barman, K. K. Nanda. The dual role of Zn–acid medium for one-step rapid synthesis of M@rGO (M = Au, Pt, Pd and Ag) hybrid nanostructures at room temperature. *Chem Commun*, 49 (2013) pp. 8949-8951.
- [46] P.D. Burton, T. J. Boyle, A. K. Datye. Facile, surfactant-free synthesis of Pd nanoparticles for heterogeneous catalysis. *J Catalysis*, 280 (2011), pp. 145-149.
- [47] R. Krishna, D. M. Fernandes, C. Dias, J. Ventura, E. V. Ramana, C. Freire, E. Titus. Novel synthesis of Ag@Co/RGO nanocomposite and its high catalytic activity towards hydrogenation of 4-nitrophenol to 4-aminophenol *Int J Hydrogen Energy*, 40 (2015), pp. 4996-5005.
- [48] F. Yu, W. Zhou, R. M. Bellabarba, R. P. Tooze. One-step synthesis and shape-control of CuPd nanowire networks. *Nanoscale*, 6 (2014) pp. 1093-1098.
- [49] J. Zhang, H. Yang, G. Shen, P. Cheng, J. Zhang, S. Guo. Reduction of graphene oxide via L-ascorbic acid. *Chem Commun*, 46 (7) (2010), pp. 1112-1114.
- [50] U. B. Demirci, O. Akdim, J. Andrieux, J. Hannauer, R. Chamoun, P. Miele. Sodium borohydride hydrolysis as hydrogen generator: issues, state of the art and applicability upstream from a fuel cell. *Fuel Cells*, 10 (2010), pp. 335-350.
- [51] T. Hawa, M.R. Zachariah. Coalescence kinetics of unequal sized nanoparticles. *J Aerosol Sci*, 37 (2006), pp. 1-15
- [52] R. M. Tilaki. A. I. zad, S. M. Mahdavi. The effect of liquid environment on size and aggregation of gold nanoparticles prepared by pulsed laser ablation. *J Nanoparticle Research*, 9 (2007), pp. 853-860.
- [53] N. T. K. Thanh, N. Maclean, S. Mahiddine. Mechanisms of Nucleation and Growth of Nanoparticles in Solution. *Chem Rev*, 114 (2014), pp. 7610-7630.
- [54] S. Ghosh, A. L. Teillout, D. Floresyona, P. Oliveira, A. Hagège, H. Remita. Conducting polymer-supported palladium nanoplates for applications in direct alcohol oxidation. *Int J Hydrogen Energy*, 40 (2015), pp. 4951-4959.

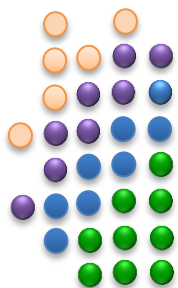
[55] B. Habibi, S. Mohammadyari. Facile synthesis of Pd nanoparticles on nanocarbon supports and their application as an electrocatalyst for oxidation of ethanol in alkaline media: The effect of support. *Int J Hydrogen Energy*, 40 (2015), pp. 10833-10846.

[56] Q. Yi, F. Niu, L. Sun. Fabrication of novel porous Pd particles and their electroactivity towards ethanol oxidation in alkaline media. *Fuel*, 90 (2011), pp. 2617-2623.

[57] Z. X. Liang, T. S. Zhao, J. B. Xu, L. D. Zhu. Mechanism study of the ethanol oxidation reaction on palladium in alkaline media. *Electrochimica Acta*, 54 (2009), pp. 2203-2208.

[58] Z. Qi, H. Geng, X. Wang, C. Zhao, H. Ji, C. Zhang, J. Xu, Z. Zhang. Novel nanocrystalline PdNi alloy catalyst for methanol and ethanol electro-oxidation in alkaline media. *J Power Sources*, 196 (2011), pp. 5823-5828.

[59] R. C. Cerritos, M. Guerra-Balcázar, R.F. Ramírez, J. Ledesma-García, L.G. Arriaga. Morphological effect of Pd catalyst on ethanol electro-oxidation reaction. *Materials*, 5 (2012), pp. 1686-1697.



CHAPTER 6

DIRECT HYDROGEN GENERATION THROUGH NaBH_4 HYDROLYSIS REACTION –POTENTIAL ROLE OF GRAPHENE NANOCOMPOSITE:

Synthesis, characterization, results and
mechanism

Chapter 6

<u>Direct hydrogen generation through NaBH₄ hydrolysis reaction –potential role of graphene nanocomposite: synthesis, characterization, results and mechanis</u>		<u>121</u>
6.1	Introduction	123
6.2	Experimental	124
6.2.1	Syntheis	124
6.2.2	Characterization techniques	125
6.2.3	Hydrogen generation test	126
6.3	Results and discussion	126
6.4	Conclusion	140
6.5	References	140

**DIRECT HYDROGEN GENERATION THROUGH NaBH₄
HYDROLYSIS REACTION –POTENTIAL ROLE
OF GRAPHENE NANOCOMPOSITE:
Synthesis, characterization, results and mechanism**

6.1 Introduction

NaBH₄ is an example which can provide clean energy without any environmental impact, easily stabilized in alkaline NaOH aqueous solution, it produces 4 moles of H₂ in presence of catalyst as shown in equation (6.1) [1-6]:



where, x denotes the excess of water for the reaction. In order to enhance the hydrogen generation rate (for on-board energy demand), a vast range of catalyst were investigated such as Ru, Pt, Pd, W, Cr, Co and Ni [7-10]. Recently, Saha *et al.* demonstrated the NaBH₄ hydrolysis using graphene supported bimetallic G-Co-Pt nanohybrid catalyst [11]. Previously, Krishnan *et al.* also reported the hydrogen generation using PtRu-LiCoO₂ [12]. Similarly, Chowdhury *et al.* used the Ru-Co-PEDOT nanocomposites as catalyst for hydrolysis of NaBH₄ [13]. However, in all these cases catalyst synthesis was not straightforward and at least one noble element was involved as a major catalyst component. In this regard, prior to process easiness and cost effectiveness it is highly desirable another efficient way for boosting the H₂ economy [14-15]. Co-B is a low price catalyst for NaBH₄ hydrolysis and works effectively, therefore catalytic study of them is a central issue for future commercialization [16-19]. However, Co-B shows some shortcomings during the catalytic process such as particles agglomeration, poor conductivity (for e⁻ transportation) and separation of catalyst after completion of reaction (from spent solution) [20-22].

Recently, graphene has gained enormous interest as a support material for anchoring of several types of NPs and has been involved in various kinds of applications [23-25]. Saha *et al.* proposed the electrocatalytic hydrolysis of NaBH₄ using graphene supported Co-Ni catalyst [26]. They synthesized the Ni NPs on graphene sheets using polyol method at high temperature (120 °C, 5 h). However, such an involvement of high temperature or toxic hydrazine hydrate (for synthesis of Ni NPs) disfavor their industrial exploitation [27-28].

Understanding the process easiness and environmental issue, we design a smart catalyst Co-B@Ni/RGO on the basis of commercially available Ni NPs (which provides more efficacy and beneficiary for synthesizing the Ni/RGO nanocomposite due to their bulk availability and consistency). This strategy easily maintain the shell-core structure (superficial attachment of Co-B NPs on magnetic Ni core). In this work, first time, we report a facile synthesis of Co-B@Ni/RGO nanocomposite for NaBH₄ decomposition in aqueous alkaline medium. Further, due to this nanostructure we have also studied the current *vs* voltage (I-V) and impedance characteristics of nanocomposite using CV and impedance techniques. Which shows the high charge density and easy electron flow in Co-B@Ni/RGO nanocomposite that may directly useful for energy storage application such as supercapacitor, and provide the wide understanding of material characteristic also for research purposes.

6.2. Experimental

6.2.1 Synthesis

All other chemicals were analytical grades and used as received and throughout in experiment Milli Q water was used. GO was synthesized by the modified Hummers method as our previous work [29]. To prepare the Ni/RGO nanocomposite, 60 mL of aqueous GO dispersion (0.5 mg/mL) was placed in round bottom (RB) flask and afterward 30 mg Ni NPs were added. Then after, for reduction of GO a freshly prepared aqueous solution of NaBH₄ (1 wt.%, 10 mL) was slowly added and continuously ultrasonicated for 1 h, at RT and finally the black product Ni/RGO was magnetically separated and repeatedly washed with Milli Q water and ethanol and dried in vacuum oven at 100 °C for 12 h. For the synthesis of Co-B@Ni/RGO nanocomposite, first a dispersion of Ni/RGO was prepared in 50 mL Milli Q water under ultrasonication (15 min) then, 600 mg of cobalt salt was mixed by mechanical stirring (30 min) at RT in three neck RB flask. To synthesize the Co-B phase on Ni/RGO, an alkaline solution of NaBH₄ (1 wt. %) was first prepared by dissolving of 180 mg NaOH in 50 mL Milli Q water. Then, it was drop mixed in Ni/RGO dispersion and mechanically stirred (800 rpm) for 45 min.

During the reaction, the flask was placed in cooling water and all vents were opened to release the produced H₂. The temperature of flask was maintained at 0 - 5 °C during the reaction in order to prevent a vigorous reaction. After completion of reaction, product was filtered and multiply washed with Milli Q water and ethanol and finally, dried in vacuum oven at 300 °C and referred as Co-B@Ni/RGO. Similar procedure was adopted to synthesis of Co-B/RGO nanocomposite in absence of Ni NPs (for comparison).

6.2.2 Characterization

Phase purity and crystallinity were characterized by X-ray diffraction (XRD) technique (Rigaku, Japan, CuK α radiation; 2θ angle range 10–80°; step 0.02 °/s). FTIR spectra were recorded in ATR powder mode. Thermogravimetric (TGA) analysis was carried out under N₂ flow in a Shimadzu TGA 50 analyzer equipped with a platinum cell. The samples were heated at a constant rate of 10 °C min⁻¹ from room temperature to 700 °C. Magnetic measurements was carried out using a vibrating sample magnetometer (VSM) from Oxford instruments, at RT with parallel magnetic field between ± 1 T at a rate of 0.3 T/min, and 40 Hz and 1.5 mm amplitude for the vibration. Surface morphology were investigated by scanning electron microscope (SEM) in EDX mode. The samples for TEM were prepared by dipping an aliquot of suspension (in acetone, 0.1 mg/ mL) on to a carbon-coated copper grid. A conventional high-resolution (HR) TEM (JEOL 2200F TEM) was performed to analyse the crystallinity and quality of samples. Cyclic voltammetry (CV) and electrochemical impedance (EIS) measurements were carried out using an Autolab PGSTAT 30 potentiostat/galvanostat (EcoChimie B.V.) controlled by the GPES and FRA software, respectively. A three-electrode system was used with the following electrodes: reference - Ag/AgCl (sat. KCl) (BAS, MF-2052); auxiliary - platinum wire (7.5 cm, BAS, MW-1032) and working - glassy carbon electrode, GCE, (3 mm diameter, BAS, MF-2012). The working cell was surrounded by a grounded Faraday cage and all studies were carried out at room temperature and under an argon flow. For the electrochemical impedance measurements was used a voltage perturbation of 10 mV rms over a frequency range from 50 kHz to 0.01 Hz with an integration time of 60 s. Ultra-pure water (Millipore, 18.2 M Ω cm, 25 °C) was used to prepare the 1M KOH electrolyte solution. Prior to modification the GCE electrode was conditioned by a polishing/cleaning procedure using diamond pastes of 6, 3 and 1 μ m (Buehler) on a nylon polishing pad (BAS Bioanalytical Systems Inc.) and finally aluminium oxide of particle size 0.3 μ m (Buehler) on a microcloth polishing pad (BAS Bioanalytical Systems Inc.). Then the electrode was rinsed with ultra-pure water and finally

sonicated for 5 min in ethanol and ultra-pure water. Dispersions used to produce the modified electrodes were prepared as follows: a 0.5% Nafion dispersion (1 mL) of the selected material Co-B/RGO, Ni/RGO or Co-B@Ni/RGO in all cases (5 mg each) was sonicated for 10 min. Electrode modification consisted in depositing a 3 μ L drop of the dispersion of the selected composite material onto the surface of the glassy carbon electrode and the solvent was evaporated under a flow of air.

6.2.3 Hydrogen generation tests

To evaluate the catalytic activity, slurry of catalysts (in Milli Q water) was introduced in a three neck RB flask. The middle neck was connected to mechanical stirrer, one side was equipped to thermometer to control the temperature. The other vent of flask was air tightened and connected with tubes and accessories for measurement of H₂ generation. The Flask was immersed in a water bath to maintain the temperature constant at set point. For hydrolysis reaction, chemicals were placed in flask. During the process, generated H₂ was released from the vent neck and passed from a surge flask to eliminate the effect of residual alkali and water. The generated H₂ was collected in a graduated jar by water displacement method and the volume of the generated hydrogen was calculated on the basis of change in height of water with respect to time.

6.3. Results and discussion

Fig. 6.1 (a) shows the XRD of GO, Ni/RGO, Co-B/RGO and Co-B@Ni/RGO nanocomposites. GO exhibits a sharp peak at around 11.01° which was correspond to the (001) basal plane and suggests the good exfoliation of graphite [29]. This is well known fact that after the vigorous oxidation of graphitic flakes in strong oxidizing environment various kind of oxygenated functionalities attaches to the graphitic plane and increases the interlayer spacing of graphitic sheets. XRD diffraction of Co-B/RGO shows a peak at 23.2° suggested the reduction of oxygen functionalities from graphitic planes [30]. In XRD diffraction spectra of Ni/RGO three additional peaks were also observed, were attributed as diffraction from (111), (200) and (220) various crystallographic planes of face-centred cubic (fcc) Ni-NPs [31-33]. In the XRD diffraction spectra of Co-B@Ni/RGO nanocomposite peak related of carbon was completely disappeared and crystalline Ni peak broadening was decreased. It might be due the formation of tiny Co-B phase on Ni NPs. Further, in order to elucidate the reaction mechanism

in more detail, we have also carried out the Fourier transform infrared (FTIR) spectroscopy. Fig. 6.1 (b) shows the FTIR spectra of GO, Co-B/RGO, Ni/RGO and Co-B@Ni/RGO nanocomposite samples (in the range of 4000-800 cm⁻¹). In FTIR spectra of GO, a strong broad band was observed in high frequency area (3400-3200 cm⁻¹) which assigned to the stretching vibration mode of -OH groups due to the surface adsorbed water molecules [30]. After the reduction, in FTIR spectra of Co-B/RGO the intensity of this band was decreased suggested the removal of surface adsorbed water molecules from graphitic planes during the reduction process.

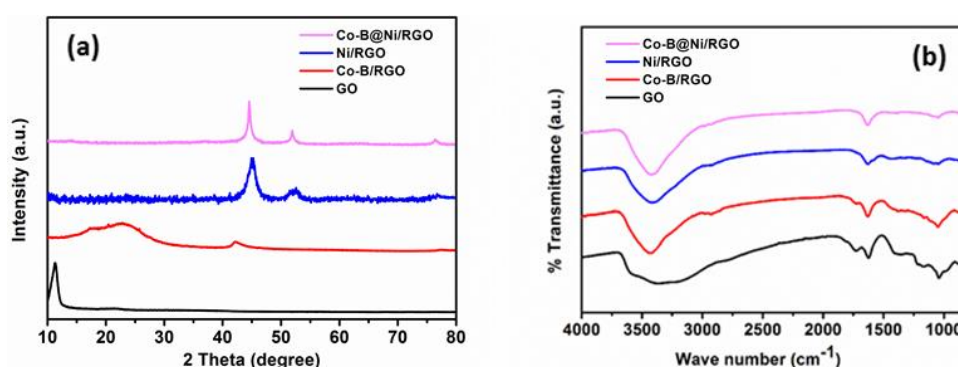


Figure 6.1 (a) XRD pattern and (b) FTIR spectra of GO, Co-B/RGO, Ni/RGO and Co-B@Ni/RGO nanocomposite.

Moreover, the peak related to the stretching vibration mode of carbonyl functionality (-C=O) at around 1725 cm⁻¹ was also deprived in reduced products clearly indicated the elimination of edge related -C=O groups and formation of GO to RGO [31]. Finally, the absorption peaks at 1380 cm⁻¹ (due to the stretching vibration of C-O of carboxylic acid) and 1120 cm⁻¹ (related of C-OH of alcohol) were also sufficiently reduced in all reduced samples compare to the GO. Further, to understand the stability of material and detail analysis of mechanism we performed the thermogravimetric (TGA) analysis under N₂ flow. Fig. 6.2 depicts the % weight loss of the GO and final product Co-B@Ni/RGO nanocomposite. TGA plot of GO shows that the instability of material it was obvious due to the various surface oxygen functional groups on graphene.

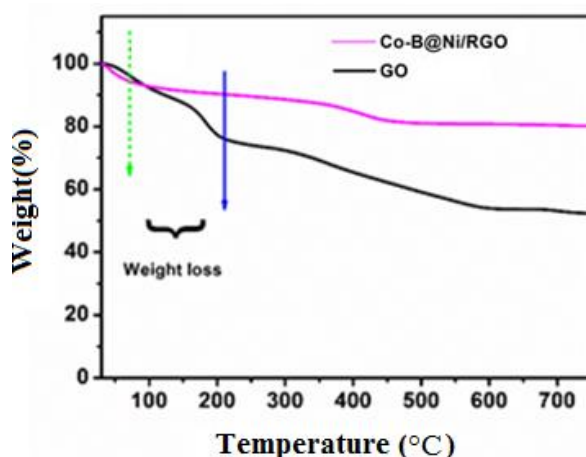


Figure 6.2 TGA of GO and Co-B@Ni/RGO nanocomposite.

In GO sample initially major weight loss was observed at 200 °C corresponding to the 23% of mass, suggested the removal of surface adsorbed water [30]. Whereas, at this temperature in Co-B@Ni/RGO only a 9.75% weight loss was observed. Moreover, in Co-B@Ni/RGO nanocomposite the final weight loss was around 15.5% at 750 °C whereas, in GO this was 39.5%. This large difference in weight loss clearly indicated the decomposition and pyrolysis of oxygen functional groups in GO at higher temperature and quite stability of Co-B@Ni/RGO nanocomposite.

Further, we have carried out the systematic microscopic investigation of initial materials (GO), intermediate composite material Co-B/RGO and Ni/RGO (after the reduction and loading of Co-B and Ni NPs within the graphene matrix) and final product Co-B@Ni/RGO nanocomposite. Fig. 6.3 (a) and (b) shows the SEM images of initial material GO in lower and higher magnifications, respectively. Images of GO clearly exhibited the few layer of graphitic carbon with typical wrinkle and flappy behaviour.

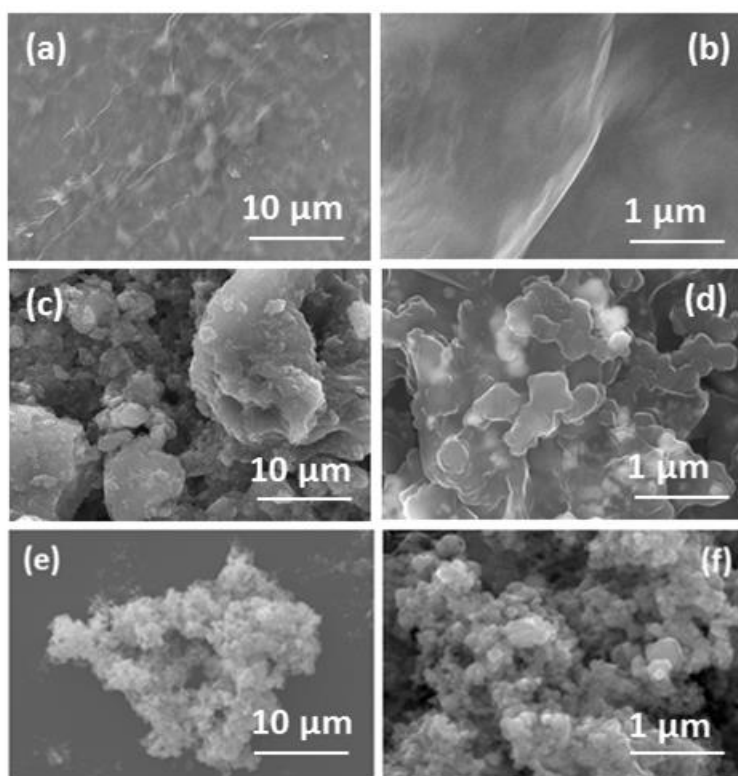


Figure 6.3 SEM images of: GO (a) and (b), Co-B/RGO (c) and (d), Ni/RGO nanocomposites (e) and (f), in lower and higher magnifications, respectively.

Fig. 6.3 (c) and (d) depicts the SEM images of intermediate species Co-B/RGO after the reduction and loading of Co-B NPs within graphene matrix. Both images show the well intercalation of Co-B NPs with graphitic flakes and image contrast in higher magnification image (white spots on black background) clearly reveals the covering of Co-B NPs by single or few layers graphene sheets. Similar situation was retained and became clearer in images 6.3 (e) and (f) after the intercalation of Ni NPs with graphene in Ni/RGO intermediate material. Moreover, images shows that Ni NPs were in spherical shape and well separated and distributed on graphene sheet without any specific agglomerations. Similar behavior was observed after the intercalation of Co-B NPs on Ni/RGO as observed in Fig. 6.4 (a) and (b). Additionally, these two images show higher density of NPs compared to previous images of Co-B/RGO and Ni/RGO indicating the successful formation of Co-B@Ni/RGO nanocomposite. Fig. 6.4 (a) in lower magnification, shows the intercalation of tiny Co-B NPs on Ni/RGO nanocomposite on superficial position. Higher magnification image (Fig. 6.4 (b)) clearly depicts the covering of small NPs within graphene layers.

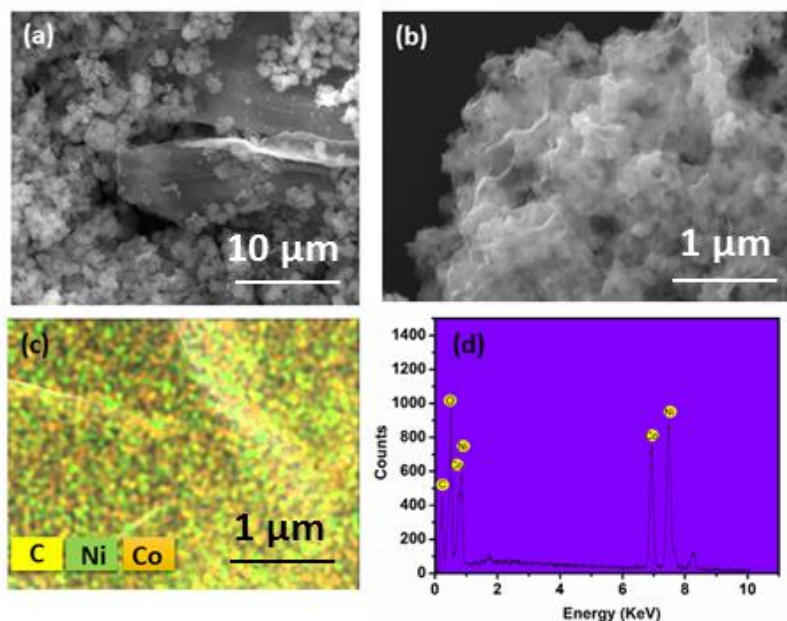


Figure 6.4 SEM images of Co-B@Ni/RGO nanocomposites (a) and (b) lower and higher magnifications, respectively. (c) Elemental mapping and (d) EDX analysis of Co-B@Ni/RGO nanocomposite.

Mechanistically, this can be explained as: during the synthesis of second entity Co-B on Ni/RGO nanocomposite the produced H₂ (between the reaction of NaBH₄ and H₂O, equation 1) became spillover [29] on Ni/RGO and migrated on to the defect sites of RGO and grafted on to the catalyst surface and saturated the carbonyl functionalities. In the next step, these extra H atom inside of catalyst system when liberated it makes the molecular H₂ which decreases the van der Waals interaction of graphene sheets and exfoliates the graphitic sheets. Moreover, to confirm the presence of Ni and Co elements within graphene layers and their distribution we have also carried out the elemental mapping (Fig. 6.4 (c)), which clearly shows the uniform distribution of both metallic entities in the Co-B@Ni/RGO nanocomposite. Fig. 6.4 (d) displays the EDX spectrum of CoB@Ni/RGO nanocomposite and results show the presence of all elements: Co, Ni, C and O with the exception of the light weight elements B and H. Fig. 6.5 (a) depicts the TEM image of GO in which thin layers of carbon sheets were observed without any specific defect inside of graphene sheet. Fig. 6.5 (b) shows the TEM image of Co-B/RGO nanocomposite in which amorphous Co-B NPs were grafted on to the folding and stacking site of graphene sheets.

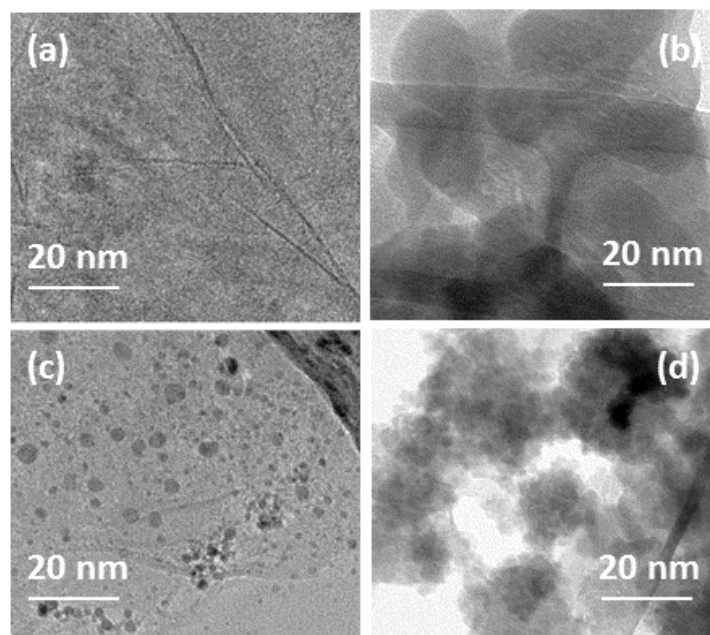
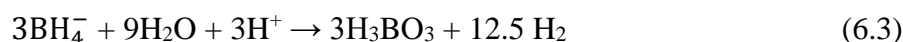
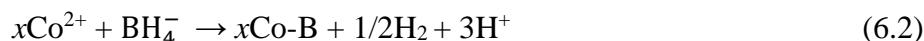


Figure 6.5 TEM images of (a) GO, (b) Co-B/RGO, (c) Ni/ RGO and (d) Co-B@Ni/RGO nanocomposites.

Fig. 6.5 (c) shows the TEM image of Ni/RGO in which small Ni NPs were encapsulated on single or few-layer graphene sheets without any agglomeration in the size range of 2-5 nm. In image, mostly Ni NPs were 10 nm indicated the simplicity and efficacy of our synthesis protocol (in which without any use of specific surface protection groups or organic functional moieties Ni NPs were adhere with graphene sheet). This was due to direct mixing of Ni NPs with GO and afterward reduction with NaBH₄ at RT. Due to this reason, various kind of GO functional groups such as carbonyl, epoxide and carboxylic functionalities holds the Ni NPs and provide site specification for them. Fig. 6.5 (d) displays the TEM image of Co-B@Ni/RGO in which discrete assemblies of Co-B@Ni/RGO were observed with small hole in RGO sheets. This was due to the disruption of graphene layer by H radicals which saturated the sp² hybridized (-C=C) bonding of RGO to sp³ hybridized (-C-H) bonding. Which led the resilience between C-C bonding and makes the defect in graphene sheet [34]. Further, we have also studied the synthesis mechanism of Co-B NPs. It has been already reported that the characteristics and properties of Co-B NPs is very sensitive on reaction conditions such as pH, temperature, ratio of NaBH₄ and OH⁻ and concentration of reacting species. All these factors significantly affected the morphology and activity of the product. At the time of reduction basically, two main reactions simultaneously proceeded: (i) reduction of Co²⁺ ion by BH₄⁻ and (ii) hydrolysis of BH₄⁻ species as represented in equation 6.2 and 6.3 [35]:



The overall reaction can be expressed as 6.4:

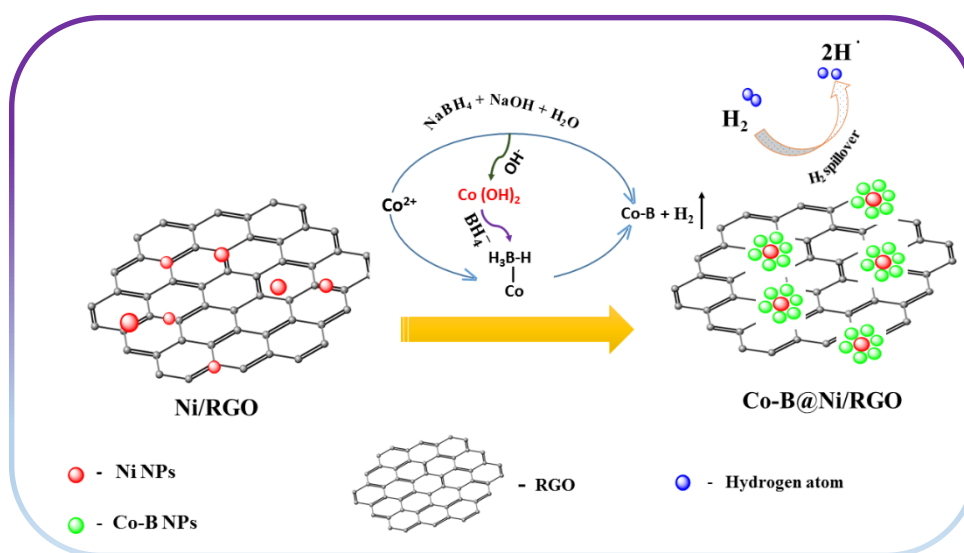
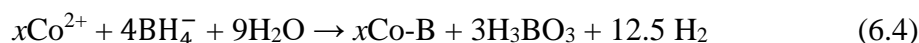


Figure 6.6 Schematic illustration of reduction of Co^{2+} ion under alkaline NaBH_4 reducing condition and also H_2 spillover mechanism on Ni/RGO and defect creation inside in graphene sheet due to H radicals.

Reaction (6.3) indicated that decomposition of BH_4^- largely dependent on pH value when it was high, the BH_4^- species is quite stable and the rate of hydrolysis was suppressed. However, high pH condition (pH ~13.25) positively affected the Co^{2+} ion reduction due to it suppresses the BH_4^- hydrolysis and increases the reduction efficiency of Co^{2+} which predominantly formed Co(OH)_2 species as shown in Fig. 6.6. Moreover, at the same time BH_4^- species try to attaches with metal units and exchanges the ligand (hydroxyl to hydride) and makes the very unstable B(OH)_4^- species which further decomposes to B(OH)_3 that finally yielded the NaBO_2 side product. During the reduction process it reacted with BH_4^- species and, suggested the transient formation of Co-BH_4 species which act as a precursor for Co-B specie. Further, we have investigated the catalytic activity of synthesized catalysts for NaBH_4 decomposition in aqueous alkaline medium. Fig. 6.7 (a) shows the comparative H_2 generation capability of three different catalysts i.e. the intermediate composites Ni/RGO and Co-B/RGO and final product Co-B@Ni/RGO at 30 °C. Experimental results exhibited the highest catalytic performance of Co-B@Ni/RGO nanocomposite for NaBH_4 decomposition. In Fig. 6.7 (a) Co-

B@Ni/RGO nanocomposite shows the fastest gaseous evolution (10 min) compare to intermediate nanocomposites that were shown 40 and 120 min, respectively. This high catalytic activity of Co-B@Ni/RGO nanocomposite can be explain on the basis of four major factors: (i) superficial attachment of boride phase on Ni/RGO support (ii) high conductivity of Ni/RGO, and (iii) hydrogen spillover on Ni/RGO. From our strategy, mostly Co-B NPs were on the Ni/RGO surface, were not within the bulk and completely exposed for catalytic reaction. Due to this they were easily contacted with BH₄⁻ species (therefore, adsorption/desorption of molecules was greatly enhanced). Moreover, high conductivity of Ni/RGO also facilitated the catalytic reaction; where, RGO played its own role and provided the support for Co-B NPs from prevention of agglomeration and facilitate the easy electron transfer [25]. Importantly, Ni works as co-catalyst and it easily spillover the H₂ to hydrogen radicals that interrupted inside of catalyst cavity and when these atomic H escapes out from the system at that location it created the vacancy and provide the channelling for entrance for BH₄⁻ species and increased the catalytic activity. According to recent report of Dai *et al.* also, interrupted hydrogen positively affected the NaBH₄ hydrolysis and able to reduce their induction period [36].

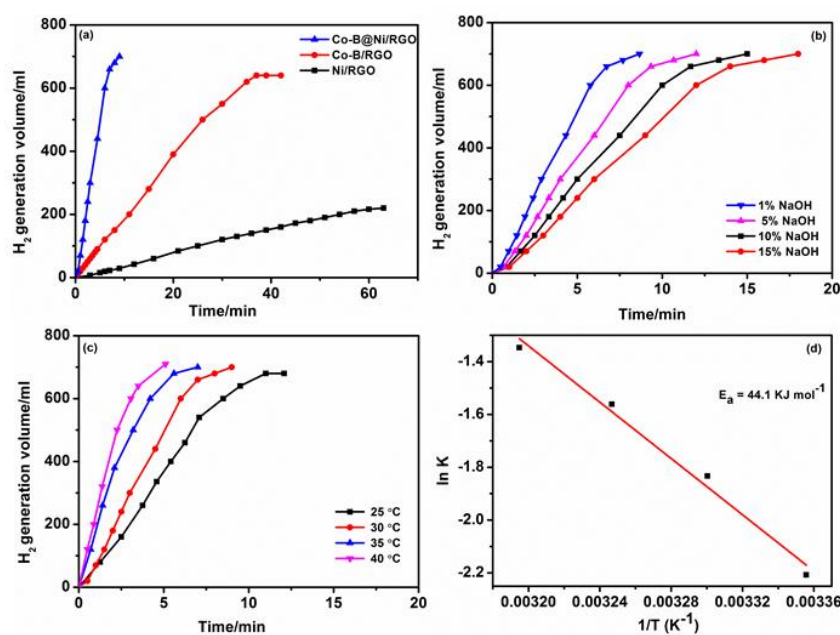


Figure 6.7 Catalytic hydrogen generation from the hydrolysis of mix solution of 1 wt. % of NaBH₄ + NaOH at 30 °C (a) comparative study of three catalysts (i) Ni/RGO, (ii) Co-B/RGO and (iii) Co-B@Ni/RGO, (b) effect of NaOH extent (1 wt. %, 5 wt. %, 10 wt %, 15 wt. %) for hydrolysis of NaBH₄ at 30 °C (c) temperature dependent comparative catalytic activity of Co-B@Ni/RGO nanocomposite at 25 °C, 30 °C, 35 °C and 40 °C. (d) Arrhenius plot ln k vs. the reciprocal temperature 1/T.

During the catalytic hydrolysis of NaBH₄ on metal centres; an intermediate species M-BH₄⁻ complex is formed which further dissociated to M-H species [36]; and whereby, negatively charged H reacts with H₂O and makes H₂ and OH⁻. This generated H₂ facilitated the formation of new active sites for hydrolysis of NaBH₄. Hydrolysis kinetics of NaBH₄ is not only dependent on catalyst performances, it affected by other factors also such as NaOH concentration and reaction temperature. Further, we have analyzed the effect of NaOH amount. It is obvious that a higher NaOH concentration would provide less hydrogen density. In order to understand the effect of NaOH concentrations on the hydrogen generation rate, a set of experiments were performed with the NaOH concentrations varied from 1 to 15 wt.% while the NaBH₄ concentration was held constant at 2 wt.%. Fig. 6.7 (b) shows the effects of NaOH concentration on the rate of reaction at 30 °C. A slightly delay of hydrogen evolution was observed for all the samples possibly due to the initial wetting of catalyst, mass-transport limitation and the pore diffusion resistance. Results indicated that when NaOH amount was highest (15 wt. %) the hydrolysis rate was slow. Whereas, at low amount of it the rate was higher. This gradual decrease of rate of reaction with increasing amount of NaOH might be due to the extra amount of NaOH produces more extant of Na⁺ that makes a quick NaBO₂ species during the hydrolysis process which hinders the active site of catalyst and retard the reaction. Moreover, high viscosity and stability of NaBH₄ at high pH imparted the rate adversely. In the next, we have analysed the effect of temperature on hydrolysis of NaBH₄. This is obvious temperature plays a vital role in many catalytic reactions and manifest the high rate of reaction due to the more number of collision of species. Kinetic studies at different temperatures were also carried out using the optimized conditions. Fig. 6.7 (c) represents the hydrogen generation kinetic curves at a solution temperature ranging from 25 to 40 °C. To minimize the effect of temperature changes due to the exothermic hydrolysis reaction, this set of experiments was carried out using 2 wt.% NaBH₄ + 1 wt. % NaOH solution. As expected, the initial hydrogen generation rate increases significantly with temperature. The influence of temperature is clearly shown by both the increasing slope values on the linear region of the plots and the decreasing induction period. For comparison of catalysts activities, the initial hydrogen generation rates k (mol min⁻¹ g⁻¹) were used to determine the activation energy by the following Arrhenius equation (6.5) [37]:

$$\ln k = \ln k_0 - (E_a/RT) \quad (6.5)$$

where, k_0 is the rate constant (mol min⁻¹ g⁻¹), R the gas constant (8.3143 kJmol⁻¹ K⁻¹), E_a the activation energy (kJ mol⁻¹), and T is the reaction temperature (K). An Arrhenius plot, in which $\ln k$ is plotted against the reciprocal of absolute temperature ($1/T$), was plotted in Fig. 6.7

(d). From the slope of straight line, the activation energy was calculated to be 43.1 kJ mol⁻¹. This value was comparably favourable with the reported results of Raney Ni-Co (52.5 kJ mol⁻¹) [38], activated carbon supported Co-B powder catalyst (57.8 kJ mol⁻¹) [20], and Ru- catalyst used by the Amendola *et al.* (47 kJ mol⁻¹) [39]. Finally, to examine the effects of catalyst loading on the hydrogen generation rate, 0.02, 0.04, and 0.08 g of the catalysts were employed. Fig. 6.8 (a) shows the hydrogen generation rate measured using the optimized catalyst and 1 wt.% NaBH₄ + 5 wt.% NaOH solution at 30 °C. As observed in Fig. 6.8 (a) with increasing amount of catalyst H₂ production rate was increased, implying that hydrogen generation rate can be determined by controlling the catalyst loading used in the reactor. Moreover, we have investigated the recyclability of catalyst after magnetic filtration and complete washing and drying of the catalyst (8 h, at 100 °C). Results shows that the successful hydrolysis of the 1 wt.% NaBH₄ + 5 wt.% NaOH solution at 30 °C in three successive cycles, with maintaining 95 % activity of its initial value indicated the robustness of catalyst for their reusability.

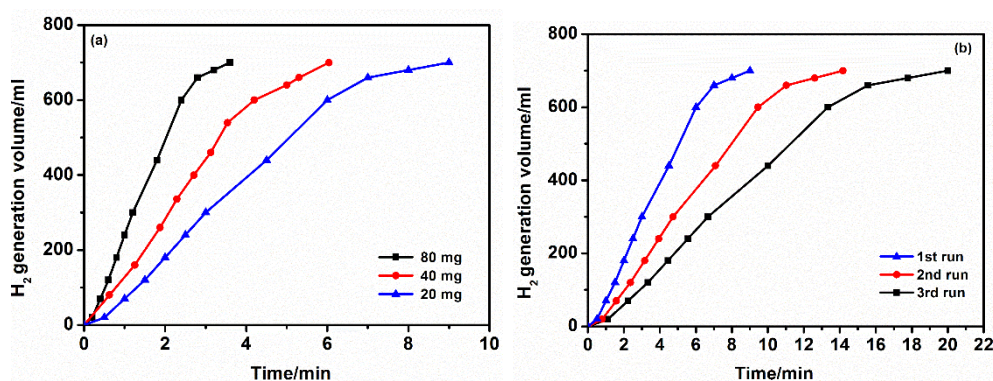


Figure 6.8 Catalytic hydrogen generation from the hydrolysis of mix solution of 1 wt. % of NaBH₄ + NaOH at 30 °C using Co-B@Ni/RGO (a) comparative study at three different weight (b) recyclability test of catalyst in three successive cycles.

Additionally, we have performed the systematic CV analysis of synthesised CoB/RGO, Ni/RGO and CoB@Ni/RGO nanocomposites in order to investigate detail catalytic mechanism and their applicability in the field of charge storage (energy storage) also. The CVs of CoB/RGO immobilized at a glassy carbon electrode, in 1 mol dm⁻³ KOH solution are shown in Fig. 6.9 (a). Under the conditions used, two pairs of peaks are observed with $E_{pc1} \approx 0.417$ V, $E_{pc2} \approx 0.026$ V, $E_{pa1} \approx 0.480$ V and $E_{pa2} \approx 0.117$ V vs. Ag/AgCl. These two pairs of peaks (1-1', 2-2') are attributed to Co^{II}/Co^{III} and Co^{III}/Co^{IV} redox couples, respectively [40]. During the first consecutive cycles in KOH 1M some adsorption of oxygen-containing species (H₂O, OH⁻) may occur leading to the presence of different cobalt species (Co(OH)₂, CoOOH, CoO₂) [41]. In the

range of scan rates (ν) between 0.010 and 0.500 V s⁻¹, both cathodic (E_{pc2}) and anodic (E_{pa2}) peak potentials varied between 0.013 and 0.043 V, which is characteristic of a quasi-reversible process where the rate of the heterogeneous electron transfer is slow compared to the time scale of the experiment. Fig. 6.9 (b) depicts the plot of $\log i_p$ vs. $\log \nu$ for CoB/RGO. Since it was difficult to establish a proper baseline for the first pair of peaks (1-1') the values corresponding to these were not inserted.

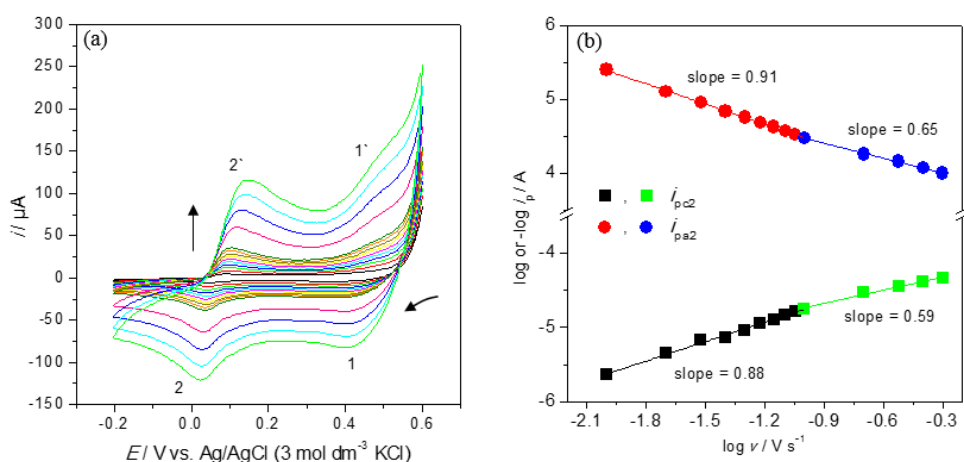


Figure 6.9 Cyclic voltammograms of Co/RGO immobilized at a GC electrode in 1 mol dm⁻³ KOH solution at different scan rates from 0.010 to 0.500 V s⁻¹ (a); Plots of $\log i_{pc2}$ and i_{pa2} vs. $\log \nu$ (b).

These results show that for scan rates between 0.010 and 0.100 V s⁻¹ both cathodic (i_{pc2}) and anodic (i_{pa2}) peak currents were directly proportional to ν (with $r = 0.994$ and 0.999 , respectively), which indicates a surface-confined redox process. However, for scan rates higher than 0.100 V s⁻¹ both i_{pc2} and i_{pa2} vary linearly with the square root of scan rate (with $r = 0.998$ and 0.997 , respectively) which indicates a change in the diffusion regime from a surface-confined to a diffusion-type behaviour. Thus, diffusion and/or migration of charge compensating counter ions (i.e. hydrated alkali ions and hydroxide or proton species) may have an effect on the rate-determining step of the overall electrochemical process [41].

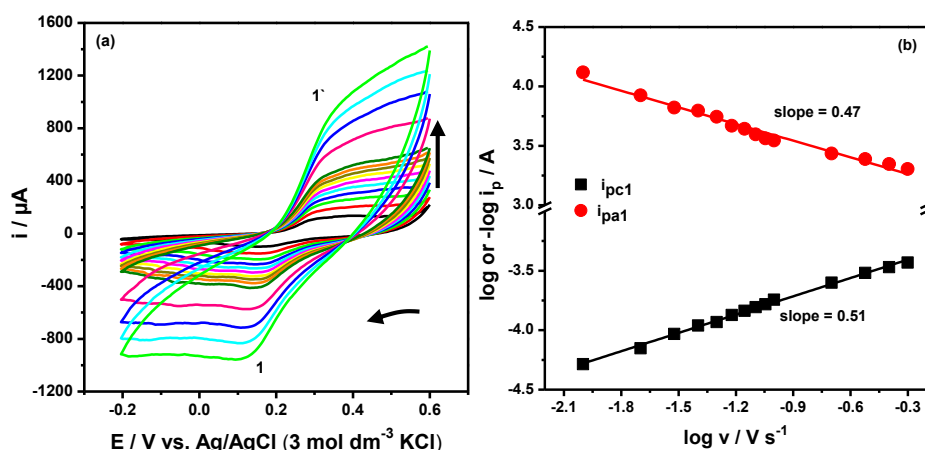


Figure 6.10 Cyclic voltammograms of CoB@Ni/RGO immobilized at a GC electrode in 1 mol dm⁻³ KOH solution at different scan rates from 0.010 to 0.500 V s⁻¹ (a); Plots of log i_{pc1} and i_{pa1} vs. log v (b).

The CVs of CoB@Ni/RGO immobilized at a GC electrode, in 1 mol dm⁻³ KOH solution are depicted in Fig. 6.10 (a). Under the same conditions as above, only one pair of peaks is observed with $E_{pc1} \approx 0.155$ V and $E_{pa1} \approx 0.321$ V vs. Ag/AgCl. Most likely, this peak has the contribution of both cobalt and nickel redox processes but as the latter is more intense, the cobalt redox process is imperceptible. In the range of scan rates between 0.010 and 0.500 V s⁻¹, both the anodic and cathodic peak potentials shifted close to 0.038 V, which is characteristic of a quasi-reversible process. Fig. 6.10 (b) depicts the plot of log i_{p1} vs. log v for CoB@Ni/RGO; these results show that both cathodic and anodic peak currents vary linearly with the square root of the scan rate (with $r = 0.996$ and 0.989 , respectively), indicating a diffusion-controlled redox process. For a better understanding of the differences between the three prepared electrodes it is shown in Fig. 6.11 the cyclic voltammograms of CoB@Ni/RGO, CoB/RGO and Ni/RGO modified GC electrodes in 1 mol dm⁻³ KOH solution at 0.10 V s⁻¹. The results show that CoB@Ni/RGO/GCE presents higher peak currents although the peak-to-peak separation (ΔE_p) is larger than Ni/RGO/GCE. Since, the specific capacitance is usually directly proportional to the area of the CV curves covered, CoB@Ni/RGO has the highest specific capacitance among the three materials used [42]. Electrochemical impedance spectroscopy was further used in order to get more insights into the prepared modified electrodes. From the cyclic voltammetry experiments and the accessible potential window, it was decided to carry out electrochemical impedance experiments in 1 mol dm⁻³ KOH solution at values of applied potential of 0, 0.1, 0.2, 0.3, 0.4 and 0.5 V vs Ag/AgCl; these values were chosen to cover most of the potential range used in CV experiments.

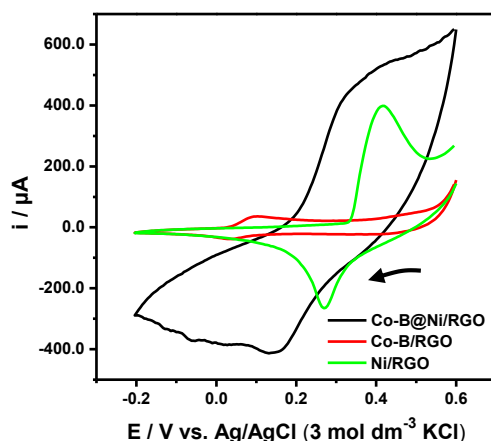


Figure 6.11 Cyclic voltammograms of CoB@Ni/RGO, CoB/RGO and Ni/RGO modified GC electrodes in 1 mol dm^{-3} KOH solution at 0.10 Vs^{-1} .

Fig. 6.12 depicts the complex plane impedance spectra of CoB@Ni/RGO modified GC electrodes in 1 mol dm^{-3} KOH solution at different applied potentials. The results show that the application of different potentials leads to considerable changes in the spectra: from 0 to 0.2 V the spectra show one depressed semicircle in the high frequency region and a linear part in the low frequency region. It is well accepted that the semicircle corresponds to kinetic control of charge-transfer process and the linear part represents the Warburg impedance, which is related to diffusion control [43].

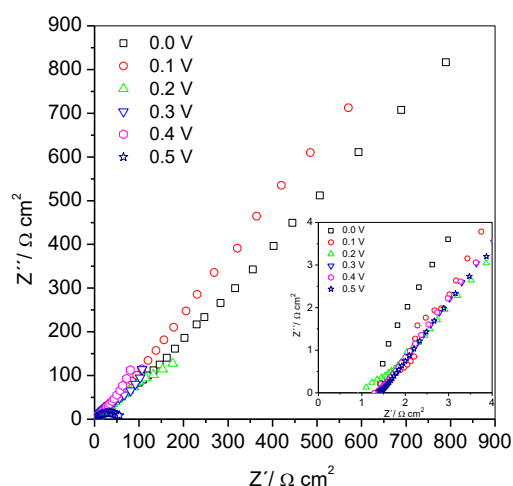


Figure 6.12 Complex plane impedance spectra of CoB@Ni/RGO modified GC electrodes in 1 mol dm^{-3} KOH solution at different applied potentials.

For 0.3 and 0.4 V only a linear part is observed which suggests that the semicircle region is very small and the spectrum is dominated by the Warburg impedance, and thence diffusion control, over nearly the whole range of frequencies examined. For 0.5 V the spectrum just presents the semicircle. Still, for all spectra, the cell resistance (R/Ω) i.e., the intercept of the real axis at high frequency is $1.4 \Omega \text{ cm}^2$ with exception of 0.2 V ($1.2 \Omega \text{ cm}^2$). Fig. 6.13 (a) depicts the complex plane impedance spectra of CoB@Ni/RGO, CoB/RGO and Ni/RGO modified GC electrodes in 1 mol dm^{-3} KOH solution at 0.5 V. The Ni/RGO presents the highest diameter of the semicircle which indicates higher transfer resistance, R_{ct} , ($\approx 200 \Omega \text{ cm}^2$), while the CoB/RGO presents the lowest ($\approx 40 \Omega \text{ cm}^2$). Compared to Ni/RGO, the R_{ct} of CoB@Ni/RGO was decreased greatly ($\approx 67\%$), suggesting that the introduction of CoB improved the electron conductivity of the new material. Also, analysis of the spectra in the high frequency region shows that the cell resistance for the three materials is similar. When a 0.4 V is applied to the system the spectra change, as it can be observed in Fig. 6.13 (b). In the low frequency range instead of the semicircle is now observed a straight line suggesting that that the spectrum is dominated by the Warburg impedance. In fact, if the high frequency range is expanded (see inset) it reveals that only Ni/RGO presents a semicircle. The low R_{Ω} and R_{ct} values suggest that CoB@Ni/RGO presents good electrochemical capacitive properties and that it should be advantageous for electrochemical applications.

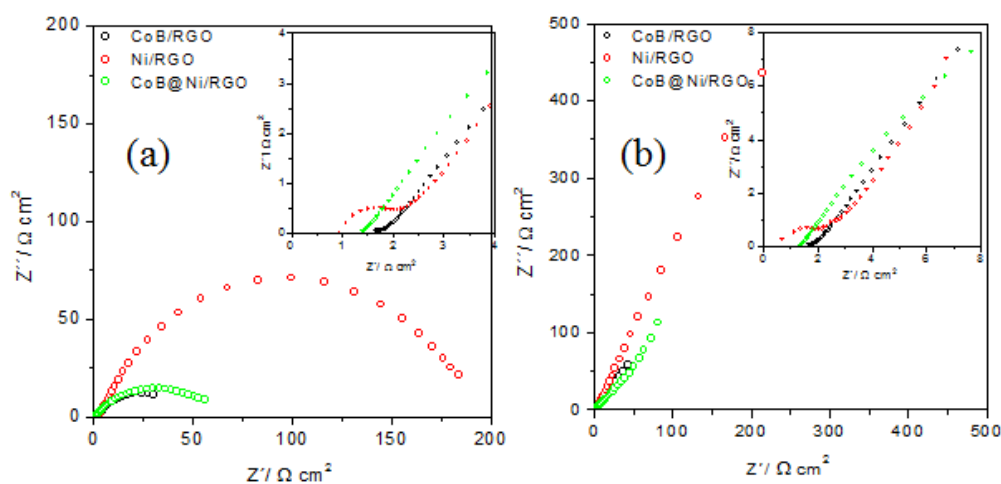


Figure 6.13 Complex plane impedance spectra of CoB@Ni/RGO, CoB/RGO and Ni/RGO modified GC electrodes in 1 mol dm^{-3} KOH solution at 0.5 V (a) and 0.4 V (b).

6.4 Conclusions

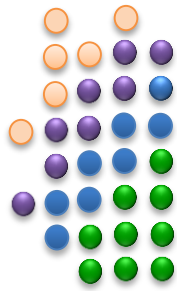
In the present study, we successfully synthesized the Co-B@Ni/RGO nanocomposite by a facile method. TEM image clearly displays the superficial attachment of the Co-B NPs on Ni/RGO entity, also defects inside of graphene layers due the produced radical hydrogen. We provide the mechanistic explanation regarding of H atoms interruption in catalyst cavity and their spillover and migration possibility. The synthesized Co-B@Ni/RGO nanocomposite exhibited their enhanced catalytic activity toward hydrolysis of alkaline mix solution of NaBH₄. CV and impedance plot clearly shows the high charge storage capability and charge conductivity in Co-B@Ni/RGO nanocomposite which may provide the future commercialization of catalyst for complete energy application viz. H₂ production and charge storage together.

6.5 References

- [1] Y. Lin, C. Cui, C. Yen, C. M. Wai. *Langmuir*, 21 (2005) pp. 11474-11479.
- [2] R. Krishna, E. Titus, S. Chandra, N. K. Bardhan, R. Krishna, D. Bahadur, J. Gracio. *J Nanosci Nanotechnol*, 12 (2012) pp. 6631-6638.
- [3] L. Tamasauskaite-Tamasiunaite, A. Radomskis, K. Antanaviciute, J. Jablonskiene, A. Balciunaite, A. Zieliene. *Int J Hydrogen Energy*, 39 (2014) pp. 4282-4290.
- [4] D. Stanicki, L. V. Elst, R. N. Muller, S. Laurent. *Current Opinion in Chemical Engineering*, 8 (2015) pp. 7-14.
- [5] L. Mazzola. *Nature Biotechnology* 21 (2003) pp. 1137- 1143.
- [6] A. Zuttel, A. Borgschulte, L. Schlapbach. Wiley-VCH Verlag GmbH & Co. KGaA, Weinheim (2008).
- [7] S. C. Amendola, P. Onnerud, M.T. Kelly, P. J. Petillo, S.L. Sharp-Goldman, M. Binder. *J Power Source*, 85 (2000), pp. 186-189.
- [8] J. H. Kim, H. Lee, S. C. Han, H. S. Kim, M. S. Song, J. Y. Lee. *Int J Hydrogen Energy*, 29 (2004), pp. 263-267.
- [9] U. B. Demirci, O. Akdim, J. Andrieux, J. Hannauer, R. Chamoun and P. Miele. *Fuel Cells*, (10) 2010 pp. 335-350.
- [10] R. Rajasree, Q. Augusto, Novais, C.M. Rangel. *Int J Hydrogen Energy*, 36 (2011), pp. 9772-9790.

- [11] S. Saha, V. Basak, A. Dasgupta, S. Ganguly, D. Banerjee, K. Kargupta. *Int J Hydrogen Energy*, 39 (2014), pp. 11566-11577.
- [12] P. Krishnan, T.H. Yang, W.Y. Lee, C.S. Kim. *J. Power Sources* 143 (2005), 17-23.
- [13] A. D. Chowdhury, N. Agnihotri, A. De. *Chem Eng J*, 265 (2015) pp. 531-537.
- [14] J. Mao, D. H. Gregory. *Energies*, 8 (2015) pp. 430-453.
- [15] P. Brack, S. E. Dann, K. G. U. Wijayantha. *Energy Sciences & Engg*, 3 (2015) pp. 174-188.
- [16] H. I. Schlesinger, H. C. Brown, A. E. Finholt, J. R. Gilbreath, H. R. Hoekstra, E. K. Hyde. *J Am Chem Soc*, 75 (1953) pp. 215-219.
- [17] C. Wu, F. Wu, Y. Bai, B. Yi, H. Zhang. *Mater Lett*, 59 (2005) pp. 1748-1751.
- [18] J. Lee, K. Y. Kong, C. R. Jung, E. Cho, S. P. Yoon, J. Han, T. G. Lee, S. W. Nam. *Catal Today*, 120 (2007) pp. 305-310.
- [19] Z. Wu, S. Ge. *Catal Comm*, 13 (2011) pp. 40-43.
- [20] J. Z. Zhao, H. Ma, J. Chen. *Int J Hydrogen Energy*, 32 (2007) pp. 4711-4716.
- [21] C. Wu, Y. Bai, D.X. Liu, F. Wu, M.L. Pang, B.L. Yi. *Catal Today*, 170 (2011) pp. 33-39.
- [22] O. Akdim, U.B. Demirci, P. Miele. *Int J Hydrogen Energy*, 34 (2009) pp. 4780-4787.
- [23] L. Wang, D. Wang, X. Hu, J. Zhu, X. Liang. *Electrochim Acta*, 76 (2012) pp. 282-287.
- [24] F. Zhang, C. Hou, Q. Zhang, H. Wang, Y. Li. *Mater Chem Phys*, 135 (2012) pp. 826-831.
- [25] R. Krishna, D. M. Fernandes, C. Dias, J. Ventura, E. Venkata Ramana, C. Freire, E. Titus. *Int J Hydrogen Energy*, 40 (2015) pp. 4996-5005.
- [26] S. Saha, S. Ganguly, D. Banerjee, K. Kargupta. *Int J Hydrogen Energy*, 40 (2015), pp. 1760-1773.
- [27] J.W. Park, E.H. Chae, S.H. Kim, J.H. Lee, J.W. Kim, S.M. Yoon, J.Y. Choi. *Mater Chem Phys*, 97 (2006), pp. 371-378.
- [28] R. Krishna, C. Dias, J. Ventura, E. Titus. *Materials Today: Proceedings*, 2 (2015) pp. 407-413.
- [29] R. Krishna, E. Titus, O. Okhay, J. C. Gil, J. Ventura, E. V. Ramana, J. J. A. Gracio. *Int J Electrochem Sci*, 9 (2014) pp. 4054 - 4069.
- [30] X. Mei, J. Ouyang. *Carbon*, 49 (2011) 5389-5397.
- [31] B. J. Li, H. Q. Cao, J. F. Yin, Y. A. Wu, J. H. Warner. *J Mater Chem*, 22 (2012) pp. 1876.

- [32] C.M. Zhao, X. Wang, S.M. Wang, Y.Y. Wang, Y.X. Zhao, W.T. Zheng. *International Journal of Hydrogen Energy*, 37 (2012), pp. 11846–11852.
- [33] Z. Wang, Y. Hu, W. Yang, M. Zhou, X. Hu. *Sensors*, 12 (2012) pp. 4860-4869.
- [34] R. Krishna, E. Titus, L. C. Costa, J. C. J. M. D. S. Menezes, M. R. P. Correia, S. Pinto, J. Ventura, J. P. Araújo, J. A. S. Cavaleiro, J. J. A. Gracio. *J Mater Chem*, 22 (2012) 10457-10459.
- [35] J.M. Lu, D.B. Dreisinger, W.C. Cooper. *Hydrometallurgy*, 45 (1997), pp. 305-322.
- [36] H. B. Dai, Y. Liang, P. Wang. *Catalysis Today*, 170 (2011) pp. 27-32.
- [37] S. Jeong, R. Kim, E. Cho, H. J. Kim, S. W. Nam, I. H. Oh, S. A. Hong, S. Kim. *J Power Sources*, 144 (2005), pp. 129-134
- [38] S. C. Amendola, S. L. Sharp-Goldman, M. S. Janjua, N. C. Spencer, M. T. Kelly, P. J. Petillo, M. Binder. *Int. J. Hydrogen Energy*, 25 (2000) pp. 969-975.
- [39] B. H. Liu, Z. P. Li, S. Suda. *J Alloys Compd*, 415 (2006) pp. 288-293.
- [40] T. Wang, Y. Yu, H. Tian, J. Hu. *Electroanalysis*, 26 (2014) pp. 2693-2700.
- [41] I. G. Casella. *J Electroanalytical Chem*, 520 (2002) pp. 119-125.
- [42] J. Xu, S. Gai, F. He, N. Niu, P. Gao, Y. Chen, P. Yang. *Dalton Trans*, 43 (2014) pp. 11667-11675.
- [43] D. M. Fernandes, M. E. Ghica, A. M. V. Cavaleiro, C. M. A. Brett. *Electrochimica Acta*, 56 (2011) pp. 7940-7945.



CHAPTER 7

GRAPHENE NANOCOMPOSITE FOR CATALYSIS REACTION:

Synthesis, characterization and results



Chapter 7

<u>Graphene nanocomposite for catalysis reaction: Synthesis, characterization and results</u>	143
7.1 Introduction	145
7.2 Cu@Ni/RGO nanocomposite	146
7.2.1 Experimental	146
7.2.2 Characterization	147
7.2.3 Catalytic reduction of 4-NP	147
7.2.4 Results and discussion	147
7.3 Ag@Co/RGO nanocomposite and its high catalytic activity towards hydrogenation of 4-nitrophenol to 4-aminophenol	156
7.3.1 Synthesis of Ag@Co/RGO catalyst	156
7.3.2 Catalytic reduction of 4-NP	156
7.3.3 Results and discussion	157
7.4 Hydrogenation of 4-nitrophenol to 4-aminophenol using Pd@NSG	163
7.5 Conclusions	166
7.6 References	166

GRAPHENE NANOCOMPOSITE FOR CATALYSIS REACTION:

Synthesis, characterization and results

7.1 Introduction

Noble metals (Pd, Ag, Au and Pt) nanoparticles based reduced graphene oxide (RGO) composites have recently gathered a lot of interest due to their high catalytic activity and chemical inertness [1-7]. However, high costs and limited number of noble metal resources urge a restricted consumption of expensive materials with retention of catalytic property for progressive research and real field of interest. A combination of other less expensive materials may be a better solution to deal with this issue. First row transition metal elements, especially Fe, Co and Ni are best suited propositions owing to their low cost, wide availability and co-catalytic activity [8-10]. A very recent work shows the methanol electro-oxidation using $\text{Fe}_3\text{O}_4@Au/RGO$ nanocomposite with high performance [11]. More interestingly, Pozun et al. systematically investigated the catalytic activity of the bi-metallic NPs catalyst for hydrogenation reaction and emphasized the role of electronic density of states (DOS) of surface species [12]. They have developed the idea based on Brønsted–Evans–Polanyi (BEP) relation for surface reactions/adsorption energies; emphasized the role of electronic structure in metals, specifically the d-band center which was first modeled by Newns. Moreover, for heterogeneous catalysis reactions, integration of metal NPs with various kind of supports is also fast growing area of research due to enhance kinetics and selectivity [13].

4-nitrophenol (4-NP) is a common organic pollutant and effluent in many drugs and dyes industries and for their reduction it has been reported that catalyst is indeed needful for the accomplishment of reaction for their conversion to 4-aminophenol (4-AP) [14]. For the reduction of 4-NP it has been reported that catalyst with hydrogen spillover capability is more pronounced [15]. For instance, very recently Krishna *et al.* reported the successful reduction of 4-NP using Ag@Co/RGO nanocomposite in a very short time (90 s) [16]. Sun *et al.* demonstrated the reduction of 4-NP using Pd/RGO nanocomposite within 120 s [17]. Similarly, Barman *et al.* presented the high catalytic activity of Pd/RGO and Pt/RGO nanocomposites towards reduction of 4-NP [18]. However, rate of reduction of 4-NP with non-noble metals catalyst was slow. For instance, Chen *et al.* demonstrated the reduction of 4-NP with Ni/RGO in 180 min [19]. The slow reduction process on Ni/RGO can be anticipated by the surface oxidation of metallic species during the reaction and further lowering the electronic conductivity.

Considering the high cost of noble metals and slow reduction process of Ni/RGO, it is crucial to develop new materials for this catalysis reaction with retention of catalytic activity and lower price. In this aspect, it is highly desirable for the higher conductive material along with spillover capability. Here we demonstrate the catalytic reduction of 4-NP to 4-AP based on transition metal doped graphene nanocomposites. We have synthesized the three different nanocatalyst systems on RGO sheets as described below and briefly introduce all of them with their catalytic activity towards the 4-NP reduction:

- (i) Cu@Ni/RGO nanocomposite
- (ii) Ag@Co/RGO nanocomposite
- (iii) Pd@Ni_xB-SiO₂/RGO nanocomposite

7.2 Cu@Ni/RGO nanocomposite

7.2.1 Experimental

In this work first, graphene oxide (GO) was synthesized by the modified Hummers method as previous reported [16]. Then Ni/RGO nanocomposite was synthesized as follows: 100 mL of aqueous GO dispersion (1 mg/mL) was placed in 4-neck round bottom (RB) flask and mechanically stirred. Afterward, 600 mg of NiCl₂.6H₂O was mixed and the temperature of reaction was gradually increased up to 85 °C. Further, under an inert atmosphere of high purity Ar gas, 18 mL of hydrazine hydrate was slowly poured inside the reaction mixture and was continuously stirred for 25 min. Then, 450 mg of NaBH₄ was very slowly added while

maintaining of stirring and inert atmosphere. Finally, 25 mL aqueous solution of NaOH (1 M) was slowly added and stirred for further 150 min. After completion of reaction the product was filtered and washed with ethanol and DD water to remove the impurities. Finally, vacuum dried at 100 °C for 3 h and referred as Ni/RGO. Finally, Cu@Ni/RGO nanocomposite was synthesized on Ni/RGO as follows: first, Ni/RGO dispersion was prepared in DD water (50 ml, 2 mg/mL) by ultrasonication (15 min) then, 600 mg of CuSO₄.5H₂O was added in aqueous dispersion and mixed for 20 min with stirring. Afterward, 1M NaOH (10 mL, aq.) solution was added in Ni/RGO dispersion to increase the pH of mixture and stirred for 10 min at RT. After stirring the precipitate was filtered and re-dispersed in 25 mL DD water by ultrasonication (15 min). Finally, 10 mL N₂H₄.H₂O with NaBH₄ (5 mg) was slowly added under inert atmosphere of N₂ and stirred for 30 min. After completion of reaction the product was filtered, washed with DD water and dried at RT.

7.2.2 Characterization

The phase purity, crystallinity and structure of GO, Ni/RGO and Cu@Ni/RGO were characterized by X-ray diffraction (XRD, Cu K_α radiation; $\lambda = 0.15414$ nm) with scan rate of 0.02° min⁻¹, 2 θ (10-80°). Raman spectra were obtained at RT in back scattering configuration with a Lab Ram HR using 532 nm laser line. Scanning electron microscopy (SEM) was performed by using SU-70 microscope. A conventional high-resolution (HR) TEM (LaB₆ TEM) was performed to analyse the crystallinity and quality of samples. UV-vis spectra were collected by Shimadzu UV-2501PC (UV-vis) spectrophotometer in the absorbance mode.

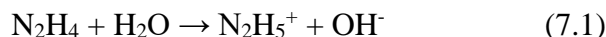
7.2.3 Catalytic reduction of 4-NP

The catalytic test of Cu@Ni/RGO nanocomposite was performed as follows: 1mL of each reactant solutions of 4-NP (1.0 mM) and NaBH₄ (0.35 M) were transferred to a quartz cuvette and mixed by mild sonication. Afterward, 5 mg of the catalyst was added in order to start the reaction and mixed. The intensity of the absorption peak at $\lambda = 400$ nm was used to monitor the process of the conversion of 4-NP to 4-AP.

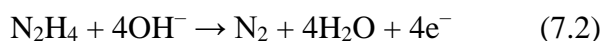
7.2.4 Results and discussion

During the reduction process, GO and Ni²⁺ ions were simultaneously reduced to RGO and Ni NPs in presence of N₂H₄.H₂O and NaBH₄ reducing agents which provides the reducing species e⁻ and H₂. In the beginning, due to the basic nature of N₂H₄.H₂O it was easily protonated

in acidic medium owing to its high pK_a value (8.1) and made the $N_2H_5^+$ species as equation 7.1 [24]:



However, at high pH in basic medium (due to $NaBH_4$ and $NaOH$) it was decomposed and evolved the inert N_2 gas and released the electrons for reduction as equation 7.2:



Moreover, during the process produced e^- reduces the Ni^{2+} ($E^0 = -0.25$ V), due to the high redox potential of N_2H_4 ($E^0 = -1.16$ V) as equation 7.3 [25]:



In addition, $NaBH_4$ also favors the reduction of Ni^{2+} and provide the reducing environment by the evolution of reducing species H_2 as equation 7.4 [26]:

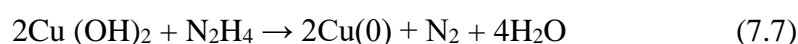


During the process, GO was also efficiently reduced to RGO due the presence of two reducing species, e^- and H_2 , as shown in equation 7.5:

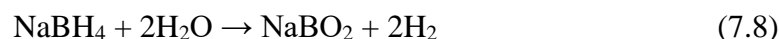


Fig.7.1 (a) displays the XRD patterns of GO and Ni/RGO. GO exhibits a sharp peak at around 10.9° corresponding to the (001) basal plane with d spacing of ($d_{001} = 0.83$ nm) [16]. This value was higher than the interlayer spacing of graphite flakes (d-spacing= 0.334 nm) due to the presence of oxygenated functional groups and intercalated water molecules. After the reduction and intercalation of Ni NPs with graphene this peak was completely diminished and new peak was observed at around 23.2° suggests that the well exfoliation of the GO oxygen containing functionalities during the reduction process. Moreover, in Ni/RGO three additional peaks were also observed at 44.5° , 51.8° and 76.76° and attributed the crystallographic diffraction planes (111), (2 0 0) and (2 2 0) of face-centred cubic (fcc) Ni (JCPDS card No. 04-0850) [27], and the highest intense diffraction peak at around 44.5° suggests that the well crystallinity of Ni-NPs. The mean crystallite size of Ni NPs in Ni/RGO nanocomposite was also calculated using Debye-Scherrer formula $d = 0.9\lambda/\beta \cos \theta_B$, where d is the average crystalline size, λ is the X-ray wavelength ($Cu K_\alpha = 1.54$ Å) used, β the angular line width of half maximum intensity and

θ_B is the angle between planes (Bragg's angle), estimated to be around 12.7 nm indicated the formation of small crystals of Ni by wet aqueous reduction method compare previously reported hydrothermal method [28]. Further, reduction of Cu^{2+} to Cu (0) and formation of Cu NPs was also confirmed by the XRD. In basic condition, initially Cu salt make the Cu (OH)₂ and precipitated out on Ni/RGO and after that in reducing condition it was easily reduced to Cu (0) as shown in equation 7.6 and 7.7 [29]:



Moreover, during the reduction of Cu^{2+} ions to Cu (0) by N_2H_4 and NaBH_4 , Ni NPs enhances the reduction process. Ni is a prominent catalyst for NaBH_4 hydrolysis reaction for fuel cell application; easily decomposes the BH_4^- species in aqueous medium in to molecular hydrogen (equation: 7.8) and concomitantly, it spillover the produced hydrogen and converted it in to radical species (equation: 7.9) [30].



XRD of Cu@Ni/RGO shows that presence of all three diffraction peaks related to various crystallographic planes of fcc crystal structure. However, all peaks were slightly down shifted and major diffraction peak (111) was located at 43.7° which clearly indicated the formation of Cu NPs [31].

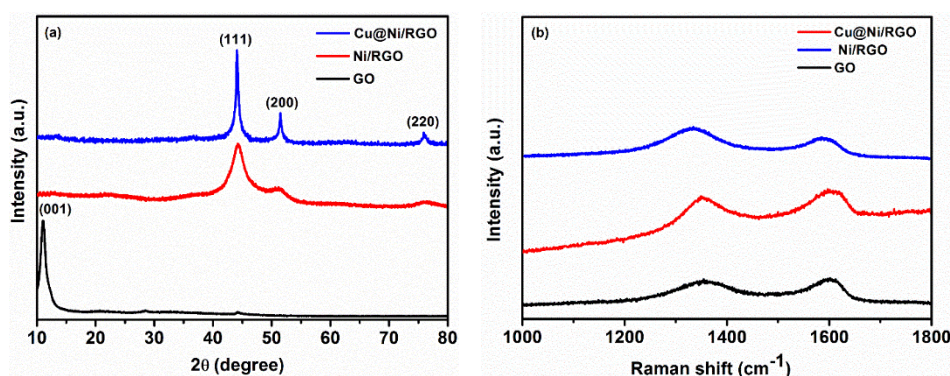


Figure 7.1 (a) XRD spectra and (b) Raman spectra of GO, Ni/RGO and Cu@Ni/RGO nanocomposite.

Further, Raman spectroscopy was used to investigate the change in carbon structure. This technique is very specific for carbonaceous materials and able to directly reflect distinction between ordered and disordered crystal structures. Fig. 7.1 (b) shows the Raman spectrum of GO, Ni/RGO and Cu@Ni/RGO nanocomposite in the range of 1000-1800 cm^{-1} . The Raman spectrum of GO displayed two characteristic D and G bands at 1352 and 1608 cm^{-1} with an I_D/I_G ratio of 0.93. This was already reported that G band is an intrinsic feature of graphene and closely related to the vibrations in all sp^2 carbon materials [32]. D band becomes prominent when defects are introduced in graphene. In GO it is activated due to the reduction in size of the in-plane sp^2 domains due to the attachment of various functionalities in edge and basal plane sites [33]. While, in Ni/RGO and Cu@Ni/RGO nanocomposite spectra these two prominent bands D and G were located at 1347 cm^{-1} and 1597 cm^{-1} and 1344 cm^{-1} and 1595 cm^{-1} with increased I_D/I_G ratio of 1.02 and 1.03, respectively, which clearly indicates the corresponding changes inside of carbon system.

Next, we have carried out systematic microscopic investigation of product Ni/RGO and Cu@Ni/RGO nanocomposite. Fig. 7.2 (a) and (b) shows the SEM images of Ni/RGO in lower and higher magnifications. Both the images depicts the well intercalation of Ni NPs with graphitic flakes and in higher magnification image clearly displays the covering of Ni NPs by single or few layers of graphene sheets. To confirm the presence of Ni we have also carried out the elemental mapping as shown in Fig. 7.2 (c), which shows the formation of small Ni NPs in spherical shape without any specific agglomeration [34]. Fig. 7.2 (d) and (e) shows the lower and higher magnification SEM images of Cu@Ni/RGO sample. Here, we clearly visualized the Cu NPs were homogeneously distributed and covered the Ni/RGO layers. In higher magnification image shows all particles were in uniform size and less than 1 μm and in spherical shape. To confirm the presence of Cu we have also carried out the elemental mapping of Cu@Ni/RGO nanocomposite as shown in Fig 7.2 (f). In which all Cu NPs were in small size and densely distributed as compare to Ni indicated the superficial attachment of Cu on Ni/RGO layers.

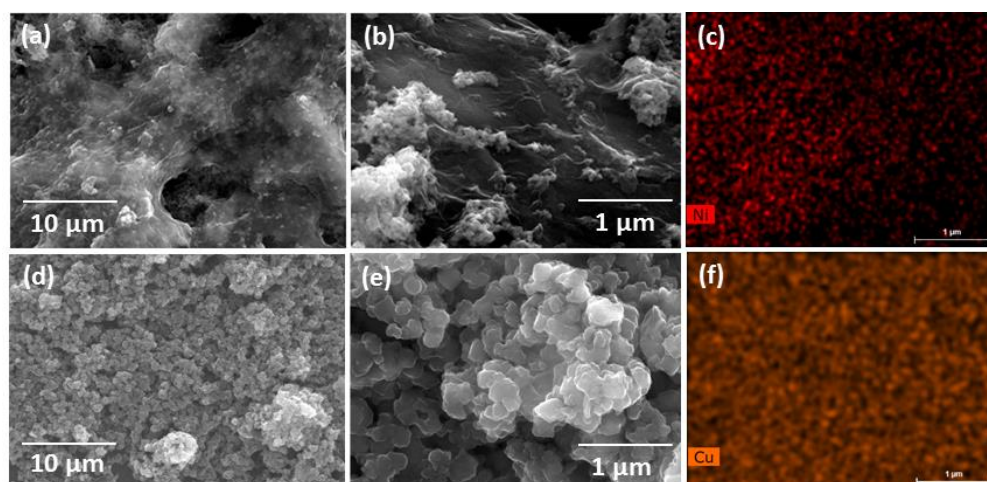


Figure 7.2 (a) and (b) SEM images of Ni/RGO in lower and higher magnifications, respectively; and (c) elemental mapping of Ni. (d) and (e) SEM images of Cu@Ni/RGO in lower and higher magnifications, respectively; and (f) elemental mapping of Cu.

Moreover, to confirm the presence of Ni and Cu elements we have also carried out the EDX analysis. Fig. 7.3 displays the EDX spectrum of Cu@Ni/RGO nanocomposite and results show the presence of all elements: Cu, Ni, O and C with the exception of the light weight element H [16].

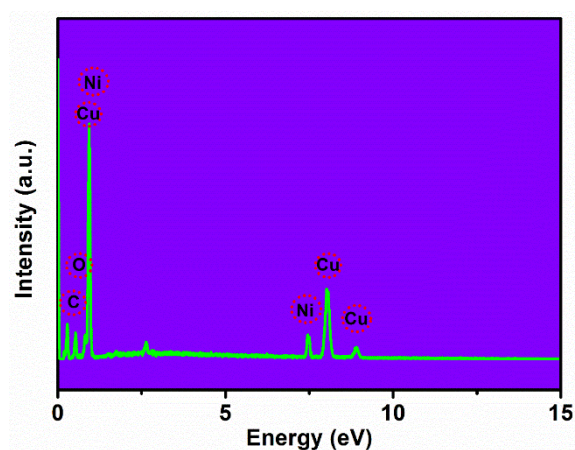


Figure 7.3 EDX spectra of Cu@Ni/RGO nanocomposite.

TEM analysis was also performed to confirm the shape, morphology and internal structure of Cu@Ni/RGO nanocomposite for detailed investigation of reduction reactions. Fig. 7.4 (a) and (b) show the TEM images of Ni/RGO nanocomposite at lower and higher magnification, respectively. Fig. 7.4 (a) clearly displays the homogeneous distribution of Ni

NPs on the graphene sheets where all particles were in spherical shape without any specific kind of agglomeration and mostly Ni NPs were attached to the graphene sheet. It was due to the electrostatic attraction of positively charged Ni^{2+} ions to negatively charged GO layers (zeta potential -37 mV at pH 7.0). The oxygen containing groups of GO acts as a surface protection agents and capping agents for Ni NPs which avoids the agglomeration of Ni NPs and prevents the nucleation and growth. TEM image shows the average particle size of Ni NPs that were estimated to be ~ 8.8 nm. Fig. 7.4 (b) shows the High-resolution TEM (HRTEM) image of Ni/RGO in which magnified region clearly shows the lattice spacing of Ni (111) with a d spacing of 0.20 nm (inset image).

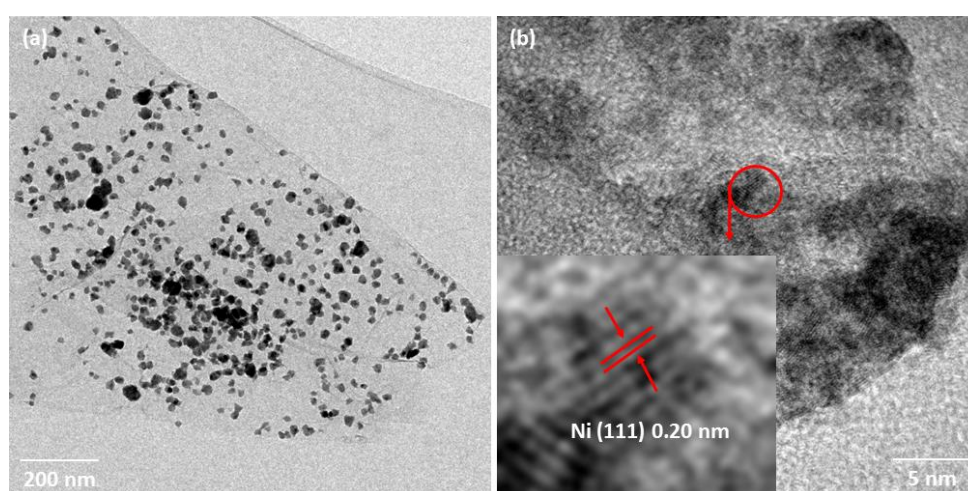


Figure 7.4 (a) and (b) TEM images of Ni/RGO in lower and higher magnifications, respectively, and corresponding HRTEM image showing the lattice spacing of Ni (111) (inset image of Fig.4b) .

Fig. 7.5 (a) and (b) shows the TEM images of Cu@Ni/RGO nanocomposite in lower and higher magnifications, respectively. Both images shows the change in graphene structure (more flappy) compared to Ni/RGO image (Fig. 7.4 (a), above). This was probably due to the additional reduction of RGO sheet by $\text{N}_2\text{H}_4 \cdot \text{H}_2\text{O}$ and NaBH_4 and subsequent, spillover the produced H_2 , which led to further exfoliation of remaining oxygen functionalities at the time of the reduction of Cu^{2+} ions to Cu NPs. In both images mostly Cu NPs were encapsulated on Ni NPs and morphology reveals the spherical shape of them. Higher magnification image shows the average particle size of Cu NPs was ~ 25 nm. This was obvious due to the superficial attachment of Cu NPs on Ni NPs. Fig. 7.5 (c) shows the HRTEM image of Cu@Ni/RGO nanocomposite in which three magnified region clearly shows the detailed internal structure of nanocomposite. Point A depicts the layer graphitic structure and corresponding inset image

reveals the lattice spacing of C (002) with a d spacing of 0.37 nm. Point B indicated the formation of highly crystalline Cu NPs and corresponding inset image reveals the inter-planar spacing of Cu (111) with a d spacing of 0.23 nm. Moreover, we have also evaluated the formation of some extent of Cu-Ni alloy during the synthesis at the boundary region of Ni NPs and Cu NPs. This was due to the difference in redox potential of Cu and Ni (+ 0.34 V, Cu || - 0.25 V, Ni vs. SHE) and at the time of mixing of Cu^{2+} ions with Ni/RGO nanocomposite some part of Ni NPs were etched by the Cu^{2+} ions and during the reduction it converted into Cu-Ni alloy as depicted by the Point C and their corresponding inset image reveals the lattice spacing of Cu-Ni alloy (111) with a d spacing of 0.206 nm.

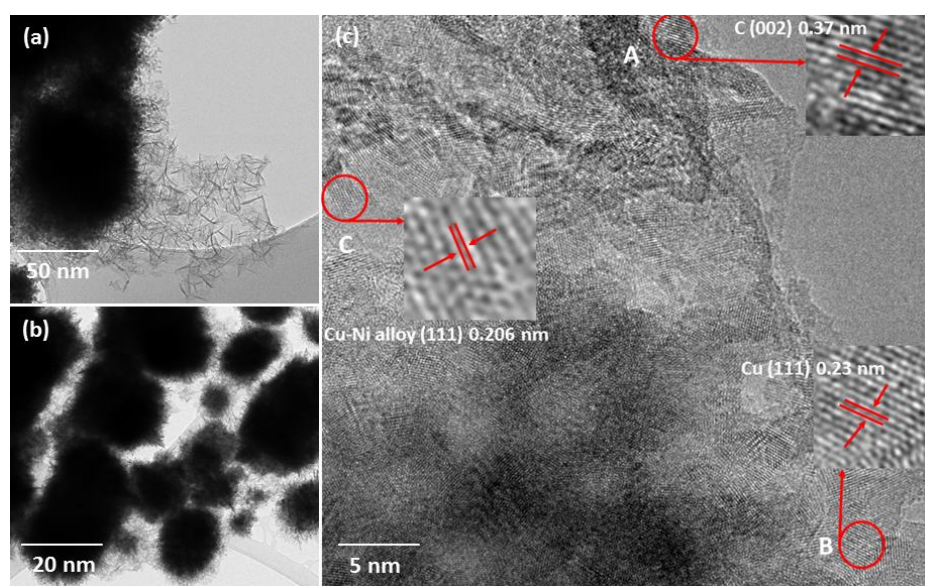


Figure 7.5 (a) and (b) TEM images of Cu@Ni/RGO nanocomposite in lower and higher magnifications, respectively, and (c) corresponding HRTEM image showing the lattice spacing of C (002) (point A, inset image of Fig. 7.5 (c)), lattice spacing of Cu NPs (111) (point B, inset image of Fig. 7.5 (c)) and lattice spacing of Cu-Ni alloy (111)) (point C, inset image of Fig. 7.5 (c)) .

Finally, we have carried out the 4-NP reduction in order to evaluate the catalytic properties of the prepared nanocatalysts. Fig. 7.6 (a) depicts the UV-vis spectra of 4-NP where initially peak at 400 nm was due to the formation of 4-nitrophenolate intermediate ion in aqueous medium (due to the increment of neutral aqueous solution alkalinity by NaBH_4). After the addition of Cu@Ni/RGO nanocomposite it was continuously decreased and almost disappeared within 90 s. Meanwhile, a new peak was appeared at ≈ 300 nm, suggests the successful reduction process and formation of 4-AP in a very short period at RT. The catalytic activity of Cu@Ni/RGO nanocomposite was much higher than previously reported many works [34]. This high catalytic activity can be attributed on the basis of catalyst conductivity and simultaneous

spillover effect. To confirm this fact we have also carried out the reduction of 4-NP by Cu/RGO and Ni/RGO nanocomposites and corresponding reduction times were 6 min and 18 min, respectively. Considering this, in bimetallic condition Cu and Ni works with synergism and provides the extra defects sites for reactions by increment of catalytic surface area. Moreover, metallic RGO surface also enhances the rate of reaction through their π - π interaction for 4-NP molecule [16], providing the high electronic charge migration accessibility and due to this electrons are easily transferred to sp^2 hybridized nitro group of 4-NP molecules.

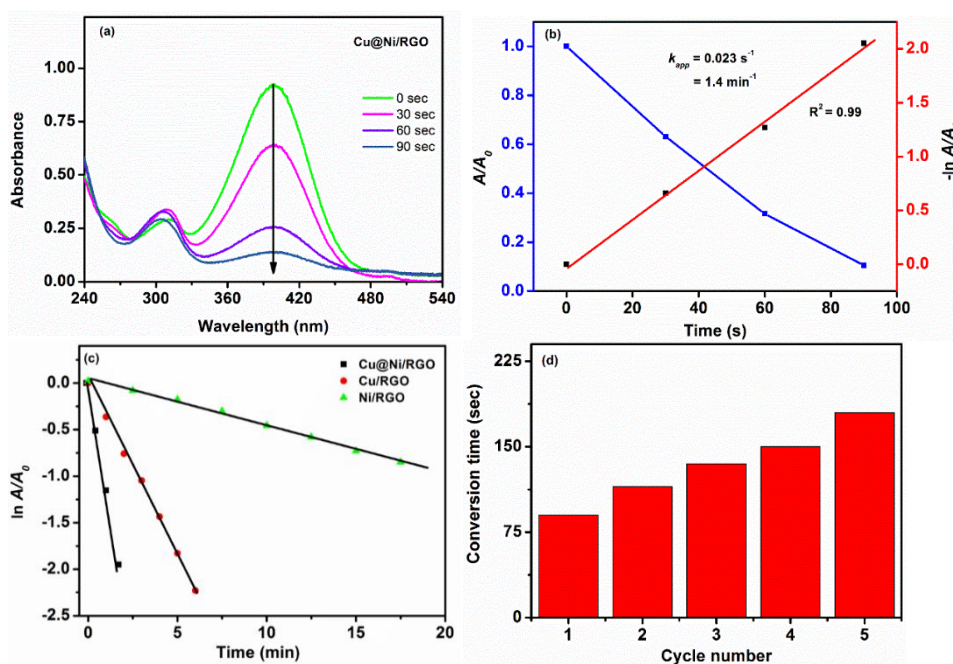


Figure 7.6 UV-vis spectra of (a) time dependent reduction process of 4-NP after the addition of Cu@Ni/RGO nanocatalyst in reaction medium. (b) Pseudo-first order plots of 4-NP reduction reaction catalysed by Cu@Ni/RGO nanocatalyst (red line) and decrement of relative absorbance (blue line). (c) Comparison of pseudo-first order plots of 4-NP reduction reaction catalysed by different catalysts Ni/RGO, Cu/RGO and Cu@Ni/RGO nanocatalyst, in the presence of NaBH_4 . (d) Stability measurement of Cu@Ni/RGO nanocatalyst during 5 successive cycles.

Further, we have performed the kinetic measurement of Cu@Ni/RGO nanocomposite as shown in Fig. 7.6 (b). Which shows the plot of A/A_0 versus reaction time (T) for the reduction of 4-NP along with plot between $\ln(A/A_0)$ and reaction time (T). In $\ln(A/A_0)$ scale a linear relationship was obtained which directly inferred the concentration of 4-NP via equation 7.10 [35].

$$k = t^{-1} \ln (A/A_0) \quad (7.10)$$

where, k is the apparent rate constant, A and A_0 are the concentrations of 4-NP at time t and 0, respectively [36]. The calculate value of k was 0.023 s^{-1} or 1.4 min^{-1} with good linear regression of R^2 of 99.97. This k value was much higher than many previously reported works [17,19,34]. Fig. 7.6 (c) shows the rate constants of Cu/RGO and Ni/RGO with comparison of Cu@Ni/RGO and about 4 and 11 times, respectively lower with them, indicating that the catalytic activity of Cu NPs can be remarkably improved by combining Ni NPs entity. Finally, we have performed the recycling test of Cu@Ni/RGO nanocomposite for reduction of 4-NP organic molecule by insertion of additional aliquots (25 μl) of reagents in same reaction cell. After each addition, the UV was recorded and the catalysts exhibited well stability towards the 4-NP reduction and corresponding time was increased up to 180 s for 5th cycle as shown in Fig. 7.6 (d), suggests the robustness of catalyst at least for 5 consecutive cycles.

7.3 Ag@Co/RGO nanocomposite and its high catalytic activity towards hydrogenation of 4-nitrophenol to 4-aminophenol

Hydrogenation of 4-NP was also achieved using a novel catalyst Ag@Co/RGO nanocomposite. A recent work demonstrates the reduction of 4-NP with Ag/RGO however, it shows a slow process [16]. This may be due to the basic difference of Ag metal regarding for dissociation of NaBH₄ reducing agent. It has been reported that Co and its borides (Co_xB) are prominent catalyst for hydrogen generation from NaBH₄. The combination of Co with Ag can provide the higher catalytic activity along with magnetic characteristic. However, Co is easily oxidized due to the easy diffusion of oxygen in crystal lattice and requires the protective layer on its surface. To solve such kind of problem we discovered a new method for easy reduction of Co²⁺ and protection of Co (0) core via using one more additional reducing agent L-AA with NaBH₄. A facile and room temperature method has been established towards the synthesis of novel catalyst Ag@Co/RGO for the hydrogenation of 4-NP.

7.3.1 Synthesis of Ag@Co/RGO catalyst

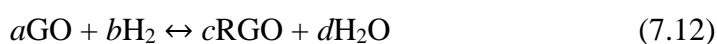
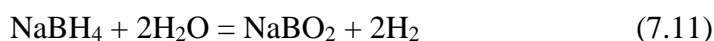
To synthesize the nanocomposite, 500 mg of CoCl₂.6H₂O was mixed in a well sonicated 35 mL dispersion of GO (3 mg/mL) via magnetic stirring (30 min) at RT in a 200 mL flask. Later, 350 mg of L-AA was added to above dispersion and dissolved by stirring (10 min). Subsequently, 15 mL of basic solution of NaBH₄ (pH 12.5) was added drop wise under continuous mechanical stirring until the hydrogen is released. The product was magnetically separated and washed with DD water and methanol and redispersed in DD water by mild sonication for 1 h at RT. Followed by, 180 mg of AgNO₃ salt was directly mixed in above dispersion and mechanically stirred for 5 min. To reduce the Ag⁺ ions, 2 mL of 1M NaBH₄ was added in presence of 50 mg L-AA and final product was filtered and washed with DD water 3-4 times to remove the impurities and dried in vacuum oven at 80 °C for 2 h.

7.3.2 Catalytic reduction of 4-NP

For catalytic testing of Ag@Co/RGO nanocomposite the reactant solutions of 4-NP and NaBH₄ were freshly prepared in molar concentration of 1.2 mM and 0.35 M, respectively. Followed by, 1 mL of both solutions were added and mixed by magnetic stirring and transferred to a quartz cuvette. Subsequently, 5 mg of catalyst was loaded into the cuvette to start the reaction. The intensity of the absorption peak at 400 nm in ultraviolet-visible (UV-vis) spectroscopy was used to monitor the process of the conversion of 4-NP to 4-AP.

7.3.3 Results and discussion

In this work, Ag@Co/RGO nanocomposite synthesized by a facile and novel method using two reducing agent L-AA and NaBH₄ under aqueous basic condition. Initially, GO was dispersed in DD water by sonication (15 min) followed by mixing of Co²⁺ salt. By this process Co²⁺ was grafted onto the negatively charged GO sheet. Further, a pre-calculated amount of L-AA was mixed in above dispersion by mechanical stirring at RT which makes the protective layer on Co²⁺. In the next step, NaBH₄ was slowly added in reaction mixture and simultaneously three process were happened as depicted in equations (7.11-7.13):



In first step, hydrogen gas is generated by the decomposition of NaBH₄, in second step it reduces the GO and in final step it makes the Co NPs. During reaction in the presence of NaBH₄ alkaline solution, L-AA became deprotonated and makes negatively charged anion and easily loose the electrons and these generated electrons also reduces the GO and Co²⁺ ion entities. Moreover, at alkaline condition it was converted into L-ascorbate ion which works as an anionic ligand and creates a blanketing barrier for environmental O₂ diffusion and protected the Co core. Further, in next step, it provide the support for Ag⁺ ions also and prevents the agglomeration of Ag NPs. Here, XRD was used to probe the reduction of GO to RGO and formation of Ag@Co/RGO nanocomposite. Fig.7.7 shows the XRD spectra of graphite powder, GO and Ag@Co/RGO nanocomposite. In the spectra, the peak related to (002) crystallographic plane of graphite powder was shifted to 11.3 degree from 26.5 degree after the oxidation process and suggests the exfoliation of graphite powder [10]. After the reduction, carbon peak related to (001) basal plane of GO was deprived and new peaks were observed at 38.39, 44.55, 64.72, 77.63 and 81.81 indicates the diffraction from (111), (200), (220), (311) and (222) crystallographic planes. The peak position and corresponding diffraction intensity from various lattice planes suggests the formation of fcc structure of crystalline Ag phase [30]. However, any specific peak of Co (0) was not observed in XRD pattern. To ascertain the presence of Co metal, further we have performed the magnetic measurements which may directly reflects the existence of metallic cobalt inside the nanocomposite.

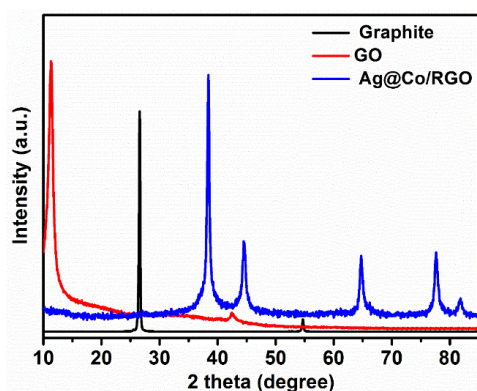


Figure 7.7 XRD spectra of GO and Ag@Co/RGO nanocompsite.

Fig. 7.8 displays the magnetic characteristic of Ag@Co/RGO nanocompsite which shows the typical ferromagnetic behaviour of M-H plot at RT with a saturation magnetization of 9.77 emu/gm and suggests the formation of Co nanocrystals within graphene matrix. In absence of L-AA, this value was much lesser and was estimated only 2.43 emu/gm. This indicates the efficacy of our synthesis procedure for preparation of magnetic Co NPs along with GO reduction. Further, in order to elucidate the structure of Ag@Co/RGO nanocomposite and reduction mechanism of graphene system in more detail, we have also carried out the Fourier transform infrared (FTIR) spectroscopy. Fig. 7.9 shows the FTIR spectra of GO and Ag@Co/RGO nanocomposite samples (in the range of 2000-1400 cm^{-1}). In GO, two sharp peaks were observed at around 1725 and 1615 cm^{-1} and first peak was attributed as C=O stretching mode of sp^2 vibrations and second peak was related to the surface adsorbed water molecule [36]. However, after the reduction both peaks were diminished and one new peak was observed at 1630 cm^{-1} which indicates the stretching mode of vibration of alkene bonding (-C=C) and suggests the restoration of graphitic structure in reduced product. To ascertain the change in carbon system Raman spectroscopy was also performed.

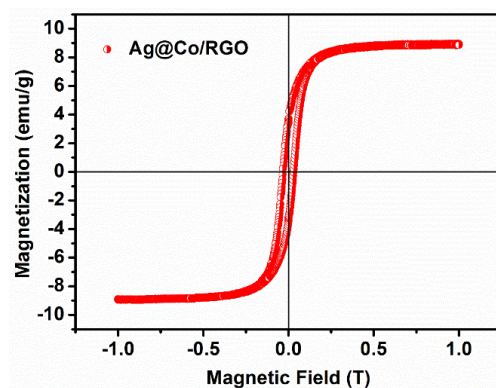


Figure 7.8 RT magnetization plot (M-H) of Ag@Co/RGO nanocompsite.

Fig. 7.10 shows the Raman spectrum of GO and Ag@Co/RGO in the range of 1000-2000 cm^{-1} . In GO spectra, two prominent bands D and G were located at 1354 cm^{-1} at 1601 cm^{-1} with respective I_D/I_G ratio of 0.95. This is well known fact that G band is an intrinsic feature of graphitic system and it corresponds to the first-order scattering of the E_{2g} mode of sp^2 domain of carbon (related to the all sp^2 carbon vibrations in long-wavelength optical phonons TO and LO) [10] and [36].

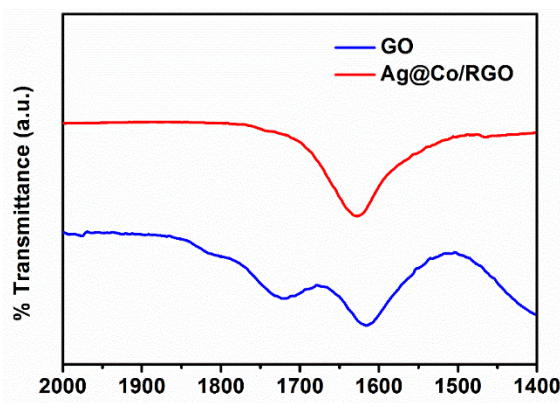


Figure 7.9 FTIR spectra of GO and Ag@Co/RGO nanocomposite.

D band is arising after the defect introduction and related to the characteristic breathing mode of A_{1g} symmetry [37]. Whereas, in Ag@Co/RGO, both D and G bands were shifted to lower wave number (red-shifted) and appeared at 1349 and 1592 cm^{-1} , respectively with increased I_D/I_G ratio of ~ 1.06 and this increment ratio clearly reveals that corresponding changes inside carbon system after the reduction due to more defects inside of graphene system.

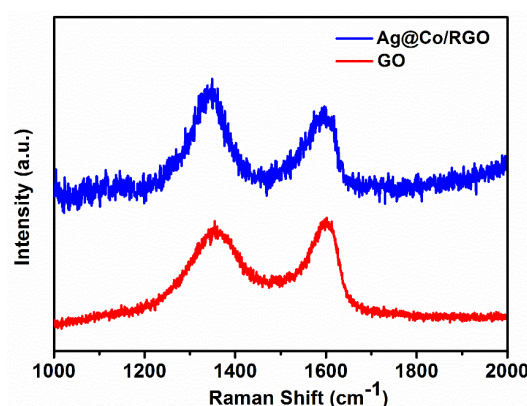


Figure 7.10 Raman spectra of Ag@Co/RGO nanocomposite.

Further, we have carried out systematic microscopic investigation of initial materials GO, RGO and Ag@Co/RGO nanocomposite to show the corresponding changes in carbon system. Fig.7.11 (a) and (b) shows the SEM images of GO and RGO respectively. Image of GO clearly exhibits the few layer of graphitic carbon with typical wrinkle behavior [37]. Image (b) displays the morphology of RGO reduced by the NaBH_4 in absence of metal salts where thin sheet of graphene was observed.

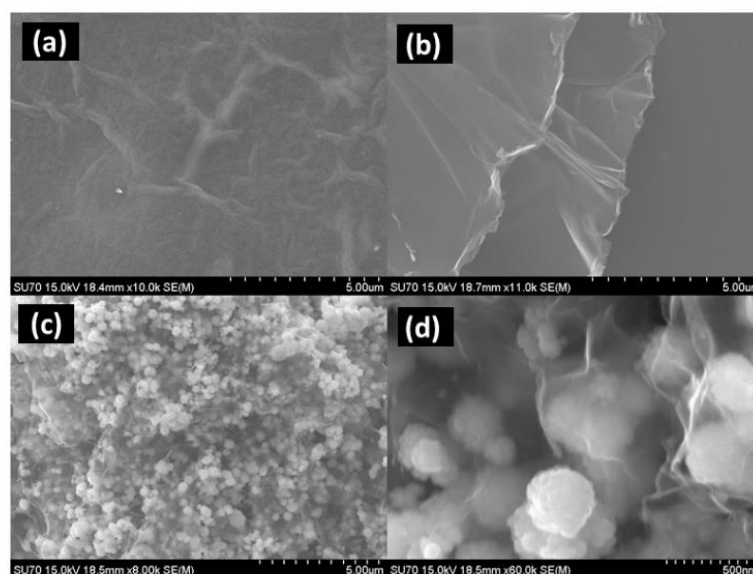


Figure 7.11 SEM images of (a) GO and (b) RGO. Images (c) and (d) Ag@Co/RGO nanocomposite in higher and lower magnifications, respectively.

Fig. 7.11 (c & d) shows the SEM images of Ag@Co/RGO nanocomposite after the loading of Ag NPs on Co. In higher magnification image it was clearly visualized that tiny Ag nanoparticles were decorated on to the surface of Co clusters and covered by the thin layer of graphene. Moreover, both SEM images shows the monodispersity and spherical nature of NPs without any specific agglomeration and indicates the efficacy of our new synthesis method. Further, to ascertain of Co and Ag elements in RGO matrix we have performed the EDX analysis also (Fig. 7.12). Which clearly shows that the presence of both metal elements.

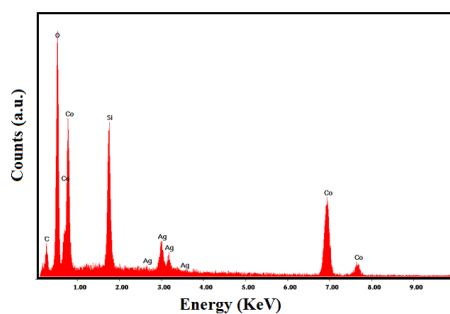


Figure 7.12 EDX spectra of Ag@Co/RGO nanocomposite.

Finally, Ag@/Co/RGO nanocomposite catalyst was applied for hydrogenation reaction of 4-NP reduction in presence of freshly prepared NaBH₄ aqueous solution. The progress of reaction was monitored by UV–visible technique. It has been reported that aqueous solution of 4-NP displays pale yellow colour and exhibit a peak at around 317 nm [31-33]. In presence of NaBH₄ solution it turned to greenish-yellow colour and shifted to 400 nm due to the formation of 4-nitrophenolate ion which retained for several hours in the absence of catalyst. After the addition of Ag@/Co/RGO nanocomposite, immediately this peak started to decrease and completely disappeared within 45 s. Fig. 7.13 (a) shows the UV-vis spectra of 4-NP reduction after the addition of catalyst. Where peak at 400 nm was diminished and a new peak was observed at around 300 nm. This indicates the successful reduction process and formation of 4-aminophenolate and high catalytic activity of Ag@/Co/RGO nanocomposite as compared to previously reported works [31-33]. Further, to investigate the role of individual metal component (Ag and Co) in graphene matrix; we have also carried out the experiment with Co/RGO and Ag/RGO without altering reaction conditions. It was noticed that reduction process was too slow in both cases as compared to Ag@Co/RGO nanocomposite and estimated time was 55 and 15 min, respectively. These results suggested that such a high catalytic activity was only achieved due to the construction of bimetallic structure with graphene. It implies that the synergism effect of metal species where Co decomposes the NaBH₄ and noble metal (Ag) spillover the hydrogen molecule into radical hydrogen [37]. Moreover, RGO also played its role and provide the support for 4-NP molecule and facilitate the easy hydrogen transfer to sp² hybridized nitro group via own π - π interactions.

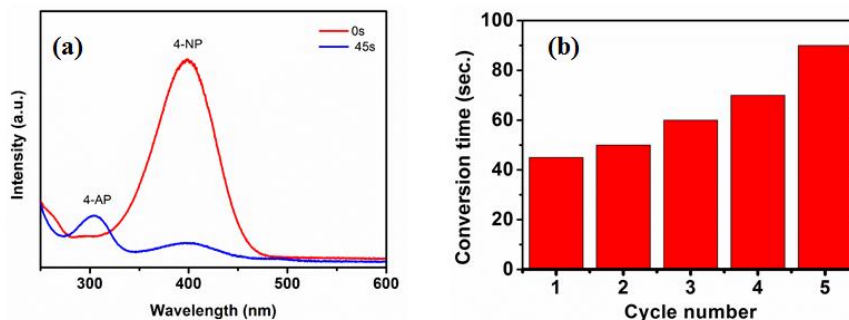


Figure 7.13 UV-Vis spectra of (a) 4-NP reduction using Ag@Co/RGO nanocomposite; (b) stability measurement of catalyst during 5 successive cycles.

Further, we have also investigated the stability of catalyst by the inserting additional aliquots (25 μ l) of reagents in same reaction cell. After each addition, the UV was recorded and the catalysts exhibited well stability towards the 4-NP reduction and corresponding time was increased up to 90 s for 5th cycle as shown in Fig. 7.13 (b) and suggests the robustness of catalyst for reduction of 4-NP organic molecule.

7.4 Hydrogenation of 4-nitrophenol to 4-aminophenol using Pd@NSG

The catalytic test of 4-NP reduction was also evaluated on Pd@NSG nanocatalyst (detailed described in chapter 3) in order to evaluate the catalytic properties of the prepared catalysts. In absence of the catalyst, NaBH₄ only produces the 4-nitrophenolate intermediate ion (peak at 400 nm) in aqueous medium due to the increment of neutral aqueous solution alkalinity which is maintained for several hours (Fig. 7.14(a)). After the addition of Pd@NSG catalyst, the peak related to 4-NP was drastically decreased and almost disappeared within 2 min (120 s) as depicted in Fig. 7.14(b). At the same time, a new peak appears at around 300 nm which suggests the successful reduction process and the formation of 4-AP confirming the high catalytic activity of Pd@NSG nanocomposite compared to previously reported works. This higher catalytic activity of Pd@NSG nanocomposite can be attributed to the presence of bi-metallic condition of two well-known hydrogenation reaction catalyst (Pd and Ni_xB). Considering this, in bimetallic condition of Pd and Ni_xB, the extra defects associated on metal nanoparticles grain boundaries (near to the interface site) allow the host species to occupy the defect centres.

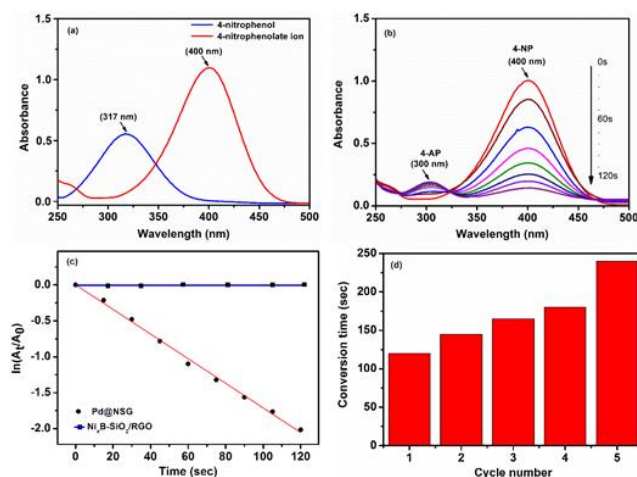


Figure 7.14 UV-vis spectra of (a) 4-NP molecule initially and after the addition of NaBH₄ in aqueous medium at 25 °C and (b) time dependent reduction process after the addition of Pd@NSG nanocatalyst in reaction medium. (c) Pseudo-first order plots of 4-NP reduction catalysed by Pd@NSG in the presence of NaBH₄ (red) and Ni_xB-SiO₂/RGO (blue). (d) Stability measurement of Pd@NSG nanocatalyst during 5 successive cycles.

Moreover, while hydride (H⁻) species come to the contact with bimetallic boundaries and faces, the different Fermi energy level of the two metal centres contacted to each other and rearranges their surface charge and provided their electronic population for reduction process

on the basis of the Hammer–Nørskov model. Due to this effect when 4-NP molecule interact with metal d-band centres; their electronic states overlap and split off into bonding and antibonding fashion. That especially, changes the d-band centre position that became farther from the Fermi energy level, antibonding states are increasingly populated and the overall chemisorption strength weakens. As Ni and Pd both belong to the d-block transition series and pursue the d^8 electronic configuration ($3d^8$ and $4d^8$, respectively) however, due to the large orbital size of Pd compared to Ni, the net repulsive force of bonding and antibonding states is higher in case of Pd. Due to this fact the 4-NP molecule bind less tightly with Pd surface and fast reaction is observed. However, high binding energy of Ni the effect was opposite and organic entity (4-NP) bounded on it tightly and restricted the further process.

In all such aspect, this was very important to evaluate the role of individual components viz. SiO_2/RGO matrix, $\text{Ni}_x\text{B-SiO}_2/\text{RGO}$, $\text{Pd-SiO}_2/\text{RGO}$ without altering reaction conditions and protocol. SiO_2/RGO matrix offers an environment to prevent aggregation of Pd- Ni_xB nanoparticles and provide the feasibility of H^\bullet radicals diffusion inside of channels and cavities. However, due to the absence of any catalytic metal centre NaBH_4 was not efficiently decomposed on it and it suffers to show any specific effect for reduction of 4-NP. Instead of that, both individual metal containing counterparts ($\text{Ni}_x\text{B-SiO}_2/\text{RGO}$, $\text{Pd-SiO}_2/\text{RGO}$) reduces the 4-NP, but the rate of reaction was too slow compared to Pd@NSG nanocomposite and estimated times were 22 (1320 s) and 120 min (7200 s), respectively. Here, the high catalytic activity of Pd-SiO₂/RGO compared to Ni_xB-SiO₂/RGO can be ascribed by the high charge transportation from Pd metal surface and its noble behavior. Whereas, Ni_xB only provides the hydrogen via hydrolysis reaction (from equation 2) but side product NaBO₂ hinders the active sites of metal catalytic centre and 4-NP molecule is not properly contacted with generated radical hydrogen. This phenomenon can be described on the basis of Langmuire-Hinshelwood (LH) model, in which both reacting species should adsorb on to the surface of catalyst metal centre, where the BH_4^- species transfer the hydrogen in a reversible manner to the surface and, simultaneously, 4-NP molecule should also be adsorbed on to the catalyst surface. In rate-determining step, both reactants (hydrogen atom and 4-NP molecule) reacts each other and the product (4-AP) should desorb from the catalyst surface and provide the free space for new reacting species. Scheme 2 illustrates the overall process of 4-NP reduction on Pd@NSG where Ni_xB, which is a prominent catalyst for NaBH_4 hydrolysis reaction for fuel cell application, easily decomposes the BH_4^- species in aqueous medium in to molecular hydrogen and concomitantly, metallic Pd spillover the produced hydrogen and converted it in to radical

species. In the next step, when 4-NP molecules come in contact with Pd@NSG nanocatalyst, the adsorbed H atoms are directly transferred to organic entity and converted it into 4-AP. In addition, metallic RGO surface also enhances the rate of reaction through their π - π interaction with 4-NP molecule where, it provides the high electronic charge migration accessibility for easy electrons transfer to sp^2 hybridized nitro group of 4-NP molecules. Further, we have performed the kinetic measurement of Pd@NSG nanocomposite as shown in Fig. 7.14 (c). The kinetics of the catalytic reaction measured as a function of time on the basis of absorbance at 400 nm.¹⁶ In this reaction, the concentration of NaBH_4 was in excess compared with 4-NP and can be regarded as constant throughout the reaction and pseudo-first-order kinetics can be applied with respect to 4-NP.

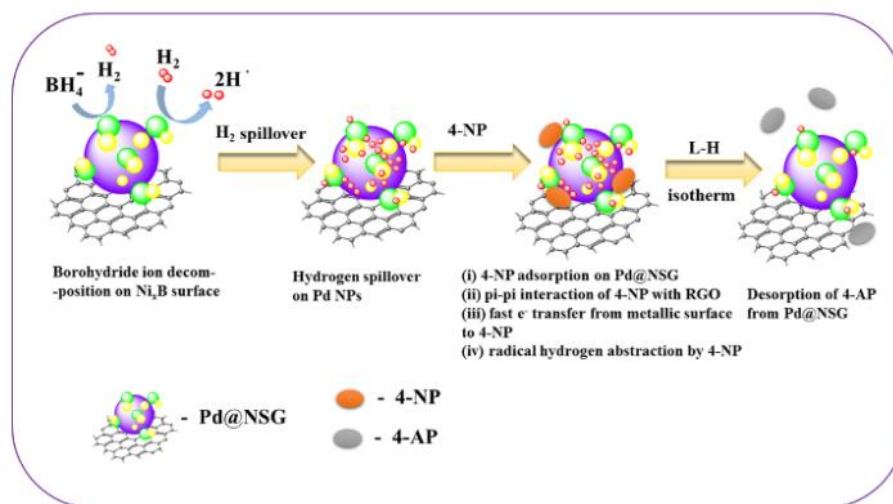


Figure 7.15 Schematic representation of 4-NP molecule reduction on Pd@NSG nanocomposite in presence of NaBH_4 in aqueous medium.

A linear relationship was obtained between $\ln(A_t/A_0)$ and reaction time (t) which directly inferred the concentration of 4-AP during the reaction as $\ln(C_t/C_0)$ as given in above equation 7.10. The calculated value of k was 0.017 s^{-1} for Pd@NSG nanocomposite, a value higher than previously reported works. From Fig. 7.14 (c) it is clearly indicated that $\ln A_{400}$ shows a good linear correlation and a R^2 of 99.97. This linear relationship for Pd@NSG catalysts, indicate that the reaction follows first-order kinetics. The rate constants for different catalysts were also estimated from diffusion-coupled first order reaction kinetics using the slopes of the straight lines. The rate constant for Pd-SiO₂/RGO was about twelve times lower than that obtained for Pd@NSG nanocomposites showing the catalytic activity of Pd nanoparticles improved remarkably by combining only with the Ni_xB entity. The rate constant

of Ni_xB-SiO₂/RGO was too low compared with Pd based nanocomposite, imposing slow kinetic behaviour (see supplementary information for detail). Finally, we have performed the recycling test of Pd@NSG nanocomposite also for reduction of 4-NP organic molecule by the insertion of additional aliquots (25 µl) of reagents in same reaction cell. After each addition, the UV was recorded and the catalysts exhibited well stability towards the 4-NP reduction and corresponding time was increased up to 240 s for 5th cycle as shown in Fig. 7.14 (d), suggests the robustness of catalyst at least for 5 consecutive cycles with an efficiency of 88 %.

7.5 Conclusions

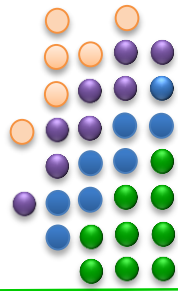
In the present study, we demonstrated the catalytic activity of three catalyst Cu@Ni/RGO, Ag@Co/RGO and Pd@NSG nanocomposites towards the reduction of environmental pollutant 4-NP at RT. All catalysts were novel composition and synthesized by the facile approach. SEM/TEM images clearly exhibited the formation of specific size of NPs on graphene sheets without any specific agglomeration. The synthesized nanocomposites displayed the ultrafast response for reduction process with remarkable high stability and catalytic activity. These features suggested the simplicity of the process and suitability of synthesis method for possible commercial exploitation of heterogeneous catalysts in reduction of nitro aromatic compounds.

7.6 References

- [1] M. Sankar, N. Dimitratos, P. J. Miedziak, P. P. Wells, C. J. Kiely, G. J. Hutchings. *Chem Soc Rev*, 41 (2012) 8099-8139.
- [2] B. Xia, F. He, L. Li. *Langmuir*, 29 (2013) pp. 4901-4907.
- [3] N. Toshima, T. Yonezawa. *New J Chem*, 22 (1998) pp. 1179-1201.
- [4] S. Liu, Y. Amada, M. Tamura, Y. Nakagawa, K. Tomishige. *Catal Sci Technol*, 4 (2014) pp. 2535-2549.
- [5] J. W. Cui, E. E. Ogabiela, J. N. Hui, Y. Wang, Y. Zhang, L. Tong, J. F. Zhang, S. B. Adeloju, X. Y. Zhang, Y. C. Wu. *Electrochem Soc*, 162 (2014) pp. B62-B67.
- [6] L. Tang, G. Yu, W. Si, Y. Ou, L. Qiao. *J. Nanoscience and Nanotechnology*, 11 (2011), pp. 10255–10261

- [7] Z.D. Pozun, S.E. Rodenbusch, E. Keller, K. Tran, W. Tang, K.J. Stevenson, G. Henkelman. *J Phys Chem C*, 117 (2013), pp. 7598–7604.
- [8] B. R.Cuenya, *Thin Solid Films*. 518 (2010) pp. 3127–3150.
- [9] A. K. Geim, K. S. Novoselov, *Nat Mater*, 6 (2007) pp. 183-191.
- [10] Y. Lan, S. Jun, M. Xiangyu, L. Wei, C. Gongzhen. *J Mater Chem A*, 1 (2013), pp. 10016–10023.
- [11] N.M. Julkapli, S. Bagheri. *Int J Hydrogen Energy*, 40 (2015), pp. 948–979.
- [12] M. Chen, Z. Zhang, L. Li, Y. Liu, W. Wang, J. Gao. *RSC Adv*, 4 (2014) pp. 30914–30922.
- [13] S.H. Kim, H. Jeong, J. Kim, I.S. Lee. *Small*, (2015) pp. 1-10.
- [14] M. Rocha, C. Fernandes, C. Pereira, S. L. H. Rebelo, M. F. R. Pereira, C. Freire *RSC Adv*, 5 (2015) pp. 5131–5141.
- [15] R. Krishna, D. M. Fernandes, V. F. Domingos, E. S. Ribeiro, J. Campos Gil, C. Dias, J.Ventura, C. Freire, E. Titus. *RSC Adv*, 5 (2015) pp. 60658-60666.
- [16] R. Krishna, D. M. Fernandes, C. Dias, J. Ventura, E. Venkata Ramana, C. Freire, E. Titus. *Int J Hydrogen Energy*, 40 (2015) pp. 4996–5005.
- [17] W. Sun, X. Lu, Y. Tong, Z. Zhang, J. Lei, G. Nie, C. Wang. *Int J Hydrogen Energy*, 39 (2014) pp. 9080–9086.
- [18] B. K. Barman, K. K. Nanda. *Appl Catal A Gen*, 491 (2015) pp. 45–51.
- [19] G. Chena, F. Wang, F. Liu, X. Zhang. *Applied Surface Science*, 316 (2014) pp. 568–574.
- [20] R. Krishna, E. Titus. *Materials Today: Proceedings*, 2 (2015) pp. 399-406.
- [21] M. Raja, J. Subha, F. B. Ali, S. H. Ryu. *Materials and Manufacturing Processes*, 23 (2008) pp. 782-785.
- [22] F. B. Effenberger, M. A. Sulca, M. T. Machini, R. A. Couto, P. K. Kiyohara, G.Machado, L. M. Rossi. *J. Nanoparticle Research*, 16 (2014) 2588 (1-10).
- [23] M. Zong, Y. Huang, H. W. Wu, Y. Zhao, P. Liu, L. Wang. *Mater Lett*, 109 (2013), pp. 112–115

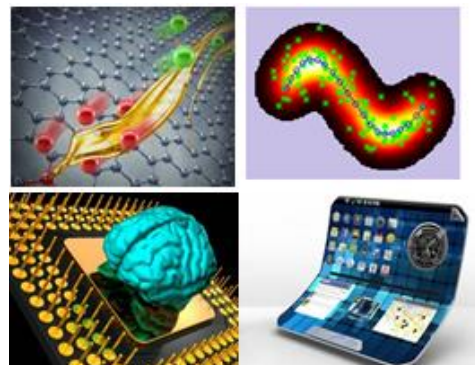
- [24] R. Krishna, C. Dias, J. Ventura, E. Titus. *Materials Today: Proceedings*, 2 (2015) pp. 407-413.
- [25] J.W. Park, E.H. Chae, S.H. Kim, J.H. Lee, J.W. Kim, S.M. Yoon, J.Y. Choi. *Mater Chem Phys*, 97 (2006), pp. 371–378.
- [26] C. Wu, F. Wu, Y. Bai, B. Yi, H. Zhang. *Mater Lett*, 59 (2005), pp. 1748–1751.
- [27] R. Krishna, E. Titus, O. Okhay, J.C. Gil, J. Ventura, E. V. Ramana, J.J.A. Gracio. *Int J Electrochem Sci*, 9 (2014), pp. 4054–4069.
- [28] B. J. Li, H. Q. Cao, J. F. Yin, Y. A. Wu, J. H. Warner. *J Mater Chem*, 22 (2012) pp. 1876.
- [29] Y. Zheng, J. Liang, Y. Chena, Z. Liu. *RSC Adv*, 4 (2014) pp. 41683-41689.
- [30] R. Krishna, E. Titus, L. C. Costa, J. C. J. M. D. S. Menezes, M. R. P. Correia, S. Pinto, J. Ventura, J. P. Araújo, J. A. S. Cavaleiro, J. J. A. Gracio. *J Mater Chem*, 22 (2012) pp. 10457.
- [31] P. H. K. Charan, G. R. Rao. *Microporous and Mesoporous Materials*, 200 (2014) pp. 101–109.
- [32] X. Mei, J. Ouyang. *Carbon*, 49 (2011) 5389-5397.
- [33] Z.J. Fan, W. Kai, J. Yan, T. Wei, L.J. Zhi, J. Feng, Y. M. Ren, L. P. Song, F. Wei. *ACS Nano*, 5 (2010), pp. 191–198.
- [34] B. K. Barman, K. K. Nanda. *Dalton Trans*, 44 (2015) pp. 4215-4222.
- [35] M.K. Joshi, H.R. Pant, H.J. Kim, J.H. Kim, C.S. Kim. *Colloids Surf. A: Physicochem. Eng. Aspects*, 446 (2014), pp. 102–108.
- [36] Z. Ji, X. Shen, G. Zhu, H. Zhou, A. Yuan. *J Mater Chem*, 2012, 22, 3471.



CHAPTER 8

ELECTRICAL AND ELECTRONICS APPLICATIONS OF GRAPHENE NANOCOMPOSITE:

Structure, measurements and results



Chapter 8

<u>Electrical and electronics applications of graphene nanocomposite: structure, measurements and results</u>	169
8.1 Introduction	171
8.2 Resistive switching device based on Ni-doped graphene oxide thin films	172
8.2.1 Fabrication of MIM structure	173
8.2.2 Measurements	173
8.2.3 Results	173
8.3 Switching characteristic of hydrogenated graphene oxide thin films	177
8.4 Resistive switching in Co/RGO nanocomposite	178
8.4.1 Resistive switching in Co/RGO nanocomposite	178
8.4.2 Synthesis of Co/RGO nanocomposite	179
8.4.3 Results and discussion	179
8.5 New hybrid material Ni(OH)₂@Ni/RGO nanocomposite for resistive switching applications: Observation of large hysteresis	180
8.5.1 Synthesis of Ni(OH) ₂ @Ni/RGO nanocomposite	180
8.5.2 Results and discussion	181
8.6 Ag@SiO₂/RGO nanocomposite for memristor application	184
8.6.1 Synthesis of Ag@SiO ₂ /RGO nanocomposite	185
8.6.2 Device fabrication of Ag@SiO ₂ /RGO nanocomposite	185
8.6.3 Results and discussion	185
8.7 Conclusions	188
8.8 References	188

ELECTRICAL AND ELECTRONICS APPLICATIONS OF GRAPHENE NANOCOMPOSITE: Structure, measurements and results

8.1 Introduction

Graphene as a single atomic layer of graphite was first isolated at 2004, and since then many properties previously predicted for this 2D structure have been confirmed experimentally [1]. The notable feature of graphene is the ability to continuously tune the charge carriers from holes to electrons (gate dependence) [2]. The major problem concern with graphene with it does not possess any band gap; electrons can flow at any energy, and the corresponding resistivity changes are small [3]. So the main focus of the graphene engineers has been to find the ways for creating an artificial band gap using such methods as applying electric fields, doping of foreign radicals/functional groups or incorporation of various kind of NPs. Due to these changes applicability of it's become more pronounced as extra defects become usable for many electrical and electronics applications such as sensing, transistor, solar cells and memristor device fabrication [4-6].

Memristor is an electrical component that limits or regulates the flow of electrical current in a circuit and remembers the amount of charge that has previously flowed through it [7]. This term first time coined in 1971 by circuit theorist Leon Chua [8]. He describe this as a missing non-linear passive two-terminal electrical component relating to the electric charge and magnetic flux linkage. Since then, the definition of memristor has been broadened to include any form of non-volatile memory that is based on resistance switching, which increases the flow of current in one direction and decreases the flow of current in the opposite direction. Therefore, memristors are important because they are non-volatile, meaning that they can retain memory without power [9].

Moreover, it is an alternative of resistive random access memory (RRAM), it is relying on the resistive switching (RS) effect occurring in a metal-insulator-metal (MIM) memory cell [10-11]. Recently, it gained lot of interests owing to its simple structure, non-destructive readout, high operation speed, long retention time, low-voltage operation and high scalability [12]. To construct the MIM structure the properties of the insulator layer is very important, it should be thin, insulator, easily transferrable to any substrate and should robust. The oxidized derivative of graphene which called as graphene oxide (GO) is one of the various insulating materials that fulfill all above requirements. It consists of a single layer of graphene bounded to oxygen in the form of carboxyl, hydroxyl, or epoxy groups. The physical properties of GO are then controlled by these chemical functionalities on the surface that can be tuned at the nanoscale [13-14]. Due to this it can be easily and uniformly transferred onto any substrate. This makes it potentially useful for the fabrication of large-scale flexible, transparent, and printable devices. Recently, reliable and reproducible resistive switching in GO thin films and conjugated-polymer-functionalized GO films have been reported. Hong *et al.* demonstrated a graphene oxide based RRAM device with excellent flexibility without degradation of memory performance upon bending [15]. However, the mechanism responsible for the RS effect of GO is still not clear. Several authors attributed the resistive switching behavior to the formation/rupture of filaments arising from the diffusion of metallic ions from the electrodes under a bias voltage. On the contrary, other studies reported that the switching effect in GO and graphene field-effect devices originates from desorption/absorption processes of oxygen-related groups on the GO sheets. Therefore, the study of new GO based materials is essential to improve the understanding of the RS mechanism and obtain nonvolatile memories with enhanced properties [7].

8.2 Resistive switching device based on Ni-doped graphene oxide thin films

In this work, firstly Ni-GO thin film was prepared. The film prepared by the assistance of polymeric hydrogel with GO. The exfoliated GO sheets were gradually added to the polyvinyl alcohol (PVA) and polyacrylic acid (PAA) mixture (weight ratio of 2: 1) which prepared from a stock solution (6 mg/ mL in DI water). During the PVA -PAA gel preparation, the temperature was maintained at 90 °C, and subsequently cooled down to room temperature. To prepare the Ni reduced graphene polymeric hydrogel, 20 mg of Ni NPs (Quantum spheres) were dispersed in above hydrogel. Finally, the polymeric hydrogel was treated by two distinct methods: in the first method the hydrogel was protonated with 200 μ L dil. HCl (series 1) and in the second

method the hydrogel was protonated with 0.5 mL of hydrazine hydrate ($\text{N}_2\text{H}_4 \cdot \text{H}_2\text{O}$) for subsequent reduction of GO to RGO.

8.2.1 Fabrication of MIM structure

The MIM structure was fabricated on Si/SiO₂ substrates by the dip coating of Ni doped GO film. After, drying of the sample at 60 °C two different types of electrodes (W, Cu) were deposited on top of them through evaporation method and constructed a MIM structure to investigate the resistive switching properties.

8.2.2 Measurements

The current-voltage (I–V) cycles of the samples were obtained using a Keithley Source Meter 2400. Macroscopic electrodes of W and Cu were fabricated on top of the Ni-doped GO sheet using e-beam evaporation and a shadow mask. During the measurements, the voltage was swept in the $0 \rightarrow V_{max} \rightarrow 0 \rightarrow -V_{max} \rightarrow 0$ sequence (where V_{max} is the max. applied voltage).

8.2.3 Results

The I–V characteristics of two representative devices are shown in Fig. 8.1. Substantial hysteresis was found in the case of samples of series 1 for both W and Cu contacts. With increasing positive voltage, the W-GO device gradually switches from the high resistance state (HRS or OFF state) to a low resistance state (LRS or ON state; Set process). By sweeping the voltage to negative values, the device recovers the HRS (Reset process). The use of Cu contacts increased the conductivity of the sample and led to clear sharp resistance variations at the well-defined Set (Reset) voltage of 1.6 V (-2.8 V). Sample of series 2 showed much smaller hysteresis, particularly when using W contacts. The use of Cu contacts again increased the samples' conductivity, although only a gradual variation of the resistance with the applied voltage was observed. Series 2 further showed a larger conductivity than samples of series 1; due to the different switching polarity of the two series, a characteristic that is maintained regardless of the deposited contacts on the surface of the samples. This result indicates that ions with different charges are involved in the switching mechanism of the two series.

In order to further unravel the switching mechanism that occurs in our Ni-doped graphene oxide samples, the I–V curves in the negative voltage region were replotted in a log-log scale (inset of Fig. 8.1). The indicated numbers denote the slopes retrieved from linear fits to the experimental curves. In the LRS state, the presented samples exhibited an Ohmic behavior with a slope of ≈ 1 . However, in the HRS state, our results suggest a trap-associated space charge limited conduction (SCLC) mechanism, with a slope of ≈ 2 . The switching mechanism on

graphene oxide based devices is usually attributed to one of two mechanisms.

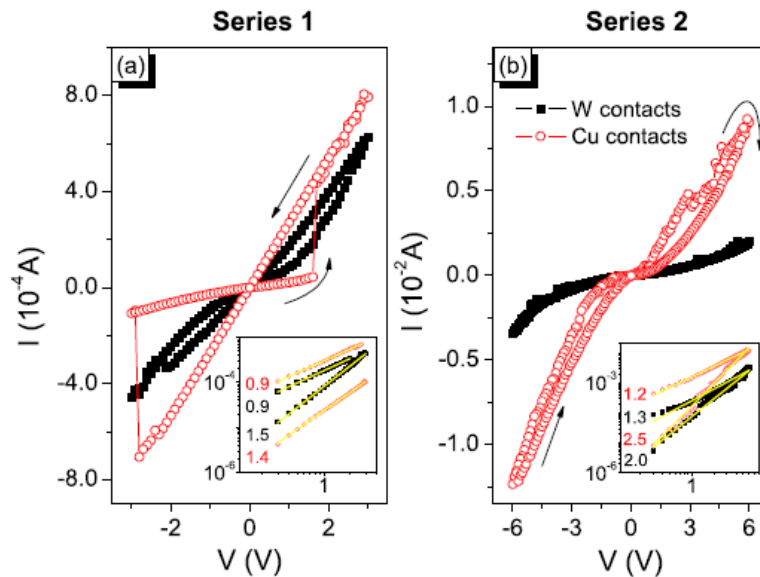


Figure 8.1 I-V characteristics of samples of series (a) 1 and (b) 2, with W (open circles) and Cu (squares) contacts. The arrows indicate the switching polarity. Inset: I-V curves in a log-log scale; lines are linear fits to the experimental data.

In the first, RS originates from the formation and rupture of conductive filaments in an insulating matrix. As described above, the switching effect in our samples has a clear dependence on the electrode material. This dependence is particularly visible in the I–V measurements of samples of series 1, where the use of copper electrodes also changed the switching mechanism of the sample (see Fig. 8.1). Some authors have already reported the influence of the electrode on resistive switching in GO. It is usually described as the formation/rupture of a metallic filament on the GO layer due to the diffusion of metallic ions under a bias voltage. While the formation of the filament leads to the LRS, its disruption under an opposite bias voltage returns the sample to the HRS. The second mechanism usually mentioned correlates switching with the dependence of the physical properties of GO on bounded oxygen groups. Related to the existence of these oxygen groups, GO has two configurations, sp^2 and sp^3 . In the sp^2 state, the conductivity of GO is increased by the introduction of p-electrons resulting from the removal of oxygen groups, while in the sp^3 state the phenomenon is reversed. When a bias voltage is applied, local rearrangements of oxygen groups in the GO layer can increase the amount of sp^2 bonds and therefore the GO conductivity (by generated p-electrons), switching the device into the LRS. Changing the voltage polarity, the oxygen ions back diffuse, reestablishing the HRS.

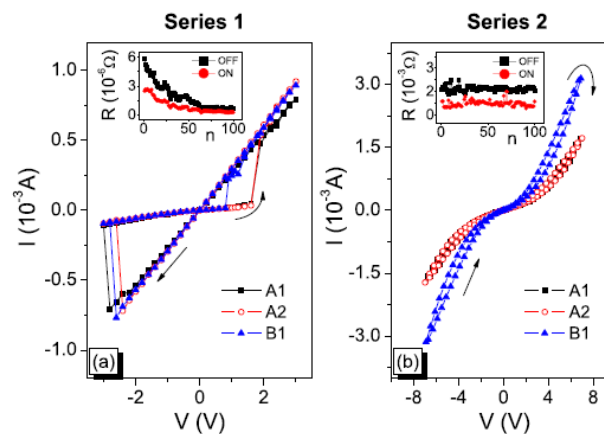


Figure 8.2 I–V characteristics of (left) series 1 and (right) series 2, with Cu contacts, produced at different times (A,B). Arrows indicate the switching polarity. Inset: endurance measurements up to 100 cycles.

From the above analysis, we can state that the mechanism of RS in graphene oxide depends on the fabrication process of the samples. In series 1, the switching is governed by the diffusion of positive ions (W^+ , Cu^+) from the metallic electrodes (as confirmed by the dependence of switching on the used contacts). On the other hand, the reversal of the switching polarity in series 2 shows that its dominant RS mechanism should be related with the migration of negative oxygen groups [16]. Both mechanisms, however, lead to an ohmic conductance in the low resistance state, indicating the formation of a percolative metallic path connecting the two electrodes. The application of an opposite bias voltage then results in switching into the HRS and a change in the electronic conduction. The reproducibility of both switching and switching direction was confirmed by measuring different samples of the same series and nominally identical samples produced at different times (Fig. 8.2). We further measured the endurance of our devices by applying positive/negative bias voltages large enough to induce RS (inset of Fig. 8.2). As in other GO-based devices, a degradation of the $R_{\text{OFF}}/R_{\text{ON}}$ ratio was observed in series 1 when cycled up to 100 times. Series 2, however, showed much more stable switching, likely due to the difference in switching mechanism.

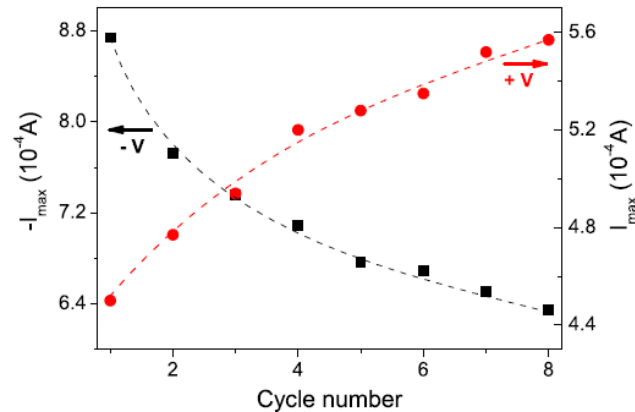


Figure 8.3 Maximum conductance of a sample of series 1 after consecutive positive (circles) and negative (squares) voltage sweeping cycles.

We also conducted a preliminary study on the activity-dependent modification abilities of graphene-based devices. Similar studies were performed in nanoscale memristive devices using tungsten oxide or co-sputtered Ag and Si as switching layers. The activity-dependent modification of the conductance of MIM samples was shown to have common properties with long-term synaptic plasticity in neuromorphic systems. Biologically plausible mechanisms for synaptic weight modification are subject to soft-bound constraints, a property shared with the MIM samples presented here. Under this constraint, synaptic modifications are dependent on the present synaptic weight and the approach to the limiting conductance is done asymptotically [17]. This property is important for generating stable and unimodal distributions for the synaptic weights. Moreover, it has been shown that improved memory storage capacity can be achieved with soft-bound synaptic plasticity. Fig.8.3 shows our results, in which consecutive positive voltage sweeps were applied in a sample of series 1, leading to a continuous decrease of the sample conductance. The reciprocal mechanisms occur with consecutive negative voltage sweeps. The continuous increase of the current towards a constant value indicates the onset of the long-term-memory (LTM) stage of the device. One can also observe the occurrence of larger steps at the initial volt-age sweeps and smaller ones when the current approaches its constant value. This supports the idea that updates tend to become smaller as learning progresses [18-20].

8.3 Switching characteristic of hydrogenated graphene oxide thin films

The RS mechanism is mostly dependent of GO material due to their resistive behaviour. Although, due to the change in internal carbon structure sp^2 to sp^3 hybridization hydrogenated graphene oxide (HGO) can also a material for switching application [3, 16]. To corroborate this point here we tested the RS behaviour in HGO sample. Fig. 8.4 represents the current *vs* voltage (I-V) plot obtained on GO and HGO (dried at 50°C for 2h) samples in the range of -10 to +10V. In the plot GO shows extremely low current whereas, HGO shows a non-linear behaviour with increase amount of current. Moreover, HGO depicts a clear hysteresis in both sides with typical phenomenon of resistive switching material. Moreover, in this sample at a certain voltage (+9V) during the positive sweep, the current value was dramatically increased, suggesting a set-like condition (SLC) or on-state. In negative bias voltage also a reset-like condition (RLC) or off-state was clearly observed, reflecting the same charge mobility by equivalent internal filament breakage in another side.

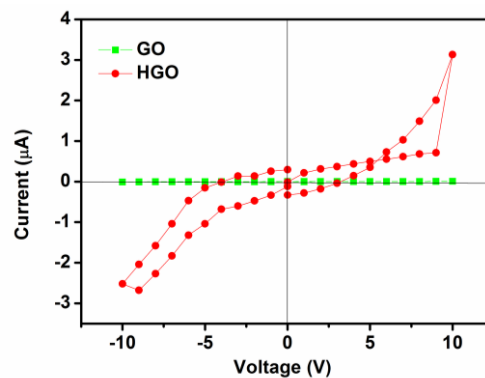


Figure 8.4 Characteristic I *vs* V curve of GO and HGO in bias range of (-10 to +10V). The voltage is swept in the direction as follows: 0 V → 10 V → 0 V → -10 V → 0 V.

For better understanding, we have also performed I-V measurements in higher voltage conditions in two different ranges -15 to +15V and -20 to +20V, respectively. Fig. 8.5 (a) also shows the progression of the current and evolution of similar resistive switching polarity in the positive region [14]. However, in the negative loop the situation was obscured and, instead of switching only hysteresis was retained inside the system. This was probably due to the recursion of internal sp^3 (-C-H) bonding and restoration of sp^2 (-C=C) graphitic structure during the process.

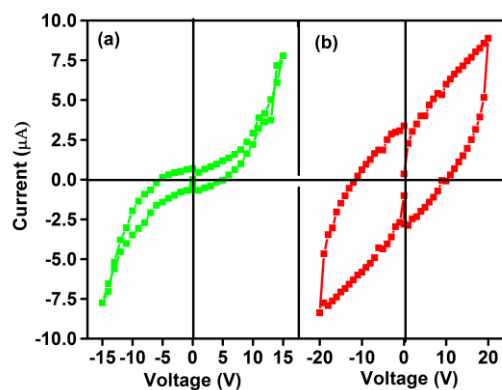


Figure 8.5 I vs V curve of HGO in bias range of (a) sweeping voltage (-15 to +15V) and (b) (-20 to +20V). The voltage is swept in the direction as follows: 0 V \rightarrow 10 V \rightarrow 0 V \rightarrow -10 V \rightarrow 0 V.

However, at higher voltage (20V), both positive and negative region represents a clear hysteresis loop without any specific switching. This was expected because, at higher voltage the whole filaments were broken and current reached the saturation and only internal charge trapping was accessible inside the system [12,14,16].

8.4 Resistive switching in Co/RGO nanocomposite

In this work, instead of Ni NPs we used the Co NPs to understand the RS mechanism based different kind of transition metal NPs. First, we have synthesized the Co/RGO nanocomposite than it was fabricated on conducting ITO thin film and investigated the response of Co/RGO nanocomposite towards RS under bias range of [-10, +10] V.

8.4.1 Synthesis of Co/RGO nanocomposite

To synthesize the Co/RGO nanocomposite, 10 mL of aqueous GO dispersion (1.5 mg/mL) was placed in a beaker and afterward $\text{CoCl}_2 \cdot 6\text{H}_2\text{O}$ (90 mg) was mixed by mechanical stirring (800 rpm) at RT. Afterward, CTAB and PVP (6.5 mg, each) were added in reaction mixture and thoroughly mixed by stirring (3 h). Then, NaBH_4 solution (0.2 M ethanol) was slowly added to the reaction mixture and the stirring was maintained for further 45 min. After completion of the reaction, the product was centrifuged (18 000 rpm) and multiply washed with ethanol and Milli Q water to remove the impurities. Finally, the product was vacuum dried at 250 $^\circ\text{C}$ for 12 h and referred as Co/RGO nanocomposite.

8.4.2 Electrical measurements

For electrical measurements, GO and Co/RGO dispersions were prepared in tetrahydrofuran (THF) and drop coated on indium-tin oxide (ITO) substrates. Both samples were dried in oven at 60 °C for 2h.

8.4.3 Results and discussion

Fig. 8.6 displays the current vs voltage (I-V) plots of GO and Co/RGO nanocomposite samples in the range of [-10, +10] V. I-V measurement of GO shows that the extremely low value of current 16 nA in (Left panel).

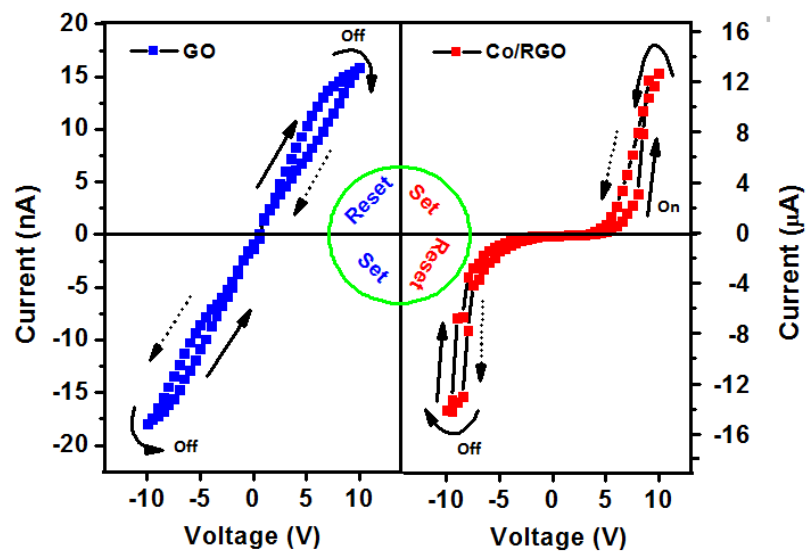


Figure 8.6 Characteristic I vs V curve of GO (Left panel) and Co/RGO nanocomposite (Right panel) in bias range of [-10, +10] V. The voltage is swept in the direction as follows: 0 V → 10 V → 0 V → -10 V → 0 V. The middle circle represents the Set and Reset like conditions of current under bias voltage, in respective quadrants.

This was obvious since GO is an insulator material which contains the various kinds of oxygen functionalities and they disrupt the sp^2 hybridized conjugated graphene network and restrict the electrons flow [14]. The main features with them in both sides (positive and negative bias ranges) are that the current value was equal with linearity and current exhibited the reset and set like conditions, as shown in middle circle in plot with notation (Left half circle) [12]. However, with Co/RGO nanocomposite the situation was completely different (Right panel). A non-linear behavior of I-V was observed with increased amount of current value (12.5 μ A). The non-linearity of I-V between [-5, +5] V can be explain on the basis of the presence of resistive $Co(OH)_2$ phases on core of metallic Co within graphene layers which restrict the flow

of electrons and behave as rectifier such as in diodes [14]. However, at high tension conditions more than (+5V and -5V) the current values were dramatically increased, possibly due to the sudden formation of filaments [13]. Interestingly, in both sides a clear hysteresis was observed and this phenomenon resembles a memristive behavior (in which current switches at certain voltage range), suggesting the complementary resistive switching kind of behavior [21]. This might be explain on the basis of two factors: (i) formation of ligament/filament at the junction points of bottom electrode and Co/RGO film on the few nm scale due to the partial oxidation of metallic Co to Co (OH)₂ and, (ii) rupture of filaments at certain point and out flow of fermi level electrons to bottom electrode side. It can also be observed that, in both sides the extent of current was equal, reflecting the same charge mobility by equivalent internal filament breakage in the other side. The interesting features were there, during the positive-sweeping of voltage the current changed in an anticlockwise direction suggesting on-state with set like conditions. On the other hand, at negative bias voltage an off-state or reset like conditions were clearly observed (right half circle, in plot).

8.5 New hybrid material Ni(OH)₂@Ni/RGO nanocomposite for resistive switching applications: Observation of large hysteresis

In this work a large hysteresis was observed under applied bias voltage in Ni(OH)₂@Ni/RGO nanocomposite. To synthesize the nanocomposite a highly efficient process was developed, which yielded the novel one dimensional (1D) array of Ni(OH)₂ on Ni/RGO nanocomposite by two step method. In first step, Ni nanoparticles (NPs) were decorated on reduced graphene oxide (RGO) by the simultaneous reduction of Ni²⁺ ions and graphene oxide (GO) under reducing conditions. In next step, one dimension (1D) arrays of Ni(OH)₂ were uniformly grown on Ni/RGO by precipitation of Ni²⁺ ions using urea and NaOH. The reduction of GO, formation of Ni/RGO and Ni(OH)₂@Ni/RGO nanocomposite were verified by various characterization techniques.

8.5.1 Synthesis of Ni(OH)₂@Ni/RGO

Ni(OH)₂ nanotubes were grown on Ni/RGO nanocomposite by homogeneous co-precipitation of nickel acetate salt in presence of urea and NaOH. First, a precalculated amount of Ni/RGO was dispersed in 60 mL DD water after exposure to ultrasound from an ultrasonic bath for 45 min then the mixture was heated at 90 °C for 1.5 h. Afterward, 300 mg of nickel acetate salt was added in above dispersion and dissolved by mechanical stirring (300 rpm). Then after, to precipitate the Ni²⁺ a precalculated amount of NaOH (300 mg) was added and

dissolved by stirring. When, it was cooled to RT, 400 mg urea was mixed and stirred for 8 h. Finally, product was collected by filtration and washed with DD water and ethanol in an attempt to remove impurities. In order to obtain a Ni(OH)₂@Ni/RGO nanocomposite product was dried at 80 °C for 8 h under vacuum [22].

8.5.2 Results and discussion

Fig. 8.7 shows the XRD spectra of GO, Ni/RGO and Ni(OH)₂@Ni/RGO nanocomposite. GO exhibits a sharp peak at around 11.01° corresponds to the (001) basal plane and indicates the good exfoliation of graphite flakes [14].

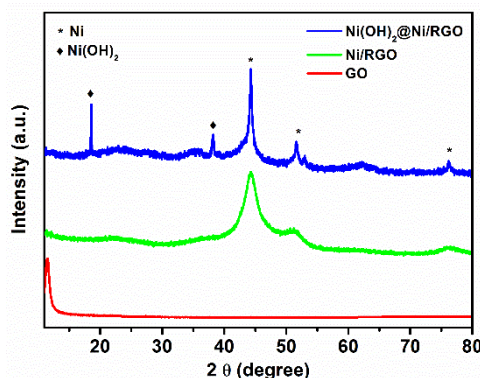


Figure 8.7 XRD pattern of GO, Ni/RGO and Ni(OH)₂@Ni/RGO nanocomposite.

The successful synthesis of Ni NPs and simultaneous reduction of GO to RGO is clearly depicted in diffraction spectra of Ni/RGO. In which GO peak was completely diminished and a new peak was evolved at 22.2° suggested the removal of intercalated water molecules and surface oxygen functionalities during the reduction process. Moreover, in Ni/RGO diffraction spectra three additional peaks were also observed and located on 44.5°, 51.8° and 76.76° and attributed as diffraction from (111), (200) and (220) various crystallographic planes of face-centred cubic (fcc) Ni (JCPDS card No. 04-0850) [14]. Further, precipitation of Ni²⁺ to Ni(OH)₂ in presence of under basic condition was also confirmed by the XRD. In basic condition Ni salt became hydrolysed and precipitated by hydroxide ions at high pH as shown in equation 8.1:



In XRD pattern of Ni(OH)₂@Ni/RGO nanocomposite two extra peaks were presented at 19.2° and 38.3° and attributed as diffraction from (001) and (101), respectively with good agreement of (JCPDS card No. 14-0117). The presence of these two peaks in XRD pattern indicated the formation of β-Ni(OH)₂ phase on Ni/RGO nanocomposite [23]. In next, we have carried out the RT field dependent magnetization (M–H) characterization of Ni(OH)₂@Ni/RGO nanocomposite as shown in Fig. 8.8. The magnetization of the samples would approach the saturation values when the applied magnetic field increases to 1 Tesla. The saturation magnetization of Ni(OH)₂@Ni/RGO nanocomposite was 4.8 emu/gm. This value is quite lower compared to bulk value of Ni 55 emu/g and previously reported Ni/RGO work [24]. The low value of saturation magnetization is due to the presence of an inert layer of Ni(OH)₂ on the surface of Ni/RGO.

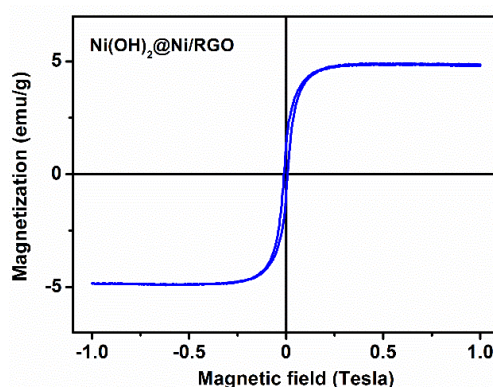


Figure 8.8 RT magnetic measurement of Ni(OH)₂@Ni/RGO nanocomposite.

The morphology of the GO, intermediate Ni/RGO and Ni(OH)₂@Ni/RGO nanocomposite were observed by scanning electron microscopy. Fig. 8.9 (a) and (b) shows the SEM images of initial material GO in lower and higher magnifications, respectively. Images of GO clearly exhibits the few layer of graphitic carbon with typical wrinkle and flappy behaviour [14]. Fig. 8.9 (c and d) depicts the SEM images of intermediate species Ni/RGO after the reduction and loading of Ni NPs within graphene matrix. Both the images depicts the well intercalation of Ni NPs with graphitic flakes [24]. The small particle size was due to the fast degree of nucleation comparative to crystal growth, especially, in presence of GO. Graphene layers works as a blanket for generated nuclei and restrict the approach of new nuclei and controlled the further growth. The distribution of NPs on graphene layer can also control by the surface functionalities of GO. Initially, surface functional groups of GO such as carboxylate

ions (COO^-) and hydroxyl ions (OH^-) behaves as a cross-linker and chelating agent and attracted the cationic specie (in our case Ni^{2+} ions from the bulk solution). After that, at the time of reduction mostly oxygen functionalities were deprive and leaves the defects on graphene sheets. Due to this when cations were reduced they specifically, anchored on graphene defects sites and were less agglomerated and provided the monodispersity of NPs on graphene layers. Moreover, *in-situ* generated N_2 and H_2 gases (by the decomposition of N_2H_4 and NaBH_4 , respectively; equations 2 and 4) also, efficiently exfoliate the graphene layers and provide the homogeneity for colloidal dispersion [22]. In this respect, both SEM images shows that Ni NPs were in spherical shape and well separated and distributed on graphene sheet without any specific agglomerations. Similar situation was retained and became more clear in Fig. 8.9 (e and f) after the intercalation of $\text{Ni}(\text{OH})_2$ on Ni/RGO intermediate material higher and lower magnifications, respectively.

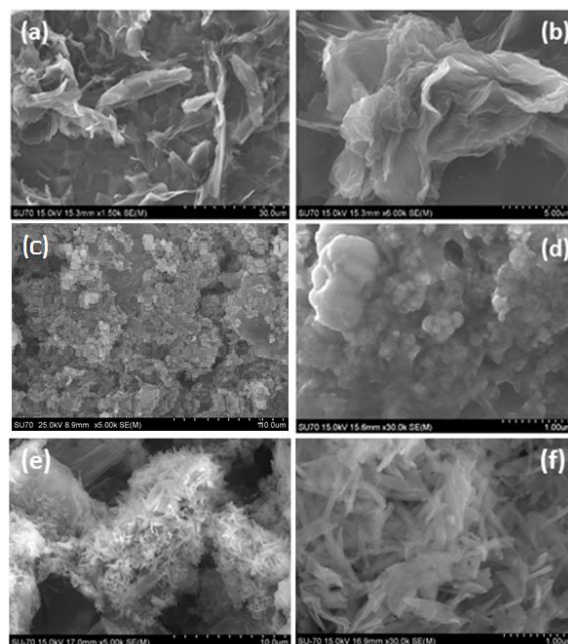


Figure 8.9 SEM images of (a and b) GO, (c and d) Ni/RGO and (e and f) $\text{Ni}(\text{OH})_2$ @Ni/RGO nanocomposite at lower and higher magnifications, respectively.

Both images shows that the high density of $\text{Ni}(\text{OH})_2$ nanotubes on graphene sheets and indicates the successful formation of $\text{Ni}(\text{OH})_2$ @Ni/RGO nanocomposite where crumpled RGO platelets were closely connected with each other and forming a 3D network structure. Moreover, in both images tubes were stacked on to the center endowing the Ni NPs and presence of highly dense 1D array of nanotubes indicated that the Ni NPs works as a nucleation center for growth site of $\text{Ni}(\text{OH})_2$ species.

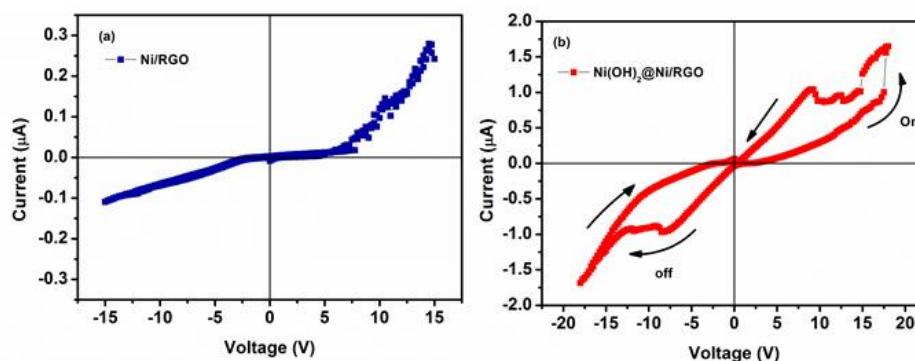


Figure 8.10 I vs V curve of Ni/RGO (Left panel) and Ni(OH)₂@Ni/RGO nanocomposite (Right panel) under bias voltages. The voltage is swept in the direction as follows: 0 V → + V → 0 V → -V → 0 V.

The I–V curves of the Ni/RGO and Ni(OH)₂@Ni/RGO nanocomposite films presented in Fig. 8.10. Fig. 8.10 (a) shows that the Ni/RGO film possess less amount of current and behaves as an insulating material, revealing their high resistance state and low current ($I \approx 10^{-7}$ A) without any hysteresis. However, Ni(OH)₂@Ni/RGO nanocomposite revealing one order increase amount of current ($I \approx 10^{-6}$ A) (Fig. 8.10 (b)). Along with, large hysteresis with nonlinear curvature and resistive switching like behavior of the current and on /off states, indicated a memristive structure [14]. At the positive sweeping voltage, the current changes in counter clockwise direction, suggesting SLC and under negative sweeping voltage, the current changes in clockwise direction, suggesting a RLC behavior [13].

8.6 Ag@SiO₂/RGO nanocomposite for memristor application

The aim of this work is finding the possibility of high conductivity with large hysteresis and resistive switching characteristics in nanomaterial. To construct the MIM structure, the role of middle layer is very important. It should form easily filament networks between the top and bottom electrodes. However, it has been observed that in some materials such as SiO₂ NPs the switching property is not very much pronounced. Even though, after the integration of GO and RGO. This might be due to the somehow charge storage between the graphene layers and buckling of carbon sheet. To circumvent such kind of problem a new strategy is require that may help to increase conductivity of the system and boost the filament formation/rupture at certain point under bias voltage.

8.6.1 Synthesis of Ag@SiO₂/RGO nanocomposite

In this work Ag NPs were integrated with SiO₂ nanotubes to make the 1-D structure of Ag@SiO₂ and further it was integrated with graphene support. The reduction of GO was achieved by the exfoliation of graphene sheet in 1M NaOH in isopropanol medium at 55 °C.

8.6.2 Device fabrication of Ag@SiO₂/RGO nanocomposite

The nanostructure of Ag@SiO₂/RGO nanocomposite was dip coated on Pt bottom electrode as shown in Fig. 8.11 and top electrode was made by Ag paint. During the measurements, the voltage swept in the direction of 0 → V_{max} → 0 → -V_{max} → 0 sequence (where V_{max} is the maximum applied voltage). No forming process was applied to activate the RS effect.

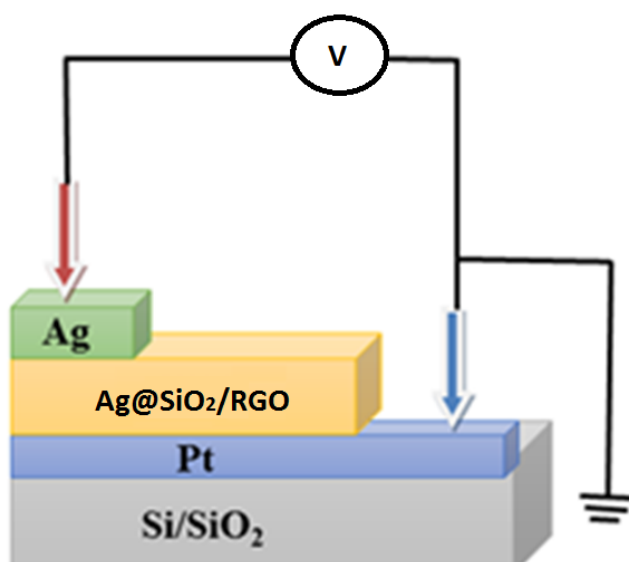


Figure 8.11 Schematic representation of device fabrication based on Ag@SiO₂/RGO nanocomposite.

8.6.3 Results and discussion

The morphology of the Ag@SiO₂/RGO nanocomposite is shown in Fig. 8.16. In which SiO₂ nanotubes were in cylindrical shapes and few micrometer range with the average aspect ratio of 1:20. Fig. 8.12 (a) and (b) displays the lower and higher magnification images of SiO₂ nanotubes, respectively. Fig. 8.12 (c) and (d) shows the SEM images of Ag@SiO₂/RGO nanocomposite in lower and higher magnification, respectively. In which the Ag NPs were well intercalated with SiO₂ nanotubes and graphene sheets were rolled to cylindrical SiO₂ nanotubes and makes the contacts to each other without any agglomeration.

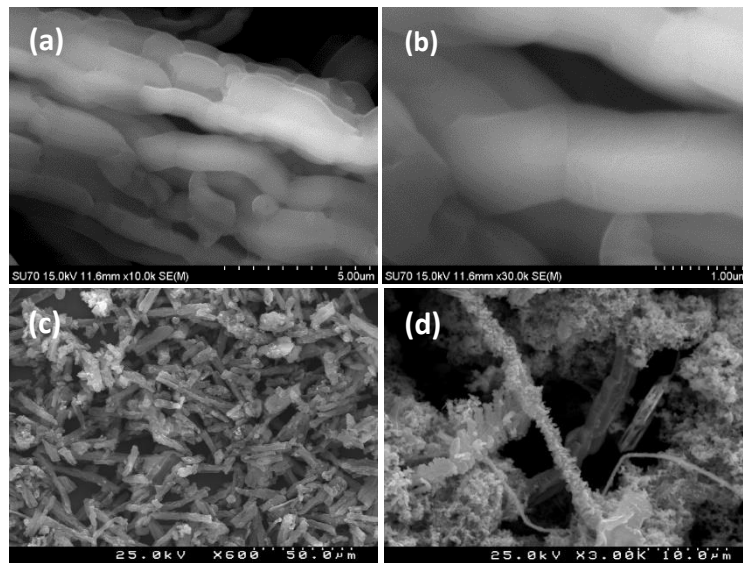


Figure 8.12 SEM images of SiO_2 nanotubes (a) and (b) in lower and higher magnifications, respectively and (c) and (d) $\text{Ag@SiO}_2/\text{RGO}$ nanocomposite at lower and higher magnifications, respectively.

Fig. 8.13 shows the I vs. V characteristic of $\text{Ag@SiO}_2/\text{RGO}$ nanocomposite in which the current suddenly increases (at certain point) under positive sweeping of voltage and reached to maximum highest capacity of system till 0.9 A (900 mA) at 0.8 V in SLC direction, suggests the “on” state of switching device.

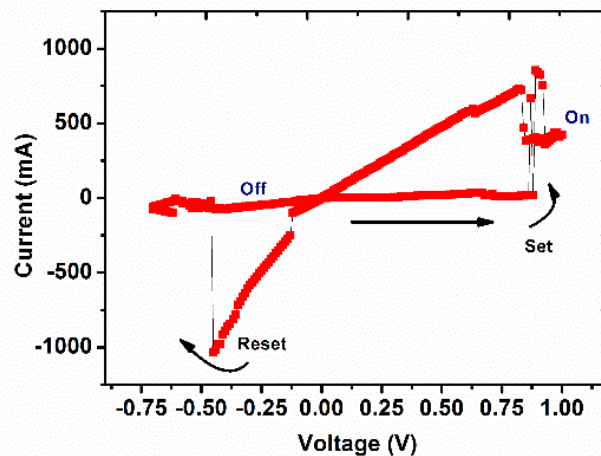


Figure 8.13 I vs V curve of $\text{Ag@SiO}_2/\text{RGO}$ nanocomposite (Right panel) under bias voltages. The voltage is swept in the direction as follows: $0\text{ V} \rightarrow +V \rightarrow 0\text{ V} \rightarrow -V \rightarrow 0\text{ V}$.

In negative direction also same behavior was observed with opposite polarity indicating current “off” and RLC condition. The high current value and switching property under very low bias applied condition can be ascribed on the basis three facts: Initially, SiO₂ nanotubes pursuit’s the insulator behavior so device shows that highest resistance state and at certain point due to the rupture of sudden filaments the conductivity was increased. Here, the presence of extra -OH groups are very important that were provided by SiO₂ nanotubes. SiO₂ is well known to make the SiO₂ (-OH) bonding and in our synthesis protocol (in basic medium) the extra hydroxyl groups (-OH) easily attached of them. Moreover, the large cylindrical structure and hollow cavity of SiO₂ nanotubes also makes two advantages: (i) it accommodated Ag NPs inside of them, which provided the highest conductivity at the time of filament rupture (extra charge to be flow), and (ii) short circuit condition through inter nanotube linkage. Moreover, presence of SiO₂ nanotubes enhances the film formation capability of RGO. It has been already reported that RGO and graphene exhibits very high water contact angle (hydrophobicity), makes difficulty for film formation in aqueous medium.

Further, to confirm the extra -OH groups on surface and Ag in cavity provide the feasibility of RS we have synthesized the Ag@KZ/RGO nanocomposite based on zeolite NPs under similar reaction conditions. It should be noted here, KZ is also a good electrical insulator material keeping the K⁺ cations inside of their cavity [24]. Interestingly, it also shows the resemblance of I-V characteristics as Ag@SiO₂/RGO nanocomposite; however, it displays some distinction with them as shown in Fig. 8.13.

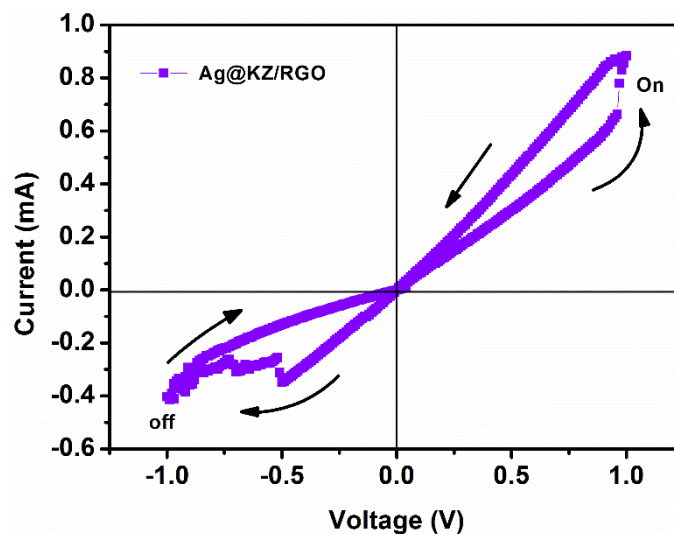


Figure 8.13 I vs V curve of Ag@KZ/RGO nanocomposite (Right panel) under bias voltages. The voltage is swept in the direction as follows: 0 V → + V → 0 V → -V → 0 V.

In Ag@ KZ/RGO nanocomposite the current was three order lesser than Ag@SiO₂/RGO nanocomposite. This was probably, due to the less conductivity of the system and less number of –OH groups on the surface. Although, it shows the continuous resistance change with bias along with hysteresis and curvature on end points of the curve, which makes the loop on both sides (set to reset and reset to set). Probably, it was due to the migration of K⁺ cations from one cavity to another in rigid alternative tetrahedral network of AlO₄⁻ and SiO₄⁻ entities under applied bias field and continuous flow of the charge inside of the system. This phenomenon arise an interesting point formation of the “pinch hysteresis loop” and small curvature at the end of the loop.

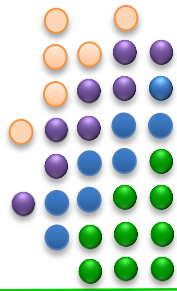
8.7 Conclusions

In summary, we have investigated the resistive switching behavior in transition metals (Ni, Co and Ag) doped nanocomposites. Results shows that resistive switching behavior highly dependent on MIM structure along with doped transition metal. The highest conductivity and resistive switching phenomenon was observed in Ag doped graphene nanocomposite; however repeatability, endurance and device stability was observed in Ni based graphene nanocomposite.

8.8 References

- [1] K. S. Novoselov, A. K. Geim, S. V. Morozov, D. Jiang, Y. Zhang, S. V. Dubonos, I. V. Grigorieva, A. A. Firsov. *Science*, 306 (2004) pp. 666- 669.
- [2] A. K. Geim, K. S. Novoselov. *Nat Mater*, 6 (2007) pp. 183-191.
- [3] R. Krishna, E. Titus, L. C. Costa, J. C. J. M. D. S. Menezes, M. R. P. Correia, S. Pinto, J. Ventura, J. P. Araújo, J. A. S. Cavaleiro, J. J. A. Gracio. *J Mater Chem*, 22 (2012) pp. 10457-10459.
- [4] Y. Wang, Y. Shao, D. W. Matson, J. Li, Y. Lin. *ACS nano*, 4 (2010) pp. 1790-1798.
- [5] X. Miao, S. Tongay, M.K. Petterson, K. Berke, A.G. Rinzler, B.R. Appleton, A.F. Hebard. *Nano Lett.*, 12 (2012), pp. 2745-2750.
- [6] H.Y. Jeong, J.Y. Kim, J.W. Kim, J.O. Hwang, J.-E. Kim, J.Y. Lee, et al. *Nano Lett.*, 10 (2010), pp. 4381-4386.

- [7] S. G. Hu, S. Y. Wu, W. W. Jia, Q. Yu, L. J. Deng, Y. Q. Fu, Y. Liu, T. P. Chen. *Nanosci Nanotechnol*, 6 (2014) pp. 729-756.
- [8] L. O. Chua. *IEEE*, 18-5 (1971) pp. 507-519.
- [9] T. Prodromakis, C. Toumazou. *ICECS*, 978-1-4244-81567-69/10/\$26.00 ©2010 IEEE”, *Electronics, Circuits, and Systems, ICECS 2010* .
- [10] D.B. Strukov, G.S. Snider, D.R. Stewart, R.S. Williams. *Nature*, 453 (2008) pp. 80–83.
- [11] M.-J. Lee, C. B. Lee, D. Lee, S. R. Lee, M. Chang, J. H. Hur, Y.-B. Kim, C.-J. Kim, D. H. Seo, S. Seo, et al., *Nat Mater*, 10 (2011) 625630.
- [12] S. Pinto, R. Krishna, C. Dias, G. Pimentel, G.N.P. Oliveira, J.M. Teixeira, P. Aguiar, E. Titus, J. Gracio, J. Ventura, J.P. Araujo. *Appl. Phys. Lett*, 101 (2012), pp. 063104.
- [13] O. Okhay, R. Krishna, M. Salimian, E. Titus, J. Gracio, L.M. Guerra, J. Ventura. *J. Appl. Phys.*, 113 (2013), p. 064307.
- [14] R. Krishna, E. Titus, O. Okhay, J.C. Gil, J. Ventura, E.V. Ramana, J.J.A. Gracio. *Int. J. Electrochem. Sci*, 9 (2014), pp. 4054–4069.
- [15] S. Hong, J. Kim, S. Kim, S.-Y. Choi, B. Cho, *IEEE Electr Device L*, 31 (2010)pp. 1005.
- [16] Zhuge et al. *Non-Volatile Resistive Switching in Graphene Oxide Thin Films, Physics and Applications of Graphene - Experiments*, Dr. Sergey Mikhailov (Ed.), ISBN: 978-953-307-217-3, InTech open (2011).
- [17] M. C. W. van Rossum, G. Q. Bi, G. G. Turrigiano. *J. Neurosci*. 20, (2000) pp.8812
- [18] S. Fusi, L. F. Abbott. *Nat. Neurosci*. 10, (2007) pp.485.
- [19] Y. Liu, T. P. Chen, Z. Liu, Y. F. Yu, Q. Yu, P. Li, S. Fung. *Appl. Phys. A* 105, (2011) pp. 855.
- [20] C. Zamarreno-Ramos, L. A. Camuas-Mesa, J. A. Perez-Carrasco, T. Masquelier, T. Serrano-Gotarredona, B. Linares-Barranco. *Front. Neurosci*. 5, (2011) pp.26.
- [21] G. Tang, F. Zeng, C. Chen, H. Liu, S. Gao, C. Song, Y. Lin, G. Chen, F. Pan
Nanoscale, 5 (2013) pp. 422-428.
- [22] R/ Krishna, C. Dias, J. Ventura, E. Titus. *Mat Today Proc*, 2 (2015) pp. 407-413.
- [23] Y. Wang, Q. Zhu, H. Zhang. *Chem Commun*, 47 (2005), pp. 5231–5233.
- [24] B. Li, H. Cao, J. Yin, Y.A. Wub, J.H. Warner. *J Mater Chem*, 22 (2012) pp. 1876–1883.
- [25] M. Salimian, O. Okhay, R. Krishna, E. Titus, J. Gracio, L. Guerra, J. Ventura, C. Freire, C. Pereira, P. R. Babu, R. S. Khairnar. *Polym Int* 62(2013) pp.1583-1588.



CHAPTER 9

Ni/RGO NANOCOMPOSITE FOR GLUCOSE BIOSENSING:

Structure, measurements and results



Chapter 9

<u>Ni/RGO nanocomposite for glucose biosensing: Structure, measurements and results</u>	190
9.1 Introduction	192
9.2 Experimental	193
9.2.1 Chemicals	193
9.2.2 Synthesis of Ni/RGO nanocomposite	193
9.2.3 Preparation of Ni/RGO/Chit95/GOx Films	194
9.2.4 Characterization techniques	194
9.3 Results and discussion	195
9.4 Conclusions	199
9.5 References	200

Ni/RGO NANOCOMPOSITE FOR GLUCOSE BIOSENSING:

Structure, measurements and results

9.1 Introduction

Recently, vast research is going on for the detection of glucose level in blood and food, particularly in aqueous solutions due to their great importance in health, research, environmental monitoring and industrial production. Diabetes mellitus is one of the leading causes of death and disability in the world. Therefore, the determination of blood glucose levels is an indispensable test for the diagnosis and management of diabetes mellitus. [1-3].

In this regard, electrochemical sensors can characterized the level of glucose, with good sensitivity, rapid and reliable response, and, more importantly, do not require laborious sample pretreatment or labeling. Furthermore, commercially available low-cost miniaturized electrode chips and hand-held workstations (which can be controlled with a smartphone) put this technology ahead their competitors in the race to develop wearable analytical tools for point-of-care solutions, in-field measurements [4-6].

In the last decade discovered graphene, has been also used for this purpose with different nanocomposite systems [7-8]. The derivative of graphene which is called as graphene oxide (GO), indeed provided the possibility of anchoring of various kind of NPs with them to fabricate the biosensor array on top of glassy carbon electrode (GCE). Due to this reason, purposely for biosensing application, many graphene nanocomposites have been prepared with chitosan, which is a deacetylated derivative of the abundant chitin polysaccharide, due to their excellent film forming ability and biocompatibility [9-16].

The most studied graphene based nanohybrids in electroanalytical applications are based on Au [11], however, high price of noble metals restricts the research environment and urges the scientific community for more economical option for such an application. For instance, a cheaper system such as Ni/RGO nanocomposite still has been barely explored for glucose biosensing [16].

In this work, we report the synthesis of Ni/RGO nanocomposite by the simultaneous reduction of Ni (II) salt with GO and their application for glucose biosensing purpose.

9.2 Experimental

9.2.1 Chemicals

Glucose oxidase from *Aspergillus Niger* (GOx, Fluka), D-(+)-glucose (Merck), tetrapotassium hexacyanoferrate trihydrate (Fluka, $K_4[Fe(CN)_6] \cdot 3H_2O$) and tripotassium hexacyanoferrate (Fluka, $K_3[Fe(CN)_6]$) were analytical grade and used as received. Chitosan deacetylated to a 95% (Chit95) was purchased from Primex (Siglufjordur, Iceland, 150-200 kDa). Other analytical grade chemicals used in this work were purchased to Sigma Aldrich. Stock solutions of acetate buffer 0.1 M (AB, pH 5) and phosphate buffer saline 0.05 M (PBS, pH 7.3, $[NaCl]=0.15$ M) were prepared in ultrapure water from a Milli-RO 3 Plus system (18.2 $M\Omega \cdot cm$ resistivity).

9.2.2 Synthesis of Ni/RGO nanocomposite

GO was synthesized from graphite powder through a modified Hummers method [15]. Ni/RGO hybrid sheets were grown *in situ* as follows: 100 mL of GO aqueous dispersion (1 $mg \cdot mL^{-1}$) were placed in a 4-neck round bottom flask and mechanically stirred at RT. Subsequently, 600 mg of nickel chloride hexahydrate ($NiCl_2 \cdot 6H_2O$) were added and the temperature was gradually increased to 85 °C. Then, 18 mL of hydrazine hydrate (65%) were slowly poured into the reaction mixture and stirred for 25 min in Ar atmosphere. Afterwards, 450 mg of sodium borohydride ($NaBH_4$) were very slowly added under stirring. Finally, 25 mL of a 1 M sodium hydroxide (NaOH) solution were added and stirred for further 150 min. The product was filtered and washed with ethanol and doubled-distilled water to remove impurities. Then, it was vacuum-dried at 100 °C for 3 h to obtain the Ni/RGO nanocomposite powder.

9.2.3 Preparation of Ni/RGO/Chit95/GOx Films

Ni/RGO/Chit95/GOx nanocomposite film was deposited onto a glassy carbon electrode (GCE, Metrohm, 6.1204.300, area: 0.06 cm²) following a sequential drop-casting procedure. GCE was polished with 0.3 μm Alumina slurry (Buehler Micropolish II) to a mirror finish and washed in water, ethanol, and acetone (15 minutes each) in an ultrasound bath. Cyclic voltammetry (CV) was performed in H₂SO₄ 0.5 M and the result compared to the typical response of clean GCE. Then, GCE was modified in three steps. First, 10 μL of Ni/RGO dispersion in ethanol (1 mg·mL⁻¹) were spread onto the GCE surface and air dried. Then, 10 μL of a Chit95 solution in AB 0.1 M (5 mg·mL⁻¹) were casted. Once dried, 10 μL of a GOx solution in PBS 0.05 M (10 mg·mL⁻¹) were dropped.

9.2.4 Characterization

The phase purity, crystallinity and structure of GO and Ni/RGO were characterized by X-ray diffraction (XRD, Cu K_α radiation; λ = 0.15414 nm) in the range 2θ=10-80° with scan rate of 0.02° min⁻¹. Fourier-transformed infrared spectra (FTIRS) were recorded in the range 1200-2600 cm⁻¹. Scanning electron microscopy (SEM) images were taken using a SU-70 microscope. Conventional high-resolution tunnelling electron microscopy (LaB₆, TEM) was performed to analyze the crystallinity and quality of the samples. Electrochemical characterization was conducted at room temperature in pure PBS 0.05 M electrolyte and in the presence of 2 mM [Fe(CN)₆]^{3-/4-} using a Voltalab PGZ301 potentiostat (Radiometer Analytical). Before measurements, the electrolyte was purged with N₂ for 10-15 min to remove O₂. Freshly annealed Pt and sanded Ag wires were used as counter and reference electrodes, respectively. Cyclic voltammetry (CV) and electrochemical impedance spectroscopy (EIS) were used to follow the construction of the film. CVs were acquired at 0.05 V s⁻¹ in the range -0.3 to 0.6 V. Impedance spectra were taken at the formal potential. A sine wave of 10 mV amplitude and decreasing frequency in the range 10 kHz - 0.1 Hz was imposed over this bias. Unless otherwise stated, the spectra were fitted to a Randles-type equivalent circuit.

9.3 Results and Discussion

Fig. 9.1 shows the XRD patterns of GO and Ni/RGO. In XRD of GO, a single sharp peak was found at around 11° which is ascribed to the diffraction of the (001) basal plane of GO [15]. The d-spacing was $d_{001}=0.83$ nm which is consistent with the interlayer distance reported for GO but higher than in graphite flakes (0.334 nm) which confirms the introduction of functional groups and intercalating water molecules. After the reduction, this peak was disappeared and, instead, a series of new bands appeared in the XRD of Ni/RGO.

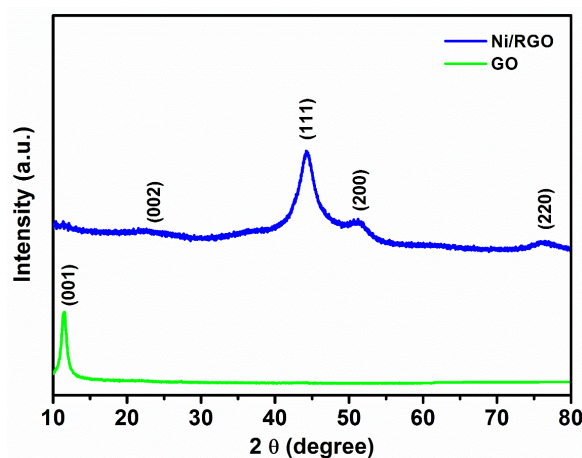


Figure 9.1 XRD of GO and Ni/RGO.

The peak at around 23° ascribed to the (002) crystallographic plane of RGO [16], strongly suggests the well accomplishment of reduction process and elimination of mostly oxygen functionalities from basal planes and edge sites of graphene. The position and intensity of the other peaks presence of Ni crystals with face centered cubic structure (fcc). The highest intensity (111) diffraction peak at $2\theta = 44.4^\circ$ confirms the formation of crystalline phase. Deeper insights on the composition of the hybrid conjugate were obtained by means of FTIR spectroscopy. The spectra gathered for the GO and Ni/RGO samples are shown in Fig. 9.2. GO featured two well-defined peaks at 1625 and 1730 cm^{-1} related to the hydroxyl bending (due to adsorbed H_2O) and asymmetric stretching of ketones ($\nu_{\text{C}=\text{O}}$), respectively. Whereas, in FTIR of Ni/RGO both bands were eliminated and instead of that a new band was observed at 1610 cm^{-1} ($\nu_{\text{C}=\text{C}}$), indicated that restoration of graphite structure. Further, the structure and morphology of the Ni/RGO nanocomposite was investigated by SEM and TEM techniques.

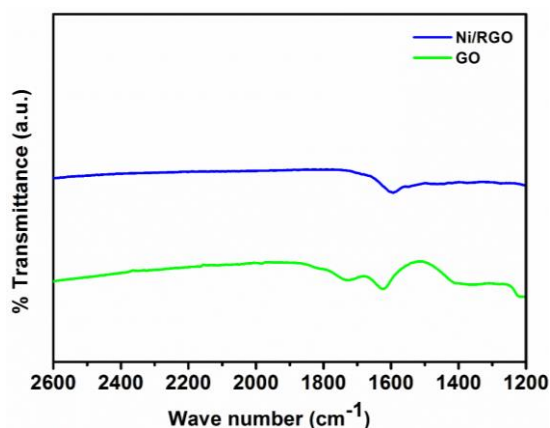


Figure 9.2 XRD of GO and Ni/RGO.

Fig 9. 3 (a) and (b) shows the SEM images of Ni/RGO nanocomposite in lower and higher magnifications, respectively. Both images shows that well intercalation of Ni NPs with graphitic flakes. Moreover, in both images mostly Ni NPs were covered and encapsulated with graphene sheets and few were observed on the surface on nanocomposite, suggested the formation of discrete assembly of Ni NPs without any specific agglomeration. Next, to better understanding we have also carried out the TEM analysis as shown in Fig 9. 3 (c) and (d) respective, lower and higher magnification images, clearly reveals that homogeneous distribution of isolated spherical Ni NPs on top of graphene sheet; without any aggregation or producing big clusters. The higher magnification TEM image displays the single Ni NP with size ranges 8-10 nm which is almost in spherical shape.

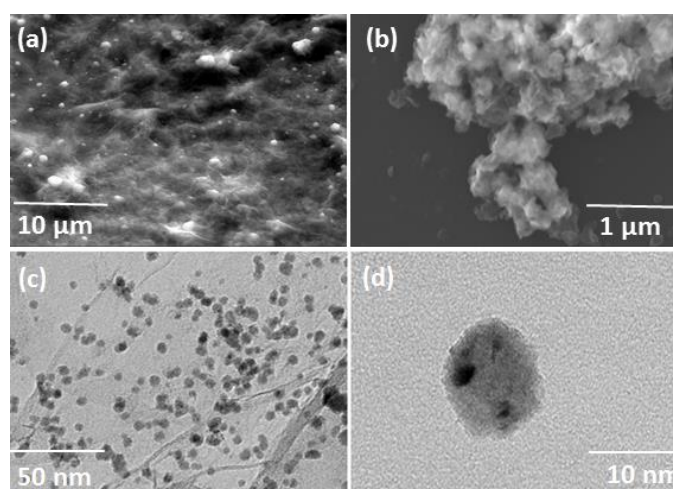


Figure 9.3 Morphological characterization of Ni/RGO nanocomposite: SEM, (a) and (b), and TEM images, (c) and (d), in lower (a and c) and higher (b and d) magnifications, respectively.

Further, as described in the experimental section, a Ni/RGO/Chit95/GOx film was assembled onto a freshly cleaned GCE through a sequential drop-casting method. The buildup process was followed by means of electrochemical measurements in pure 0.05 M PBS.

Fig. 9.4 presents the CVs registered for bare GCE, GCE/GOx, GCE/Chit95, GCE/Chit95/GOx, and GCE/Ni/RGO. As it is seen, the direct adsorption of GOx on GCE induced a partial blockage of the electroactivity. Accordingly, the integrated charge for GCE/GOx (red solid line) was reduced in a 45 % compared to that at the bare GCE (black solid line). This is evidencing a poor conformational stability for the enzyme on this surface. The unfolding of GOx must yield a hydrophobic layer that significantly reduces the capacitance of the GCE (i.e. the amount of charge stored in its interfacial double layer).

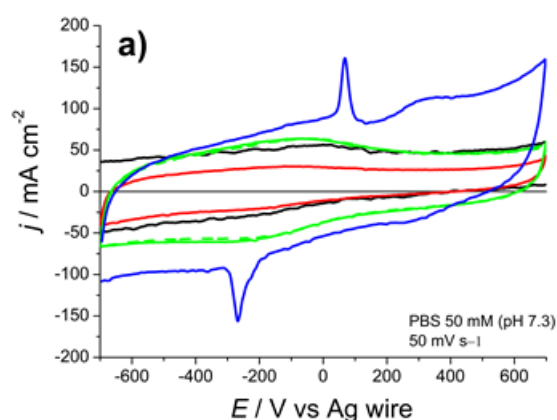


Figure 9.4 CV response of different modified electrodes: GCE (black), GCE/GOx (red), GCE/Chit95/GOx (green, dash), GCE/Chit95 (green, solid) and GCE/Ni/RGO (blue), respectively in 50 mM PBS solution with scan rate of 50 mVs⁻¹.

In contrast, the electroactivity was enhanced at the GCE/Chit95 electrode (green solid curve). Because of its high degree of deacetylation, chitosan may form a highly positively charged film under the working conditions. Hence, solution anions (and their associated water) would diffuse into the film to keep the electroneutrality. Thereby, the capacitance of the electrode must be boosted as reflected by the increased non-faradaic current densities. Contrary CV of GCE/Chit95/GOx (green dashed line) shows negligible changes compared to GCE/Chit95. This result indicates that stability of GOx is significantly improved when supported on chitosan which could be due to: (1) the GCE surface is densely covered by Chit95, or (2) the surface area of the Chit95 film is much higher than GCE's and, then, the impact of

GOx unfolding is minimized. But, after all, the most notable changes in the shape of the CVs were shown for the GCE/Ni/RGO electrode (blue solid line in the figure). On one hand, a large increase in the capacitive current was noticed throughout the whole studied potential range. This is a common observation in graphene-modified electrodes and is due to the high surface-to-volume ratio of graphene and its positive impact in the capacitance. On the other hand, a pair of sharp peaks can be identified at +0.07 and -0.27 V. Despite the significant differences in shape and peak positions (which could be due to the different experimental conditions of synthesis and characterization), a broad peak potential separation, ΔE_P , was found in both cases. The changes induced to this profile upon the successive deposition of Chit95 and GOx layers. The deposition of Chit95 only resulted in a very slight decrease of the non-faradaic current (double layer). However, after the application of both modification steps, the peak currents decreased significantly. In this regard, almost negligible anodic and cathodic peaks were registered for the GCE/Ni/RGO/Chit95/GOx electrode. This result strongly suggests that the exposed surface of the Ni NPs is increasingly passivated with the deposition of the biopolymer and the enzyme layers. Fig. 9.5 presents the interrogations tests performed by CV (Fig 9.5 (a)) and EIS (Fig 9.5 (b)) for bare GCE, GCE/GOx, GCE/Chit95/GOx, and GCE/Ni/RGO/Chit95/GOx in 0.05 M PBS (pH 7.3) + 2 mM $[\text{Fe}(\text{CN})_6]^{3-/4-}$ + 1 mM glucose (dashed lines).

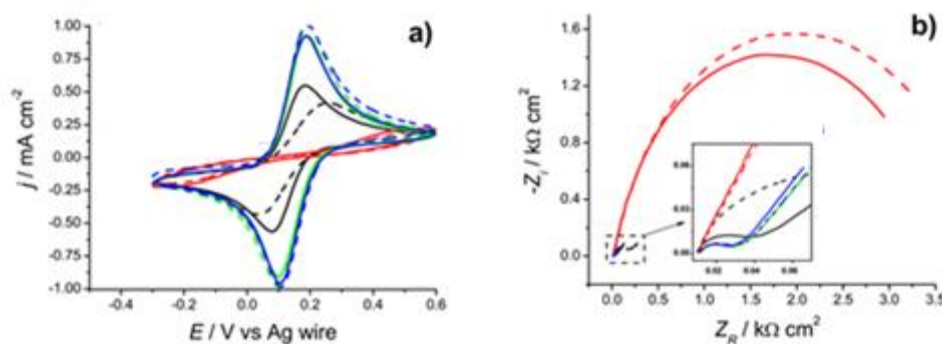


Figure 9.5 (a) CV response of different modified electrodes: bare GCE (black, dash), GCE/GOx (black, solid), GCE/Chit95/GOx (green), and GCE/Ni/RGO/Chit95/GOx (blue solid and dash after the cycles) in 0.05 M PBS (pH 7.3) + 2 mM $[\text{Fe}(\text{CN})_6]^{3-/4-}$ + 1 mM glucose (dashed lines). (b) Nyquist plot of GCE/Ni/RGO/Chit95/GOx electrode obtained at 0.15 V using a 10 mV amplitude. The plots were fitted to a Randles equivalent circuit, double layer capacitance (C_{DL}) and charge transfer resistance (R_{CT}).

The most relevant physical parameters derived from these measurements can be summarized as: in the absence of glucose, the $[\text{Fe}(\text{CN})_6]^{3-/4-}$ probes exhibited good reversibility on a bare GCE. However, as happened with the non-faradaic currents in the direct adsorption of GOx (GCE/GOx, red line), it led to a strong blockage of the faradaic processes. Its Nyquist plot presented a semicircle in the high-medium frequency range which was much larger than the one of bare GCE (black solid line).

In this frequency region, the total impedance is controlled by the apparent charge transfer resistance, R_2 , so that wider semicircles are typically ascribed to lower values of the apparent electron transfer rate constant, k^{ET}_{app} . Agreeing with this qualitative observation, the quantitative value of R_2 (derived in this case from fitting to an equivalent circuit without Warburg element: R_1QR_2) increased by two orders of magnitude to 60.2 k Ω . Whereas, after the modification of the electrode with Ni/RGO as GCE/Ni/RGO/Chit95/GOx electrode, the current density was increased (blue solid line), inferring the redox process on the surface of the new modified electrode which was increased after the 10 cycles, suggested the high catalytic activity and robustness of the Ni/RGO nanocomposite system towards the glucose bio-sensing application.

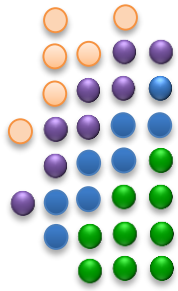
9.4 Conclusions

In this work, we successfully demonstrated the synthesis of Ni/RGO nanocomposite. The structure and morphology were well characterized with XRD, FTIR, SEM and TEM techniques. The response of Ni/RGO nanocomposite was evaluated for glucose biosensing in PBS buffer solution at RT. Results show that the good CV response of the modified GCE/Ni/RGO/Chit95/GOx electrode compared to bare one, indicated the applicability of Ni/RGO for glucose biosensor application also.

9.5 References

- [1] S. Wild, G. Roglic, A. Green, R. Sicree, H. King. *Diabetes Care*, 27 (2004) pp.1047-1053.
- [2] R. R. Holman, S. K. Paul, M. A. Bethel, D. R. Matthews, H. A. Neal. *N Engl J Med*, 359 (2008) pp. 1577-1589.
- [3] J. D. Newman, A. P. Turner. *Biosens Bioelectron*, 20 (2005) pp. 2435-2453.
- [4] J. Wang. *Chem Rev* 108 (2008) pp. 814-825.
- [5] B. Hock. *Anal Chim Acta* 347 (1997) pp. 177-186.
- [6] X. L., Luo, A., Morrin, A. J. Killard, M. R. Smyth. *Electroanalysis* 2006, 18, 319-326.

- [7]K. S. Novoselov, D. Jiang, F. Schedin, T. J. Booth, V. V. Khotkevich, S. V. Morozov, A. K. Geim. PNAS USA, 102 (2005) pp. 10451-10453
- [8] M. Pumera Mater Today, 14 (2011) pp. 308-315.
- [9]C. Shan, H. Yang, D. Han, Q. Zhang, A. Ivaska, L. Niu. Biosens Bioelectron 25(2010) pp. 1070-1074.
- [10]H. Wu, J. Wang, X. Kang, C. Wang, D. Wang, J. Liu, I. A. Aksay, Y. Lin. Talanta 80 (2009) pp. 403-406.
- [11]K. Turcheniuk, R. Boukherroub, S. Szunerits. J Mat Chem, B 3 (2015) pp. 4301-4324.
- [12]K-J. Huang, L. Wang, J. Li, T. Gan, Y-M. Liu. Measurement, 46 (2013) pp. 378-383.
- [13]B. J. Li, H. Q. Cao. J Mater Chem, 21 (2011) pp. 3346-3349.
- [14]H. Qi, C. Wang, N. Cheng. Microchim Acta, 70 (2010) pp. 33-38.
- [15]R. Krishna, E. Titus, L. C. Costa, J. C. J. M. D. S. Menezes, M. R. P. Correia, S. Pinto, J. Ventura, J. P. Araújo, J. A. S. Cavaleiro, J. J. A. Gracio. J Mater Chem, 22 (2012) pp. 10457-10459.
- [16] Q. Chi, J. Zhan, S. Dong, E. Wang. Electrochim Acta, 39 (1994) pp. 2431-2438.



CHAPTER 10

CONCLUSIONS

CONCLUSIONS:

Graphene oxide (GO), the raw material for the synthesis of graphene, was harnessed in various ways to accomplish the synthesis of novel transition metal doped graphene products. Facile and energy efficient methods were employed without using any harmful and toxic chemicals in bulk. The synthesized products were fabricated for diverse applications including energy and electrical applications.

One of the achievements, include the facile synthesis of hydrogenated reduced graphene oxide (HRGO) via hydrogen spillover mechanism. A new strategy has been employed for the reduction and hydrogenation of GO using bulk metallic Ni in acidic medium. Raman, FTIR and XPS were employed to probe the successful hydrogenation of GO to HRGO and results exhibits the same. Moreover, due to the concern of bulk Ni solubility in acidic medium further, Ni NPs were also used as a second approach which shows the accomplishment of reduction reaction within 3 h. The advantage of this method is the change in hybridization state of carbon structure as sp^2 ($-C=C$) to sp^3 ($C-H$) which might be extremely illusive for the fabrication of semiconductor/supercapcitive devices via tuning of band gap and metal dopant concentration.

For hydrogen storage, Pd@NSG nanocomposite was successfully synthesized. In this work a new innovative strategy has been developed for the synthesis of nanocomposite by a facile and cost effective method. In this work, only 2 wt.% of Pd was used and rest was Ni_xB-SiO_2/RGO . Moreover, we have elaborated the synthesis of tiny Pd NPs (size ranges of ~2.5-4 nm) and their superficial attachment on base material using the green and facile approach. Here,

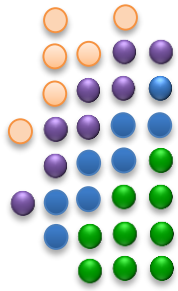
a detailed spillover mechanism is established based on facile H_2 dissociation on Pd (active sites) activator and subsequent transportation of hydrogen atom on receptor sites (Ni_xB - SiO_2 /RGO). Further, H_2 uptake measurements up to 50 bar pressure clearly exhibited the 14 times more storage at RT in Pd@NSG nanocomposite compared to SiO_2 /RGO. For the better understanding of hydrogen storage in porous materials a theoretical modelling work also performed using the grand canonical ensemble Monte Carlo (GCMC) simulations of single-component of small molecule hydrogen and NaA framework based on zeolite system.

In addition to hydrogen storage, efforts were also made for the hydrogen production at RT without using any toxic chemicals or expensive catalyst materials. For the hydrogen production two distinct approaches has been used, first is the electrochemical oxidation of ethanol in basic medium and second is the $NaBH_4$ hydrolysis in alkaline solution. Both methods produces the clean hydrogen energy with a cost-effective manner. For electrochemical oxidation of ethanol a novel catalyst, Pd@ Ni_xB /RGO nanocomposite was synthesized by a facile method. The structure and morphology of Pd@ Ni_xB /RGO nanocomposite were characterized by several techniques such as XRD, FTIR, SEM and TEM. The average size of as-synthesized Pd@ Ni_xB NPs on RGO were about 8-12 nm without any specific agglomeration as revealed by TEM. CV measurements of Pd@ Ni_xB /RGO nanocomposite for ethanol electrooxidation reaction (EOR) shows their promising electrocatalytic behavior. CV shows the high current density which was modified and increased upon cycling after 50 cycle, indicated the high catalytic activity and CO tolerance capability as compared to the unsupported Pd@ Ni_xB NPs. Further, CA measurement shows the better stability of the Pd@ Ni_xB /RGO nanocomposite compared to the Pd@ Ni_xB NPs which indicated the role of graphene support. For hydrolysis of $NaBH_4$ in alkaline medium we have successfully synthesized the Co-B@Ni/RGO nanocomposite by a facile method. TEM image clearly displays the superficial attachment of the Co-B NPs on Ni/RGO entity along with defects inside the graphene layers due the *in-situ* generated radical hydrogen. We provided the mechanistic explanation regarding H atoms interruption in catalyst cavity and their spillover and migration possibility. The synthesized Co-B@Ni/RGO nanocomposite exhibited their enhanced catalytic activity towards the hydrolysis of alkaline mix solution of $NaBH_4$. CV and impedance plot clearly shows the high charge storage capability and charge conductivity in Co-B@Ni/RGO nanocomposite which may provide the future commercialization of catalyst for complete energy application viz. H_2 production and charge storage together. Moreover, graphene based nanocomposites were used for 4-NP pollutant reduction to resolve the water pollution issue, and results shows

that high performance of all nanocatalysts with their robustness and recyclability for catalysis reaction.

Finally, graphene based nanocomposites has been employed for electrical and electronics applications such as fabrication of memristive device. In the work of activity-dependent modifications in Ni-doped graphene oxide thin films results clearly reflects the cumulative study of role of nickel metal for reduction of oxygen functionalities and changes in electronic behavior of graphene oxide (GO) which led the resistive switching (RS) behavior in thin film. Moreover, Ni/RGO nanocomposite also employed for glucose biosensing application and results shows their promising behavior for such an application.

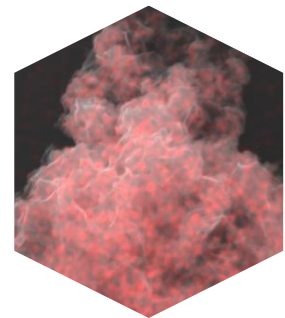
In summary, various kind of graphene based nanocomposites were synthesized and tested for many energy related applications in constraint lab proximities. The future efforts is bulk synthesis of graphene based nanocomposites in a more facile and cost effective manner. Further work will be focused on more detailed analysis and characterizations of graphene based transition metal doped nanocomposites, along with their durability testing for real field of energy applications to resolve the climate change issue and improvement of human life and sustainability of green planet.



Appendix

**Graphene
+
Transition metals**

- (i) Graphene conversion
- (ii) Graphene decoration
- (iii) Graphene multicatalytic applications



APPENDIX:**A1: Graphene conversion**

Graphene is the basic building block of low dimensional carbon materials such as carbon nanotubes (1D) and fullerenes (0D). As a truly two dimensional (2D) system graphene possess unique electronic properties compared to conventional semiconductors. In order to explore their remarkable properties in nanoelectronics, it would be highly desirable to produce a bandgap in graphene, and therefore, huge efforts have been made to explore the properties of one dimensional graphene. However, synthesis of one dimensional graphene structures with uniform dimension, morphology and chemical structure remains challenging. Recently, many hybrid structures of graphene reported including growth of carbon nanowire using chemical vapor deposition (CVD) at high temperature. Particularly, graphene cut into size <100nm categorized as one dimensional graphene or graphene ribbons, and due to this reason a specific electronics effect theoretically predicted in graphene nanoribbons which called as negative differential resistance (NDR). This NDR effect offers a variety of applications in nanoelectronics including amplification, logic and memory [1].

In the beginning, the graphene nanoribbons (GNRs) has been fabricated with specific well defined shapes by multistage cutting of graphene in the presence of nickel catalyst and emphasized the role of hydrogen as cutting tool. Later, several methods have also been developed to produce the GNRs such as plasma etching, ion implantation and laser annealing of graphene sheet. However, in all of these methods the experimental conditions beyond the ambient environment which limits the wide applicability of process [2].

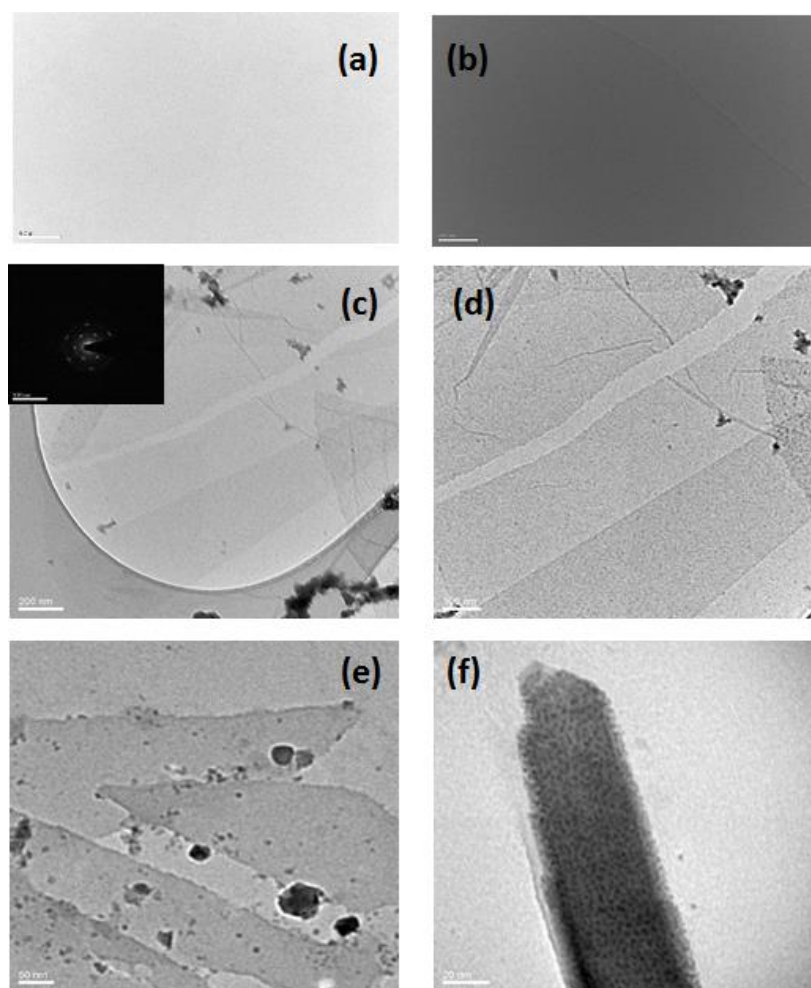


Figure A.2 (a,b) TEM images of GO. (c,d,e and f) TEM images of graphene nanobelts. Inset of c) shows the corresponding SAED of graphene and Ni NP.

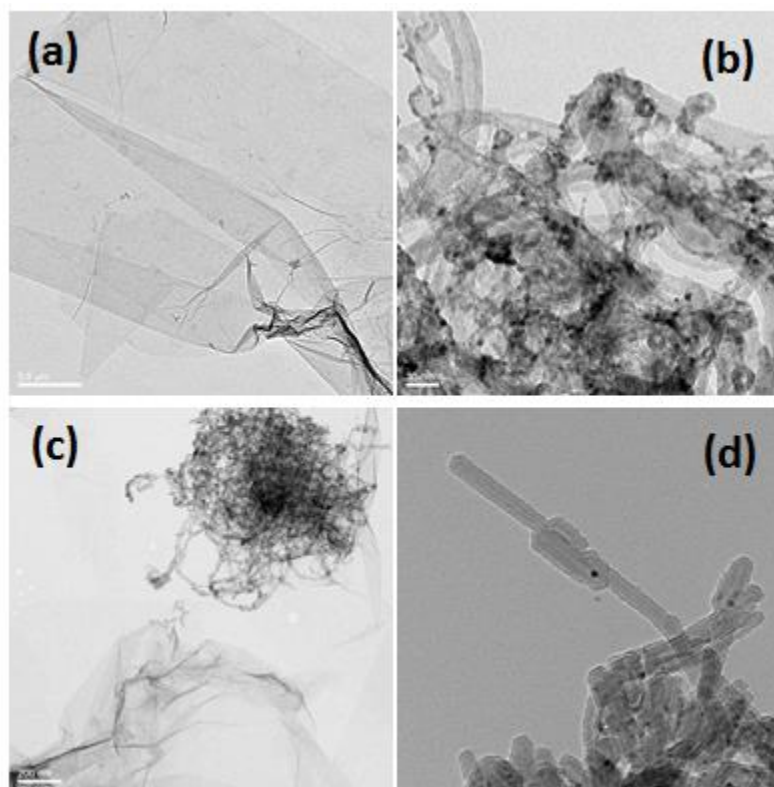


Figure A.3 Conversion of graphene to one dimensional array: (a) TEM images of GO. (b) and (c) TEM images of graphene tubes. (d) TEM image of graphene nanowire.

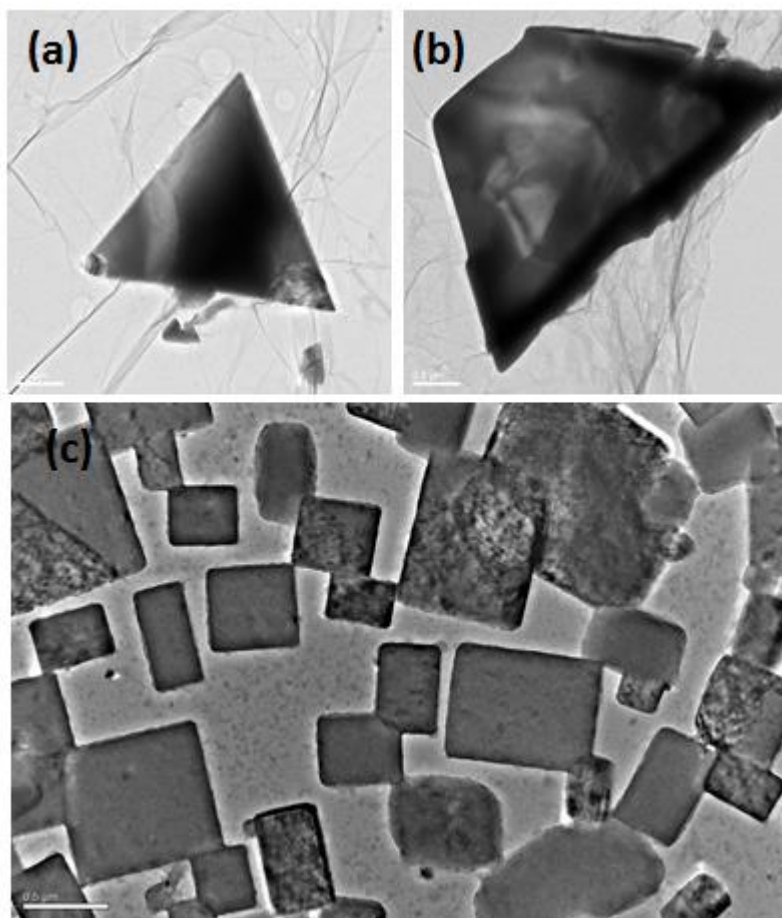


Figure A.4 Conversion of graphene to geometry (a) TEM images of graphene triangle. (b) TEM images of graphene parallelogram. (c) TEM image of graphene square and rectangle shapes.

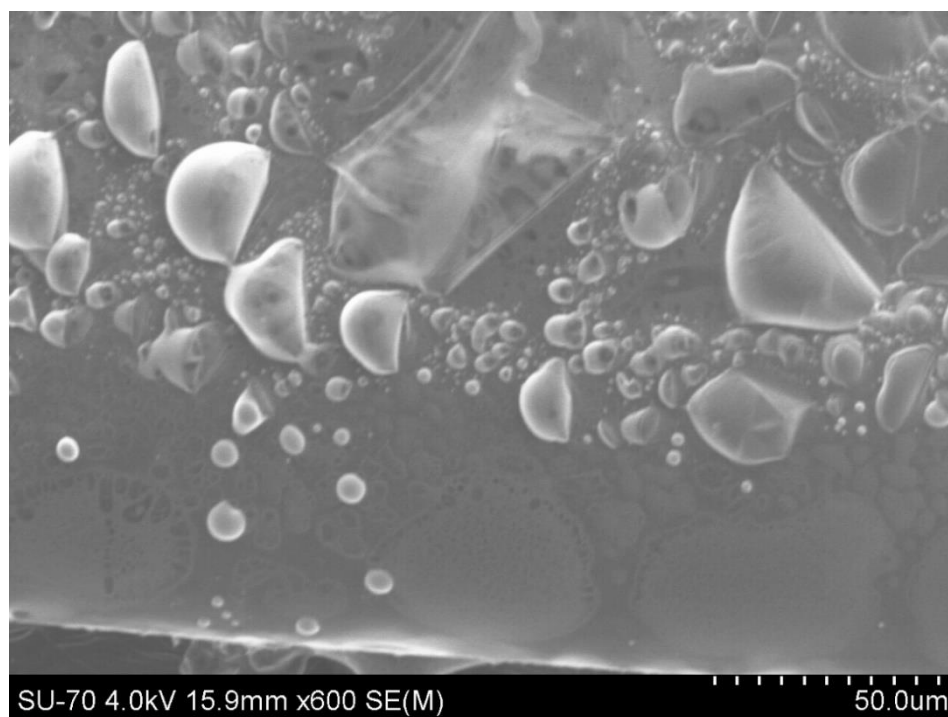


Figure A.5 Graphene fabrication: SEM image of graphene sheets stitching to graphene nano-balloons filled with H_2 gas can use for further energy transportation medium and for catalysis reduction reactions.

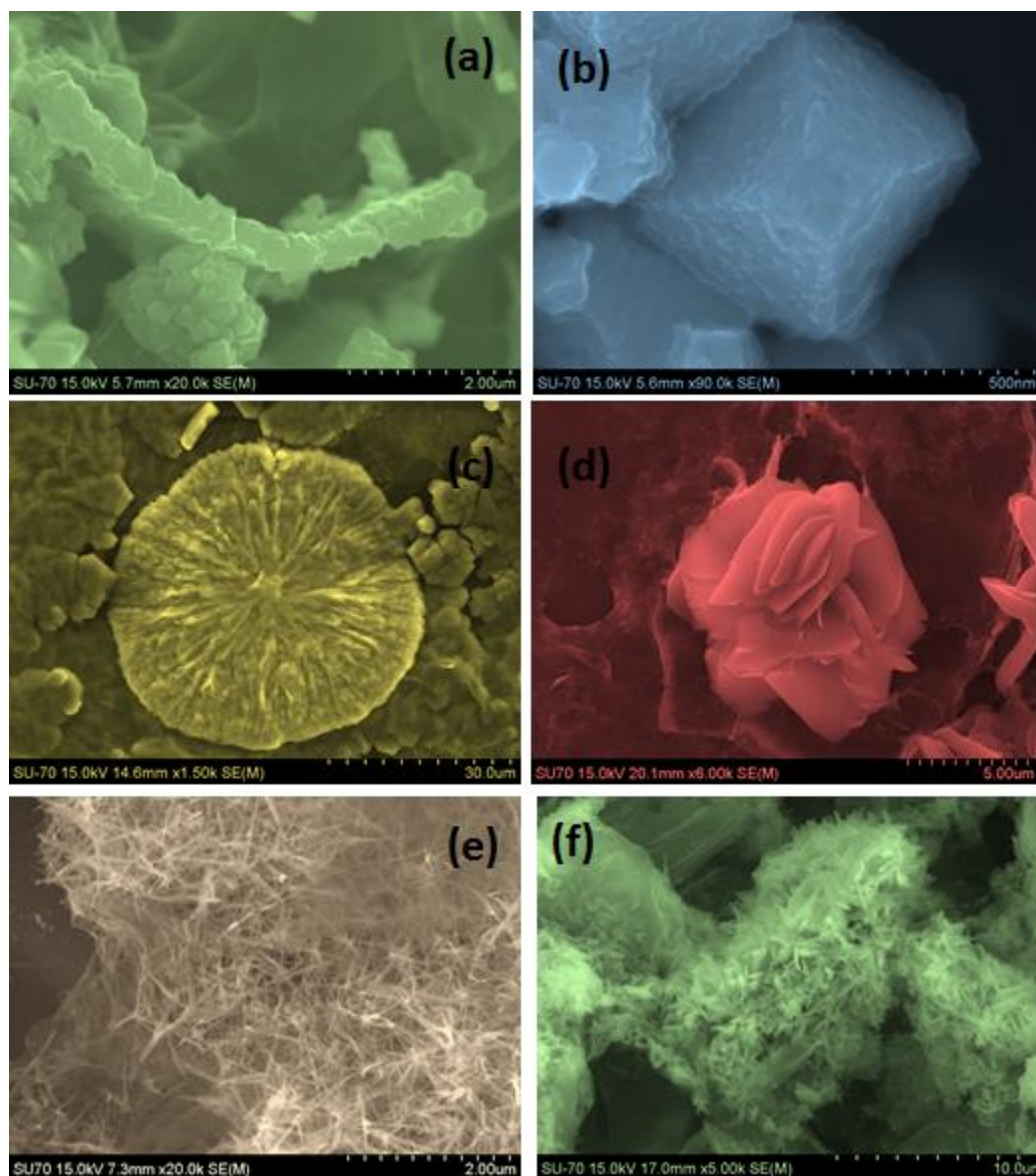
A2: Anchoring of graphene nanosheet with various type of NPs

Figure A.6 Graphene sheet decoration with different kind of NPs: SEM image (a) Cu NPs chain on graphene sheet. (b) Cu nanopyramid. (c) Ni NPs nanoflower on graphene. (d) Conversion of graphene sheets to nanorose with assistance of Cu^{2+} ions. (e) MnO_2 nanowire on graphene sheet and (f) One dimensional array of Ni/Ni(OH)₂ on graphene.

A3: Multicatalytic applications of Pd@Ni/RGO nanocomposite

- (i) Formic acid electro-oxidation [3]
- (ii) Potassium dichromate reduction [4]
- (iii) Methelene blue (MB) dye removal [5]

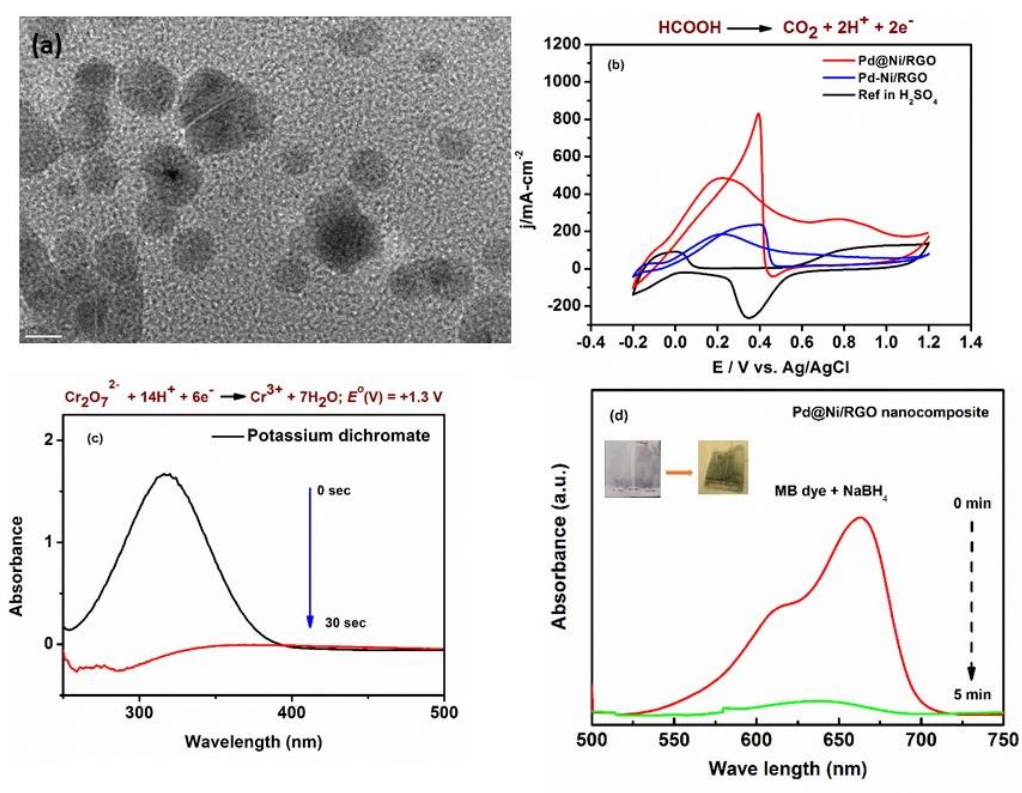


Figure A.7 (a) TEM image of Pd@Ni/RGO nanocomposite. Applications of Pd@Ni/RGO nanocomposite for various catalysis reactions (b) Electro-oxidation of formic acid, (c) Potassium dichromate reduction, and (d) MB dye reduction.

References

- [1] R. Krishna, E. Titus, M. Salimian, O. Okhay, S. Rajendran, A. Rajkumar, J. M. G. Sousa, A. L. C. Ferreira, J. C. Gil, J. Gracio. Hydrogen Storage for energy application, Intech Open, Europe (2012). ISBN: 978-953-51-0731-6, InTech, DOI: 10.5772/51238
- [2] L. Ci *et al.* Nano Res, 1 (2008), pp.116-122.
- [3] Y. She, Z. Lu, W. Fan, S. Jewell and M. K. H. Leung. J. Mater Chem, 2 (2014), pp.3894-3898.
- [4] K. Bhowmik, A. Mukherjee, M.K. Mishra, G. De. Langmuir, 30 (2014), pp. 3209-3216.
- [5] H. Ammar, L. Hinda, K. Mohamed, E. Elimame, G. Chantal, H. Jean-Marie. Appl Catal B, 31 (2001), pp. 145-157.